CHARACTERIZATION OF THE BASAL HYDRAULIC SYSTEM OF A SURGE-TYPE GLACIER: TRAPRIDGE GLACIER, 1989–92

by

DANIEL BURTON STONE

B.A., University of Colorado, 1988

A THESIS SUBMITTED IN PARTIAL FULFILLMENT OF
THE REQUIREMENTS FOR THE DEGREE OF
DOCTOR OF PHILOSOPHY

in

THE FACULTY OF GRADUATE STUDIES

Department of Geophysics and Astronomy

We accept this thesis as conforming
to the required standard

THE UNIVERSITY OF BRITISH COLUMBIA

April 1993

In presenting this thesis in partial fulfilment of the requirements for an advanced degree at the University of British Columbia, I agree that the Library shall make it freely available for reference and study. I further agree that permission for extensive copying of this thesis for scholarly purposes may be granted by the head of my department or by his or her representatives. It is understood that copying or publication of this thesis for financial gain shall not be allowed without my written permission.

(Signature) _____

Department of GEOPHYSICS & ASTRONOMY

The University of British Columbia
Vancouver, Canada

Date 30 APRIL 1993

ABSTRACT

Subglacial hydrology is a critical issue in understanding glacier and ice-sheet dynamics. This is especially true for surge-type glaciers, which are distinguished by their regular, quasi-periodic alternation between slow and fast flow regimes (Meier and Post, 1969); the fast flow during a surge is thought to be caused by rapid sliding brought about by sustained high basal water pressure. How sustained high pressures develop and how the subglacial distribution of water influences glacier sliding are fundamental unsolved questions.

We describe an investigation of the water drainage system beneath Trapridge Glacier, a surge-type glacier in Yukon Territory, Canada. We take two different approaches to characterizing the basal hydraulic system of the glacier. The first approach is *borehole response testing*, which involves changing the basal water pressure in the vicinity of a borehole and simultaneously observing the drainage system's response. We develop a theoretical model that describes the movement of water, induced by response tests, in a coupled borehole–subglacial flow layer. The model encompasses a broad range of flow regimes, from laminar Darcian flow in a thick permeable unit to turbulent sheet flow in a very thin layer. Important terms in the model are highlighted by a dimensional analysis. We show how the model can be used in numerical simulations to generate predicted data, which can be compared with field observations. We use our model as the basis for a formal inversion scheme that is aimed at objectively quantifying model parameters associated with subglacial water flow. Response test data from Trapridge Glacier are inverted to obtain estimates of hydraulic properties of the basal drainage system.

The second approach that we have taken involves direct measurement of the properties of subglacial water. Year-round measurements of subglacial water pressure, turbidity, and electrical conductivity were made at intervals ranging from 2–20 minutes

for three consecutive years. Turbidity and conductivity were measured using new subglacial sensors that we designed and constructed. The data in this study are unique and important because they were obtained directly at the glacier bed and because they span multiple summer and winter seasons. Spontaneous changes in the subglacial drainage system have been recorded and are sometimes accompanied by a release of stored basal water. In general, a single, stable drainage configuration cannot be identified. Instead, we infer a seasonal progression of drainage structures from the data. The complex behavior of the drainage system points to a dynamic subglacial environment, one in which the basal hydrology is governed by the combined influences of the glacier thermal regime, meltwater input, sediment movement, and mechanical interactions with the overlying ice.

TABLE OF CONTENTS

LIST OF TABLES

LIST OF FIGURES

LIST OF SYMBOLS

	Chapter 2
a	multiplication constant
G	electrical conductance (S)
I	current (A)
I_0	reference current (A)
$\mathcal{I}$	light intensity (cd)
$\mathcal{I}_0$	reference light intensity (cd)
K_c	cell constant (m^{-1})
L	light path length (m)
R	resistance (Ω)
R_0	reference resistance (Ω)
V	voltage (V)
V_0	reference voltage (V)
V_e	excitation voltage (V)
σ	electrical conductivity ($S\,m^{-1}$)
σ_s	conductivity of standard solution ($S\,m^{-1}$)
τ	turbidity (m^{-1})

	Chapters 3 and 4, Appendix B
a	multiplication constant
A	viscous energy loss weighting coefficient
b	thickness of subglacial aquifer (m)
B	kinetic energy loss weighting factor
c_f	skin friction coefficient
C	Chézy coefficient
C_1	defined constant ($BS_0(1-n)/8gn^3$)
C_2	defined constant ($4K^2C_1$)
d	diameter of spherical grains or circular conduit (m)

LIST OF SYMBOLS (con't.)

d_i	predicted datum
d_i^{obs}	observed datum
$\delta d_i^{\mathrm{obs}}$	estimated uncertainty in observed datum
D	diffusivity ($\mathrm{m^2\,s^{-1}}$)
$\mathbf{e}$	misfit vector
e_i	misfit of i^{th} datum, vector component
E	total data misfit
$E_{\%}$	percentage misfit
f_0	Darcy friction factor
F	force (N)
g	gravitational acceleration ($\mathrm{m\,s^{-2}}$)
h	height of water column (m)
h_0	initial hydraulic head, characteristic water column height (m)
h_{B}	hydraulic head at glacier bed (m)
h_{i}	thickness of glacier ice (m)
h_{s}	height of water column displaced by slug (m)
h_{T}	height of water column representing top surface forcing (m)
h_{w}	height of borehole water column (m)
h_z	elevation head (m)
$h^\star$	dimensionless water column height
$h_{\mathrm{B}}^\star$	dimensionless hydraulic head at glacier bed
$h_{\mathrm{T}}^\star$	dimensionless height of water column representing top surface forcing
H_{e}	effective water column height (m)
k	permeability of porous medium ($\mathrm{m^2}$)
K	hydraulic conductivity ($\mathrm{m\,s^{-1}}$)
m_i	model parameter
m_i^0	initial model parameter value
m_i^{est}	estimated model parameter value

LIST OF SYMBOLS (con't.)

δm_i^{est}	estimated uncertainty in model parameter value
M	number of model parameters
n	porosity
n'	Manning roughness coefficient
N	number of data
p	fluid pressure (Pa)
P	momentum ($kg\,m\,s^{-1}$)
q	fluid volume flux, specific discharge ($m\,s^{-1}$)
q_0	characteristic fluid volume flux ($m\,s^{-1}$)
$q^\star$	dimensionless fluid volume flux
r	radial coordinate (m)
r_0	characteristic radius (m)
r_f	filter radius (m)
r_w	well, borehole radius (m)
r'	non-dimensionalization constant (m)
$r^\star$	dimensionless radial coordinate
R	logarithmic radial coordinate
Re	Reynolds number
Re$'$	critical Reynolds number
S	storativity
S_0	solid surface to volume ratio (m^{-1})
S_s	specific storage (m^{-1})
t	time (s)
t_0	characteristic time (s)
$t^\star$	dimensionless time
T	transmissivity ($m^2\,s^{-1}$)
x	Cartesian coordinate (m)
α	solid skeleton compressibility (Pa^{-1})

LIST OF SYMBOLS (con't.)

β	fluid compressibility (Pa^{-1})
γ	exponent
ζ	skin friction parameter
η	dynamic viscosity ($kg\,m^{-1}\,s^{-1}$)
λ	trade-off parameter
ν	velocity of solids ($m\,s^{-1}$)
ξ	Ergun parameter
ρ_w	density of water ($kg\,m^{-3}$)
τ	shear stress (Pa)
v	fluid velocity ($m\,s^{-1}$)
$\bar{v}$	mean fluid velocity ($m\,s^{-1}$)
Υ	transmissivity parameter
Φ	objective function
Φ_d	data misfit component of objective function
Φ_p	parameter misfit component of objective function
χ	diffusivity parameter
	Chapter 6
A	cross-sectional area perpendicular to flow direction (m^2)
A_c	cross-sectional area of conduit (m^2)
A_T	total cross-sectional area of flow (m^2)
dh/dx	longitudinal head gradient
dh/dz	vertical head gradient
h	height of crevasse (m)
K	hydraulic conductivity ($m\,s^{-1}$)
L	length of crevasse (m)
n'	Manning roughness coefficient
q	specific discharge ($m\,s^{-1}$)
$\bar{Q}$	mean discharge ($m^3\,s^{-1}$)

LIST OF SYMBOLS (con't.)

r	radius of circle (m)
R	hydraulic radius (m)
Δt	time interval (h)
$\bar{v}$	mean fluid velocity ($\mathrm{m\,s^{-1}}$)
V_d	water volume input per day ($\mathrm{m^3}$)
w	width of crevasse (m)
θ	angle
	Appendix A
g	gravitational acceleration ($\mathrm{m\,s^{-2}}$)
h_B	hydraulic head at $\mathcal{P}(x,y,z)$ (m)
m_f	mass of fluid (kg)
m_s	mass of solids (kg)
n	porosity
p	fluid pressure (Pa)
p_0	reference fluid pressure (Pa)
p_a	atmospheric pressure (Pa)
$\mathcal{P}$	position in Cartesian coordinate system (m)
q_j	fluid volume flux vector ($\mathrm{m\,s^{-1}}$)
t	time (s)
V	volume of REV ($\mathrm{m^3}$)
x,y,z	Cartesian coordinates (m)
u_j	grain displacement vector (m)
u_x,u_y,u_z	components of grain displacenent vector (m)
α	solid skeleton compressibility ($\mathrm{Pa^{-1}}$)
β	fluid compressibility ($\mathrm{Pa^{-1}}$)
δ_{jk}	Kronecker delta
ϵ	incremental volume strain

LIST OF SYMBOLS (con't.)

ϵ_{jk}	incremental strain tensor
θ	fractional area
λ	Lamé constant (Pa)
μ	Lamé constant (Pa)
ν_j	velocity vector of solids ($\mathrm{m\,s^{-1}}$)
ρ_0	density of fluid at reference pressure ($\mathrm{kg\,m^{-3}}$)
ρ_f	density of fluid ($\mathrm{kg\,m^{-3}}$)
ρ_s	density of solids ($\mathrm{kg\,m^{-3}}$)
σ	incremental fluid pressure (Pa)
σ_{jk}	incremental total stress tensor (Pa)
σ'_{jk}	incremental effective stress tensor (Pa)
τ_{jk}	total stress tensor (Pa)
τ'_{jk}	effective stress tensor (Pa)
v_j	velocity vector of fluid ($\mathrm{m\,s^{-1}}$)
ψ	height of water column (m)
$\partial/\partial x_j$	differential vector operator (∇) ($\mathrm{m^{-1}}$)
d/dt	material derivative operator ($\mathrm{s^{-1}}$)
d^3r	infinitesimal volume unit ($\mathrm{m^3}$)

PREFACE

Portions of Chapter 2 dealing with turbidity and conductivity sensors have been accepted for publication by the *Journal of Glaciology* (Stone and others, 1992). Chapter 3 forms a separate paper which has also been accepted for publication by that journal (Stone and Clarke, 1992). Sections of Chapters 2 and 5 dealing with subglacial turbidity and water pressure variations were presented at the Fall Meeting of the American Geophysical Union held in San Francisco on 4–8 December 1989. The 1990 release event, discussed in Chapters 5 and 6, was the topic of a presentation at the Fall Meeting of the American Geophysical Union held in San Francisco on 7–11 December 1992. Preliminary results that have been incorporated into Chapters 4 and 5 were presented at annual meetings of Northwest Glaciologists held in Tacoma, Washington and Vancouver, British Columbia on 6–7 December 1991 and 4–5 December 1992 respectively.

ACKNOWLEDGEMENTS

This work could not have been completed without the help of a great many people. First of all I wish to acknowledge my advisor, Garry Clarke. He graciously contributed many fruitful ideas to this work and patiently watched as I worked through other, often less rewarding ones. Throughout it all he has provided advice, encouragement, and an outstanding example of how to work carefully and creatively.

I wish to express my gratitude to Erik Blake, for selflessly sharing both ideas and expertise (on a number of subjects) and for patiently helping me through the early days of my graduate research. Extended discussions with Tavi Murray and Jeff Schmok were very helpful. I was assisted in the field aspects of this study by a number of people; I especially wish to acknowledge Tavi Murray, Urs Fischer, Brian Waddington, Mathew Jull, Marc Gérin, and Paul Langevin. Critical scientific advice and guidance were given by my committee members R. Don Russell, J. Leslie Smith, and Tadeusz Ulrych, and by Uri Ascher and Robert G. Ellis. I am also grateful for the computing assistance and resources provided by Bob Barron and Rick Grubin of the National Center for Atmospheric Research.

This research has been supported by the National Sciences and Engineering Research Council of Canada, The University of British Columbia, Geddes Resources Limited, and Cominco Canada. Logistical support for the field work was provided by the Kluane Lake Research Station, operated by the Arctic Institute of North America.

Support from friends and family are necessary for the completion of any major piece of work. I am grateful to all my friends. I am especially grateful to my parents, who gave me a strong start in life and were always willing to let me choose my own way. Galen and Linnea receive special thanks for enduring my extended absences and for helping Mom during those times. If there were one thought that I could best express by words in this thesis, I would devote it to my wife, Maureen; that thought would contain my wholehearted appreciation for all that she has suffered through, and my sincere thankfulness for all that she has done.

Chapter 1

INTRODUCTION

"There is at present no reasonably complete theory of the flow of water beneath glaciers and ice sheets."

- J. Weertman, 1972

How water flows beneath glaciers is a central question of glaciology, having bearing on both practical and scientific topics. From a practical point of view, knowledge of subglacial water flow has important applications: (1) The sudden drainage of glacier-dammed lakes has resulted in extensive damage in many parts of the world, including Alaska, Canada, Iceland, and Peru. Also, glacier surges can pose serious threats to downstream structures. As communities, highways, and pipelines are developed in mountainous regions, prediction of glacier-dammed outbursts and sudden glacier advances becomes increasingly important; (2) In parts of Asia, Canada, and Europe, much of the water supply used for irrigation and generation of hydroelectricity comes from glacier-fed rivers. Forecasting the flow of these rivers is a significant concern, and requires an understanding of how water is stored in and moves through glaciers; (3) Water collected from beneath glaciers is used to generate hydroelectric power in the Alps and in Norway. The success of projects such as these depends on knowledge of where and how subglacial drainage takes place.

From a scientific point of view, the routing of subglacial water and its role in basal processes are important elements in understanding glacier and ice-sheet dynamics. Spatial and temporal changes in the subglacial drainage system influence basal sliding and are recognized as key factors in glacier surging. In turn, the subglacial drainage system affects basal sediments, deformation of which rearranges hydrologic passageways and contributes to glacier velocity. Subglacial hydrology is thus a critical issue in

studying the dynamics of temperate glaciers, as well as warm-based polar glaciers and ice sheets and many ice streams.

This thesis describes an investigation of the water drainage system beneath a surge-type glacier.

1.1 Glacier surging

Surge-type glaciers comprise a unique class of glaciers. They are distinguished by their regular, quasi-periodic alternation of slow and fast flow regimes (Meier and Post, 1969). The general characteristics of these glaciers are as follows: (1) Surge-type glaciers surge repeatedly and at intervals that, in many cases, are roughly constant for individual glaciers; (2) During a surge, ice speeds can increase by factors of 10 or more, promoting the rapid transfer of ice from an upglacier "reservoir area" to a downglacier "receiving area"; (3) The active surge period is short ($<$ 1 to $\sim$ 6 years) relative to the intervening quiescent phase ($\sim$ 15 to $>$ 100 years); (4) Between surges, ice mass accumulates in the reservoir area and is lost from the receiving area.

A small percentage of all glaciers are surge-type. Although they are found in several parts of the world, there are many glaciated regions in which none exist; they tend to be geographically concentrated. In western North America, surge-type glaciers have been identified in the mountain ranges of Alaska, Yukon Territory, and northwestern British Columbia (Post, 1969). There are no surge-type glaciers identified in other parts of British Columbia or Alberta, nor anywhere in the United States outside Alaska (Paterson, 1981). Even in regions where they do exist, only some glaciers will surge. Furthermore, their distribution within these regions is not random. In the St. Elias Mountains, for instance, the principle concentration of surge-type glaciers is centered near Steele Glacier in the northern end of the range (Clarke and others, 1986).

The phenomenon of glacier surging raises intriguing questions: (1) Why are surges periodic? (2) Why do only some glaciers surge, and not all? (3) What triggers a

surge? (4) How are surges sustained? (5) Are all surges governed by the same physical processes? The restricted geographical distribution of surge-type glaciers suggests that there is some environmental control on surging. Obvious factors like local climate, geologic setting, thermal regime, and glacier geometry have been considered (Post, 1969; Clarke and others, 1986; Clarke, 1991; Wilbur, unpublished; Hamilton, unpublished); none have been shown to fully explain surge behavior. However, it is now recognized that the fast flow of ice during a surge is caused by rapid sliding, which is brought about by sustained high basal water pressure (Raymond, 1987). How sustained high pressures develop and how the subglacial distribution of water enables rapid sliding are fundamental unsolved questions.

1.2 Previous work on subglacial water flow

Present understanding of subglacial water flow systems has been gained from theoretical deductions and, to a lesser extent, from field observations. Early studies of glacier sliding (e.g., Weertman, 1957; Lliboutry, 1958) considered basal water as a thin sheet or film between ice and bedrock. Weertman (1962) realized, however, that it is difficult to establish a water sheet of significant thickness, and Nye (1973) demonstrated that a thin sheet could not be the main agent for transferring meltwater down the glacier bed. As alternatives to sheet flow, drainage through discrete channel systems have been considered: Networks of conduits incised upward into basal ice (Shreve, 1972; Röthlisberger, 1972) are called R-channel or tunnel systems; water flow conduits etched downward into bedrock (Nye, 1973) are referred to as N-channels. Weertman (1972) examined the possibility that basal water flows through a network of coexisting ice tunnels and N-channels. Walder (1986) and Kamb (1987) have described subglacial drainage through interconnected water-filled cavities. A common component in all these theories is the view that the basal drainage system is located at the contact between clean ice and impermeable bedrock. An alternative view is that subglacial drainage

takes place over and through a permeable sediment bed (Boulton and Jones, 1979; Clarke and others, 1984; Shoemaker, 1986; Boulton and Hindmarsh, 1987; Clarke, 1987; Walder and Fowler, 1992).

Prior to the advent of hot-water drilling, direct connections with subglacial flow systems were generally limited to naturally occurring features, such as moulins and crevasses. In the last decade, hot-water drilling equipment and techniques have been developed and refined. The drilling of boreholes through glacier ice is now routine. Despite these advances, most field investigations of subglacial water flow have focused only on measuring one or more of the following quantities: basal water pressure, water input and output, and the transit time of a tracer from an injection point to an outlet stream. Of these, only water pressure is measured directly at the glacier bed.

Measurement of basal water pressure has been central to many glaciological investigations (Mathews, 1964; Iken, 1972; Hodge, 1976; Engelhardt, 1978; Hodge, 1979; Kamb and others, 1985; Iken and Bindschadler, 1986; Hooke and others, 1989; Engelhardt and others, 1990b). In comparison to measurements of water pressure, subglacial measurements of other properties related to basal water flow are rare. Engelhardt and others (1990a) measured the electrical conductivity of water beneath Ice Stream B in West Antarctica as part of a salt injection experiment. Blake (unpublished) measured d.c. resistivity and natural electrical potentials at the bed of Trapridge Glacier, Yukon Territory. Almost without exception, the data that are available have been collected during the few weeks of summer field seasons. Although the winter behavior of subglacial drainage systems is often discussed, there are virtually no data available to guide such discussions. Thus, there is a definite need for further observations of drainage system behavior on a year-round basis.

The most common method for studying subglacial water flow involves determining the velocity of a tracer that has moved through the drainage system (e.g., Stenborg, 1969; Krimmel and others, 1973; Behrens and others, 1975; Burkimsher, 1983;

Brugman, unpublished; Hooke and others, 1988; Seaberg and others, 1988; Willis and others, 1990; Fountain, 1992). Typically, salt or a fluorescent dye are used as tracers. Parcels of "naturally labeled" water having known, specific origins have also been used. Humphrey and others (1986), for example, used turbidity pulses in water flowing from beneath Variegated Glacier, Alaska, to estimate mean water velocity in the hydraulic system. Electrical conductivity has been used successfully by Collins (1979) as a basis for distinguishing between the surface melt and basal components of discharge from two alpine glaciers in Switzerland. Fountain (1992) used electrical conductivity and discharge measurements to infer the subglacial source regions of streams emerging from South Cascade Glacier in Washington State. An entirely different approach is to interpret subglacial flow conditions from the occurrence and spatial distribution of surficial deposits and landforms in recently deglaciated areas (e.g., Walder and Hallet, 1979). In all of these approaches, subglacial hydraulic conditions are inferred from proglacial observations. The work presented in this thesis is significantly different in this respect; we use a variety of measurements made directly at the glacier bed to characterize the basal drainage system.

1.3 Trapridge Glacier

1.3.1 Description

Our study was performed on Trapridge Glacier, a surge-type glacier located in the northern St. Elias Mountains, Yukon Territory, Canada (Fig. 1.1). The glacier is small (length $\approx$ 4 km, width $\approx$ 1 km), relatively thin (depth $\approx$ 80 m), and has an average surface slope of about 7° over the ablation area. The direction of ice flow is roughly 10° north of East. At present the glacier ranges in elevation from $\sim$ 2250 m to $\sim$ 2800 m.

Trapridge Glacier has a subpolar thermal regime; the melting point is reached only near the bed, and temperate basal ice is bounded by a margin of cold ice at subfreezing temperatures. Furthermore, the glacier rests on a sediment substrate which

is water-saturated and deforming (Blake, unpublished; Blake and others, 1992). These conditions influence both subglacial water flow and ice dynamics, as evidenced by the surface hydrology (discussed below) and the glacier geometry. A striking feature of Trapridge Glacier in its present state is the vertical ice cliff at the glacier terminus (Fig. 1.2b). This cliff develops from a wave-like bulge that forms over the boundary between warm- and cold-based ice (Clarke and others, 1984). Clarke and Blake (1991) have shown that the zone of transition from warm- to cold-based ice migrates down-glacier, but at a slower rate than that of the bulge.

The bulge also marks the boundary between the reservoir and receiving areas. Observations from 1969 to the present show that Trapridge Glacier has been gradually accumulating ice mass upstream from the bulge and, concurrently, losing mass from the area downstream (Clarke and Blake, 1991). Remnant ice below the present terminus position has almost completely disappeared; thus, the entire receiving area is now virtually deglaciated.

1.3.2 Surge history

Trapridge Glacier last surged sometime between 1941 and 1949. Sharp (1947) described the glacier as "advancing rapidly" in July 1941, but photographs taken by Sharp in 1941 do not clearly indicate that a surge was in progress at this time. There is also some uncertainty in the timing of the last surge because the present geometry of Trapridge Glacier is similar to that of the 1941 photographs, and the glacier is not currently surging (Fig. 1.2). There are no reported observations of Trapridge Glacier between fall 1941 and summer 1949 when Sharp observed from the air that "the glacier was advanced far beyond its terminal position of 1941" (Sharp, 1951, p. 111). Subsequent aerial photographs, taken in 1951 as part of a photogrammetric survey by the Canadian Government, clearly show that a surge had taken place (Clarke and others, 1984, Fig. 3).

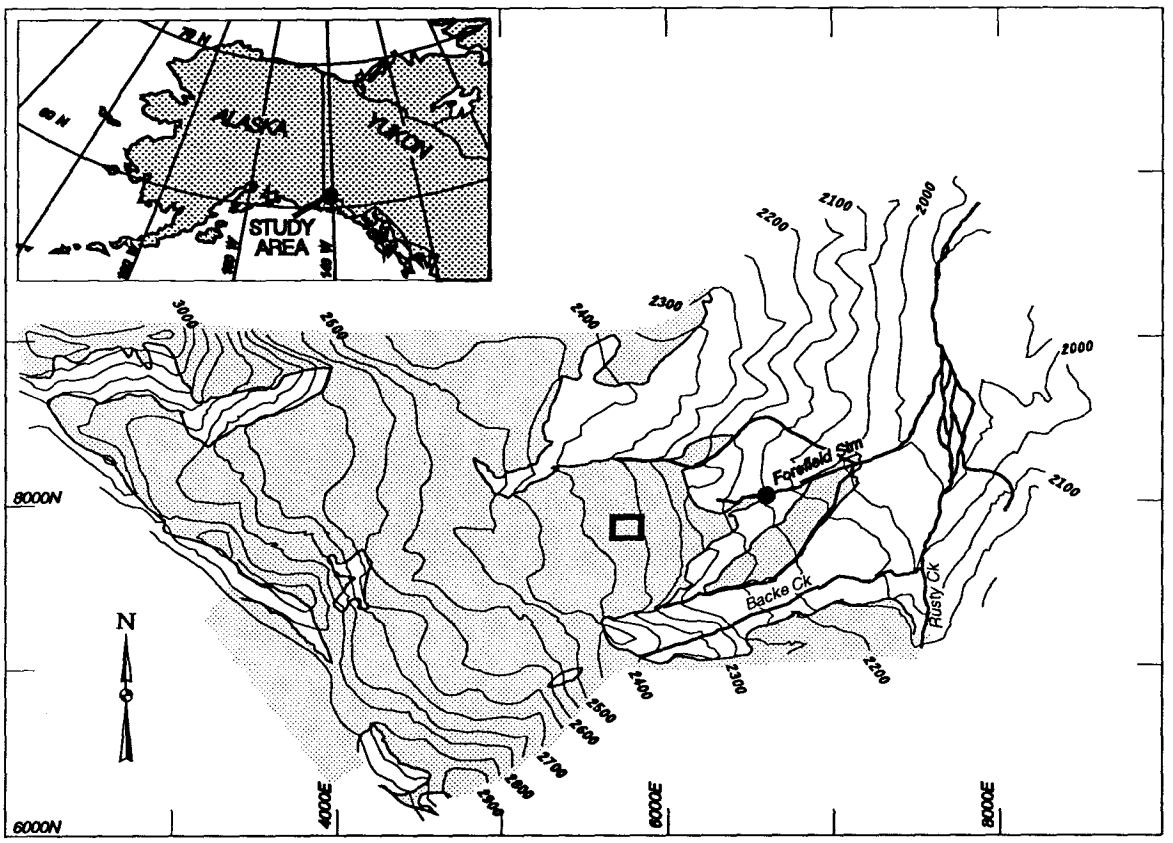

Fig. 1.1: Trapridge Glacier study site. (a) Location map of the study site in southwestern Yukon Territory. (b) Topographic map of Trapridge Glacier. The shaded area represents glacier ice, based on 1981 aerial photography. Surface streams are indicated by heavy lines. Data discussed in this thesis were collected in a central region in the ablation area, indicated by the rectangular box. The location of the forefield stream site is shown by the solid circle.

Based on the terminus position shown in the 1941 and 1951 photographs, the glacier advanced more than 1 km in this interval.

1.3.3 Geologic setting

Trapridge Glacier is situated in the Steele Creek drainage basin, which discharges into the Donjek River. The geology of this basin has been described by Sharp (1943). Near the glacier, bedrock consists of low-grade metamorphic carbonates and highly

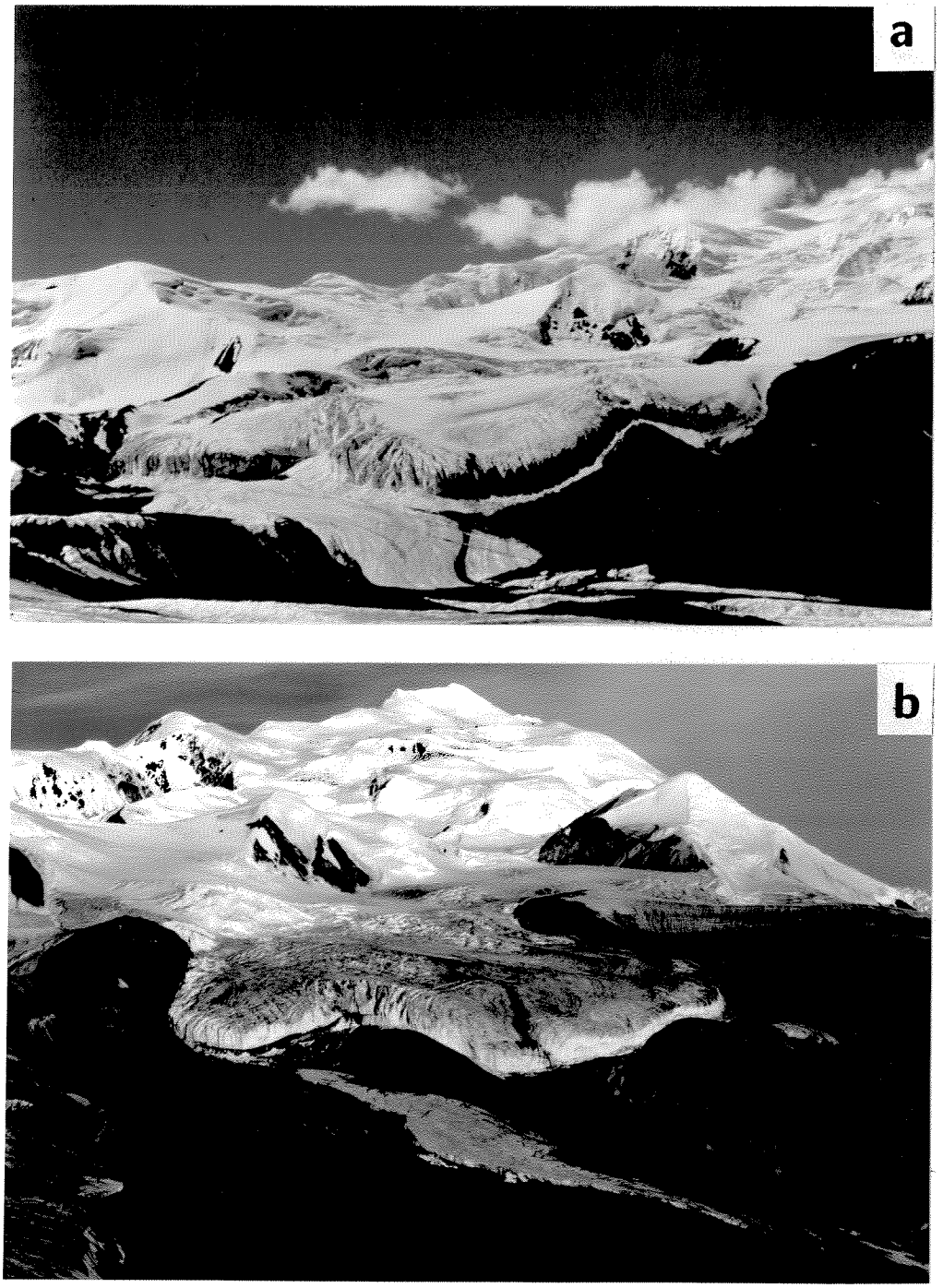

Fig. 1.2: Trapridge Glacier, 1941 and 1989. (a) Photograph taken 7 July 1941 by R. P. Sharp. (b) Photograph taken 27 July 1989 by D. B. Stone. Note the two sediment-covered ridges that emerge at the front of the glacier, one on each side of the center moraine. Stream cuts in the proglacial sediments are visible between the ridges.

fractured basalts. Granitic intrusions are found in the headwalls directly above the glacier. In the glacier forefield—the presently deglaciated region immediately in front of the terminus—portions of two bedrock ridges are exposed. These ridges are aligned nearly parallel to the direction of ice flow and are being overridden by the glacier as it advances. A thick (up to $\sim 10\,\mathrm{m}$), poorly-sorted alluvial deposit lies in the depression between the ridges. Both the ridges and the alluvium are covered by a layer of till having variable thickness (roughly 0–3 m). Between the bedrock ridges, the forefield sediments are deeply cut by a network of stream channels. The ridges and the stream channels are evident in Figure 1.2b.

1.3.4 Surface hydrology

Three surface streams flow from Trapridge Glacier: one from the north margin, one from the south margin, and a central stream between the bedrock ridges (Fig. 1.1). All three streams merge before they reach Rusty Creek at the bottom of the valley. In this thesis we will only be concerned with the central "forefield" stream; our work has focused on the central part of the glacier where lateral subglacial drainage is discouraged by the two bedrock ridges. As part of our investigation, we have collected water samples and monitored the forefield stream at a site located above its confluences with the two marginal streams. Both the glacier study area and the forefield stream monitoring site are shown in Figure 1.1.

The forefield stream consists of an arborescent network of channels deeply incised into the proglacial sediments. Meltwater from the glacier surface pours off the terminal ice cliff and feeds the stream. Except for occasional "release events" (discussed in Chapter 5), there are no clear indications that subglacial water is carried by the forefield stream. Unlike many warm-based glaciers, subglacial water flow is not concentrated in large channels at the terminus of Trapridge Glacier; the upper branches of the forefield

stream do not emanate from beneath the glacier. Where exposed, proglacial sediments in direct contact with the vertical terminus are frozen to the ice.

Within 100 m of the present terminus position the forefield stream cuts become deep ($\sim$ 5 m), and structural features in the proglacial sediments are exposed; cross-bedding is found lower down in the alluvial deposit, and both the alluvium and the overlying till are cut in places by nearly vertical intrusions of a dark silty material. In addition to these features, seeps and small water flows emerge from the sediment walls. The seeps and flows typically occur in the alluvial deposit and are not consistently associated with any particular structure or contact.

1.4 Thesis overview

A persistent question is how water is evacuated from the central glacier bed. Clarke and others (1984) hypothesized that subglacial drainage takes place as groundwater flow, passing beneath the frozen region near the terminus. This idea has been supported by the 1985–86 fieldwork of Christopher Smart (Smart and Clarke, submitted). The research presented in this thesis also indicates that groundwater flow is an important component of the subglacial drainage system. Our work, however, takes important steps beyond earlier investigations; we provide quantitative estimates of the hydraulic properties that govern water flow through the basal sediments, and we present multi-year, *in situ* measurements of properties related to the flow of subglacial water. These records demonstrate that the subglacial drainage system has a complex behavior which is only partially revealed during short, mid-summer windows of observation.

In this thesis we discuss two different approaches that we have taken to characterize the basal hydraulic system of Trapridge Glacier. The first approach is *borehole response testing*, which involves changing the basal water pressure in the vicinity of a borehole and simultaneously observing the drainage system's response. Data collected

during response tests can be used to estimate subglacial hydraulic properties. In Chapter 3 we develop a theoretical framework for borehole response tests. Because turbulent conditions are sometimes encountered when these tests are performed on glaciers, standard groundwater flow models cannot adequately describe the observed responses. Our development includes turbulent effects, and thus leads to new theoretical refinements. We also demonstrate how our theory can be applied to field data. We use our theory in formal inversions of response test data collected on Trapridge Glacier to quantify hydraulic properties of the basal drainage system. These estimates are the first *in situ* determinations of hydraulic conductivity and compressibility of a subglacial porous medium. The inversion methodology and our results are discussed in Chapter 4.

The second approach that we have taken involves direct measurement of the properties of subglacial water. In Chapter 5 we present measurements of basal water pressure, turbidity, and electrical conductivity that were made directly at the bed of Trapridge Glacier. Turbidity and conductivity were measured with new subglacial sensors that we developed as part of this study. The measurements were made at intervals ranging from 2–20 minutes for three consecutive years; at present, these observations comprise the only *in situ* multi-year record of the behavior of a subglacial hydraulic system. Interpretation of these data has led to a qualitative characterization of the basal drainage system, which is the subject of Chapter 6.

Field observations are the basis for the work presented in this thesis. Thus, we begin in Chapter 2 with a description of our subglacial instruments and their field usage.

Chapter 2

SUBGLACIAL INSTRUMENTATION

The data presented in this study were obtained from three different types of sensors: pressure, turbidity and electrical conductivity. The sensors were installed in boreholes that had been drilled to the glacier bed using a high-pressure, hot-water system. Measurements obtained with these sensors provide direct indications of basal hydraulic conditions, water flow, and subglacial provenance. The pressure sensors that we used are standard commercial products that we modified for protection in the subglacial environment. The turbidity and electrical conductivity sensors have been designed and built by us specifically for use beneath glaciers. In this chapter we describe the construction, calibration, and field usage of these instruments.

2.1 Pressure

2.1.1 Description of the device

To measure subglacial water pressure we use commercially available sensors that give an output voltage proportional to pressure. The sensors are compatible with corrosive media and typically have a pressure range of 0–2 MPa (0–300 psi). Because it is impractical to provide an atmospheric reference, we use "absolute" or "sealed-gage" devices; "absolute" sensors measure pressure in reference to a vacuum whereas "sealed-gage" sensors are referenced to a standard atmosphere. To protect sensors from mechanical destruction in the subglacial environment we encase them in casting resin, leaving only the pressure port exposed.

2.1.2 Calibration

We calibrate pressure sensors in water-filled boreholes as follows: Each sensor is connected to a length of wire that is sufficient to reach the glacier bed. The wire is marked

with vinyl tape just above the sensor, and every 10 m thereafter. The distance between the first tape mark and the pressure sensor diaphragm defines the "offset", which is included when calculating the true depth of the sensor. The sensor is suspended in a water-filled borehole and allowed to come to thermal equilibrium. Once equilibrated, the sensor is lowered into the borehole until the first tape mark touches the top surface of the water column. The sensor is held in this position while the depth and output voltage are recorded. The sensor is then lowered to the next tape mark and the measurement/lowering process continues until the bottom of the borehole is reached. Measurements are also taken as the sensor is pulled up out of the borehole.

For an ice thickness of ~70 m this procedure gives roughly 16 independent measurements of sensor output voltage as a function of water depth. More data points could be added by halving the distance between tape marks, but we have found this to be unnecessary. Because output voltage is proportional to pressure within the specified operating range of the sensors, we use the method of linear least squares to obtain regression coefficients for each sensor. The coefficients obtained by this procedure allow pressure sensor output voltage to be converted to a static water column height above the sensor.

2.2 Turbidity

2.2.1 Description of the device

The basic components of the turbidity sensor are a light source, two photodetectors, and a voltage regulator (Fig. 2.1a). For the light source we use a miniature incandescent lamp manufactured by Spectro (part no. 8097). This source provides nearly spherical illumination, thereby reducing geometric constraints on construction. Because the intensity of an incandescent source will change if the supply voltage varies or if the filament degrades, we use two detectors—a reference detector that monitors an internal light path through the sensor, and a sample detector that monitors a

light path through the water gap. We use photo-Darlington detectors (Motorola, part no. MRD711) having a spectral response centered at $\sim$ 940 nm. These detectors are amplified phototransistors and act as current sources, passing a current proportional to the flux of infrared-wavelength photons incident upon the transistor base.

In constructing turbidity sensors, caution must be exercised to prevent the detectors from operating under optically-saturated conditions; this is especially important for the reference detector. Under saturated conditions, detectors are insensitive to changes of source intensity. To prevent saturation, we have found that the intensity of incident light can be reduced, when necessary, by partially covering the detector faces with small pieces of black electrical tape.

If the sensor is in thermal equilibrium with its surroundings, variations in reference measurements result only from changes in source intensity, assuming that there is no variation in ambient light. Sample-detector measurements depend on the source intensity and on the number of infrared-wavelength photons that pass through the water gap; because our sensors are transmission devices, more photons reach the sample detector when the path is unobstructed than when intervening scatterers are present. As explained later, turbidity measurement is based on the ratio of currents from the reference and sample detectors.

A series 7800 voltage regulator provides a constant 8 V supply for the light source and for collector inputs of the detectors (Fig. 2.1b). By including the regulator as part of the sensor assembly, voltage variations due to different lead wire lengths or changes in voltage of the surface power supply are unimportant, provided that the regulator is adequately supplied. In addition to the basic components, a small signal diode (1N4148) and a capacitor (0.1 μF) are used to protect and stabilize the regulator (Horowitz and Hill, 1989, p. 341). Two 1 kΩ resistors serve as loads on the emitter outputs of the detectors. To minimize wire costs, the entire circuit operates on four

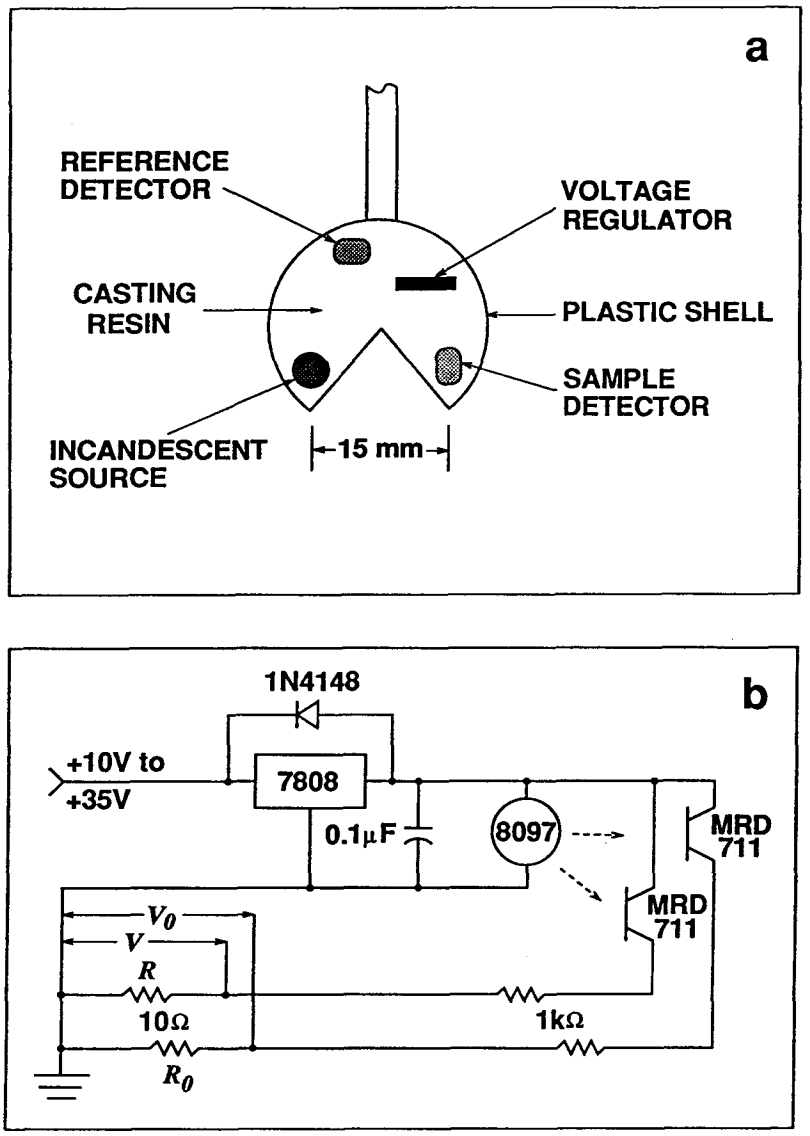

Fig. 2.1: Turbidity sensor schematic and circuit diagram showing the relative positions and physical connections of electronic components. (a) The basic components are an incandescent light source, two infrared photo-Darlington detectors—one for the reference light path and one for the light path through the water sample, and a voltage regulator. These components are housed in a plastic shell and then sealed in a casting resin that does not degrade in the presence of mineralized water. (b) Circuit diagram for turbidity sensor and voltage measurement. Shown in this diagram are the unregulated supply voltage from the surface (upper left), the sensor components (middle and right), and the voltage measurement circuit (lower left).

conductors: one for each detector, one for the voltage regulator supply, and one for ground.

As shown in Figure 2.1a, the sensor components are housed in a spherical shell out of which a wedge has been cut; we have found that table tennis balls work well for this purpose. Our design has two important features: it is small enough to fit down unreamed boreholes, and the wedge-shaped water gap reduces the possibility that the sample path will become clogged. The electronic components inside the plastic shell are sealed in a casting resin. In selecting a casting material, chemical reactions of the resin with mineralized water must be considered. We have found that Sun Cure—a clear laminating resin available from Industrial Formulators of Canada—is excellent. The sensor is cast in a two-stage process. First, the sensor is positioned so that one of the planes forming the wedge provides a level surface; one half of the sensor is then filled with resin and allowed to harden. When this stage is finished, the sensor is rotated so that the other wedge plane is horizontal, and the remaining portion of the sensor is cast.

2.2.2 Calibration

Turbidity is usually defined as the reduction in intensity of a beam of light passing through a suspension:

$$\frac{\mathcal{I}}{\mathcal{I}_0} = \exp(-\tau L) \tag{1}$$

where $\mathcal{I}$ is the intensity of light after passing through a length L of suspension, $\mathcal{I}_0$ is the intensity of the unobstructed light beam, and τ is the turbidity (Kerker, 1969; Melik and Fogler, 1983; Gregory, 1985). In general, phototransistors have nonlinear behaviour over the full collector–emitter voltage range. However, for small changes the response is approximately linear (Bliss, 1983 p. 4-13). Under these conditions there is a

direct relation between the photo-induced current I and the intensity of incident light, $I \propto \mathcal{I}$, and Equation (1) can be rewritten as

$$\frac{I}{I_0} = \exp(-\tau L) \tag{2}$$

where I_0 is the current induced by the unobstructed light beam. To use expression (2), the value of I_0 must be known. However, we cannot simultaneously measure the intensity of incident light through both "clear" and turbid paths with the same detector. Thus we employ the reference detector to monitor an internal path and provide an approximate measure of I_0. Solving Equation (2) for τ, and using Ohm's law to rewrite current in terms of voltage V and resistance R, we obtain

$$\tau = -\frac{1}{L} \ln\left(\frac{R_0 V}{R V_0}\right) \tag{3}$$

where subscripted quantities refer to the reference circuit. The turbidity sensors we have described employ nearly identical components in close proximity. Under these conditions $R_0 \approx R$, and the last expression reduces to

$$\tau = -\frac{1}{L} \ln\left(\frac{V}{V_0}\right). \tag{4}$$

There are several factors that complicate measurement of the actual intensity of the undisturbed beam by the reference detector: (1) the source may not be a perfect isotropic radiator; (2) the detectors are not identical and may not be optimally oriented; (3) the separation distances between the source and each detector may be different; (4) the reference and sample light paths can have different optical properties, even when the sensor is not in a suspension. Because of these factors, we include a positive constant a that multiplies the reference voltage—in essence allowing correction of the measured reference intensity. With this modification, Equation (4) becomes

$$\tau = -\frac{1}{L} \ln\left(\frac{V}{a V_0}\right). \tag{5}$$

It is possible to estimate the value of a for a given sensor by measuring the voltages from both detectors when the sensor is in "clear" water. In this case $\tau \approx 0$ and, from Equation (5), we see that $a = V(\text{clear})/V_0$. We have made these measurements for a number of sensors and have found that values of a are in the range $0.6445 \leq a \leq 1.006$. For some of our early, prototype sensors the necessary calibration measurements were not made; when this information is unavailable we ordinarily set $a = 1$. Equation (5) defines our usage of the term "turbidity". With this relation, turbidity sensor calibration entails measuring the water gap path length L and estimating a reference intensity correction value for the constant a.

For subglacial measurements, a calibration relating τ to suspended sediment concentration is unrealizable, since it requires detailed knowledge of suspension properties or representation of the suspension based on a limited number of samples. Caution against using such calibrations is clearly advised by manufacturers of commercial turbidity sensors:

> Because several factors affect the intensity of light scattering, it is inaccurate to relate scattered light measurements directly to the number or weight concentration of suspended solids. Direct correlation can be done only if suspended solids factors such as size distribution, shapes, refractive indices and absorptivities remain constant and only the concentration changes—an impractical consideration in many cases.

(Hach and others, 1990, p. 4). We have made numerous laboratory tests in which the suspended sediment concentration, for a given grain size distribution, was carefully controlled. Our investigations have shown that turbidity depends strongly on the grain size distribution of the suspension; smaller grains comprising less total mass can produce turbidity values much greater than larger grains having more total mass. To be fully accurate the size, number concentration, and light scattering properties of all

particles in the suspension must be known at all times. This requirement is further complicated if the suspension is not uniformly mixed. Because such information is unavailable, turbidity sensors are sometimes calibrated by collecting samples of the suspension while readings are being made, then subsequently analyzing the samples to determine sediment concentration (e.g., Humphrey and others, 1986). While this procedure may be suitable for surface streams, it cannot be applied to subglacial water flow because a large number of samples cannot be easily collected from the glacier bed and because samples that are collected will likely be altered by the time they reach the glacier surface. For these reasons we have not used turbidity readings to estimate suspended sediment concentration of subglacial water.

2.3 Electrical conductivity

2.3.1 Description of the device

The electrical conductivity sensor consists of two parallel cylindrical electrodes embedded side-by-side in a nonconducting material and housed in a protective tube (Fig. 2.2). The electrodes are stainless steel rods 6.35 mm (0.25 in) in diameter and 76.2 mm (3.0 in) long. They are press-fit into a pre-drilled, solid nylon cylinder having a diameter of 25.4 mm (1.0 in) and a length of 50.8 mm (2.0 in). The rods extend 6.35 mm (0.25 in) from the measurement end of the nylon cylinder and are separated by a center-to-center spacing of 12.7 mm (0.5 in). To allow solder connections for lead wires, small brass pins are inserted into the interior ends of the rods. The brass pins are placed in pre-drilled holes and fixed to the rods with a flux and low-temperature solder that bonds to stainless steel. The entire assembly is placed in a section of ABS or PVC conduit 101.6 mm (4.0 in) long and having an inside diameter of 25.4 mm (1.0 in). The conduit is then filled with an electrically-insulating casting resin. Important features of this design are similar to those previously discussed for our turbidity sensors: small

size, and a geometry that reduces the possibility of clogging. Additionally, the use of stainless steel minimizes electrode corrosion.

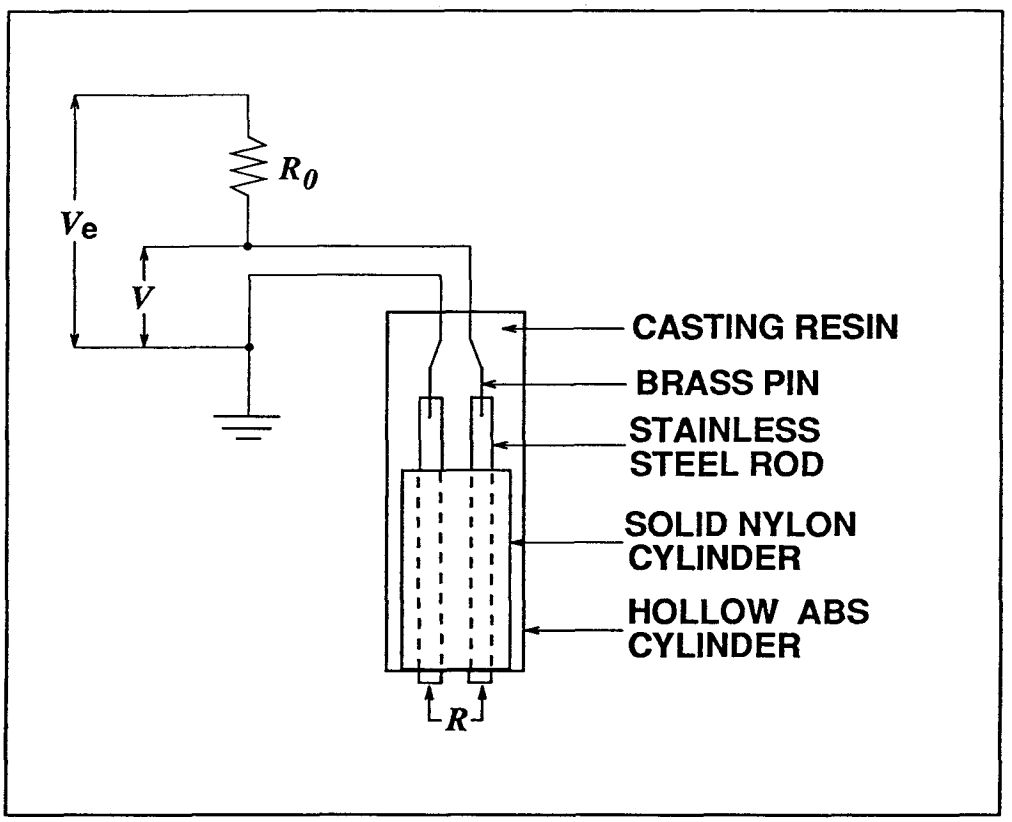

Fig. 2.2: Electrical conductivity sensor showing basic design and measurement circuit. Stainless steel rods are press-fit into a pre-drilled, solid nylon cylinder. To allow solder connections for lead wires, brass pins are inserted into the interior ends of the rods. The entire assembly is placed in a section of ABS or PVC conduit, which is then filled with casting resin. With this device the conductance of basal water can be determined by means of an a.c. half-bridge measurement.

2.3.2 Calibration

A standard reference solution is required for conductivity sensor calibrations. We prepare our own reference solutions using potassium chloride and freshly distilled water, but conductivity standards are also available from commercial suppliers. According to

Jones and Bradshaw (1933), a 1 kg solution containing 0.745263 g of KCl in distilled water in a vacuum will have a conductivity of $0.07736\,\mathrm{S\,m^{-1}}$ at 0° C. Our standard solutions are prepared in air by dissolving ~ 0.7452 g of KCl in enough distilled water to yield exactly one liter. The conductivity of our standard solution differs slightly from that described by Jones and Bradshaw (1933) because we have implicitly assumed that one liter of solution weighs exactly 1 kg, and because we have not applied a vacuum correction. Nevertheless, discrepancies arising from differences in the preparation procedures are small and do not appreciably influence calibration accuracy.

The reference solution is used to obtain a cell constant value for each sensor. The cell constant K_c is the constant of proportionality between conductivity σ and conductance G:

$$\sigma = K_c G. \tag{6}$$

The cell constant depends on sensor geometry and has dimensions $[\mathrm{L}^{-1}]$. For simple geometries, K_c can be analytically determined if the inter-electrode distance and electrode surface areas are known. Unfortunately, conductivity sensors having simple geometries, such as parallel plates or concentric cylinders, tend to accumulate debris between the electrodes when used in a glacial environment. Our sensors have been designed to avoid clogging. Because of this design, the cell constants cannot be determined analytically. Thus, values for K_c are found by submerging the electrodes in the standard solution and measuring the resistance R between them. Since $G = 1/R$, measured resistances can be multiplied by the known conductivity σ_s of the standard solution to obtain the cell constants:

$$K_c = R\,\sigma_s. \tag{7}$$

Electrical conductivity of aqueous solutions is strongly dependent on temperature because the conduction process is electrolytic and ion mobility always increases with

temperature. To minimize the effects of temperature variation, our standard solution is held constant at 0° C throughout the calibration procedure. To achieve this, we pass a cooled fluid through a curved copper tube that has been placed in the bottom of the solution container. The solution is continuously stirred during calibrations to ensure a uniform temperature distribution.

In a given year, all sensors are simultaneously calibrated in the same solution. Typically, we record solution temperature and sensor readings at 2 minute intervals for at least 40 minutes using Campbell CR10 dataloggers. To approximate the conditions under which our sensors are used in the field, we apply an excitation of 250 mV and use a nominal reference resistance of 10 kΩ (±2%) for each sensor. (The measurement procedure is described in the following section.) For each sensor, the mean value of the set of measurements is computed. These values are then used to calculate individual cell constants according to Equation (7).

2.4 Field usage

2.4.1 Inclinometry

Many of our applications require accurate knowledge of the spatial position of sensors. For instance, networks of pressure sensors are used to calculate the hydraulic gradient field, and turbidity and electrical conductivity are used to estimate the rate and direction of basal water flow. To accurately locate the bottoms of boreholes we include inclinometry as a standard part of our installation procedure. Before sensors are installed, we use a custom-designed inclinometer to determine the bottom displacements of boreholes relative to their surface positions; the surface coordinates are determined by surveying. The inclinometer and procedure that we use has been described in detail by Blake and Clarke (1992). With this system, we are able to determine the subglacial locations of sensors to an accuracy of 20–30 cm.

2.4.2 Installation

We position our sensors ~ 0.25–0.5 m above the bottom of the borehole. If a sensor is placed too low, it may become packed with debris or sheared by glacier motion; if a sensor is placed too high, it will be removed from the active flow region. For solitary sensors, weight must be added to promote sinking. If all three types of sensors are to be installed in the same borehole, we usually place the conductivity sensor immediately above the turbidity sensor and the pressure sensor ~ 0.25 m above the others; we fix their relative positions using self-vulcanizing tape. Once in place, the sensors are tethered by their lead wires to an ice screw at the surface.

2.4.3 Measurement procedures

The pressure sensors we use have strain gauges bonded to their diaphragms in Wheatstone bridge configurations. A measurement is obtained from one of these sensors by providing an excitation voltage to the device and recording the differential voltage across opposite nodes of the bridge (Horowitz and Hill, 1989, p. 1001). This procedure is easily accomplished with Campbell dataloggers.

As illustrated in Figure 2.1b, a turbidity reading is obtained by measuring the voltage drop across a $10\,\Omega$ precision resistor for both the reference and sample detectors. The measured voltages are used, with Equation (5), to calculate turbidity. Before the first measurement is made, the lamp is turned on and allowed to warm up for 2 s. We delay 0.5 s between measurements to allow switching transients to decay. Power to the sensor is then turned off until the next measurement is to be made.

Electrical conductivity is measured using the circuit shown in Figure 2.2. To avoid polarization effects, the sensor voltage is measured twice in quick succession, with the excitation voltage polarity reversed between measurements. The two readings are averaged to obtain a single value. This procedure constitutes an a.c. half-bridge

measurement and is a standard function on Campbell dataloggers (Campbell Scientific, 1989). The conductance is obtained from the following relation:

$$G = \frac{1}{R_0}\left(\frac{V_e}{V} - 1\right) \tag{8}$$

where V_e is the excitation voltage, V is the measured voltage, and R_0 is the reference resistance. Conductance values, obtained by this procedure, are combined with the known cell constants according to Equation (6) to obtain conductivity. For optimal performance, values of V_e and R_0 should be chosen to maximize output fluctuations within the measurement range. Typically, we use an excitation voltage of $V_e = 250\,\mathrm{mV}$ and a reference resistance of $R_0 = 10\,\mathrm{k}\Omega$.

2.5 Discussion

We have run all three types of sensors at intervals ranging from 2–20 minutes for more than a year without failure. The continuous records we have obtained with these instruments are evidence of their reliability and longevity. An attractive feature of the turbidity and electrical conductivity sensors is their low cost; the parts for either sensor can be obtained for roughly $10 U.S.

Because of their low cost, it is feasible to deploy subglacial arrays of turbidity and electrical conductivity sensors. Arrays of these sensors can be used to estimate the rate and direction of water flow at the bed. For instance, when boreholes connect with the subglacial drainage system, nearby sensors register turbidity and conductivity pulses. Conductivity sensors can also be employed in borehole-to-borehole tracer tests, using ordinary salt as the tracer.

In some respects the subglacial environment is better suited than the subaerial one for measurements of pressure, turbidity and electrical conductivity. Although risk of mechanical destruction is a concern, the absence of thermal fluctuations is advantageous

to all three types of sensors. For turbidity sensors the complete absence of ambient light is a major benefit.

Lastly, and of greatest importance, the best approach to studying subglacial drainage is to monitor water flow *in situ*, rather than rely on inferences based on proglacial observations.

Chapter 3

THEORY OF BOREHOLE RESPONSE TESTS

3.1 Introduction

It is widely recognized that subglacial water flow systems play a key role in regulating the motion of glaciers and ice streams. However, understanding of the morphologies and hydraulic properties that characterize subglacial flow systems remains incomplete. Perhaps nowhere is the influence of the basal drainage system on glacier motion better demonstrated than in the case of a glacier surge. This is embodied in the review by Raymond (1987): "A pivotal question in the surge mechanism concerns the cause of buildup of stored water and high basal water pressure. ... Major questions concerning how water flows in a distributed system of basal cavities or other passages and how this water affects sliding need to be addressed."

In this chapter we seek to characterize subglacial flow conditions by estimating hydraulic parameters that regulate water flow at the bed. In what follows, we develop a theoretical model of water motion in a coupled borehole–subglacial flow system. Our approach does not follow the traditional view that clean ice overlies rigid bedrock. Instead, we present the model with the idea that glacier ice can rest on unlithified permeable sediments. This picture of the glacier bed is suggested by the observations of Boulton and Jones (1979), Clarke and others (1984), Alley and others (1986), Blankenship and others (1986), Boulton and Hindmarsh (1987), and Engelhardt and others (1990b). The description we present is cast in terms of groundwater flow through a saturated porous medium (Boulton and Jones, 1979; Shoemaker, 1986; Clarke, 1987); however, our mathematical characterization also allows consideration of other distributed flow configurations: flow as a sheet or thin film between ice and

bedrock (Weertman, 1957 and 1964; Lliboutry, 1968; Kamb, 1970), flow through interconnected water filled cavities (Walder, 1986; Kamb, 1987), and distributed channelized flow, either through an ice–bedrock network (Weertman, 1972) or over basal sediments (Boulton and Hindmarsh, 1987; Walder and Fowler, 1992). For interconnected cavities or distributed channel networks, physical descriptions of the actual flow systems are not given by our model; instead these systems are represented, in a general way, as permeable units having equivalent hydraulic characteristics. Although the theory is relevant to many subglacial flow regimes, our model does not apply to certain drainage configurations. Flow through a single channel incised upward into basal ice (Röthlisberger, 1972; Shreve, 1972) or downward into bedrock (Nye, 1973) is not described by our model because such configurations do not constitute widespread interconnected sets of flow paths.

To focus our discussion, basal water flow will be represented as occurring beneath a glacier that rests on a saturated substrate through which a significant amount of water is transmitted. In hydrogeologic terminology, an aquifer is a layer, formation, or group of formations of geologic material, saturated with water, and having a high degree of permeability (de Marsily, 1986). Thus, the glacier bed we consider will be referred to as a subglacial aquifer.

In groundwater studies, well response tests are commonly used to evaluate aquifer properties. These tests consist of disturbing the equilibrium hydraulic head in the aquifer by changing the amount of water in a well and observing the equilibrium recovery, either in the same well or in nearby wells. In the simplest case a parcel of water is suddenly removed from an equilibrated well and water level in the well is monitored until the predisturbed value is regained. In an analogous technique, boreholes through a glacier that penetrate a confined basal aquifer can be used to observe fluctuations of hydraulic head within the confined layer. Surprisingly, application of this technique has received little attention in glaciological studies. Hodge (1976) measured water level

drops in boreholes while drilling through South Cascade Glacier, Washington. He also reported inducing damped oscillations by suddenly displacing water in the boreholes with the drill tip. Engelhardt (1978) described borehole water level fluctuations in Blue Glacier, Washington that were induced by pumping additional water into the borehole. He used these observations to obtain "insight into the hydraulic characteristics of the interconnecting passageways" beneath Blue Glacier. Christopher Smart (unpublished) has measured borehole drainage rates and the responses of boreholes following episodes of pressurization and release. Engelhardt and others (1990a) have observed the rates of water level lowering as boreholes reached the base of Ice Stream B in Antarctica.

We begin by developing a theoretical framework for borehole response tests. Following this we examine important physical aspects of the model, as highlighted by dimensional analysis. We use a dimensionless formulation to predict the responses of coupled borehole–subglacial water flow systems having different hydraulic characteristics. Next, we demonstrate how the theoretical description is used to estimate hydraulic parameters by comparing model results with data collected in 1989 and 1990. We conclude with a discussion of the model, its limitations, and its generalization to a wide range of subglacial flow regimes.

3.2 Theory

3.2.1 Types of disturbance

In the following sections we present a model that simulates the response of a coupled borehole–aquifer system to three different types of disturbance, corresponding to field observations that we have made. One type of response occurs when a water-filled borehole is suddenly opened to the basal aquifer. Such a situation arises, for instance, when the bed is reached by hot water drilling and the borehole becomes connected to the subglacial flow system. We refer to this process as a connection-drainage disturbance. Another type of response is observed when the water level in an open borehole connected

to the basal aquifer is displaced from its equilibrium position and allowed to recover. The simplest way of inducing this type of response is to lower a sealed pipe into the borehole, wait a sufficient amount of time for the water level to re-equilibrate, and then quickly remove the pipe. This procedure is widely used in groundwater studies and is commonly referred to as a slug test. A slightly more complicated test involves pressurizing the air in a borehole that is sealed at the top and observing the response when the pressure is suddenly released. Because it is difficult to seal the borehole perfectly, in practice the pressure is usually released before the water level has stabilized. We refer to this type of disturbance as a packer test.

High flow velocities are rarely encountered in most subsurface hydrologic applications. Thus, standard groundwater flow models (e.g., Cooper and others, 1965; van der Kamp, 1976) typically neglect energy losses in the borehole and the effects of turbulent flow. During a connection-drainage disturbance, however, a substantial volume of water can drain from the borehole in a short period of time. Under these conditions, water flow may be turbulent, both in the borehole and in the subglacial aquifer near the borehole. Because flow velocities can be significant in some of the situations that we will consider, energy loss terms and turbulent effects will be included in the following development.

3.2.2 Motion of water in the borehole

Water flow in a borehole of radius r_w is described by the parameters shown in Figure 3.1. Following standard procedures for well response analyses (e.g., Cooper and others, 1965; van der Kamp, 1976; Kipp, 1985), a well screen or filter of radius r_f is included as part of the geometrical description. Such filters are not actually used in our field studies, but disturbances at the bottom of the borehole due to drilling likely result in excavations that are conveniently represented by a filter. To facilitate treatment of water flow between the borehole and the subglacial aquifer, it is assumed that the

filter fully penetrates the permeable layer and that flow into or out of the borehole is uniformly distributed across the entire aquifer thickness.

In the case of Trapridge Glacier, response tests sample a basal aquifer that is confined above by the glacier ice and below by a thin aquitard of low-permeability till. This aquitard, in turn, overlies thicker units having higher degrees of permeability. These sediment layers are indicated in the inset in Figure 3.1; the hydraulic conductivity of the basal flow layer K_1 is presumed to be much greater than the conductivity of the aquitard K_2. The overall subglacial sediment structure and its implications for the drainage conditions beneath Trapridge Glacier are discussed in detail in Chapter 6.

For packer tests, water level fluctuations are induced by sealing the borehole at the top, pressurizing it, then suddenly releasing the pressure. The pressure rise p during these tests can be expressed as the height h_T of a water column that would produce an equivalent fluid pressure at its base: $p = \rho_w g h_T$, where ρ_w is water density and g is the acceleration due to gravity. Thus, for packer tests, the disturbance can be represented as a downward-directed surface force acting on the top of the water column:

$$F_{top} = -\pi {r_w}^2 \rho_w g h_T. \tag{3.1}$$

For connection-drainage disturbances and slug tests there are no additional pressure forcings; hence, $h_T = 0$ in these cases.

When water in the basal aquifer is stationary, the borehole water level represents the static or piezometric head in the immediate vicinity of the borehole bottom. Under these conditions piezometric head is equivalent to hydraulic head (de Marsily, 1986, p. 51). When water flows in the basal aquifer, hydraulic head increases as kinetic energy is gained by the fluid; the increased hydraulic head is manifested as a rise in the borehole water level. In either case, hydraulic head $h_B(r,t)$ in the basal aquifer acts to regulate the borehole water level. Assuming that the water column height is much greater than the aquifer thickness b, and that $h_B(r,t)$ is uniform over the distance

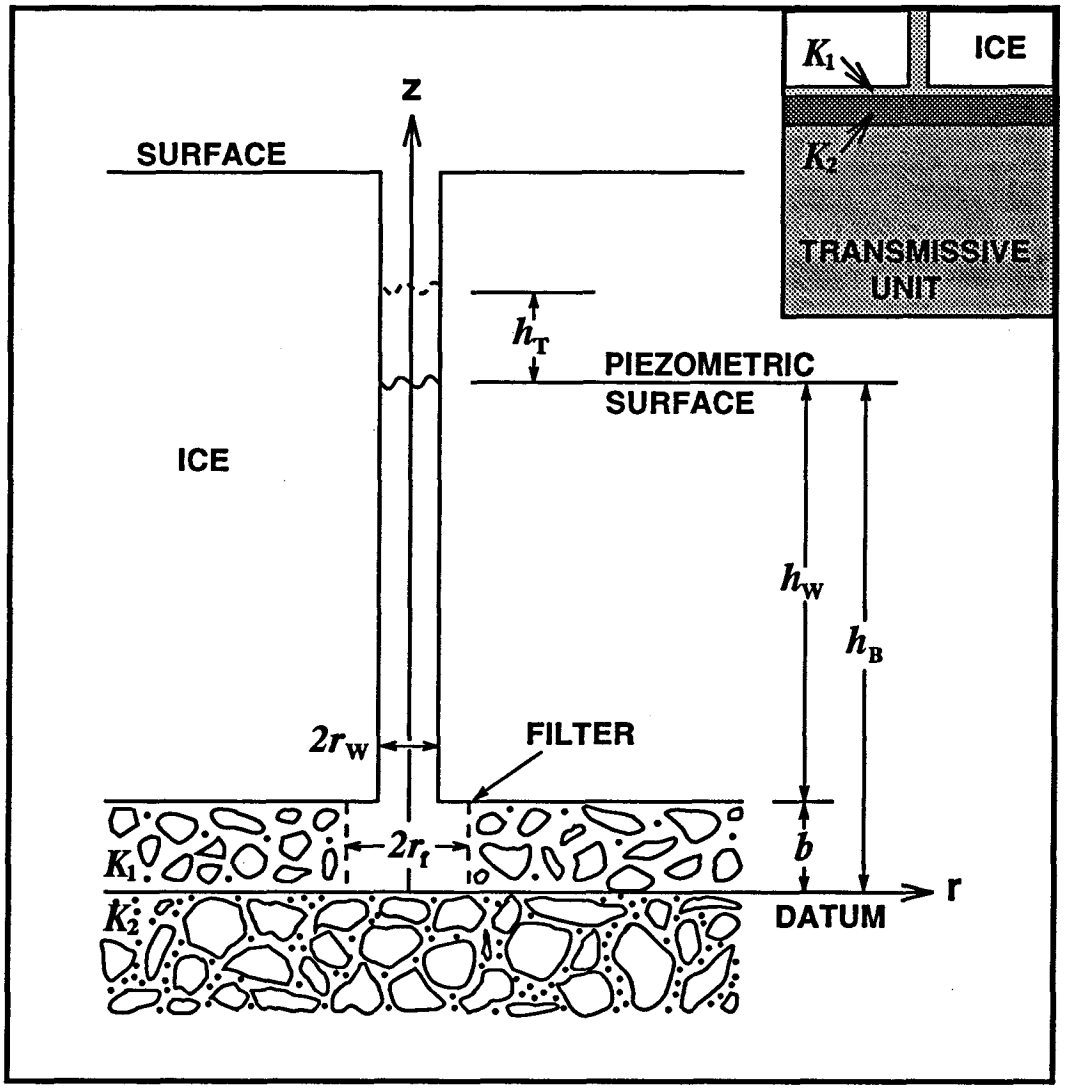

Fig. 3.1: Model geometry showing parameters and variables that regulate flow in the vicinity of a borehole. A basal layer of uniform thickness b and hydraulic conductivity K_1 is assumed to rest on an aquitard having conductivity $K_2 \ll K_1$. In the case of Trapridge Glacier, the aquitard is thin and rests on thicker units having higher degrees of permeability, as shown in the inset. Water from a borehole of radius r_w is introduced into the flow layer at the filter radius r_f. Disturbances causing water to enter or leave the basal aquifer are produced by suddenly changing the borehole water column height h_w or by changing the pressure acting at the top of the borehole. In the model, the pressure change is expressed as the height h_T of a water column that would produce an equivalent fluid pressure at its base. In the absence of flow, the piezometric surface represents the hydraulic head h_B in the basal aquifer.

of the filter radius, hence $h_B(r \leq r_f, t) = h_B(0, t)$, the upward-directed surface force supporting the water column is

$$F_{\text{bottom}} = \pi {r_w}^2 \rho_w g h_B(r_f, t). \tag{3.2}$$

If τ_0 is the frictional shear stress acting at the wall of the borehole, the force exerted by the borehole wall on the water column is

$$F_{\text{side}} = 2\pi r_w h_w \tau_0 \tag{3.3}$$

where h_w is the height of water above a point at the bottom of the borehole. In fluid mechanics, it is customary to define the skin friction coefficient c_f in a long pipe by

$$c_f = \frac{2\tau_0}{\rho_w \bar{v}^2} \tag{3.4}$$

where $\bar{v}$ is the mean fluid velocity in the pipe (Kay and Nedderman, 1985, p. 170). Thus, the frictional force acting on the water column can be expressed as

$$F_{\text{side}} = -\pi r_w \rho_w h_w c_f \operatorname{sgn}(\bar{v}) \bar{v}^2 \tag{3.5}$$

where $\operatorname{sgn}(x)$ is the algebraic sign function (Bracewell, 1978, p. 61); this is included to account for the fact that the frictional force acts in a direction opposite to the mean velocity. The downward-directed gravitational body force acting on water in the borehole is

$$F_{\text{body}} = -\pi {r_w}^2 \rho_w g h_w. \tag{3.6}$$

If we assume that $\bar{v}$ represents a uniform water velocity over the borehole cross-section, and that water compressibility is a negligible component of the rate of change of water column height, we have

$$\bar{v} = \frac{dh_w}{dt} = \frac{dh}{dt} \tag{3.7}$$

where $h(t) = h_w(t) + b$. In this case the momentum P of water in the column can be written as

$$P = \pi {r_w}^2 \rho_w h_w \frac{dh}{dt}. \tag{3.8}$$

The total force acting on the water column will be equal to the rate of momentum outflow across the bottom surface of the borehole plus the rate of change of momentum in its interior. Thus,

$$\begin{aligned} \frac{d}{dt}\left(\pi {r_w}^2 \rho_w h_w \frac{dh}{dt}\right) - \pi {r_w}^2 \rho_w \left(\frac{dh}{dt}\right)^2 = &- \pi {r_w}^2 \rho_w g h_T + \pi {r_w}^2 \rho_w g h_B(r_f, t) \\ &- \pi r_w \rho_w h_w c_f \operatorname{sgn}\left(\frac{dh}{dt}\right)\left(\frac{dh}{dt}\right)^2 \\ &- \pi {r_w}^2 \rho_w g h_w \end{aligned} \tag{3.9}$$

where terms involving water column velocity have been rewritten in accordance with (3.7). The first term is the time rate of change of momentum of the water column, the second is the flux of momentum across the borehole base,* and the righthand-side terms correspond to the sum of forces expressed by Equations (3.1), (3.2), (3.5), and (3.6).

---

* The second term in Equation (3.9) was not originally present in this work; in the course of reviewing this thesis, its omission was pointed out by Dr. Charles Raymond. The model results presented here, and in the following chapter, were obtained from expressions that did not include this term. We have subsequently tested our original results by including this term and recomputing modeled solutions. The tests that we made included "worst-case scenarios" in which the momentum transfers were significant. Our test results showed no visibly-discernable variations from the originally modeled solutions. Numerically, the omission of this term amounted to discrepancies of less than one part per thousand. Because of the insignificant contribution of this term, our original results are still valid to the stated accuracy.

In general, the skin friction coefficient in (3.9) depends on both the Reynolds number Re and the wall roughness (Prandtl, 1952). For a pipe of internal diameter d, the Reynolds number expresses the ratio of inertial to viscous forces: $\mathrm{Re} = \rho_w \bar{v} d/\eta$, where η is the dynamic viscosity of the fluid and $\bar{v}$ is its mean velocity. Because our present concern is only with straight vertical conduits in ice, we will assume that wall roughness can be neglected. With this assumption, the relationship between the skin friction coefficient and Reynolds number is of the form

$$\begin{aligned} c_f &= a\,\mathrm{Re}^{-\gamma} \\ &= a\left(\frac{\eta}{\rho_w \bar{v} d}\right)^{\gamma} \end{aligned} \tag{3.10}$$

where a and γ are positive constants. For Reynolds numbers $\lesssim 2000$ the flow in a smooth pipe will be laminar with $a = 16$ and $\gamma = 1$; otherwise, for values of Re up to about 10^5, the flow will be turbulent with $a = 0.079$ and $\gamma = 0.25$ (Kay and Nedderman, 1985).

Boreholes through glaciers usually have small radii compared to their lengths; a typical borehole through the ice of Trapridge Glacier has a radius of 0.05 m and a length of 70 m. Thus, we consider a borehole to be a long smooth pipe. If water velocity in the borehole is such that $\mathrm{Re} \lesssim 2000$, the laminar form of (3.10), combined with the momentum conservation expression (3.9), leads to

$$h\frac{d^2h}{dt^2} + \left[\left(\frac{8\eta}{\rho_w {r_w}^2}\right) h\frac{dh}{dt}\right] + gh = g\left(h_B(r_f, t) - h_T\right). \tag{3.11}$$

Equation (3.11) is the differential equation that describes the height of water h in the borehole at any time t. In writing the final form of this expression, we have made use of two previous assumptions; namely, $\bar{v} = dh/dt$ and $h_w \gg b$, so that $h \approx h_w$. Also note that $\mathrm{sgn}\,(dh/dt)$ does not appear in the frictional term because direction is given by the velocity, which now appears to the first power. The skin-friction coefficient will be slightly underestimated by Equation (3.11) when $2000 \lesssim \mathrm{Re} \lesssim 10^5$. As we will

show, however, skin friction is a minor component of the borehole–aquifer system. Thus, switching from the laminar to the turbulent form of (3.10) represents a small correction to an insignificant term. For these reasons, we will simplify our model and not consider a separate friction coefficient for turbulent flow in the borehole.

The standard approach to interpretations of slug tests in a transient mode involves type curve analysis (Papadopulos and others, 1973), and is based on an expression given by Cooper and others (1967). In different developments, expressions describing displacement of the water level from an initial position of equilibrium in a coupled well–aquifer system have been derived by Cooper and others (1965) and by Kipp (1985). Like Equation (3.11), these expressions were based on conservation of momentum. Kabala and others (1985) used the framework of Cooper and others (1965) in numerical modeling of the responses of well–aquifer systems to sudden changes of water levels. In their developments, Cooper and others (1965) and Kipp (1985) neglected loss of momentum due to skin friction. It was shown by van der Kamp (1976) that this term is important only in cases where the well radius is very small (say ≤ 0.01m), or when oscillations are slowly damped, or if the initial displacements are large compared to the well radius. Because some of our observations include large initial displacements, we will retain all of the terms in Equation (3.11).

3.2.3 Motion of water in the aquifer

Movement of water in the basal aquifer is assumed to obey the following balance equation:

$$-\frac{\partial q_j}{\partial x_j} = \rho_w g(\alpha + n\beta)\frac{\partial h_B}{\partial t} \tag{3.12}$$

where q_j is the fluid volume flux vector (specific discharge), n is porosity, and α and β are constant compressibility coefficients for the porous medium and the fluid respectively. Equation (3.12) is based on conservation of fluid and solid mass and is a standard

expression appearing in many developments of the equation of transient groundwater flow (Jacob, 1940; De Wiest, 1966; Cooper, 1966; Gambolati and Freeze, 1973; Bear and Verruijt, 1987); a derivation of Equation (3.12), which highlights the underlying assumptions, is given in Appendix A. In summary, the assumptions made in the development of (3.12) are as follows: (i) displacements of solid grains occur only in the vertical direction; (ii) thickness and density of the overlying material are constants and atmospheric pressure fluctuations are negligible; (iii) temporal changes in fluid pressure are much greater than the rate at which pressure gradients are advected by motion of the solid skeleton; (iv) the fractional change in the fluid volume flux is much greater than the fractional change in fluid density. We recognize that the first assumption is valid only if horizontal deformations of the sediments can be disregarded with respect to the vertical deformations. Verruijt (1969) has explored this assumption and has shown that in some cases—though not all—the errors introduced by this assumption will be negligible. The second assumption is justified by the observation that time scales of overburden pressure variation are much greater than the duration of a response test. Assumption (iii) will be of questionable validity in some cases, as mentioned by Gambolati and Freeze (1973). However, for the situation with which we shall be concerned—purely radial fluid flow—assumption (iii) will automatically be satisfied if assumption (i) is true; under these conditions the fluid and solid skeleton velocities are orthogonal and there will be no advection of pressure gradients due to skeleton displacements. The final assumption also seems reasonable because the fluid we are concerned with is water, which is only very slightly compressible; thus we expect that the fractional change in fluid density will be extremely small.

For borehole response tests, the time scales over which observations take place are usually much smaller than the normal time scales over which hydraulic head in a subglacial aquifer varies. In the case of Trapridge Glacier, subglacial water pressure typically varies over a period of hours, whereas the duration of a borehole response test

is, at most, a few minutes (Fig. 3.2). Furthermore, because our disturbances are small compared to natural pressure variations, it is likely that response tests influence only a local portion of the glacier bed in the vicinity of the borehole. Thus, response tests represent small brief perturbations. For these reasons, we suggest that the following simplification is reasonable: the region immediately surrounding the borehole can be treated as a horizontal and homogeneous aquifer in which the pressure gradient will be independent of azimuth for the duration of a response test. If we also assume that the aquifer is isotropic, we can restrict our attention to one-dimensional radial flow in the region surrounding the borehole.

We wish to combine Equation (3.12) with a constitutive relation that is applicable to large flow velocities; the range of small discharges for which Darcy's law is valid limit its usefulness to linear laminar flow regimes. Thus, we adopt an expression, suggested by Ergun and Orning (1949, Eqn. 6), that facilitates a smooth transition between laminar and turbulent flow in a porous medium. After conversion to our notation, and modification to allow for radial flow direction, the constitutive relation can be written as

$$\frac{\partial h_B}{\partial r} = -\left(\frac{5A\eta {S_0}^2(1-n)^2}{\rho_w g n^3}\right) q + \mathrm{sgn}\left(\frac{\partial h_B}{\partial r}\right)\left(\frac{BS_0(1-n)}{8gn^3}\right) q^2 \qquad (3.13)$$

where q is the radial component of the volume flux vector, S_0 is the surface-to-volume ratio of solids, and A and B are positive constants that control partitioning between the two right-hand-side terms. With appropriate choices of A and B, the head change will be dominated by the first term on the right side of (3.13) in laminar flow; the second term will dominate when the flow is turbulent. By inspection we see that both terms on the right side of (3.13) are negative when $\partial h_B/\partial r < 0$ and $q > 0$, corresponding to flow away from the borehole. Also, when $\partial h_B/\partial r > 0$ and $q < 0$ both terms on the right side of (3.13) are positive; in this case flow is directed back towards the borehole.

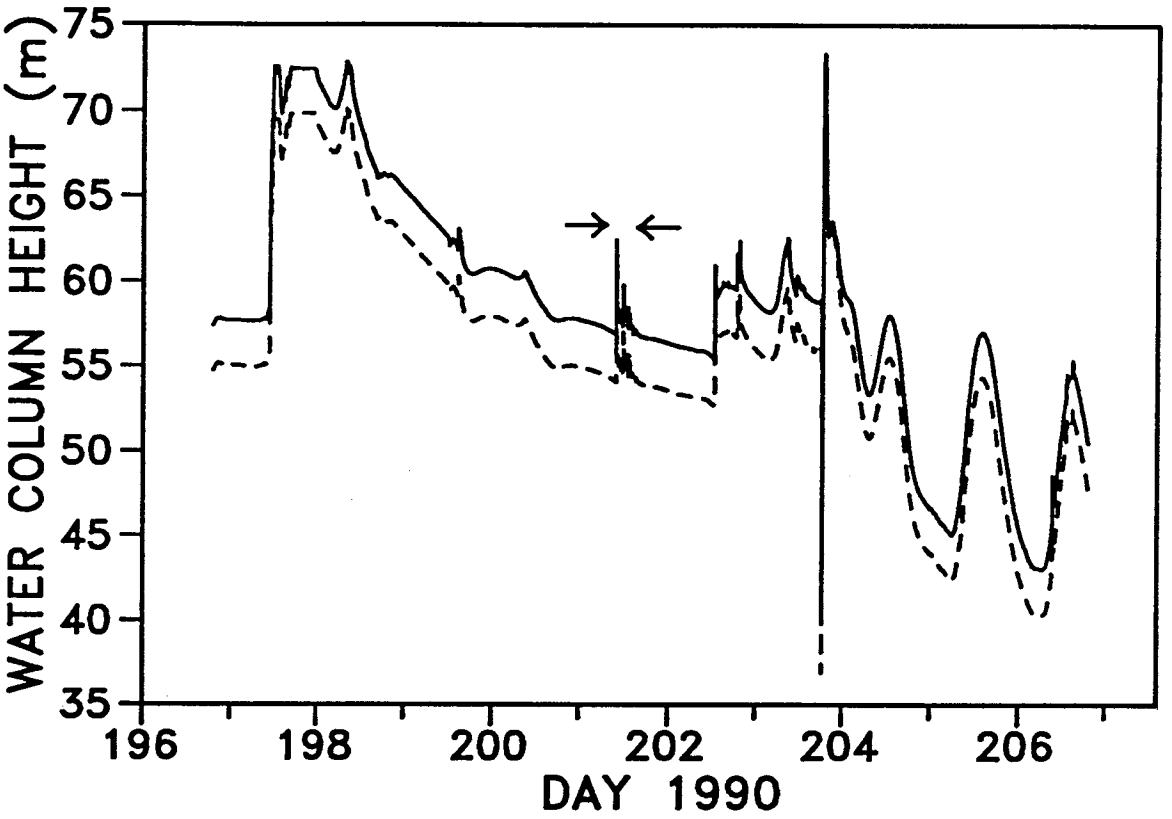

Fig. 3.2: Variation of water pressure beneath Trapridge Glacier during summer 1990 as recorded by two sensors, 90P01 (solid line) and 90P02 (dashed line), 18.8 m apart at the glacier bed. Day 200 corresponds to 19 July. Data were collected by these two sensors at two minute intervals for the entire period shown. Arrow tips delimit the duration of sixteen individual response tests in the same borehole. Natural pressure fluctuations typically occur over time scales that are large compared to the duration of a single response test. Note that sensors 90P01 and 90P02—separated from the hole in which these tests were being performed by, respectively, 19.0 m and 10.4 m—recorded nearly simultaneous responses.

Equation (3.13) can be simplified if we assume that the Kozeny-Carman relation is applicable in a subglacial environment. This relationship between permeability k and porosity is given by

$$k = \frac{n^3}{5{S_0}^2(1-n)^2} \tag{3.14}$$

(Carman, 1956). If we combine (3.14) with the usual definition of hydraulic conductivity K where

$$K = \frac{k\rho_w g}{\eta} \tag{3.15}$$

(e.g., Bear, 1972, p. 109) then the constitutive relation can be rewritten in terms of hydraulic conductivity. In this case (3.13) becomes

$$\frac{\partial h_B}{\partial r} = -\frac{A}{K} q + \text{sgn}\left(\frac{\partial h_B}{\partial r}\right)\left(\frac{BS_0(1-n)}{8gn^3}\right) q^2. \tag{3.16}$$

As stated, it is readily apparent that the last expression reduces to the one-dimensional form of Darcy's law in cylindrical coordinates, $q = -K(\partial h_B/\partial r)$, if $A = 1$ and $B = 0$. Therefore, without loss of generality, we will set $A = 1$ for the remainder of our development. With A fixed, a suitable choice for B still permits relative proportioning between head loss in laminar and turbulent flow regimes.

Before obtaining the final flow equation, we must solve the quadratic expression (3.16) for q. The two roots of Equation (3.16) are

$$q_1 = \frac{K^{-1} + \sqrt{K^{-2} + 4\,C_1\,\text{sgn}\,(\partial h_B/\partial r)\,(\partial h_B/\partial r)}}{2\,C_1\,\text{sgn}\,(\partial h_B/\partial r)} \tag{3.17a}$$

and

$$q_2 = \frac{-2\,(\partial h_B/\partial r)}{K^{-1} + \sqrt{K^{-2} + 4\,C_1\,\text{sgn}\,(\partial h_B/\partial r)\,(\partial h_B/\partial r)}} \tag{3.17b}$$

(Press and others, 1986, p. 145) where we have simplified our notation by defining the constant $C_1 = BS_0(1-n)/8gn^3$. Because we require that a negative head gradient produce a positive volume flux, the second root must be chosen. Noting that the magnitude of the head gradient can be written as

$$\left|\frac{\partial h_B}{\partial r}\right| = \text{sgn}\left(\frac{\partial h_B}{\partial r}\right)\frac{\partial h_B}{\partial r}, \tag{3.18}$$

simplification of (3.17b) leads to

$$q = -(2K)\frac{\partial h_B}{\partial r}\left[1 + \left(1 + C_2\left|\frac{\partial h_B}{\partial r}\right|\right)^{\frac{1}{2}}\right]^{-1} \tag{3.19}$$

where $C_2 = 4K^2C_1$.

We are now ready to combine the fluid flow equation (3.12) with the constitutive relation (3.19). Since we are considering only radial flow, (3.12) can be written in terms of the radial component of q_j in cylindrical coordinates as

$$-\frac{1}{r}\frac{\partial}{\partial r}(r\,q) = S_s\frac{\partial h_B}{\partial t} \tag{3.20}$$

where we have introduced specific storage $S_s = \rho_w g(\alpha + n\beta)$. Physically, S_s represents the volume of water released from storage when a unit decline in hydraulic head occurs in a unit volume of aquifer. For confined aquifers of constant thickness b it is customary to define aquifer storativity S and transmissivity T as follows:

$$S \equiv S_s b \tag{3.21}$$

and

$$T \equiv Kb \tag{3.22}$$

(e.g., Bear, 1972, p. 215). Using these definitions, and substituting (3.19) into (3.20), we obtain

$$\frac{1}{r}\frac{\partial}{\partial r}\left\{r\frac{\partial h_B}{\partial r}\left[1 + \left(1 + C_2\left|\frac{\partial h_B}{\partial r}\right|\right)^{\frac{1}{2}}\right]^{-1}\right\} = \left(\frac{S}{2T}\right)\frac{\partial h_B}{\partial t}. \tag{3.23}$$

With (3.18), the last equation can be expanded and rearranged to give the partial differential equation governing water flow in the aquifer:

$$\frac{\partial h_B}{\partial t} = \frac{2T}{S}\left\{\left(\frac{\partial^2 h_B}{\partial r^2} + \frac{1}{r}\frac{\partial h_B}{\partial r}\right)\left[1 + \left(1 + C_2\left|\frac{\partial h_B}{\partial r}\right|\right)^{\frac{1}{2}}\right]^{-1}\right.$$
$$\left. - \frac{C_2}{2}\frac{\partial^2 h_B}{\partial r^2}\left|\frac{\partial h_B}{\partial r}\right|\left[1 + \left(1 + C_2\left|\frac{\partial h_B}{\partial r}\right|\right)^{\frac{1}{2}}\right]^{-2}\left(1 + C_2\left|\frac{\partial h_B}{\partial r}\right|\right)^{-\frac{1}{2}}\right\}. \tag{3.24}$$

As a consistency check, we see that a laminar flow regime corresponds to a weighting coefficient value of $B = 0$; in this case $C_2 = 0$ and (3.24) reduces to the standard radial diffusion equation,

$$\frac{\partial^2 h_B}{\partial r^2} + \frac{1}{r}\frac{\partial h_B}{\partial r} = \frac{S}{T}\frac{\partial h_B}{\partial t} \tag{3.25}$$

(e.g., de Marsily, 1986, p. 162), that arises from Darcy's law.

Before considering borehole–aquifer coupling, we note that values for the weighting coefficient B can be calculated based on porosity and a critical Reynolds number Re' for the aquifer. For porous media, a flow transition occurs when $10 \leq \mathrm{Re} \leq 100$ (de Marsily, 1986, p. 74); during this transition the flow regime changes from laminar to turbulent. Ergun and Orning (1949) show that for $\mathrm{Re} \approx 60$, with $n = 0.35$, the two terms on the right-hand-side in Equation (3.13) have nearly equal effects upon pressure drop. If we choose Re' to be the critical Reynolds number at which the terms are of equal magnitude, and simplify our picture of the porous medium by assuming spherical solid grains, we obtain the following expression for the weighting coefficient: $B = 240\,(1 - n)/\mathrm{Re}'$.

3.2.4 Coupling between borehole and aquifer water motion

The rate at which water flows into or out of the borehole must be equal to the rate at which it leaves or enters the aquifer, if there is no storage within the filter. This is consistent with our previous assumptions; namely, that water compressibility is a negligible component of the rate of change of water column height and that discharge is uniform across the filter. (Note that water compressibility is not neglected in the aquifer, only in the borehole.) Under these conditions, continuity of water volume requires that

$$-\pi {r_w}^2 \frac{dh}{dt} = 2\pi r_f b\, q(r_f, t) \tag{3.26}$$

where $q(r_f, t)$ is the radial volume flux across the filter. Solving the last expression for the discharge across the filter and combining the result with Equation (3.16) leads to

$$\frac{\partial h_B(r_f, t)}{\partial r} = \left(\frac{{r_w}^2}{2 r_f T}\right)\left[\frac{dh}{dt} + \mathrm{sgn}\left(\frac{dh}{dt}\right)\left(\frac{C_1 {r_w}^2}{2 r_f b}\right)\left(\frac{dh}{dt}\right)^2\right] \tag{3.27}$$

where we have used the fact that $\partial h_B/\partial r$ and dh/dt have the same algebraic sign. In effect, Equation (3.27) couples water flow in the borehole and water flow in the basal aquifer: terms involving borehole water velocity dh/dt are evaluated from the solution of Equation (3.11); the radial head gradient at the filter $\partial h_B(r_f, t)/\partial r$ is obtained from the solution of Equation (3.24).

3.3 Non-dimensionalization

In the previous section we developed a model of water flow in a combined borehole–subglacial aquifer system. The model requires input of material constants, as well as geometric and hydraulic parameters. Unfortunately, model inputs tend to be combined in ways that do not permit straightforward assessment of their individual contributions. (Transmissivity $T = Kb$, for instance, is an important term containing two parameters of interest: hydraulic conductivity and aquifer thickness.) To obtain insight into inherently non-unique parts of the model, we turn to dimensional analysis. This approach provides an efficient way to examine parameter sensitivities and highlights key physical aspects of the model.

3.3.1 Dimensionless formulation

We start by defining dimensionless variables as follows: time $t^\star = t/t_0$; volume flux $q^\star = q/q_0$; radial distance $r^\star = r/r_0$; water column height $h^\star = h/h_0$; hydraulic head $h_B^\star = h_B/h_0$; surface forcing $h_T^\star = h_T/h_0$. The characteristic constants t_0, q_0, r_0, and h_0 are arbitrary, but reasonable choices should involve time, flux, and length scales that are representative of the actual physical system. With this consideration in mind,

we set the characteristic water column height equal to the height of water in an open, undisturbed, equilibrated borehole. (As will be subsequently discussed, this value of h_0 also corresponds to that used in dimensional simulations.) With h_0 fixed, the remaining characteristic values follow naturally:

$$t_0 = \left(\frac{h_0}{g}\right)^{\frac{1}{2}}, \tag{3.28}$$

$$q_0 = \frac{Kh_0}{r_0}, \tag{3.29}$$

$$r_0 = r_f. \tag{3.30}$$

For a porous medium of hydraulic conductivity K, q_0 represents the specific discharge under a constant head gradient h_0/r_0. As defined, the time constant t_0 approximates the theoretical period of oscillation expected for a vertical U-tube manometer (Prandtl, 1952, p. 50).

The final dimensionless quantities we define are the laminar-flow skin-friction parameter

$$\zeta = \left(\frac{8\eta}{\rho_w {r_w}^2}\right)\left(\frac{h_0}{g}\right)^{\frac{1}{2}}, \tag{3.31}$$

the diffusivity parameter

$$\chi = \left(\frac{K}{S_s {r_f}^2}\right)\left(\frac{h_0}{g}\right)^{\frac{1}{2}}, \tag{3.32}$$

the transmissivity parameter

$$\Upsilon = \left(\frac{2Kb}{{r_w}^2}\right)\left(\frac{h_0}{g}\right)^{\frac{1}{2}}, \tag{3.33}$$

and the Ergun parameter

$$\xi = \left(\frac{K^2 B S_0 (1-n) h_0}{2 r_f g n^3}\right). \tag{3.34}$$

The relative importance of skin friction in controlling the rate of laminar water flow in the borehole is characterized by the number ζ. A frictionless borehole wall corresponds to $\zeta = 0$. The number χ characterizes the relative importance of diffusion in regulating flow in the subglacial aquifer. As $\chi \to \infty$, disturbances in the borehole tend to immediately alter the hydraulic head in the aquifer. Conversely, $\chi \approx 0$ means that the head distribution in the surrounding aquifer will not be affected by borehole disturbances. Similarly, the number Υ indicates the importance of advection in the vicinity of the borehole. In this case, as $\Upsilon \to \infty$, water tends to be transmitted instantaneously from the borehole into the aquifer, while $\Upsilon \to 0$ leads to a perfectly unconnected borehole (i.e., one for which there is absolutely no leakage into the glacier bed). Finally, the Ergun parameter ξ characterizes the importance of turbulent transport in subglacial water flow. For $\xi = 0$ the flow is purely laminar. On the other hand, large values of ξ indicate that the dominant flow regime is turbulent, and the deviation from Darcy's law becomes apparent. Typical values for dimensionless parameters are discussed in a section (3.4.3) and again in Chapter 4.

With these definitions, the governing equations (3.11), (3.19), (3.20), (3.26) can be written in dimensionless form:

$$h^\star \frac{d^2 h^\star}{dt^{\star 2}} + \zeta h^\star \frac{dh^\star}{dt^\star} + h^\star = h_{\mathrm{B}}^\star(1, t^\star) - h_{\mathrm{T}}^\star, \tag{3.35}$$

$$q^\star = -(2)\frac{\partial h_{\mathrm{B}}^\star}{\partial r^\star}\left[1 + \left(1 + \xi\left|\frac{\partial h_{\mathrm{B}}^\star}{\partial r^\star}\right|\right)^{\frac{1}{2}}\right]^{-1}, \tag{3.36}$$

$$-\frac{1}{r^\star}\frac{\partial}{\partial r^\star}(r^\star q^\star) = \frac{1}{\chi}\frac{\partial h_{\mathrm{B}}^\star}{\partial t^\star}, \tag{3.37}$$

$$q^\star(1, t^\star) = -\frac{1}{\Upsilon}\frac{dh^\star}{dt^\star}. \tag{3.38}$$

Motion of water in the borehole is now described by Equation (3.35), while (3.37) governs water flow in the subglacial aquifer. The constitutive relation is expressed by Equation (3.36) and the input boundary condition, coupling (3.35) and (3.37), is given by Equation (3.38).

Recasting the problem in non-dimensional form has simplified the mathematical description; we are left with four dimensionless parameters upon which model solutions depend. These parameters highlight the fundamental physics in the model and allow examination of model sensitivities in a straightforward way.

3.4 Simulations

3.4.1 Solution procedure

A set of finite-difference expressions corresponding to Equation (3.23) or (3.37) was solved simultaneously with a system of two first-order differential equations equivalent to the second-order (3.11) or (3.35) using an implicit, fifth-order, Runge-Kutta scheme with adaptive time stepping (Hairer and Wanner, 1991). Details of the numerical formulation are given in Appendix B. Computational efficiency was enhanced by using two staggered spatial grids upon which nodes were logarithmically spaced according to the transformation $R = \ln(r/r')$ (e.g., Jarvis and Clarke, 1974), where $r' = 1.0$ m is a non-dimensionalizing constant that does not rescale the problem. Staggered grids allow specification of hydraulic head on one grid and convenient calculation of head gradient and volume flux on the other. This procedure eliminates the necessity of evaluating derivatives higher than first-order and eases implementation of the boundary conditions. The logarithmic transformation decreases nodal spacing in the vicinity of the borehole, where head changes are the greatest, and reduces the required number of nodes. The resulting algorithm is sensitive to spatial step size. Through detailed analysis we have determined that consistent solution results are obtained for constant logarithmic step sizes $\Delta R \leq 0.22$.

3.4.2 Boundary and initial conditions

Using staggered spatial grids, the input boundary condition is conveniently given by Equation (3.26) or (3.38), with r_f corresponding to the first node on the flux grid. We allow two possibilities for the outer boundary condition: a boundary of prescribed head or a boundary of prescribed head gradient. In particular, we have used special cases of these general boundary conditions. We consider the subglacial flow layer to be "open" to water flow if, at some distance from the borehole, the pre-existing head value h_0 remains undisturbed. This situation imposes a constant head boundary condition $h_B(r_{max}, t) = h_0$ and, for suitably large values of r_{max}, approximates an infinite aquifer. Alternatively, we consider the system to be "closed" to water flow if, at some distance from the borehole, the hydraulic head gradient is zero. This condition describes a no-flux boundary, in which case $q(r_{max}, t) = 0$. For dimensionless simulations the outer boundary conditions are $h_B^*(r_{max}^*, t) = 1$ or $\partial h_B^*(r_{max}^*, t)/\partial r^* = 0$, corresponding to constant head and zero gradient boundaries respectively. Regardless of which boundary condition is used, it is reasonable to expect that at a sufficiently large radius disturbances in the borehole will not be sensed—physically or numerically. In testing this limit numerically, our simulations have shown that, for slug and packer tests, the model is insensitive to the prescribed outer boundary condition when $r_{max} \geq 20\,\text{m}$. The radius of influence is larger than this for connection-drainage tests.

A "closed" system, such as the one we have described, does not represent a typical aquifer because it fails to transmit a significant amount of water. Nevertheless, we have included this possibility because there are times when large portions of the bed beneath Trapridge Glacier appear not to drain. At these times subglacial water is ponded, but water can still be moved about within these regions. (For instance, water pumped down a borehole sometimes causes flow out of neighboring boreholes.) Response tests performed under these conditions still allow estimation of subglacial hydraulic properties.

In the case of a connection-drainage simulation the initial conditions are as follows: the head is uniform within the aquifer so that all nodal positions represent the same hydraulic potential $h_B(r,0) = h_0$; the borehole is full of water so that the height of the water column is equal to the ice thickness $h(0) = h_i$; water in the borehole is stationary $dh/dt = 0$. For dimensionless simulations, the corresponding initial conditions are $h_B^*(r^*,0) = 1$, $h^*(0) = h_i/h_0$, and $dh^*/dt^* = 0$. For slug and packer tests we again assume that the hydraulic head is initially uniform throughout the aquifer and that the borehole water level is stationary when the tests begin. Before the system is disturbed, water level in the open borehole represents an equilibrium with the basal aquifer. In the case of a slug test simulation, the initial water column height is set equal to the uniform head within the aquifer, minus the height of water h_s displaced by the slug: $h(0) = h_B(r,0) - h_s$. In the case of a packer test simulation, the initial water column height is simply $h(0) = h_B(r,0)$. For dimensionless slug tests simulations, the initial conditions are $h_B^*(r^*,0) = 1$, $h^*(0) = 1 - h_s/h_0$, and $dh^*/dt^* = 0$. For dimensionless packer test simulations, the initial conditions are $h_B^*(r^*,0) = h^*(0) = 1$ and $dh^*/dt^* = 0$.

3.4.3 Sensitivity analysis

Connection-drainages involve the sudden opening of water-filled boreholes to the basal aquifer. Such disturbances can result in a wide range of responses, making them particularly well-suited for a sensitivity analysis. The effects of the skin friction parameter ζ, diffusivity parameter χ, transmissivity parameter Υ, and Ergun parameter ξ on the character of connection-drainage disturbances are shown in Figure 3.3. By independently varying these parameters we can assess their individual contributions to the overall response and also predict what the responses would be for flow systems with vastly different hydraulic characteristics.

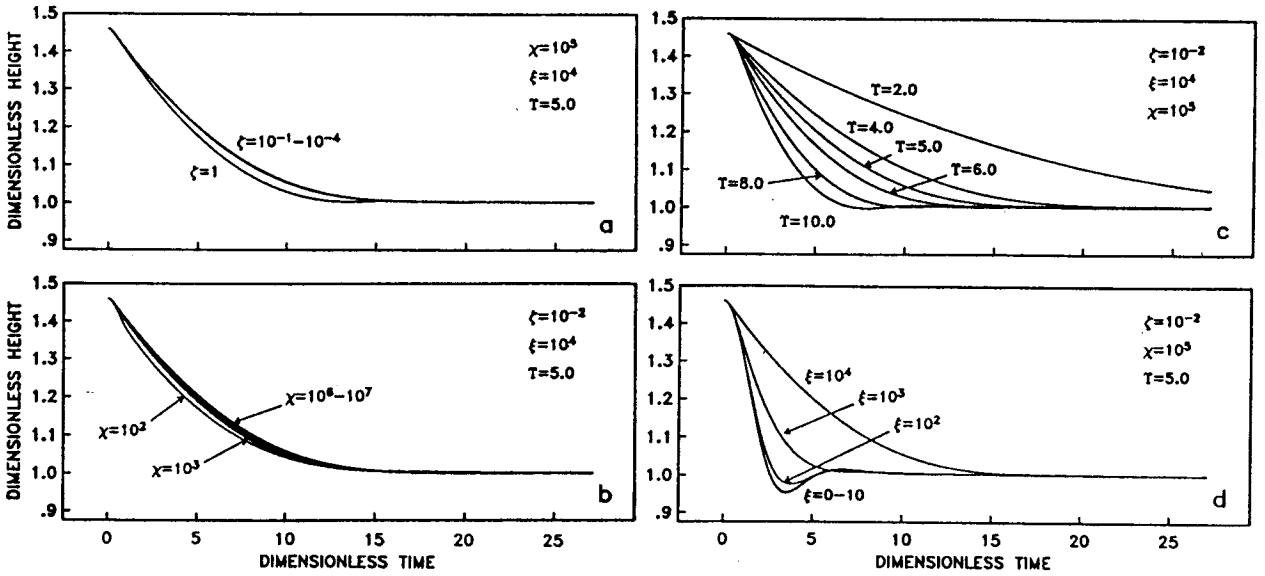

Fig. 3.3: Results of dimensional analysis showing model sensitivity to the four free parameters. (a) Wide variations of the skin friction parameter ζ have virtually no influence on simulation results. Trapridge Glacier boreholes correspond to $\zeta \approx 0.01$, indicating that frictional energy loss at the borehole wall is an insignificant process in the coupled borehole–subglacial aquifer system. (b) Large values of the diffusivity parameter χ suggest that diffusion is an important process in the basal flow layer. However, solution character is insensitive to χ as evidenced by the small changes that result from variation of χ over several orders of magnitude. (c) Small variations of the transmissivity parameter Υ have a strong influence on the rate at which water flows out of the borehole and into the aquifer, and vice versa. Despite this sensitivity, Υ is small in magnitude compared with χ. Such a comparison indicates that advection in the vicinity of the borehole is less important than diffusion for the overall system. (d) The Ergun parameter ξ characterizes the importance of turbulent transport in the basal flow layer. For $\xi = 0$ the flow regime is purely laminar. Larger values of ξ correspond to increasing deviations from Darcy's law. Typical values of the Ergun parameter indicate that flow in the basal layer is strongly regulated by the effects of turbulence. Furthermore, the character of simulated solutions is also sensitive to ξ. For the simulations shown, a transition between underdamped and overdamped responses occurs somewhere in the range $10^2 < \xi < 10^3$.

Figure 3.3a shows the importance of skin friction in controlling the rate of change of water column height, assuming flow in the borehole is laminar. If $h_0 = 50\,\text{m}$ then $\zeta = 1$ requires a borehole radius of less than 0.006 m, an unrealistically small value. Boreholes having reasonable radii, say 0.05 m, lead to smaller values of the skin friction parameter, corresponding to diminishing importance of skin friction. As can be seen in Figure 3.3a, for $\zeta \leq 0.1$ the solution results are nearly identical. This result supports the previously discussed conclusion of van der Kamp (1976); namely, that under most conditions skin friction can be neglected.

The influence of diffusion on the character of connection-drainage disturbances is illustrated in Figure 3.3b. Larger parameter values, corresponding to increasing importance of water storage, result in slower drainage rates. It is readily apparent that a large change (five orders of magnitude) in the diffusion parameter value results in only small changes in the drainage response; for $10^4 \leq \chi \leq 10^7$ the differences between solution results are barely perceptible. Thus, connection-drainage solutions appear to be relatively insensitive to diffusion. However, the large values of χ calculated from model inputs indicate that diffusion is still an important process governing the flow.

Figure 3.3c shows the influence of transmissivity in the immediate region surrounding the borehole. The drainage response following a connection is seen to be extremely sensitive to transmissivity parameter values; small variations of Υ (less than one order of magnitude) give rise to a wide range of responses. Parameter values in the range $\Upsilon \leq 8$ produce overdamped responses, while for $\Upsilon \geq 10$ the solutions are underdamped. Although solution character appears to be strongly dependent on advection in the vicinity of the borehole, typical values of the transmissivity parameter are small in comparison with the diffusivity and Ergun parameters. This suggests that advection near the borehole plays an overall less important role than either diffusion or turbulence in the basal aquifer.

Figure 3.3d demonstrates the importance of turbulent transport in the aquifer. For $\xi = 0$, turbulence is neglected and the flow is purely laminar. Ergun parameter values $0 \leq \xi \leq 100$ are seen to result in underdamped solutions, while for $\xi \geq 1000$ the system is overdamped. Thus, the character of the response is also sensitive to ξ. Values of ξ in the range $10^3 \leq \xi \leq 10^5$, calculated from model inputs, indicate that turbulent flow in the aquifer is important in regulating borehole drainage after a connection.

The underdamped responses that are predicted for certain dimensionless parameter values indicate that the borehole-aquifer system is capable of sustaining force-free oscillation. This behavior has been observed during response tests conducted under more traditional (i.e., non-glacial) conditions (e.g., Bredehoeft and others, 1966; van der Kamp, 1976; Krauss, 1977). Such oscillations resemble those of the classic spring–mass system: the column of water in the borehole plus some portion of the water in the aquifer constitute the mass of the system; the restoring force is provided by the difference between the pressure head in the aquifer and the nonequilibrium water level in the borehole; the damping force arises from the friction that accompanies water flow through the borehole and aquifer. Transition between overdamped and underdamped responses depends on the mass of water in motion and the system's ability to transmit this water. Hence, the degree of damping depends on h_0, r_w, S, and T—geometric and hydraulic quantities that are contained in the dimensionless variables χ and Υ. In the case of a connection-drainage, the inertial force is significant due to the large mass of water involved. The Ergun parameter ξ plays an important role in this case because the frictional losses in turbulent flow are an important component of the damping force. As Figure 3.3d illustrates, an underdamped response is predicted when turbulent effects are ignored.

3.4.4 Results

As a demonstration of the theoretical model we compare connection-drainage, slug test, and packer test simulations with field observations in Figures 3.4, 3.5, and 3.6 respectively. In Table 3.1 we have listed the model parameter values that were used to obtain the simulated solutions. These solutions were achieved through trial and error forward modeling; parameters were adjusted to obtain the best visual fits between the data and the simulated solutions. We compare simulated solutions with field observations in this chapter only to demonstrate model usage. Thus, the model inputs listed in Table 3.1 should not be misconstrued as final results; better estimates of subglacial hydraulic properties are determined by inverse modeling, which is the subject of the following chapter.

Our convention for identifying response tests involves a sequence of six or seven numbers and characters: The first two-digit number shows the year that the test was performed. This is followed by a two-character string—CD indicates a connection-drainage test, ST a slug test, and PT a packer test. Next comes a two-digit number identifying the borehole in which the test was performed. For slug and packer tests, the final character indicates the sequential position in a series of tests of the same type and in the same borehole. Thus, 90ST38E denotes the fifth slug test in borehole number 38 during the 1990 field season.

The data shown in Figures 3.4 and 3.5 were collected from the same borehole in early afternoon on Day 206 during the 1990 field season. As can be seen in Figure 3.2, the background head at this time was roughly 45 m. Based on similar observations during the 1989 field season, the data shown in Figures 3.6a and 3.6b were obtained when background head values were 42 m and 7 m respectively.

Parameter	*Symbol*	*Value*	*Units*
Physical constants (same for all simulations)			
Gravity acceleration	g	9.8	$m\ s^{-2}$
Water density	ρ_w	1.0×10^3	$kg\ m^{-3}$
Water viscosity	η	1.787×10^{-3}	$kg\ m^{-1}\ s^{-1}$
Water compressibility	β	4.4×10^{-10}	Pa^{-1}
Aquifer compressibility	α	1.0×10^{-8}	Pa^{-1}

Figure number		3.4	3.5	3.6a	3.6b	
Model inputs						
Ice thickness	h_i	70.0	70.0	70.0	70.0	m
Borehole radius	r_w	0.05	0.05	0.05	0.05	m
Filter radius	r_f	0.08	0.08	0.08	0.08	m
Maximum model radius	r_{max}	200.0	200.0	200.0	200.0	m
Initial hydraulic head	h_0	46.65	21.5	52.75	37.5	m
Aquifer thickness	b	0.041	0.039	0.055	0.055	m
Aquifer porosity	n	0.35	0.4	0.4	0.4	
Hydraulic conductivity	K	0.067	0.45	0.38	0.9	$m\ s^{-1}$
Critical Reynolds number	Re'	60.0	55.0	55.0	55.0	
Derived quantities (not used in simulations)						
Aquifer transmissivity	T	0.00275	0.0176	0.0209	0.0495	$m^2\ s^{-1}$
Aquifer storativity	S	4.08	3.89	5.48	5.48	$(\times 10^{-6})$
Kinetic energy loss factor	B	2.60	2.62	2.62	2.62	
Characteristic water level	h_0	46.7	21.5	52.8	37.5	m
Characteristic time	t_0	2.18	1.48	2.32	1.96	s
Characteristic length	r_0	8.00	8.00	8.00	8.00	$(\times 10^{-2})$ m
Characteristic volume flux	q_0	39.1	121	251	422	$m\ s^{-1}$
Skin friction parameter	ζ	12.5	8.47	13.3	11.2	$(\times 10^{-3})$
Diffusivity parameter	χ	2.30	10.4	13.8	27.6	$(\times 10^5)$
Ergun parameter	ξ	6.79	44.9	85.4	221	$(\times 10^3)$
Transmissivity parameter	Υ	4.80	2.08	3.88	77.5	

Table 3.1: Parameters for borehole response simulations. (Physical constants and model inputs are listed exactly as they were specified for the simulations shown. All calculations were made in double precision. Derived quantities are stated to three significant figures with rounding.)

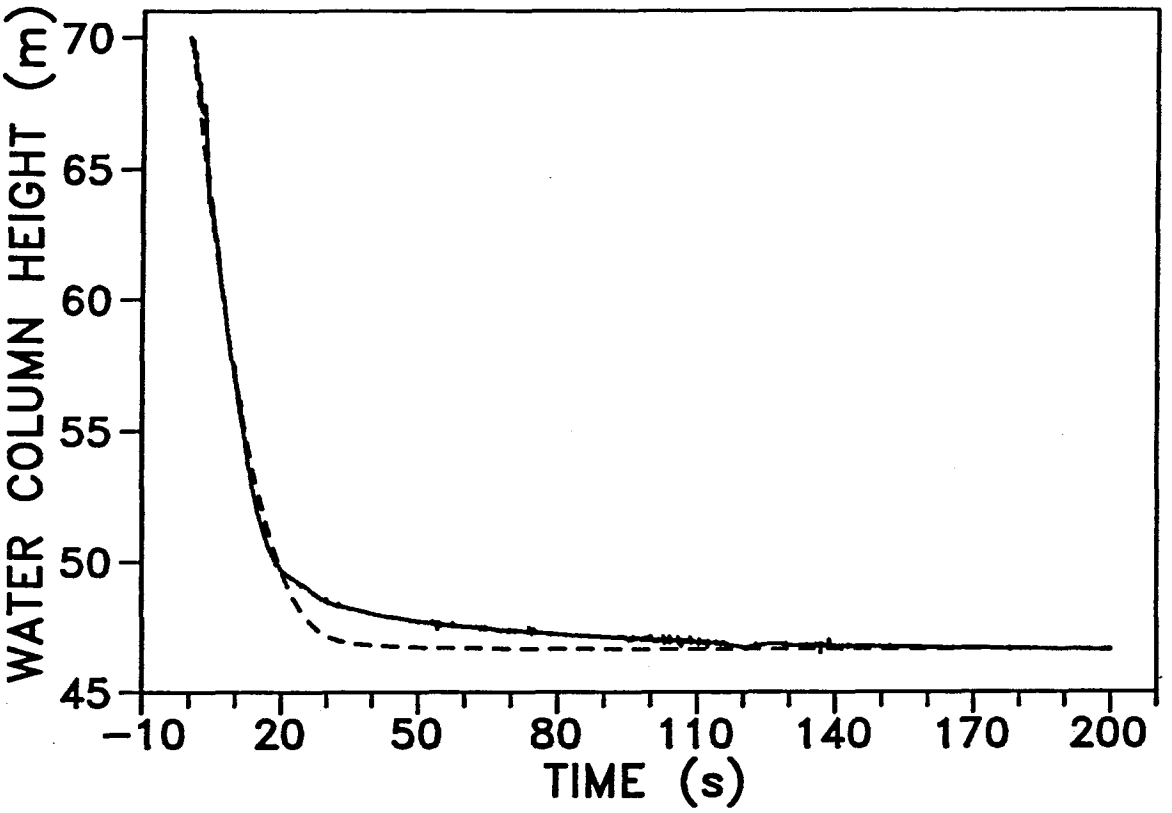

Fig. 3.4: Borehole connection observation 90CD38 (solid line) from summer 1990 and modeled drainage response (dashed line). Divergence between observed and modeled results becomes apparent near the end of the connection when the head gradient is small and might be due to water input from the drill, a contribution that is ignored in the model.

A connection drainage observation in Borehole 38 during summer 1990 (designated 90CD38) is shown in Figure 3.4, along with a modeled drainage response. During this observation the borehole water level dropped approximately 20 m in 20 s; thus, the mean water velocity was about 1.0 m s^{-1} during the initial moments of connection. This velocity, together with the simulation input values, implies a mean specific discharge of roughly 0.3 m s^{-1} at a distance of 0.1 m from the borehole center. Such high water transfer rates motivated our use of a nonlinear constitutive relation to characterize the subglacial aquifer. As the borehole water level approaches the equilibrium head value, simulated and observed results diverge. The model predicts a more rapid return to

predisturbed conditions than actually occurs. For this particular connection, modeled and observed results converge to the background head value approximately 120 s after the connection.

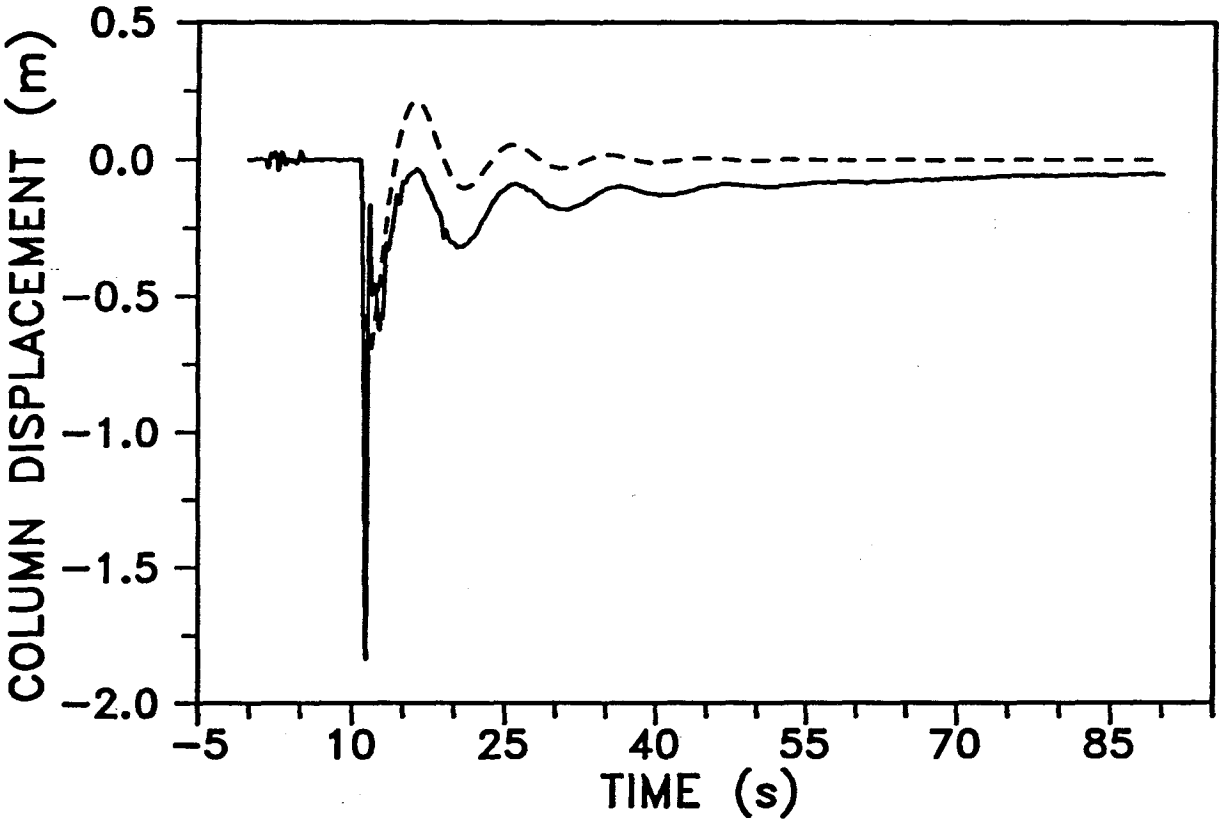

Fig. 3.5: Slug test 90ST38A (solid line) from summer 1990 and simulated slug test response (dashed line). While the model predicts oscillations about the predisturbed water level, observed oscillations take place about a lower level. Note that this particular test was performed just before noon on Day 206, corresponding to 25 July 1990, during a rapidly rising pressure limb (see Fig. 2).

Figure 3.5 shows the first of a series of slug tests performed in Borehole 38 during summer 1990 (designated 90ST38A) and a simulated slug test response. The negative initial water-column displacement corresponds to removal of the slug. After the slug is withdrawn, the model predicts an oscillatory response about the predisturbed water

level, given the inputs that we have used. The measured response is also oscillatory—however, it does not oscillate about the predisturbed water level, but rather about a lower level. Similar responses have been observed during several different series of slug tests; repeated tests result in lower re-equilibrated water levels. We shall discuss this discrepancy subsequently.

Two packer tests performed in Borehole 68 during summer 1989, together with simulated responses, are shown in Figure 3.6 (note the different vertical scales). The first, 89PT68B (Fig. 3.6a), was performed at 1820 on Day 209. The second, 89PT68C (Fig. 3.6b), was performed at 1055 the following day. Because the borehole had frozen shut overnight, it was reopened in the morning of the second day. As with slug tests, the model and the inputs that we have chosen predict oscillations about the predisturbed water level, whereas actual fluctuations are about a somewhat lower level. The oscillations recorded during packer test 89PT68B are more rapidly damped and are of longer period relative to those observed during test 89PT68C. Comparison of model input parameters (Table 3.1) reveals that smaller head and larger conductivity values result in higher frequency oscillations that are less quickly damped.

3.5 Discussion

Generally good agreement between observed and modeled results demonstrates that borehole response tests, together with the theoretical framework we have developed, can be used to estimate subglacial hydraulic properties. The uniqueness of these estimates is a separate issue that we shall address in the next chapter.

Significant temporal changes in hydraulic conductivity, suggested by model inputs for the simulations shown in Figure 3.6, are not expected in conventional groundwater flow systems. However, such changes are not unreasonable in a subglacial sediment layer. One possibility is that water discharge from the drill causes fine sediments to be entrained and transported away from the borehole. Alternatively, basal sediments

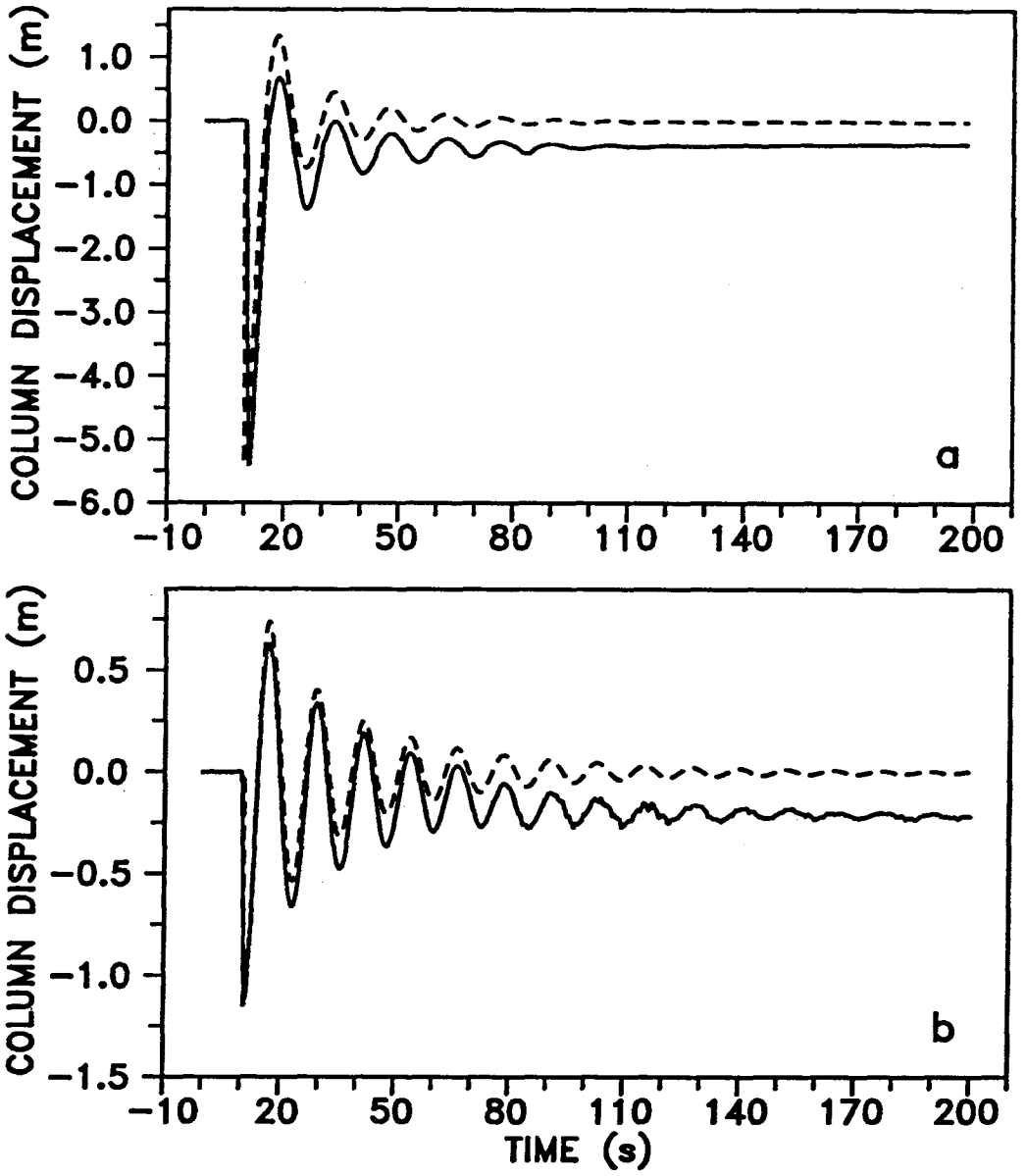

Fig. 3.6: Packer tests (a) 89PT68B and (b) 89PT68C (solid lines) from summer 1989, together with simulated packer test results (dashed lines). Note the different vertical scales. As with slug tests, the model predicts oscillations about the predisturbed water level, whereas actual fluctuations are about a somewhat lower level. These two tests were performed in the same hole on two successive days—the borehole was reopened in the morning of the second day.

might be deforming at a nonuniform rate, thereby changing the porosity. In either case hydraulic conductivity would be altered.

As previously mentioned, the simulations shown in Figures 3.4, 3.5, and 3.6 are intended to demonstrate model usage. In these simulations, parameter variations were intentionally limited to highlight those to which we have found the model is most sensitive. It is important to realize that focusing on sensitive parameters is a natural tendency with forward modeling, and that this approach can fail to produce a fully-consistent set of hydraulic parameters. For example, in connection with Figure 3.6 we alluded to the possibility that differences in the modeled responses are due only to changes in initial head and hydraulic conductivity values. For these simulations all other parameters were held constant. However, according to Equations (3.14) and (3.15), changes in hydraulic conductivity must be accompanied by changes in porosity and/or the surface-to-volume ratio of solids. Such inconsistencies must be resolved when seeking actual hydraulic parameters estimates, and we again emphasize that the model inputs listed in Table 3.1 should not be construed as final results.

3.5.1 Discrepancies between observed and modeled results

In comparing measured and simulated responses, several discrepancies have been noted, suggesting the possibility that there are additional properties or processes that are not included in our model. Based on initial simulations, we have discovered the following discrepancies between observed and modeled results: (i) simulated borehole connections recover to the equilibrium head value more rapidly than observed connections; (ii) slug and packer tests result in lower re-equilibrated water levels, whereas the model predicts that predisturbed levels will be regained; (iii) initial head values specified for slug or packer test simulations are typically lower than those that actually existed at the times of the response tests. We will now briefly discuss these discrepancies.

Divergence between observed and simulated borehole connection results might be explained by continued injection of water from the drill during the drainage observation. In practice, there is a lag between the time that water begins to drain from the hole and the time that hot water ceases to be delivered to the bed by the drill; typically this interval is on the order of a few minutes. Since water input from the drill is not included in our model, we expect that there will be a difference between observed and simulated results. Furthermore, because discharge from our drill (approximately 13 liters min^{-1}) is much less than discharge from the borehole during the initial moments of a rapid drainage (roughly 470 liters min^{-1} in the case of 90CD38), this difference will be apparent only after most of the water has drained from the borehole—when the head gradient is small. In an effort to simplify the model, we have ignored water input from the drill. As a result, the model will tend slightly to misrepresent actual hydraulic system values when applied to borehole connections after the initial drawdown. In particular, hydraulic conductivity, porosity, and aquifer thickness will be underestimated while the critical Reynolds number for the flow layer will be overestimated.

In the case of slug and packer tests, re-equilibrated water-column heights are consistently observed to be lower than the predisturbed levels, whereas the model always predicts a return to the initial position. This situation is schematically illustrated in Figure 3.7. We have considered a number of possible explanations for this discrepancy: changes in background pressure, changes in sensor position, poor testing procedure, temporary water storage in the aquifer, and water expulsion from the immediate flow region. Inversion results presented in the following chapter suggest that the most likely explanation for this discrepancy is inappropriate parameter estimates. In the next few paragraphs we consider the alternative possibilities, reserving the discussion of parameter estimates for Chapter 4.

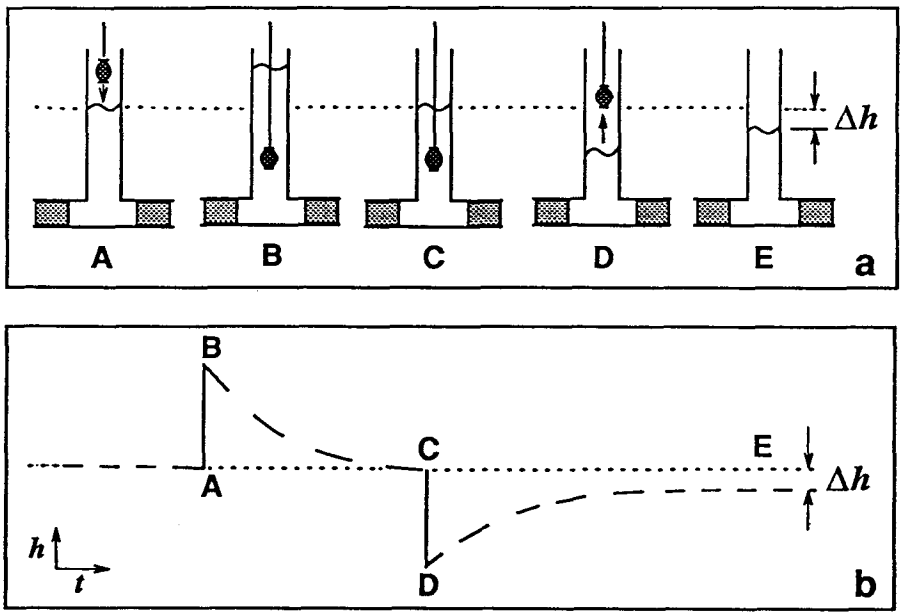

Fig. 3.7: Conceptual slug test showing reduced water levels following response tests. Part (a) shows slug insertion and removal, along with the associated displacements of borehole water level. Temporal changes in water column height h, as measured by a pressure sensor in the borehole, are sketched in part (b). Dotted lines indicate initial water levels, and the dash lengths in part (b) represent approximately one minute of observation. The slug is inserted into the borehole at point A and the disturbance produces an immediate rise in water level, corresponding to the A-B transition. The insertion creates a pressure imbalance at the bottom of the borehole which causes water to flow from the borehole into the subglacial aquifer, as shown between B and C. At C the borehole water level has returned to its original position and the slug is removed, again creating a pressure imbalance. In response to this imbalance, water flows back into the borehole, as indicated between D and E. The water level does not, however, recover to its initial value within the observation time window.

First, the tests might have been performed at a time during which basal water pressure was decreasing. For slug test 90ST38A, however, this possibility can be immediately ruled out. The entire series of tests in Borehole 38 was performed around noon on Day 206 during a rising pressure limb (Figs. 3.2 and 3.8). Many observations, during both rising and falling pressure limbs, have shown that large scale changes in

basal water pressure contribute to, but cannot fully account for, lowered water levels following response tests.

Second, there is the possibility that the pressure sensor used to measure water-column height is repositioned during the tests. However, we have not observed gradual recovery of hydraulic head between tests, as would be expected if the sensor were drifting back to its initial position. Furthermore, we have used weighted sensors and, on occasion, sensors wires have frozen to borehole walls during extended series of tests. In these cases sensor motion is clearly restricted, yet the same effects are observed. Thus, we think it is unlikely that these effects result from changes in sensor position.

A third possibility is that the tests were not conducted properly. In particular, borehole water level observations might have been terminated before pore pressure had fully recovered from the disturbances. To assess this possibility, we carefully examined slug test 90ST38A (Fig. 3.5). The full test is shown in Figure 3.8; the increase in water level at 128 s corresponds to slug insertion and the sharp decrease at 358 s occurred when the slug was removed. As previously mentioned, basal water pressure was increasing during this test. Because the borehole water level was rising when the slug was removed, it is evident that the system had largely recovered from the initial disturbance. Thus, the recovery interval following insertion ($\leq$ 230 s) was less than the period of observation following slug removal ($\geq$ 260 s). These observations indicate that discrepancies between observed and predicted post-disturbance water levels cannot be explained by poor testing procedure, at least in this case.

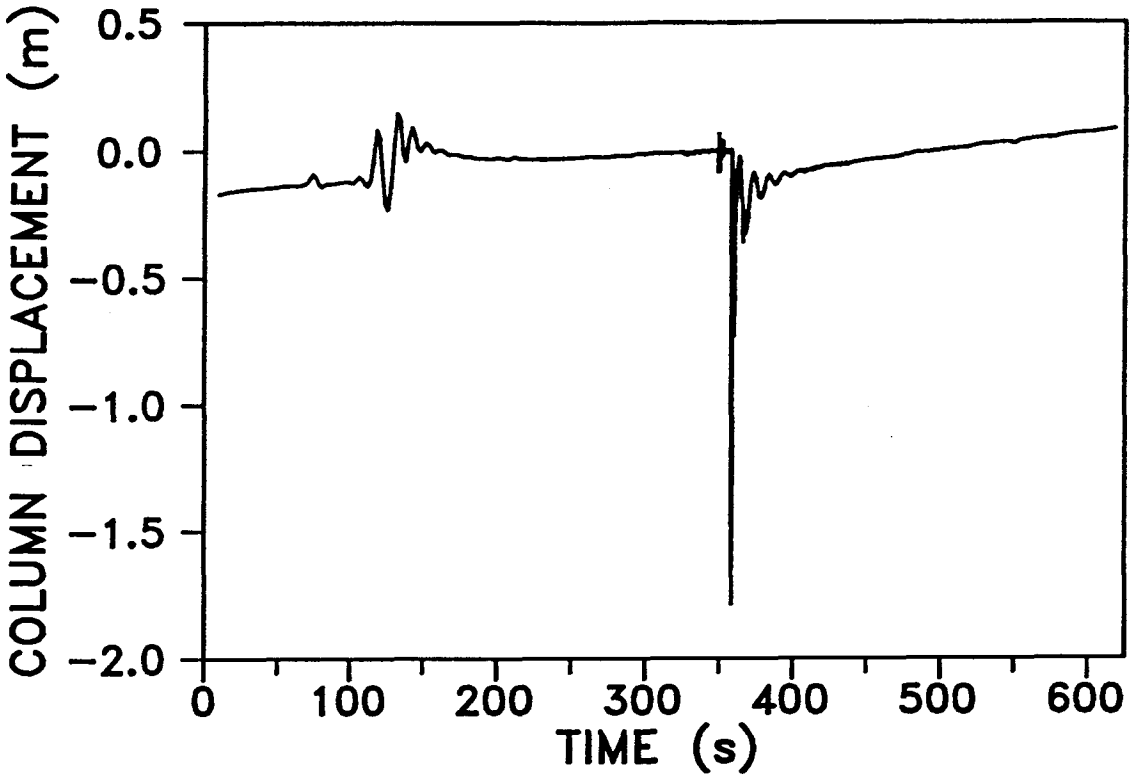

Fig. 3.8: Slug test performed in Borehole 38 during the 1990 field season (90ST38A). Starting time for this test corresponds to 1448 on Day 206 (25 July). The initial rise at 128 s was caused by slug insertion; the sharp drop, and subsequent oscillations, resulted when the slug was removed at 358 s. The sampling interval during removal was 0.0625 s. Observation continued for 260 s following slug removal. Column displacement is given relative to the water level at the time the slug was removed. Throughout this test, the background head in the subglacial aquifer was gradually rising; the test is superimposed on this trend.

A fourth possibility arises if water can be temporarily stored within the subglacial flow layer. The mechanisms by which this process could take place necessarily involve the mechanical properties of the aquifer; in particular, different compressibilities of the porous medium would be required—one for swelling and one for consolidation. While this possibility cannot be ruled out, further investigations, requiring detailed knowledge of the physical properties of subglacial sediments, would be called for.

A fifth possibility is that water is expelled from the surrounding flow region when the borehole is overpressurized and not immediately replaced when the pressure is reduced. One way that water might leave the subglacial flow layer is by leakage into the underlying sediments. Alternatively, supply-limited lateral flow could also result in a temporary loss of water if the discharge capacity exceeded the rate of input. In reality, it is unlikely that the subglacial flow layer will be perfectly confined as we have assumed. It may also be argued that even if the aquifer is horizontal and homogeneous near the borehole, it is probably not so throughout the entire flow region. Because the subglacial flow layer is probably not perfectly confined and homogeneous, it is possible that reduced water levels following slug or packer tests are the result of water expulsion from the active flow region.

Another point of discussion concerns the differences between observed borehole water levels prior to slug or packer tests and the initial head values specified for corresponding simulations. As previously mentioned, the background head value was approximately 45 m at the time of slug test 90ST38A, whereas the specified initial head value for the simulation shown in Figure 3.5 was 21.5 m. Kabala and others (1985) mention similar discrepancies between measured and predicted water column heights:

> "the effective height of the water column H_e ... does not always tune the model to the period of oscillation observed in the field. *Van der Kamp* [1976] also mentions the discrepancies between measured and 'predicted' effective height."

Like Kabala and others (1985), our simulations show that the period of oscillation can be matched by adjusting the initial height of water in the borehole. Since the borehole water volume represents a mass upon which the force of gravity acts, and because oscillation period depends on mass for other potential energy systems (e.g., a mass on a spring), we have considered the possibility that the volume of water in the

borehole may be overestimated by our model. However, modifications to allow for non-cylindrical boreholes—thereby reducing water volume—do not appreciably reduce the simulated period of oscillation.

Subsequent analysis has shown that discrepancies between the observed initial head values and those specified for simulations is most likely due to inappropriate choices of model input parameters; modifications to the model are not required. A full discussion of this analysis and the associated model input parameters is given in the following chapter.

3.5.2 Generalizations to other flow systems

We have previously stated that our model can be applied to distributed sheet and channelized flow regimes as well as to flow in a saturated porous medium. For drainage through a very thin layer, the representation provided by our model is directly analogous to sheet-like flow as discussed, for example, by Weertman (1972). To illustrate this connection, consider the relations governing flow between infinite parallel walls separated by a distance b. For one-dimensional laminar flow, the analytic expression relating specific discharge and hydraulic head gradient is

$$q = -\left(\frac{\rho g b^2}{12\eta}\right)\frac{\partial h_B}{\partial x} \tag{3.39}$$

(Todd, 1959, p. 315; Bear, 1972, p. 692), and for turbulent flow, standard empirical formulas give

$$q = \begin{cases} -\left(\dfrac{gb}{f_0}\right)^{\frac{1}{2}} \operatorname{sgn}\left(\dfrac{\partial h_B}{\partial x}\right)\left|\dfrac{\partial h_B}{\partial x}\right|^{\frac{1}{2}} & \text{(Darcy-Weisbach)} \\ -\dfrac{1}{n'}\left(\dfrac{b}{2}\right)^{\frac{2}{3}} \operatorname{sgn}\left(\dfrac{\partial h_B}{\partial x}\right)\left|\dfrac{\partial h_B}{\partial x}\right|^{\frac{1}{2}} & \text{(Gauckler-Manning)} \\ -C\left(\dfrac{b}{2}\right)^{\frac{1}{2}} \operatorname{sgn}\left(\dfrac{\partial h_B}{\partial x}\right)\left|\dfrac{\partial h_B}{\partial x}\right|^{\frac{1}{2}} & \text{(Chézy)} \end{cases} \tag{3.40}$$

(Francis, 1975, p. 218-219; Henderson, 1966, p. 91-101) where f_0, n', and C are respectively the Darcy friction factor, the Manning roughness parameter, and the Chézy coefficient. Note that in presenting the formulas in (3.40) we have used the hydraulic radius for an infinite sheet of thickness b and also made the sign corrections that are necessary to account for flow direction. The analogy between flow through porous media and Weertman-like sheet flow is immediately obvious if we express Equation (3.16) in terms if x derivatives and set $A = 1$:

$$\frac{\partial h_B}{\partial x} = -\frac{1}{K}q + \operatorname{sgn}\left(\frac{\partial h_B}{\partial x}\right)\left(\frac{BS_0(1-n)}{8gn^3}\right)q^2. \tag{3.41}$$

For low values of specific discharge, Equation (3.41) gives $q = -K(\partial h_B/\partial x)$ and suggests the correspondence $K = \rho g b^2/12\eta$ between Darcian flow and laminar sheet flow. For large values of specific discharge, Equation (3.41), in accordance with (3.18), gives

$$q = -\left(\frac{8gn^3}{BS_0(1-n)}\right)^{\frac{1}{2}} \operatorname{sgn}\left(\frac{\partial h_B}{\partial x}\right)\left|\frac{\partial h_B}{\partial x}\right|^{\frac{1}{2}} \tag{3.42}$$

and suggests the correspondence

$$\left(\frac{8gn^3}{BS_0(1-n)}\right)^{\frac{1}{2}} = \begin{cases} \left(\dfrac{gb}{f_0}\right)^{\frac{1}{2}} & \text{(Darcy-Weisbach)} \\ \dfrac{1}{n'}\left(\dfrac{b}{2}\right)^{\frac{2}{3}} & \text{(Gauckler-Manning)} \\ C\left(\dfrac{b}{2}\right)^{\frac{1}{2}} & \text{(Chézy).} \end{cases} \tag{3.43}$$

Thus, for both laminar and turbulent sheet flow, the relationships between specific discharge and hydraulic head gradient are represented by analogous expressions in our model. Furthermore, it is worth noting that the constitutive relation (3.41) does more than just represent laminar and turbulent flows—it also provides a continuous solution for the transition between these regimes. Analyses of linked cavity configurations (Walder, 1986; Kamb, 1987) yield expressions that, like Equations (3.40), involve

$(\partial h_B/\partial x)^{\frac{1}{2}}$, but the coefficients involve numerous geometrical variables that would be challenging to disentangle. For cavity configurations, networks of arborescent or braided channels, and other distributed systems our model provides estimates of the hydraulic properties of permeable layers that "effectively" characterize the actual flow systems. In these cases our model suggests alternate—but hydraulically equivalent—representations of the real drainage configurations.

3.6 Concluding remarks

We have presented a physical framework that allows estimation of subglacial hydraulic properties, when combined with field observations of boreholes responding to induced changes in basal water pressure. In general, agreement between responses predicted by the model and those we have observed is satisfactory. To this extent, our theory seems to provide a reasonable description of the coupled borehole-subglacial flow layer system. We have also shown that our model can be applied to a variety of distributed drainage systems. As such, it is potentially useful for many wet-based glaciers.

In the initial applications of our theory to experiments conducted on Trapridge Glacier, we have encountered limitations of the forward modeling procedure. Of particular significance is the fact that we were unable to remove obvious discrepancies between simulated results and field observations by standard forward modeling techniques. These limitations have not seriously compromised our ability to demonstrate model usage; instead, they have exposed potentially interesting aspects of the basal water flow system.

Because response tests are restricted to a small region of influence near the borehole, application of this model to many different borehole response tests—separated both in space and time—is a means by which the distribution of hydraulic parameters can be quantified. This approach is useful for understanding the heterogeneous properties of subglacial drainage systems.

Chapter 4

INVERSION OF BOREHOLE RESPONSE TEST DATA

4.1 Introduction

The physical properties of a system govern its response to a disturbance. In many cases this behavior can be used to probe the system's physical attributes. We are interested in the hydraulic properties that govern subglacial water flow. In this chapter we develop and apply a methodology for estimating subglacial hydraulic properties from observations of a drainage system's response to sudden changes in basal water pressure. We examine three types of pressure disturbances, which are particularly easy to produce and observe: connection-drainage, slug test, and packer test. Collectively, we refer to these different types of disturbances and observations of the responses that they induce as *borehole response tests.*

In the previous chapter we developed a theory of borehole response tests. Our theory relates the physical properties of a borehole–subglacial aquifer system to a disturbance response; the physical properties are cast as model parameters and the disturbance response comprises a set of predicted borehole water level data. We have shown that the theory can be used to generate predicted data which can be compared with field observations. Calculating the response of a borehole–subglacial aquifer system, as we have done, from a given theory and set of model parameters constitutes solving a "forward problem".

In contrast to the "forward problem", an "inverse problem" begins with observed data and is guided by a theoretical model or principle toward an estimate of the model parameters (Menke, 1989). Forward theory focuses on describing the underlying physics of a particular system; inverse theory uses known or assumed physics and focuses on

specific properties of the system. The capability of providing quantitative information about model parameters makes inversion a valuable tool for estimating subglacial hydraulic properties.

Although the application of formal geophysical inverse techniques is not new to glaciology (e.g., Blankenship and others, 1987; MacAyeal and others, 1991; MacAyeal, 1992), they have not before been used to estimate subglacial hydraulic properties from borehole data. This is due, at least in part, to the prior lack of a borehole–drainage system model that accounts for high-gradient test conditions; standard models, such as those used in groundwater hydrology, do not include the effects of turbulent flow. Under high gradient conditions brought about by hydraulic testing, turbulent effects can play an important role in highly transmissive systems, including fractured bedrock, karst terrain, and sand and gravel aquifers—any one of which might be found subglacially. Recently, McElwee and others (1992) have considered the nonlinearities associated with turbulent flow in a sand and gravel aquifer. Theirs is a steady state model, however, and does not describe the transient problem that we have addressed.

In what follows, we present an inversion methodology that is based on our borehole response model. We use the method to invert response test data from Trapridge Glacier. Our goal in this chapter is twofold: (1) to further develop the theory and practice of borehole response testing as a tool for assessing subglacial hydraulic properties, and (2) to estimate hydraulic properties of the basal drainage system of Trapridge Glacier.

4.2 Methodology

4.2.1 Data selection and processing

Inversion schemes use data to obtain estimates of model parameters. Thus, a natural starting point is with the data themselves. During the summer field seasons of 1989, 1990, and 1991 we performed 85 borehole response tests on Trapridge Glacier. In this chapter we present inversions of data from nine different response tests, three

of each type: connection-drainage, slug test, and packer test. By selecting an equal number of each type of test, we have tried to strike a balance between the dual goals of further developing borehole response testing, and of estimating the subglacial hydraulic properties of Trapridge Glacier.

We have performed numerous borehole response tests, but we have not attempted to invert every data set; inadequate or poorly-controlled data have been excluded. In some cases the data that we collected are unusable because we did not monitor borehole water levels for sufficient periods of time prior to and following the disturbances. In these cases, background trends in basal water pressure cannot be distinguished from the disturbance responses. Also, because re-equilibration is difficult to judge in the field, many of our slug tests were performed before the system had fully recovered from previous disturbances. Tests performed under such conditions give post-disturbance responses that are not fully-described by our model. The data that we have selected to invert come from the tests in which background trends in basal water pressure and other influences—such as nearby drilling—are best-known.

We used pressure sensors suspended in boreholes to monitor water levels during response tests. Readings of borehole water pressure were collected every 0.0625 s during disturbances, while background trends and long term recoveries were recorded at 2.0 s intervals. As will be subsequently discussed, the forward model and the initial conditions are scaled according to the background hydraulic head at the time that a particular response test took place. To facilitate this scaling, we processed the data to put them in a standardized format. The processing procedure was as follows: Each data set was fit with an interpolating spline (Press and others, 1989, p. 88), and data having a uniform spacing of 0.125 s were generated from it. We used a normalized Gaussian filter having a width of 11 data points to remove noise from the uniform data sets. For connection-drainage tests, the data were shifted so that readings prior to connections correspond to a water-column height equal to the glacier thickness (assumed

to be 70.0 m). For slug and packer tests, data were shifted so that water-level readings represent displacements relative to a pre-disturbance datum (defined to have a value of zero).

The procedure for standardizing slug and packer test data is illustrated in Figure 4.1, and is explained here. Data prior to initial disturbances, shown as dashed segments in Figures 4.1a and 4.1c, were fitted with straight lines. These straight line fits represent background trends in basal water pressure at the times that the tests were performed; we removed background pressure trends by subtracting the fitted straight lines from the data. As a final step, we shifted the data so that pre-disturbance water levels define a zero datum. This allows the data to be expressed as displacements relative to that datum (Figs. 4.1b and 4.1d; dashed segments represent the datum).

Processing slug and packer test data as we have done readily shows if and when the system fully recovers from disturbances during a test. As can be seen in Figure 4.1b, the water level had returned to its original position (taking into account the background trend) by the time the slug was removed, but data collection ceased before the system had fully recovered from the disturbance. For the test shown in Figure 4.1d, the water level had not returned to its original position when the slug was removed. These examples demonstrate a difficulty with borehole response testing; namely, determining, in the field, whether or not the system has re-equilibrated.

4.2.2 Inversion scheme

The borehole response model that we developed in Chapter 3 represents a nonlinear functional relationship f between the model parameters m_i and the predicted borehole water level data d_i, which we may express as $f(m_i) = d_i$. If the model accurately describes the geometry and physics of the subglacial water flow system, and if the initial conditions and model parameters are well-known, then d_i will closely approximate observed response test data d_i^{obs}. To gauge the accuracy of the model and how well its

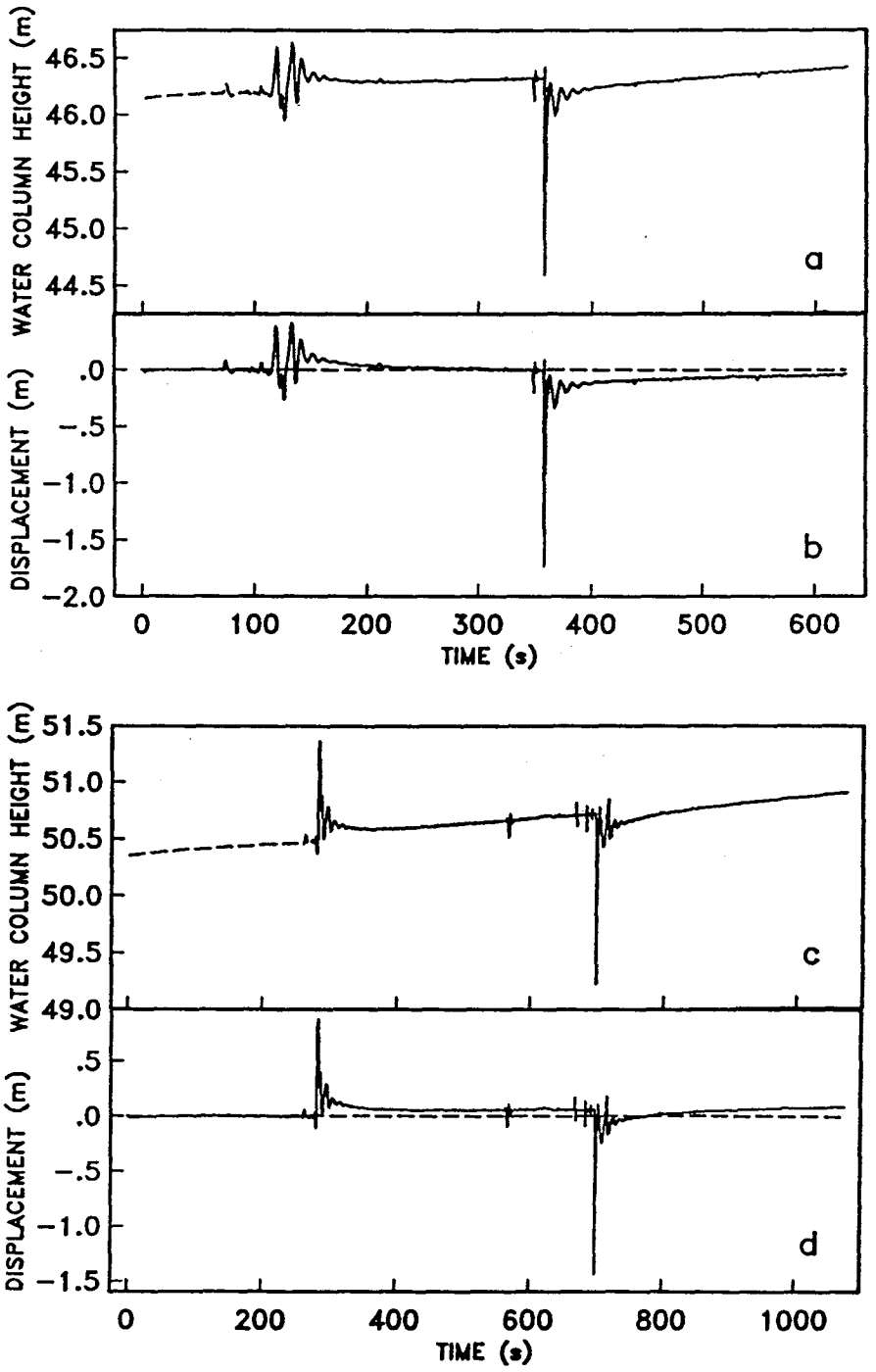

Fig. 4.1: Removal of background trends illustrated for two slug tests: (a) 90ST38A and (c) 90ST38E. The procedure is explained in the text. (b) For 90ST38A the system was fully re-equilibrated at the time the slug was removed. (d) In the case of 90ST38E the slug was removed when the water level was higher than its pre-disturbed value.

inputs are known, a measure of the discrepancy between predicted and observed data is required. The method of least squares is commonly employed for this purpose. Our inversion scheme uses the least-squares method, but has added complexity because the predicted data must be obtained through numerical integration of a nonlinear function.

The idea behind the method of least squares is to find a set of model parameters such that the predicted data d_i are as close as possible, in terms of Euclidean distance, to the observed data d_i^{obs}. In this method, "closeness" is measured by the data misfit $e_i = d_i^{\text{obs}} - d_i$, and the best set of model parameters is the one that leads to the smallest total data misfit

$$E = \sum_{i=1}^{N} \left(d_i^{\text{obs}} - d_i\right)^2 \tag{4.1}$$

where N is the number of data and E is the squared Euclidean length of the vector $\mathbf{e}$ having components e_i (Menke, 1989, p. 36). For many applications it is desirable to weight individual data misfit terms according to the estimated uncertainties in the observed data δd_i^{obs}, and to normalize the total misfit by dividing by N. These modifications, applied to Equation (4.1), lead to the following objective function:

$$\Phi = \frac{1}{N} \sum_{i=1}^{N} \left(\frac{d_i^{\text{obs}} - d_i}{\delta d_i^{\text{obs}}} \right)^2 . \tag{4.2}$$

The goal is to obtain the smallest value of Φ, since this minimizes the total misfit between predicted and observed data. However, in using our response tests model it is necessary to modify (4.2) because the inversion algorithm must be restricted to searching a region of model space in which numerical solutions can be computed. The differential equations that comprise the forward model are coupled, stiff, and nonlinear. Under these circumstances numerical integration fails if model parameters are too unrealistic. Modification of (4.2) is also required to regularize the inversions. Regularization assures that small changes in the data will produce small changes in the model

parameter estimates, so that the solution remains stable (Tikhonov and Arsenin, 1977, p. 48). To guide and regularize inversions, we add a second term to the right hand side of Equation (4.2) that measures the parameter misfit. The resulting expression is

$$\Phi = \frac{1}{N}\sum_{i=1}^{N}\left(\frac{d_i^{\text{obs}} - d_i}{\delta d_i^{\text{obs}}}\right)^2 + \lambda\frac{1}{M}\sum_{i=1}^{M}\left(\frac{m_i - m_i^{\text{est}}}{\delta m_i^{\text{est}}}\right)^2 \tag{4.3}$$

where M is the number of parameters, m_i^{est} are estimates of the parameters that minimize Φ, δm_i^{est} are the uncertainties associated with each m_i^{est}, and the trade-off parameter λ is an adjustable constant that determines the relative importance of the parameter and data misfit terms. The estimated parameter uncertainties δm_i^{est} are used to specify the relative reliability of the parameter estimates, so that better-constrained parameters can exert greater influence.

A simplified representation of Φ, showing the numerical solution space boundary and the distinction between m_i and m_i^{est}, is given in Figure 4.2. Also illustrated in this figure is the difference between local and global minima of Φ, a topic that we will subsequently discuss, and the distinction between estimated model parameters m_i^{est} and initial parameter values m_i^0.

By virtue of the parameter misfit term in Equation (4.3), an optimal solution—the set of model parameters that results in the smallest value of the objective function—will not necessarily correspond to the smallest total data misfit. We are forced, by the nonlinear nature of the forward model and its numerical method of solution, to accept a trade-off between being able to compute predicted data and fitting the observed data. In most cases this trade-off does not greatly compromise our results; the degree to which λ influences the final value of Φ is examined below.

In its fully-dimensioned form the borehole response model depends on 10 geometric and hydraulic parameters, some of which are coupled and cannot be individually distinguished. Coupling between model parameters suggests that the non-dimensional

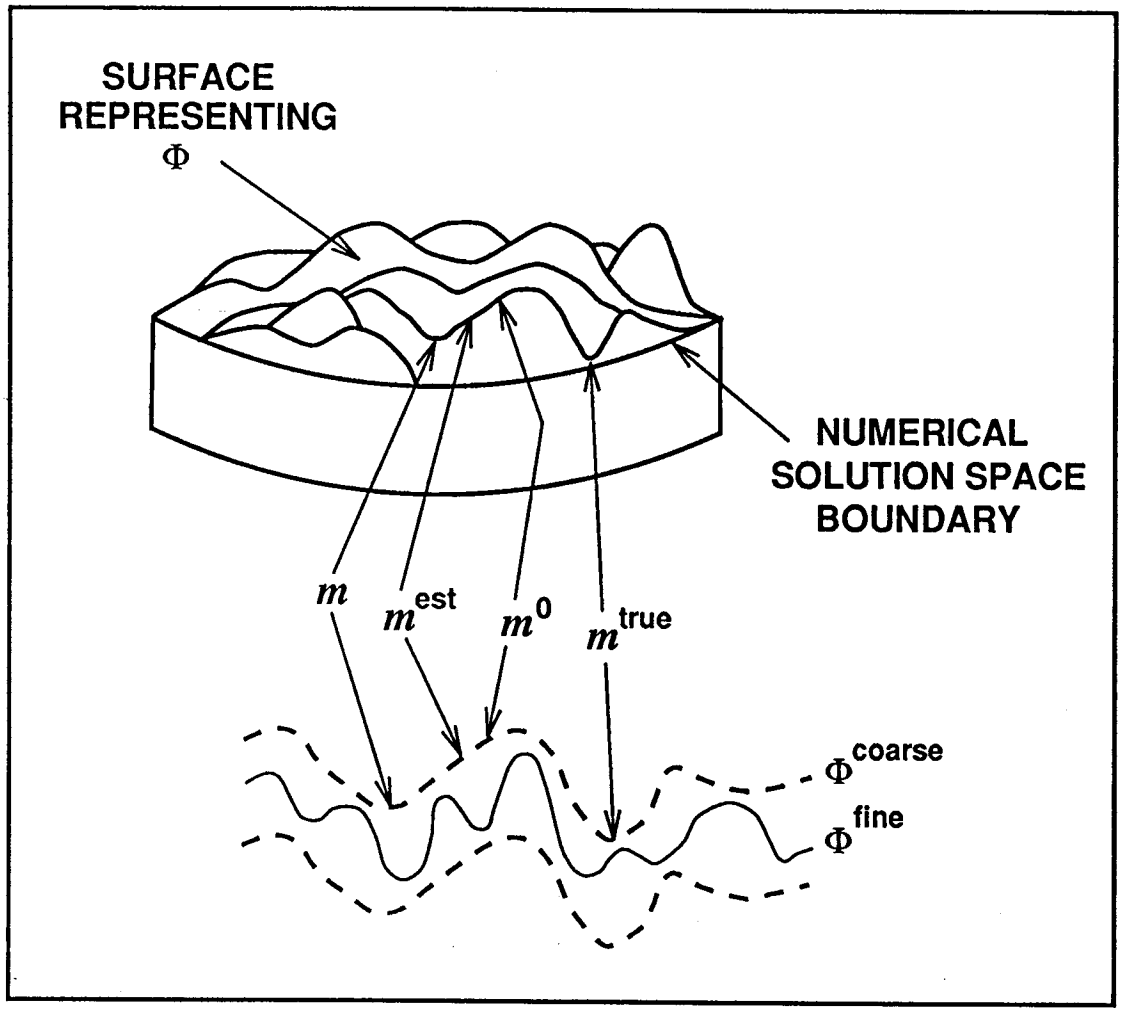

Fig. 4.2: Simplified representations of the objective function surface and the numerical solution space boundary. The objective function Φ guides the inversion routine to regions of model space in which numerical solutions can be computed. The upper part of the figure illustrates how surface topography will influence the search for an optimal set of model parameters m. Because the quasi-Newton method is based on Taylor series expansions, it is not possible to guarantee that a globally optimal parameter set m^{true} will be found. The lower part of the figure illustrates the difference between surface topography (coarse) and roughness (fine). The distinction between Φ^{coarse} and Φ^{fine} depends on the sensitivity of the forward model to changes in model parameters. Allowing for different initial parameter values m^0 and estimated optimal values m^{est} aids in distinguishing between Φ^{coarse} and Φ^{fine}.

formulation of the model, which was described in Chapter 3, should be used for inversions. The non-dimensional formulation has the added benefit of reducing the required number of model inputs.

4.2.3 Inversion parameters and model inputs

The borehole response model depends on four dimensionless parameters: the skin friction parameter ζ, the diffusivity parameter χ, the transmissivity parameter Υ, and the Ergun parameter ξ. These parameters have been previously defined (Eqns. 3.31–3.34) as

$$\zeta = \left(\frac{8\eta}{\rho_w {r_w}^2}\right)\left(\frac{h_0}{g}\right)^{\frac{1}{2}}, \tag{4.4}$$

$$\chi = \left(\frac{K}{S_s {r_f}^2}\right)\left(\frac{h_0}{g}\right)^{\frac{1}{2}}, \tag{4.5}$$

$$\Upsilon = \left(\frac{2Kb}{{r_w}^2}\right)\left(\frac{h_0}{g}\right)^{\frac{1}{2}}, \tag{4.6}$$

$$\xi = \left(\frac{K^2 B S_0 (1-n) h_0}{2 r_f g n^3}\right) \tag{4.7}$$

where the right-hand-side quantities are as defined in Chapter 3. We have restated the expressions here to emphasize the fact that all four dimensionless parameters must be non-negative, if the solution is to be physically plausible. To enforce non-negativity of model parameters, we distinguish between inversion and model parameters and we define the inversion parameters as the natural logarithms of the model parameters; hence, $m_1 = \ln \zeta$, $m_2 = \ln \chi$, $m_3 = \ln \Upsilon$, and $m_4 = \ln \xi$. This scheme requires that antilogarithms of inversion parameters be taken before computing forward model solutions.

For inversions of connection-drainage and packer test data we include a fifth parameter. In the former case this parameter specifies the time of the connection. For packer test inversions, the fifth parameter specifies the maximum pressure achieved in pumping up the borehole. Neither of these quantities are accurately known, and they can significantly influence inversion results. By including them as inversion parameters we obtain optimal estimates of these quantities. However, because they are not of hydrologic interest, we will exclude them from further discussions.

The uncertainties that we associate with estimated inversion parameters are based on plausible upper and lower limits for the dimensionless model parameters. We have selected plausible limits for ζ on physical grounds, by considering only realistic values for the borehole radius. Plausible bounds for the other parameters were chosen based on preliminary forward modeling results. The difference between the logarithms of the limits assigned to the plausible model parameters is the uncertainty that we associate with a given estimated inversion parameter: $\delta m_i^{\text{est}} = \ln m_i^{\text{upper}} - \ln m_i^{\text{lower}}$. With this definition, better-constrained parameters, such as ζ, are associated with a smaller uncertainty.

The forward model requires input of quantities other than model parameters. Material constants such as the density, viscosity, and compressibility of water must be specified, as well as geometric quantities like the ice thickness, and the inner- and outer-boundary radii. The outer-boundary condition must also be specified. For the inversions that we will present here, we have used an "open" boundary condition. As described in Chapter 3, this condition corresponds to a constant head boundary. Thus, we assume that the preexisting hydraulic head in the flow layer is unaffected by response-test disturbances at a sufficient distance from the borehole; this distance corresponds to the outer-boundary radius. Values of adjustable non-parameter inputs, which were held constant for all inversions, are listed in Table 4.1.

Model input	Symbol	Value	Units
Ice thickness	h_i	70.0	m
Outer boundary radius	r_{max}	200.0	m
Inner boundary radius	r_f	0.05	m
Uncertainty in data	δd_i^{obs}	0.05	m
Uncertainty in ln ζ^{est}	δm_1^{est}	2.3	
Uncertainty in ln χ^{est}	δm_2^{est}	18.4	
Uncertainty in ln Υ^{est}	δm_3^{est}	8.3	
Uncertainty in ln ξ^{est}	δm_4^{est}	9.2	
Trade-off parameter	λ	0.01	

Table 4.1: Forward model inputs held constant for inversions.

In addition to the inputs listed in Table 4.1, the model also requires input of the background hydraulic head h_0 at the time a particular response test was performed. This quantity is not a constant and must be known or estimated for each test. It is used, in the nondimensionalized model, to scale both the hydraulic head variables and the time (Eqn. 3.28). Values of h_0 are listed in Table 4.3, along with the estimated model parameters that were used in the inversions.

4.2.4 Inversion procedure

To minimize the objective function (Eqn. 4.3), parameters in the forward model are adjusted using a quasi-Newton method. The inversion algorithm that we use is a double precision optimization routine given by Kahaner and others (1989, p. 372). We have tailored the algorithm to mesh with the numerical solution method of the forward model; this was necessary to ensure that changes in model parameters, which are made by the inversion routine, produced numerically distinguishable changes in the forward model solution. Thus, the sensitivity of the forward model limits the precision of Φ and determines the distinction between topography and roughness of the objective function surface (Fig. 4.2).

The inversion method requires (1) a way of solving the forward problem, (2) a measure of model success in fitting the observed data, and (3) initial estimates of model parameters. Our numerical response tests model satisfies the first requirement, and the second is provided by the objective function. The third requirement—providing estimates of model parameters—is handled iteratively in the following way: We start an inversion with model parameters that are known from forward modeling to produce a reasonable fit to the observed data. At this stage, the estimated set of model parameters represents our best guess of what the final solution will be. When the inversion is complete, the final set of model parameters will correspond to a minimum value of Φ. We then start a second inversion by setting the initial model parameter estimates equal to the final parameter values that were previously found. When the second inversion is complete, we compare the final value of Φ with that of the first inversion. In many cases the two values of Φ agree to our specified level of precision. (Changes in Φ smaller than the precision that we specify—four significant digits—correspond to parameter changes that do not appreciably alter the forward model solution.) In some cases, however, additional inversions are required to reach consistent final values of Φ; these situations can be encountered when the parameter misfit is significant. The end result of this iterative procedure is a "best-fitting" model.

A "best-fitting" model, for our purposes, is one in which the total data misfit E is minimum. To evaluate the relative success of "best-fitting" models the percentage misfit $E_{\%}$ is commonly used. This quantity, defined as

$$E_{\%} = 100 \times \left[\frac{1}{N} \sum_{i=1}^{N} \left(\frac{d_i^{\text{obs}} - d_i}{d_i^{\text{obs}}} \right)^2 \right]^{1/2}, \tag{4.8}$$

indicates the accuracy of a given set of predicted data; smaller percentage misfits are associated with more accurately predicted data. In the following sections we will use $E_{\%}$ as a measure of how well inversions succeed in fitting the data.

The iterative inversion procedure is illustrated using data from slug test 90ST38A (Fig. 4.3). The initial model parameter estimates and associated values of Φ and $E_{\%}$ are listed in Table 4.2. The dashed line in Figure 4.3a is the forward model solution based on our initial parameter estimates. In this particular case, we were intentionally trying to fit only the long-term trend, not the initial oscillations. The dashed line in Figure 4.3b was computed using the final set of parameters that were obtained by the first inversion. These final estimates were then used as the starting values for a second inversion, which resulted in the solution shown in Figure 4.3c. As can be seen in Table 4.2, our initial model parameter estimates resulted in a value of $E_{\%} = 0.2$. After the first inversion $E_{\%}$ had been reduced to 0.1, and the fit to the observed data was noticeably improved. The values of Φ and $E_{\%}$ following the second inversion did not significantly change from that of the first inversion, although the values of χ and Υ changed slightly. In this particular case, we performed a third inversion to ensure that Φ remain unchanged. The final inversion gave the solution shown in Figure 4.3d.

	m^{est}			m^{final}
Figure	4.3a	4.3b	4.3c	4.3d
Iter.	0	1	2	3
ζ	1.000×10^{-2}	2.300×10^{-3}	2.300×10^{-3}	2.300×10^{-3}
χ	$1.000 \times 10^{+3}$	3.730×10^{-2}	3.617×10^{-2}	3.621×10^{-2}
Υ	5.000×10^{-1}	1.070×10^{-1}	1.051×10^{-1}	1.057×10^{-1}
ξ	$1.000 \times 10^{+3}$	2.520×10^{-3}	2.520×10^{-3}	2.520×10^{-3}
Φ	5.201	1.296	1.296	1.296
$E_{\%}$	0.2	0.1	0.1	0.1

Table 4.2: Initial estimates of model parameters m^{est} for inversions of slug test 90ST38A data, as shown in Figure 4.3. The iterative inversion procedure gave final estimates of model parameters m^{final} that were substantially different from the starting values listed in column a.

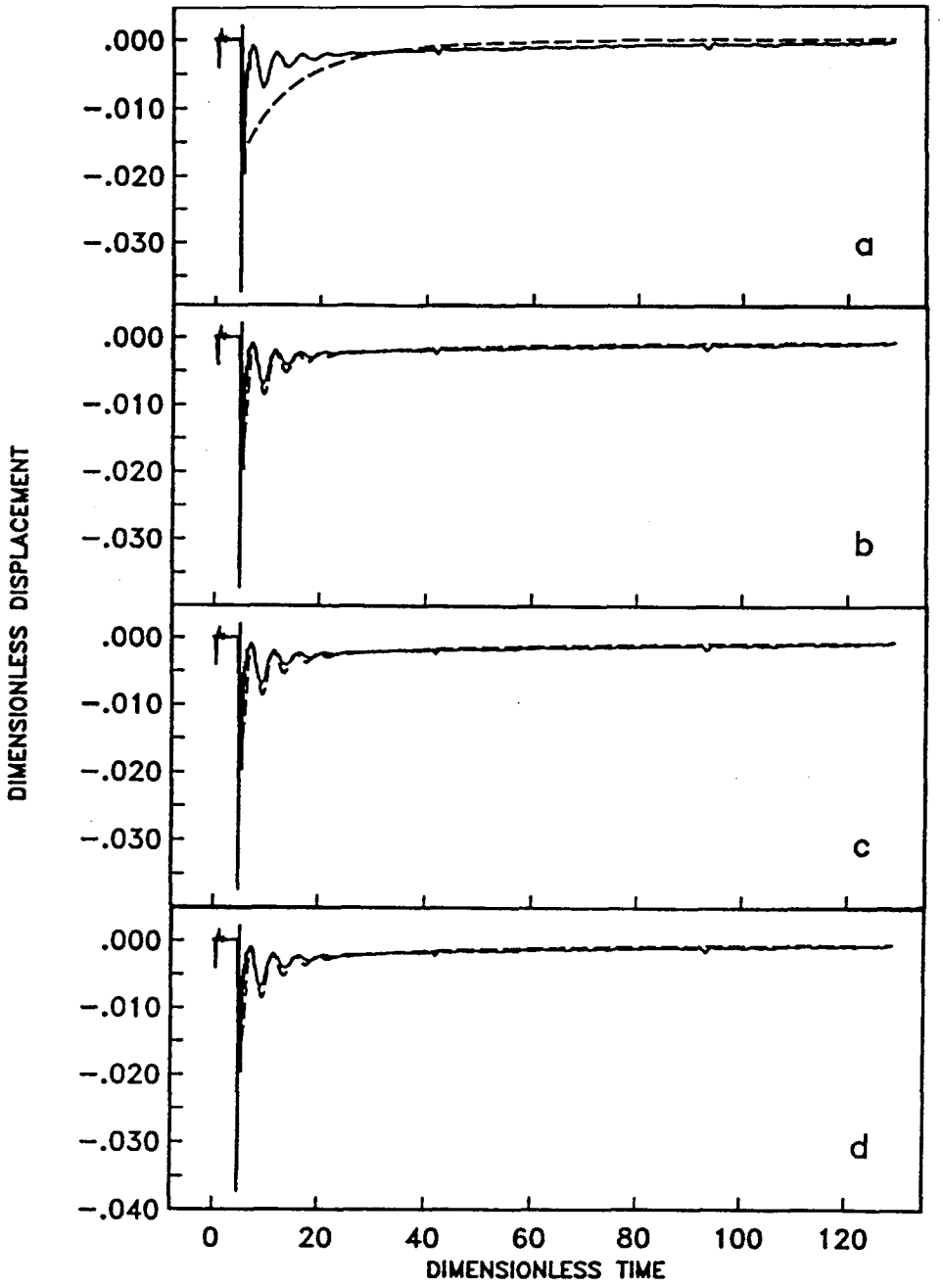

Fig. 4.3: Iterative inversion procedure illustrated with data from slug test 90ST38A (solid lines) and modeled results (dashed lines). Model input parameters are listed in Table 4.2. The procedure is explained in the text.

4.2.5 Nonuniqueness and uncertainty

Optimization methods that are based on Taylor expansions, such as the quasi-Newton method, are guided by information on how a function behaves near a given point; they lack detailed information about a function's behaviour over the entire region. These methods are sensitive to initial starting conditions because the algorithm has only local information with which to search for a solution. Local conditions are further emphasized in our case by the parameter misfit term in the objective function. It is easy to imagine the objective function as a surface having many hills and valleys, and the particular valley bottom that we end up in depends on where on the surface we start our search. This sensitivity to initial starting conditions implies uncertainty in the final solution, as the result of an inversion might be a local minimum of Φ, not a global minimum. We must also consider the possibility of nonuniqueness, as there may be two or more equally deep valley bottoms representing multiple minima of equal depth. These points are illustrated in Figure 4.2. To help locate a global minimum, a uniform grid search technique could be used. However, this procedure would be too costly for inversions of multiple response tests.

4.3 Sensitivity analysis

The objective function can be separated into two terms, one representing the data misfit Φ_d and one representing the parameter misfit Φ_p: $\Phi = \Phi_d + \lambda\Phi_p$ where

$$\Phi_d = \frac{1}{N}\sum_{i=1}^{N}\left(\frac{d_i^{obs} - d_i}{\delta d_i^{obs}}\right)^2 \qquad (4.9a)$$

and

$$\Phi_p = \frac{1}{M}\sum_{i=1}^{M}\left(\frac{m_i - m_i^{est}}{\delta m_i^{est}}\right)^2. \qquad (4.9b)$$

We have examined the influence of the trade-off parameter λ on the final values of Φ_d and Φ_p by varying only λ in repeated inversions of data from one response test

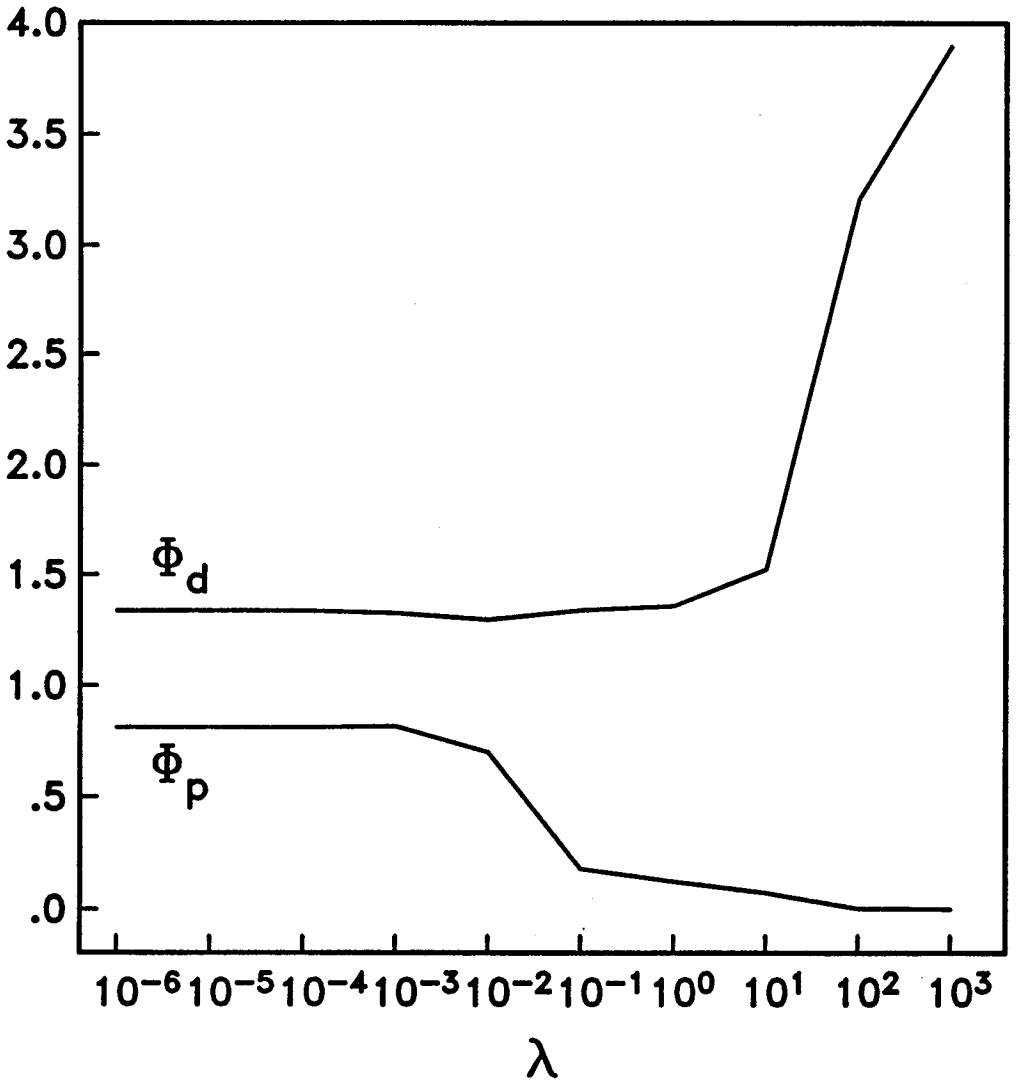

Fig. 4.4: Trade-off curve based on inversions of slug test 90ST38A data: size of data Φ_d and parameter Φ_p misfit terms as a function of trade-off parameter λ.

(90ST38A); we performed ten inversions, changing λ by one order of magnitude each time. The initial model-parameter estimates for these inversions were the same as those listed in column (a) of Table 4.2. We point out that for $\lambda = 0.01$, an inversion started with these initial parameter estimates produced the final set of parameters listed in column (b) of Table 4.2. The final parameters that were found in this inversion were substantially different from the initial estimates. Thus, this particular inversion

approximates a worst-case scenario; the total parameter misfit is large, so the influence of λ should be strongly felt.

Final objective function values resulting from these inversions were used to generate relationships between λ and the two misfit terms (Fig. 4.4). These relationships show that the data misfit is virtually constant for $\lambda \leq 10^{-2}$, while it changes rapidly for $\lambda > 1$. Also, the parameter misfit is gradually reduced as λ is increased and the requirement of closely matching initial parameter estimates becomes dominant. It is apparent that for $\lambda \leq 10^{-2}$ the parameter misfit term does not significantly contribute to the final value of Φ, since the data misfit is large relative to $\lambda\Phi_p$. On the other hand, for $\lambda \geq 10^{-1}$, the parameter misfit term forces an appreciable increase in Φ_d and moves the solution away from the desired goal of fitting the data. Larger values of λ will force a quicker recovery when "out-of-bounds" parameters are encountered, but this benefit should not override our objective of fitting the data. Based on this analysis, we have maintained a constant value of $\lambda = 0.01$ for all the inversions that we present here.

4.4 Inversion results

We have inverted nine sets of response test data that were collected on Trapridge Glacier during the 1990 field season. The starting points for these inversions are given in Table 4.3. Estimated parameter values that were found by the inversions were used to generate final sets of predicted data. The final parameter values are given in Table 4.4. Comparisons of predicted and observed data are given in three figures, each showing a single type of test: connection-drainage (Fig. 4.5), slug test (Fig. 4.6), and packer test (Fig. 4.7). To facilitate comparison of predicted and observed data, we have used background hydraulic head values (Table 4.3) to nondimensionalize observed data.

	m^{est}				
	ζ	χ	Υ	ξ	h_0 (m)
90CD23	1.00×10^{-2}	1.10×10^{5}	1.90×10^{0}	2.50×10^{2}	62.0
90CD38	1.00×10^{-2}	1.10×10^{5}	1.90×10^{0}	2.50×10^{2}	46.6
90CD59	1.00×10^{-2}	1.10×10^{5}	1.90×10^{0}	2.50×10^{2}	49.8
90ST38A	2.30×10^{-3}	3.62×10^{-2}	1.06×10^{-1}	2.52×10^{-3}	46.1
90ST38E	2.30×10^{-3}	3.62×10^{-2}	1.06×10^{-1}	2.52×10^{-3}	50.3
90ST38G	2.30×10^{-3}	3.62×10^{-2}	1.06×10^{-1}	2.52×10^{-3}	51.4
90PT58A	2.30×10^{-3}	1.00×10^{-1}	3.00×10^{-1}	2.50×10^{-3}	49.7
90PT58B	2.30×10^{-3}	1.00×10^{-1}	3.00×10^{-1}	2.50×10^{-3}	49.5
90PT61C	2.30×10^{-3}	1.00×10^{-1}	3.00×10^{-1}	2.50×10^{-3}	61.0

Table 4.3: Initial estimates of model parameters and hydraulic head for the inversions shown in Figures 4.5, 4.6, and 4.7.

The three connection-drainage observations shown in Figure 4.5 were recorded in boreholes in close proximity; the maximum separation distance was 34.9 m (Holes 38 and 59), and the minimum distance was 5.3 m (Holes 23 and 38). Boreholes 23, 38, and 59 were drilled on 16 July, 25 July, and 4 August respectively. In all three cases the final parameter values were similar, and the inversion solutions gave good fits to the observed data.

	m^{final}				
	ζ	χ	Υ	ξ	$E_{\%}$
90CD23	9.95×10^{-3}	4.11×10^{4}	3.84×10^{0}	2.22×10^{3}	0.4
90CD38	1.00×10^{-2}	9.59×10^{4}	1.69×10^{0}	1.25×10^{2}	0.6
90CD59	9.99×10^{-3}	9.49×10^{4}	2.74×10^{0}	1.69×10^{3}	0.4
90ST38A	2.30×10^{-3}	3.62×10^{-2}	1.06×10^{-1}	2.52×10^{-3}	0.1
90ST38E	2.29×10^{-3}	9.29×10^{-2}	2.14×10^{-1}	2.52×10^{-3}	0.1
90ST38G	2.30×10^{-3}	3.58×10^{-2}	1.14×10^{-1}	2.52×10^{-3}	0.1
90PT58A	2.14×10^{-3}	2.16×10^{-2}	1.76×10^{-6}	2.50×10^{-3}	97.5
90PT58B	2.41×10^{-3}	2.62×10^{-1}	1.31×10^{-6}	2.50×10^{-3}	97.2
90PT61C	2.32×10^{-3}	6.62×10^{-1}	1.76×10^{-7}	2.50×10^{-3}	98.6

Table 4.4: Final estimates of model parameters and percentage misfits for the inversions shown in Figs. 4.5, 4.6, and 4.7.

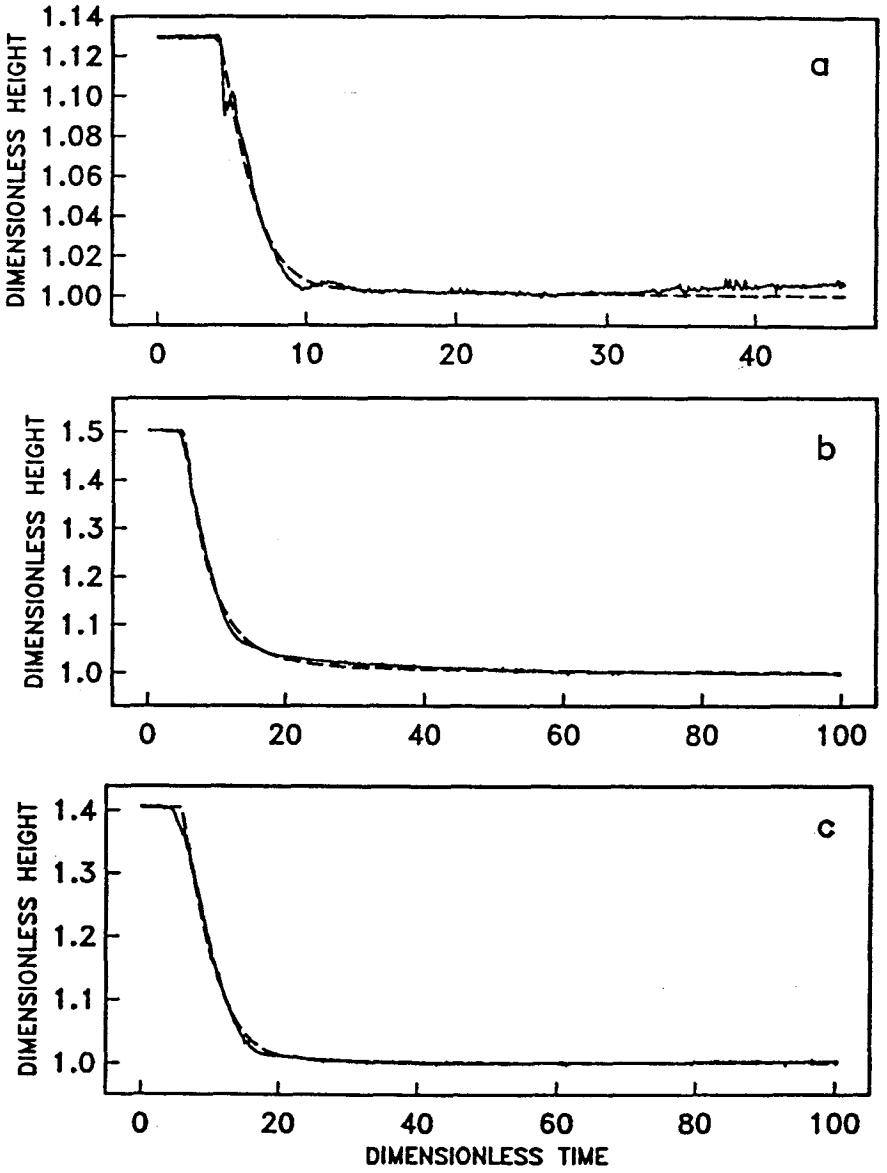

Fig. 4.5: Connection-drainage data (solid lines) and inversion results (dashed lines): (a) 90CD23; (b) 90CD38; and (c) 90CD59.

Figure 4.6 shows three slug tests performed in the same borehole (Hole 38) on 25 July. The first test was performed at 1448 (Fig. 4.6a), the second at 1654 (Fig. 4.6b), and the third at 1730 (Fig. 4.6c). A slight rising trend in the observed data—persisting above the pre-disturbance water level—is evident in Figure 4.6b. We have observed similar responses during other tests which were performed before the system had fully

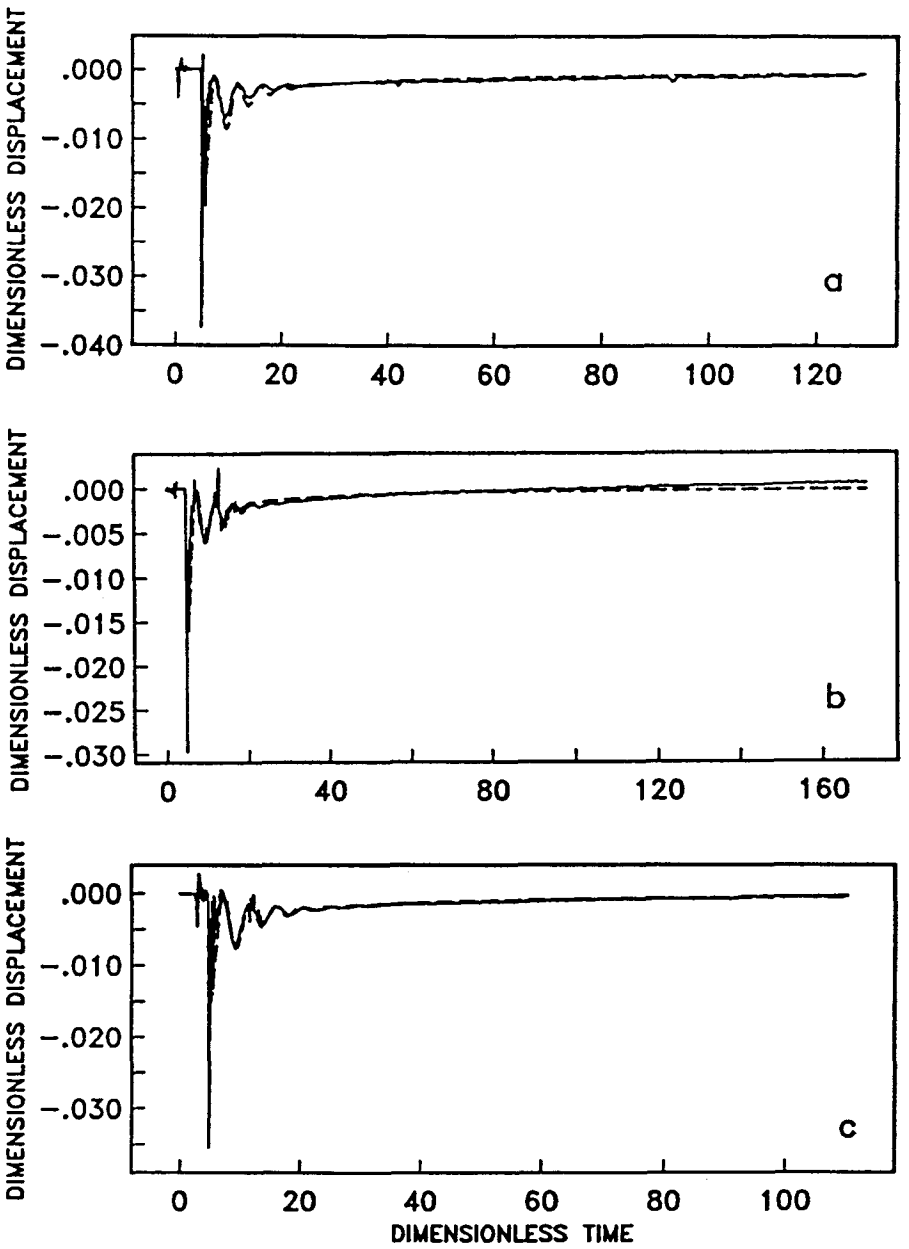

Fig. 4.6: Slug test data (solid lines) and inversion results (dashed lines): (a) 90ST38A; (b) 90ST38E; and (c) 90ST38G.

recovered from previous disturbances; in this particular case, we have already noted that slug test 90ST38E was performed before the water level had returned to its original position (Fig. 4.1d).

The three sets of slug test data were well-fit by inversion-generated model parameters. Of particular significance is the fact that discrepancies between observed and modeled results—apparent in the forward-modeled solution presented in Chapter 3—have been eliminated by a judicious choice of model parameters. Final parameter values are consistent for all three inversions of slug test data. However, final values differ—substantially for χ and ξ—from those obtained by inversions of connection-drainage data. Drainage observation 90CD38 and the three slug tests all took place in the same borehole, yet significantly different parameter estimates were obtained from the two different types of tests. Furthermore, inversion results for the three connection-drainage observations are similar, even though the observations were made in different boreholes. These results suggest that there may be important differences between the two types of tests—either in the hydraulic properties to which they are sensitive, or in the kinds of systems that they sample.

Packer tests are shown in Figure 4.7. To a first-order approximation, the inversions succeed in fitting the large scale characteristics of the data. However, good fits to the detailed features of the tests were not obtained. Inversions of packer test data were, in general, less successful than those of connection-drainage and slug test data. A particularly interesting characteristic of packer tests is the positive and persistently-increasing displacement trend following the release of pressure in the borehole. This trend is not predicted by our model, and it strongly influences inversion results. We further discuss this trend in the next section.

4.5 Discussion

4.5.1 Data processing

An important part of our overall methodology is the data processing stage, particularly the removal of background pressure trends. We have simplified our mathematical description of the borehole–subglacial aquifer system by assuming that response tests

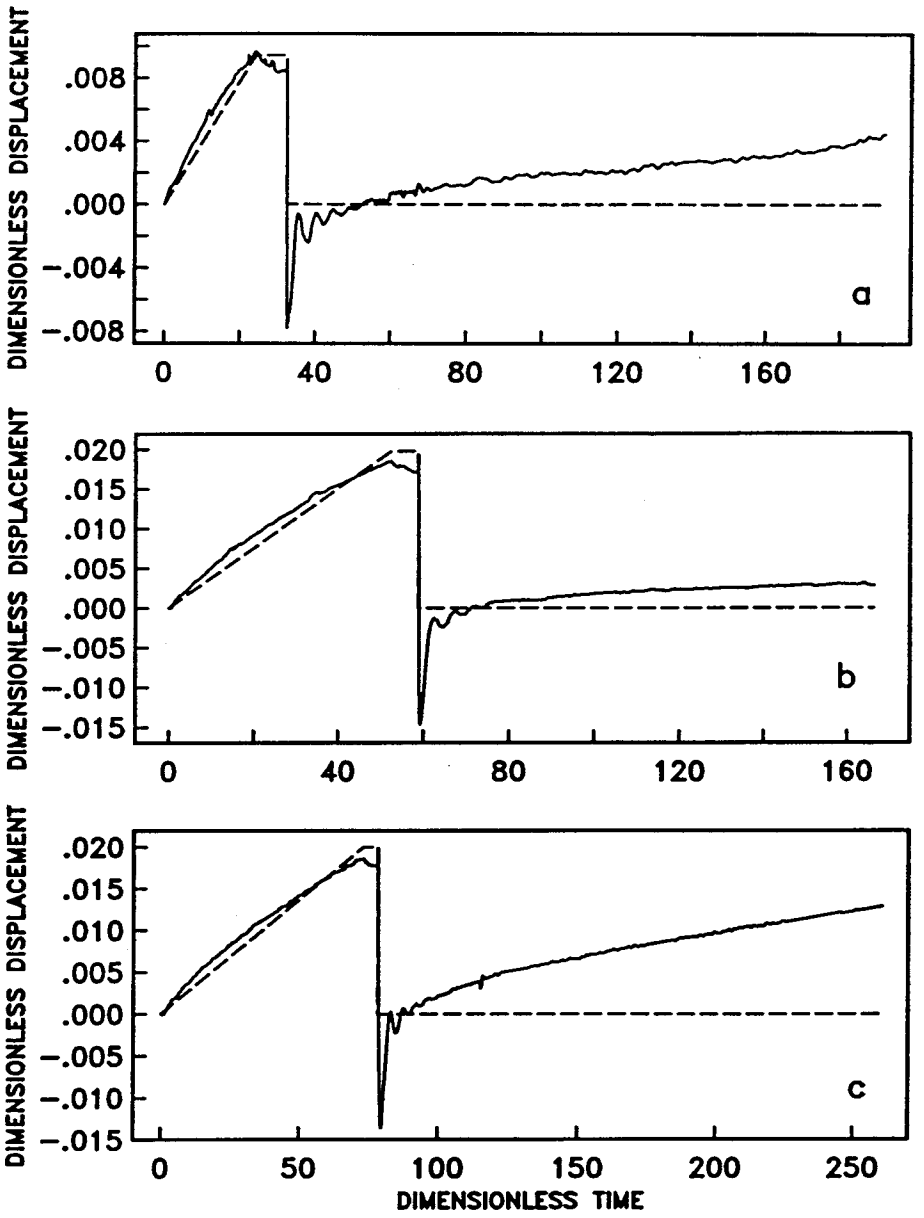

Fig. 4.7: Packer test data (solid lines) and inversion results (dashed lines): (a) 90PT58A; (b) 90PT58B; and (c) 90PT61C.

are small brief perturbations to the system. The removal of background trends isolates these perturbations. For obvious reasons, background trends cannot be measured prior to connection-drainage observations, unless other pressure sensors exist nearby and are in a common part of the drainage network. However, it may be possible to extrapolate

backwards based on long-term post-disturbance trends. For the drainage observations that we have made, we are unable to correct for background trends because we did not collect long-term data following connections.

The removal of background pressure trends from observed data readily shows if and when the system fully recovers from previous disturbances. Thus, qualitative assessments of how well the tests were performed can be made. Without real-time data processing, it is difficult to separate background trends from disturbances while in the field. As a result, some tests will be better-performed than others. Removing background trends helps identify the better-performed tests.

4.5.2 Packer tests

We have previously noted the positive, post-release displacement trends in the packer test data that we have inverted. Similar post-release responses were recorded during all of our 1990 packer tests. Positive water-column displacement, relative to the pre-disturbance water level, suggests that additional water—besides that which is displaced during pump-up—refills the borehole following the release of pressure. Alternatively, the trend could be an artifact of our data processing, introduced when we standardize the data for inversions.

In Figure 4.8 we consider the second possibility: Our standardization procedure consists of removing the background pressure trend that exists before a disturbance. For the test shown in Figure 4.8 (90PT58B), the background trend is evident in the nearly linear segment of the original data (solid curve) prior to $t \approx 225\,\mathrm{s}$. (For ease of comparison we have DC-shifted the original data, so that both it and the standardized data have the same initial value.) We fitted a straight line to the linear segment, and then subtracted this line from the original data to obtain the standardized data (short dashed curve) that we inverted. The pre-disturbance equilibrium level—taking into account the background trend—is indicated by the long dashed line. After the

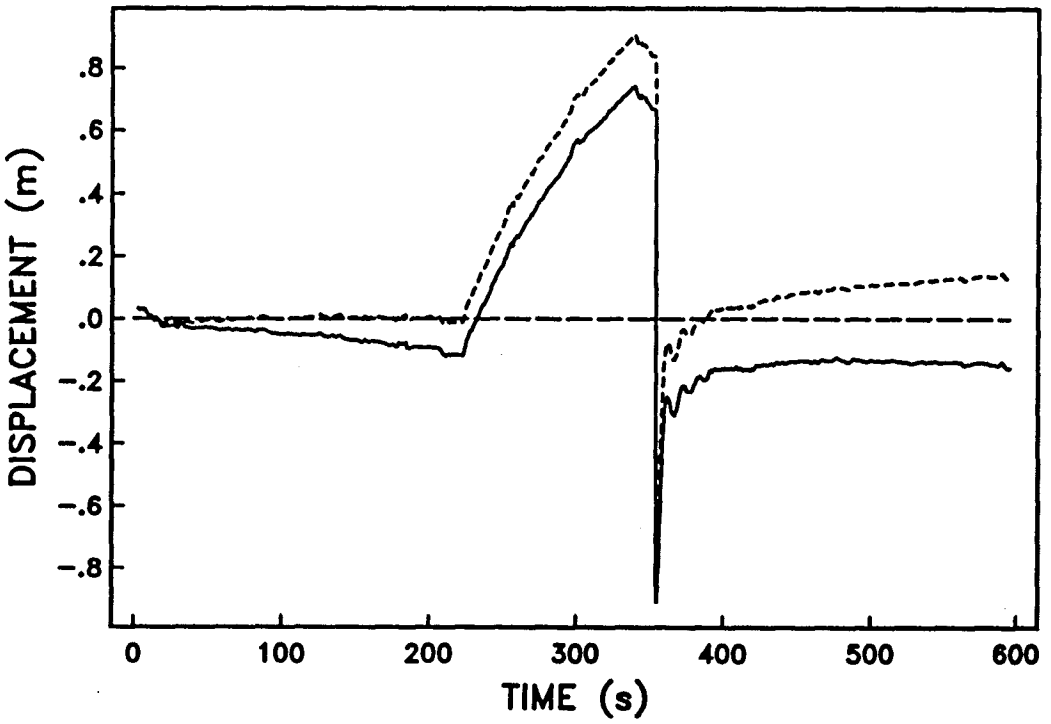

Fig. 4.8: Removal of background trend from packer test 90PT58B. The original data is shown by the solid curve and the short dashed curve is the standardized data that we inverted. The zero displacement reference—relative to the pre-disturbance equilibrium level with the background trend removed—is indicated by the long dashed line.

pressure was released, the displacement of the standardized data gradually became positive, and it continued to increase for the duration of the observation. In looking at the original data, a visual extrapolation of the linear trend prior to pressurization shows that the post-release response rises above the extrapolated equilibrium level, indicating that the positive displacement tendency exists before standardization. The post-release behavior is not, therefore, due to data processing effects.

The other possibility—that more water refills the borehole after the pressure is released than was initially displaced during pressurization—suggests a complex and, perhaps, hysteretic response to packer test disturbances. Because this behavior is

poorly-understood, and because the inversions were only marginally successful, we will not use these packer-test results to estimate subglacial hydraulic properties.

4.5.3 Subglacial hydraulic properties

Borehole response testing is a relatively simple way to assess the spatial and temporal variability of subglacial hydraulic properties. The data sets that we have inverted illustrate this point: the set of connection-drainage observations provides insight into spatial variability of the basal flow layer because the observations were made at different locations; the suite of slug tests can be used to characterize short-term temporal changes because all three tests were performed at a single location. Over the length and time scales that these response tests span, our inversion results show no clear evidence for spatial or short-term temporal variability (Table 4.4). We note that this (null) result does not imply that the subglacial drainage system was homogeneous throughout the 1990 field season, but only that the few tests that we have considered do not reveal any particular trend.

We can make further use of inversion results by returning to the definitions of the model parameters. For instance, using Equation (4.4), we can determine the borehole radius for a given value of ζ, since other quantities that appear in this equation are well-constrained:

$$r_w = \left[\frac{8\eta}{\rho_w \zeta}\left(\frac{h_0}{g}\right)^{1/2}\right]^{1/2}. \tag{4.10}$$

The borehole radius is not an especially interesting parameter, but its calculation does serve as a check on the plausibility of inversion results. Values of ζ are roughly 0.0023 to 0.01 (Table 4.4). When $h_0 = 50\,\mathrm{m}$, these values correspond to boreholes having radii in the range $0.06\,\mathrm{m} \leq r_w \leq 0.12\,\mathrm{m}$. (Values of the physical constants are listed in Table 3.1.) This range is reasonable for the boreholes that we have used.

More interesting hydraulic parameters can be revealed as follows: Dividing Equation (4.4) by (4.6) yields the transmissivity

$$T = \left(\frac{4\eta}{\rho_w}\right)\frac{\Upsilon}{\zeta}. \tag{4.11}$$

Dividing (4.5) by (4.6) and solving for the storativity gives

$$S = \frac{1}{2}\left(\frac{r_w}{r_f}\right)^2\frac{\Upsilon}{\chi}. \tag{4.12}$$

The hydraulic diffusivity—defined as $D \equiv T/S = K/S_s$ (de Marsily, 1986, p. 162)—can be obtained directly from Equation (4.5),

$$D = r_f^2\left(\frac{g}{h_0}\right)^{\frac{1}{2}}\chi. \tag{4.13}$$

We also know that storativity S and transmissivity T are defined as

$$S = \rho_w g b(\alpha + n\beta) \tag{4.14}$$

and

$$T = Kb \tag{4.15}$$

(Eqns. 3.21 and 3.22 respectively). Combining (4.12) and (4.14) yields the aquifer compressibility

$$\alpha = \left[\left(\frac{1}{2\rho_w g b}\right)\left(\frac{r_w}{r_f}\right)^2\frac{\Upsilon}{\chi}\right] - n\beta, \tag{4.16}$$

while (4.11) and (4.15) give the hydraulic conductivity

$$K = \left(\frac{4\eta}{\rho_w b}\right)\frac{\Upsilon}{\zeta}. \tag{4.17}$$

We note that when $\alpha \geq 10^{-8}\,\mathrm{Pa}^{-1}$ the second term on the right-hand-side of (4.16) is negligible, since $n\beta \approx 10^{-10}\,\mathrm{Pa}^{-1}$. Thus, for $\alpha \geq 10^{-8}\,\mathrm{Pa}^{-1}$, Equation (4.16) provides a reasonable estimate of α, even if the porosity n is not accurately known.

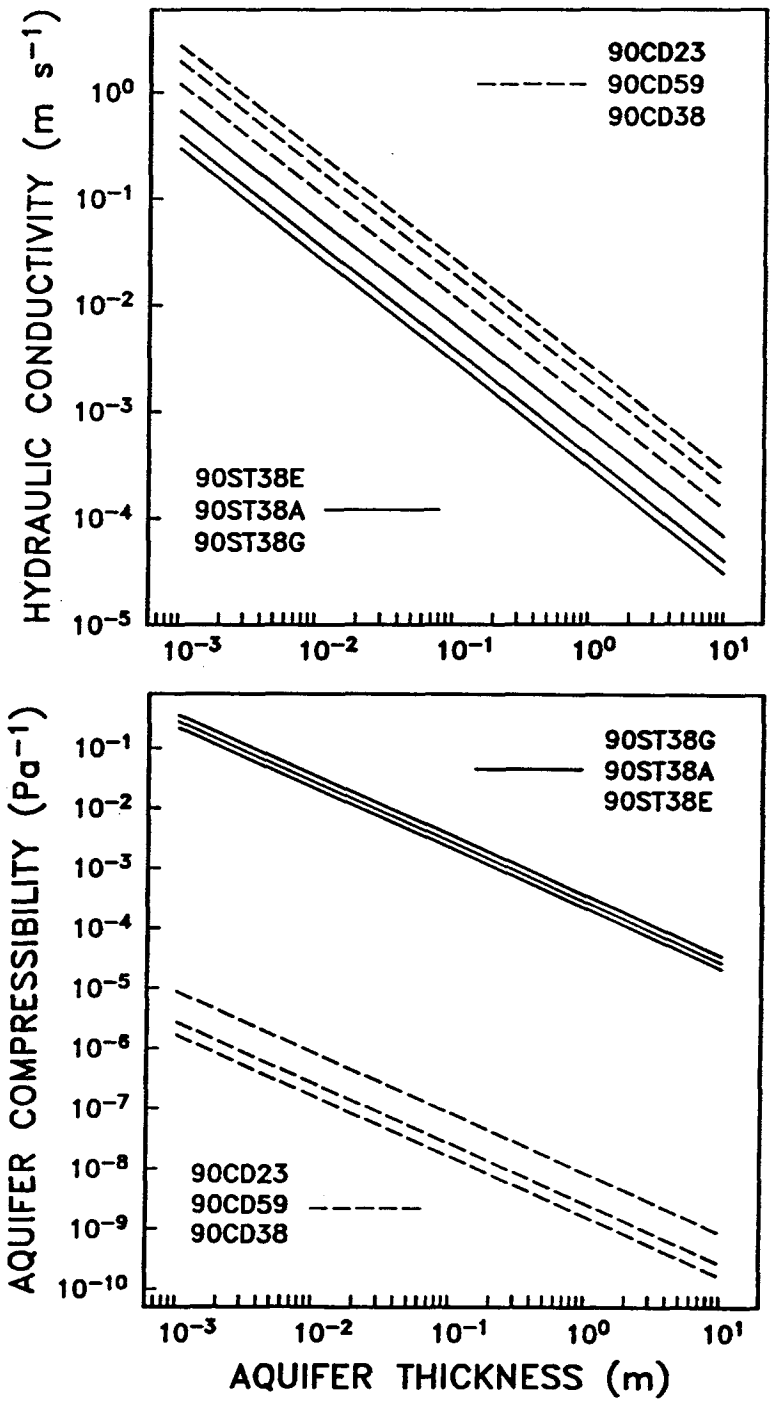

Fig. 4.9: Estimated ranges of hydraulic conductivity and aquifer compressibility as a function of flow layer thickness.

We have used inversion results and Equations (4.16) and (4.17) to estimate values of α and K for various aquifer thicknesses (Fig. 4.9). Hydraulic conductivity estimates that are based on drainage observations are only slightly higher than those estimated from slug tests. For a 0.01 m thick flow layer, estimated conductivities are in the range 0.02–0.2 $\mathrm{m\,s^{-1}}$; this range, which encompasses both types of tests, is consistent with the conductivities expected of an unconsolidated deposit of coarse sand or fine gravel (Freeze and Cherry, 1979, p. 29).

In contrast to hydraulic conductivity, estimates of aquifer compressibility are much lower (five orders of magnitude) for connection-drainage observations than they are for slug tests. Based on connection-drainage estimates, a 0.01 m thick flow layer has a compressibility of roughly 10^{-6}–$10^{-7}\,\mathrm{Pa^{-1}}$, while for slug tests a layer of the same thickness has an estimated compressibility of about $2\text{–}5\times10^{-2}\,\mathrm{Pa^{-1}}$. Some clays and sands have compressibilities in the range that we have estimated from connection-drainage observations (Freeze and Cherry, 1979, p. 55). Compressibility estimates from slug tests are much higher than those expected of geologic materials under most conditions. Papadopulos and others (1973) have stated that, for low transmissivity formations, the water level recovery following a slug test is insensitive, even to order of magnitude changes in the storage coefficient (and, hence, to changes in aquifer compressibility). The degree to which this insensitivity affects more highly transmissive systems—such as the subglacial one that we are considering—is uncertain.

Harvey (1992) has demonstrated that, on average, specific storage is overestimated by slug tests. Our large compressibility estimates might, at least in part, be an artifact of such overestimation. However, aquifer compressibility is not necessarily a physical constant; as noted in Appendix A, it may vary with the initial state of stress. Thus, it is reasonable to speculate that the compressibility of the flow layer changes in response to the sudden input of water that accompanies a connection. During a connection, water that drains out of the borehole either flows away from the borehole, or is stored

in the subglacial sediments, or possibly both. If some of the water is retained in the flow layer then the specific storage $S_s = S/b$ is increased, and hence, by (4.14), so is α. This picture is consistent with our findings that α is larger when estimated from slug tests than it is when estimated from drainage observations, since slug tests necessarily follow connections. Thus, variable compressibility must also be considered.

Changes in aquifer compressibility are largely due to the rearrangement of sediments, a dynamic process that is enhanced in an unstable environment. A layer of saturated sediment in direct contact with overlying glacier ice exemplifies geologic material in a potentially unstable setting. The setting is potentially unstable for two reasons: (1) basal shear stress is not static—it changes when ice fractures, as ice moves over obstacles at the bed, and in response to changes in ice thickness—and (2) rapid input of water to the bed, perhaps resulting from an intense rainstorm or the sudden draining of a water-filled crevasse, can causes localized reductions in shear strength as the surface area of contacts between grains is reduced. Either situation—increased basal shear stress or reduced shear strength—can lead to the rearrangement of a subglacial sediment layer.

These considerations—variable compressibility and a potentially unstable flow layer—suggest that borehole connections might significantly alter basal hydraulic conditions. In light of this, it is interesting to note that hydraulic conductivity estimates are similar for the two types of tests; it is conceivable that the near-borehole conductivity could increase as fine sediments are flushed away during a connection, but this does not seem to be the case. If the conductivity changes in response to a connection then it must do so almost instantly. Of greater interest, because of its implications for glacier surging, is the suggestion that subglacial conditions are conducive to basal water storage.

4.5.4 Differences between drainage observations and slug tests

Connection-drainage observations and slug tests give significantly different inversion results. This is most clearly indicated in the case of Borehole 38, where both types of tests were performed. Differences in results from the two types of tests are not due to spatial heterogeneity or poorly performed tests, as evidenced by the consistency of final parameter values for a particular type of test. One possible explanation for these differences has already been discussed. If subglacial conditions are appreciably altered by borehole connections then the two types of tests sample different kinds of systems. There is another reason why we might expect the tests to give different results; connection-drainage observations and slug tests differ fundamentally in the hydraulic properties to which they are sensitive and in the surrounding aquifer volumes that they sample. In particular, turbulent flow in the basal layer is a crucial aspect in rapid borehole drainages, but has very little impact on slug tests. As discussed in Chapter 3, the critical Reynolds number, which is embedded in ξ, specifies the transition between turbulent and laminar flow regimes. Thus, the Ergun parameter characterizes the importance of turbulent transport in subglacial water flow; very small values of ξ correspond to a laminar flow regime, whereas large values of ξ indicate that the dominant flow regime is turbulent. For plausible porosities and grain sizes, values of ξ greater than $\sim 10^2$ correspond to turbulent flow, given the conductivities that we have estimated. In a slug test the head gradient disturbance, which drives flow, is small and contrasts strongly with the large disturbance caused by a connection. Hence, we expect that values of ξ will be smaller for slug tests than for drainage observations. We also expect that ξ will be a relatively unimportant parameter in the case of slug tests, since small gradient disturbances will not produce turbulent flow. Our results are consistent with these expectations: (1) Inversions of connection-drainage data give much higher estimates of ξ than those obtained from slug tests; (2) Inversions of slug test data show

no variation in the final values of ξ, indicating that slug tests are insensitive to the hydraulic properties embedded in the Ergun parameter.

4.6 Summary and concluding remarks

In this chapter we have further developed borehole response testing as a tool for assessing subglacial hydraulic properties. The inversion methodology that we have described contributes significantly to the effectiveness of this tool; inversions have resulted in better fits to the observed data than we were able to achieve by forward modeling alone. Thus, we have shown that inversion should be an integral part of the overall procedure.

By attempting to invert data from different kinds of response tests, we have discovered the importance of removing background trends from the data. We have also been confronted with the possibility that our model does not fully describe packer tests, although this matter is still undecided. In any case, we have found that the additional complexity of packer tests makes them less useful than either drainage observations or slug tests. Comparisons of inversion results from connection-drainage observations and slug tests have revealed fundamental, as well as possibly consequential, differences between the two types of tests. At the same time, inversions of drainage and slug test data have been extremely successful, and we infer from this that the model comes close to accurately characterizing the basal hydraulic system.

Inversions of response test data from Trapridge Glacier have provided estimates of model parameters that characterize hydraulic properties of the basal region in which the tests were performed. Based on these estimates, and the inferred accuracy of the model, we draw the following conclusions about the subglacial hydraulic system: (1) In response to sudden pressure disturbances, water flow at the glacier sole is concentrated in a hydraulically confined sediment layer (or at least it can be effectively characterized by such a representation); (2) The transmissivity of the flow layer is approximately 3–$30\times10^{-4}\,\mathrm{m^2\,s^{-1}}$; (3) The flow layer must be fairly thin ($\leq 0.1\,\mathrm{m}$), since the hot-water

drill does not penetrate deeply into subglacial sediments. In this case, transmissivity estimates suggest that the flow layer is comprised of coarse sand or fine gravel; (4) Flow layer compressibility estimates are variable and are largest when estimated from slug test data. The large values of compressibility estimated from slug tests are probably, in part, artifacts of the tests themselves. However, given that slug tests were performed shortly after connections, it is also possible that the flow layer retains significant amounts of water in a transient state following drilling disturbances.

In this and the previous chapter we have investigated the estimation of subglacial hydraulic properties by borehole response testing. Engelhardt (1978) used similar procedures to estimate the hydraulic characteristics of interconnecting subglacial passageways on Blue Glacier, Washington. He obtained estimates of the lengths and radii of circular conduits connecting boreholes to main subglacial channels. In a different approach, Engelhardt and others (1990b) have used laboratory measurements to determine the hydraulic conductivity of sediment collected from beneath Ice Stream B in West Antarctica. Our estimates of the hydraulic conductivity and compressibility of the porous medium beneath Trapridge Glacier are the first *in situ* determinations of these subglacial hydraulic properties.

Perhaps the most revealing aspect of the response tests that we have performed on Trapridge Glacier is the clear indication that a highly transmissive flow system exists at the glacier bed. In subsequent chapters we consider a second approach to characterizing the basal hydraulic system of Trapridge Glacier; namely, direct measurement of the properties of subglacial water. We shall see that both approaches lead to a consistent overall view of subglacial drainage.

Chapter 5

PROPERTIES OF SUBGLACIAL WATER: OBSERVATIONS

The best approach to studying subglacial drainage is to monitor water flow *in situ*, rather than inferring basal conditions exclusively from proglacial observations. We have measured basal water pressure, turbidity, and electrical conductivity directly at the bed of Trapridge Glacier for three full years. Measurements of these properties provide direct indications of basal hydraulic conditions, water movement, and subglacial provenance. In this chapter we show a portion of the data that we have collected and we discuss the main features of our observations. An interpretation of these data—leading to a qualitative characterization of the basal drainage system—is reserved for the following chapter.

5.1 Communication with the subglacial hydraulic system

Our data were collected using the sensors and installation procedures described in Chapter 2. To reach the glacier bed and install the sensors, we drilled boreholes through the ice—a process that involves melting a nearly vertical column of ice through the glacier using a continuous flow of hot water. The simple act of drilling by this method provides information about the subglacial hydraulic system. When we are drilling through the glacier, hot water is being pumped down the borehole and ice is continuously being melted. When there is no outlet for this water, except at the surface, the borehole remains full. When the drill reaches the bed, there are two possible outcomes: (1) the borehole can remain full of water, or (2) water can drain from the borehole and be dispersed beneath the glacier. In the first case we refer to the borehole as being "unconnected", since water does not leave the borehole and

appears to remain hydraulically isolated from other waters at the bed. In the second case we refer to the borehole as being "connected", since hydraulic communication with the subglacial drainage system has clearly been established. Hydraulically active and inactive regions of the bed are, therefore, immediately revealed by hot-water drilling. Our success in achieving connected boreholes during the 1989–92 drilling seasons varied—both spatially and temporally—within a given season, and from year to year. In some cases, a region having connected boreholes one year yielded only unconnected boreholes the following year. Also, boreholes that were initially connected sometimes became unconnected after a period of time, and vice-versa.

In the absence of flow, water levels in connected boreholes reflect the hydrostatic fluid pressure at the base of the borehole. Trapridge Glacier presently has an ice thickness of about 75 m in the central region where our measurements were made. Thus, a water column height of 67.5 m is roughly equivalent to the hydrostatic ice-overburden pressure. "Super-flotation" pressures refer to water levels in excess of the ice-overburden pressure. On rare occasions, we have observed water flow out of connected boreholes, indicating that basal water greatly exceeded the ice-flotation pressure in that vicinity. The subglacial origin of water flowing out of these boreholes was confirmed by its muddy appearance.

Connected boreholes act as piezometers; the hydraulic head at a point immediately beneath the borehole is approximated by the height of the water column plus an arbitrary elevation-offset term. In principle, therefore, it should be possible to calculate hydraulic head gradients from water level measurements in different boreholes having known sensor positions. In practice, such efforts are frustrated by the general lack of hydraulic communication between subglacial sensors. This issue is taken up later in the chapter.

5.2 Presentation of data

The data shown below are representative of the subglacial water pressure, turbidity, and electrical conductivity signals that we have recorded during a three-year period when the glacier was not surging. They encompass a broad range of responses and illustrate commonly-occurring patterns and trends. The data can be naturally divided into two categories: (1) summer and (2) year-round observations. Our presentation is structured around this division.

Our naming convention for sensors is similar to that used to identify borehole response tests; individual sensors are identified by a two digit code, followed by a one- or two-character string, and ending with an additional two digits. The meaning of each field is illustrated in the following example: 89P02 refers to a pressure sensor that was prepared for subglacial usage in 1989 and was the second in a series of similar sensors for that year. For turbidity and conductivity sensors, the "P" is replaced by "TB" and "C" respectively. (Note that this convention does not imply that a particular sensor was installed in the specified year; although this is usually the case, an "89" sensor could have been installed in 1990 or 1991.) In an analogous fashion, individual boreholes are identified, for example, as 90H05, which represents the fifth borehole drilled during the 1990 field season.

For reference, we have plotted the map positions of sensors at the bed during the month of July in 1989, 1990, and 1991 (Figs. 5.1–5.3). Subglacial sensor positions have been determined from surveys and borehole inclinometry. For sensors that overwintered, we have estimated subglacial positions for the following summer by projecting them downglacier, in accordance with the annual surface displacement vector—determined from survey measurements of stakes in the vicinity of the sensors—and taking into account the small contribution due to internal deformation of ice (estimated to be $\sim 0.24\,\mathrm{m\,yr^{-1}}$). Thus, for example, the estimated displacement of sensor 89P07 was $+31.710\,\mathrm{m}$ East and $+5.645\,\mathrm{m}$ North between July 1989 and July 1990.

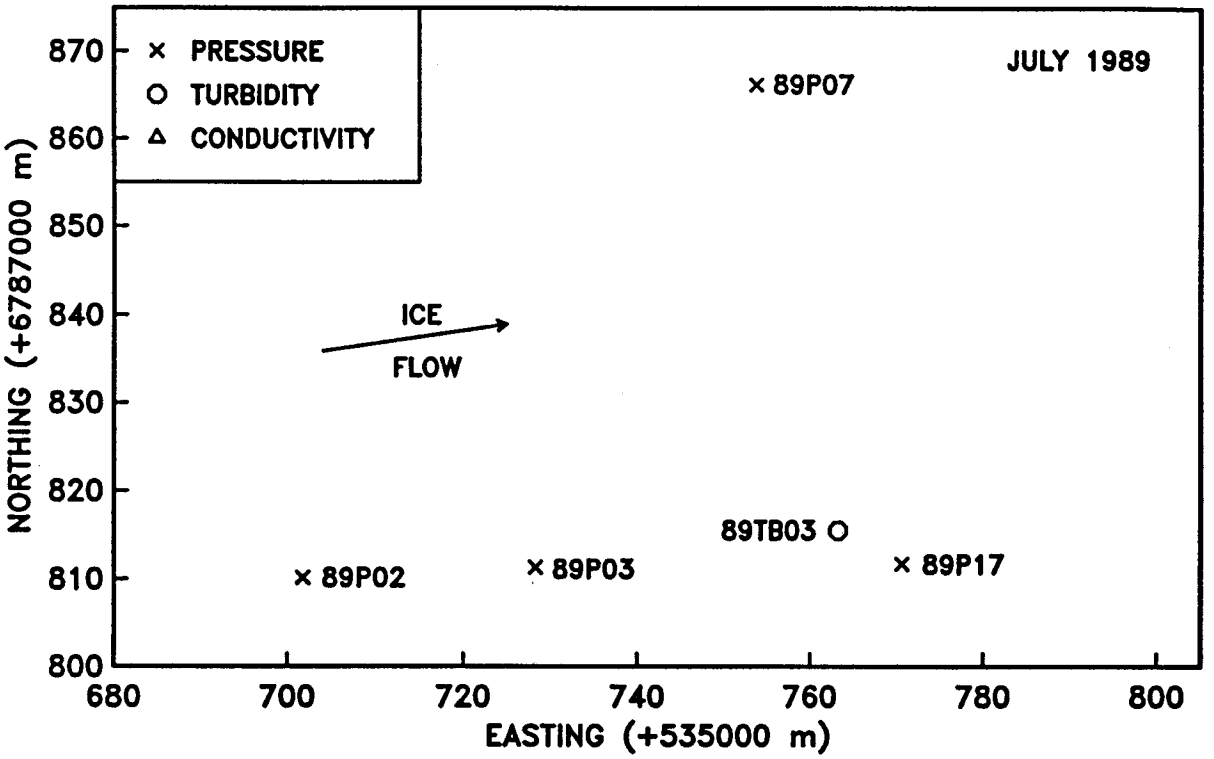

Fig. 5.1: Positions of sensors in July 1989.

During the summer field seasons we collected data at two minute intervals. Summer data have been plotted at this resolution. For the rest of the year the interval between measurements was increased to 20 minutes, due to datalogger memory constraints. In presenting year-round observations we have selected every tenth sample from the summer data series. Hence, year-round data are presented at a constant sampling interval of 20 minutes, eliminating a possible bias towards the higher frequency variations in summer. The data have been only minimally processed: with the exception of turbidity, the records have not been processed beyond applying calibration information; turbidity records have also been slightly smoothed using an 11-point Gaussian filter. We have used linear interpolation between data points for both summer and year-round observations. With only one exception (the 1989 pressure records in Fig. 5.4), there are no gaps in the data presented below.

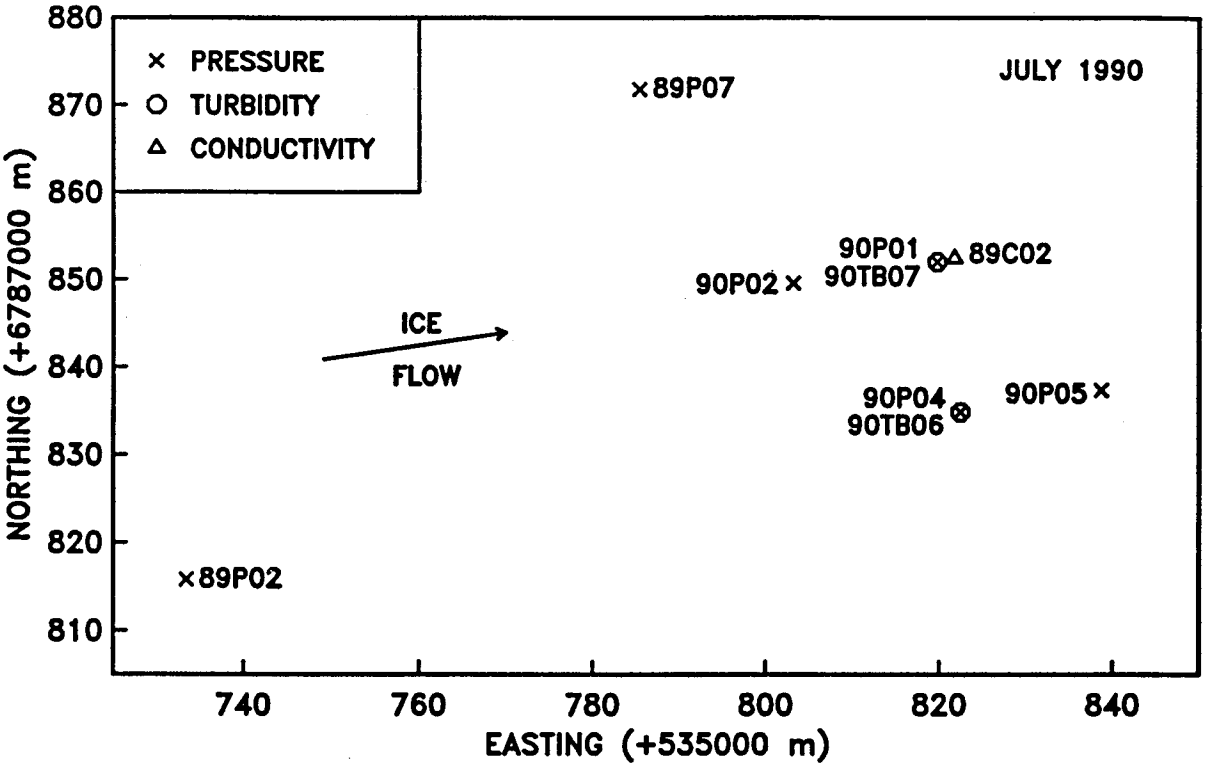

Fig. 5.2: Positions of sensors in July 1990.

Water-pressure signals contain a rich store of information, providing insights into the physical environment as well as the mechanical and hydrological forcings and responses. Their nature is also highly variable, unlike the typical behavior of turbidity and electrical conductivity signals. Furthermore, water-pressure records are abundant relative to either turbidity or electrical conductivity, due to the on-going development of turbidity and conductivity sensors during the course of our field work. (In 1989, for instance, only two of the three prototype turbidity sensors were functional, and in 1990, conductivity sensors were not ready for installation until near the end of the field season.) For these reasons, water-pressure measurements are emphasized in the following sections.

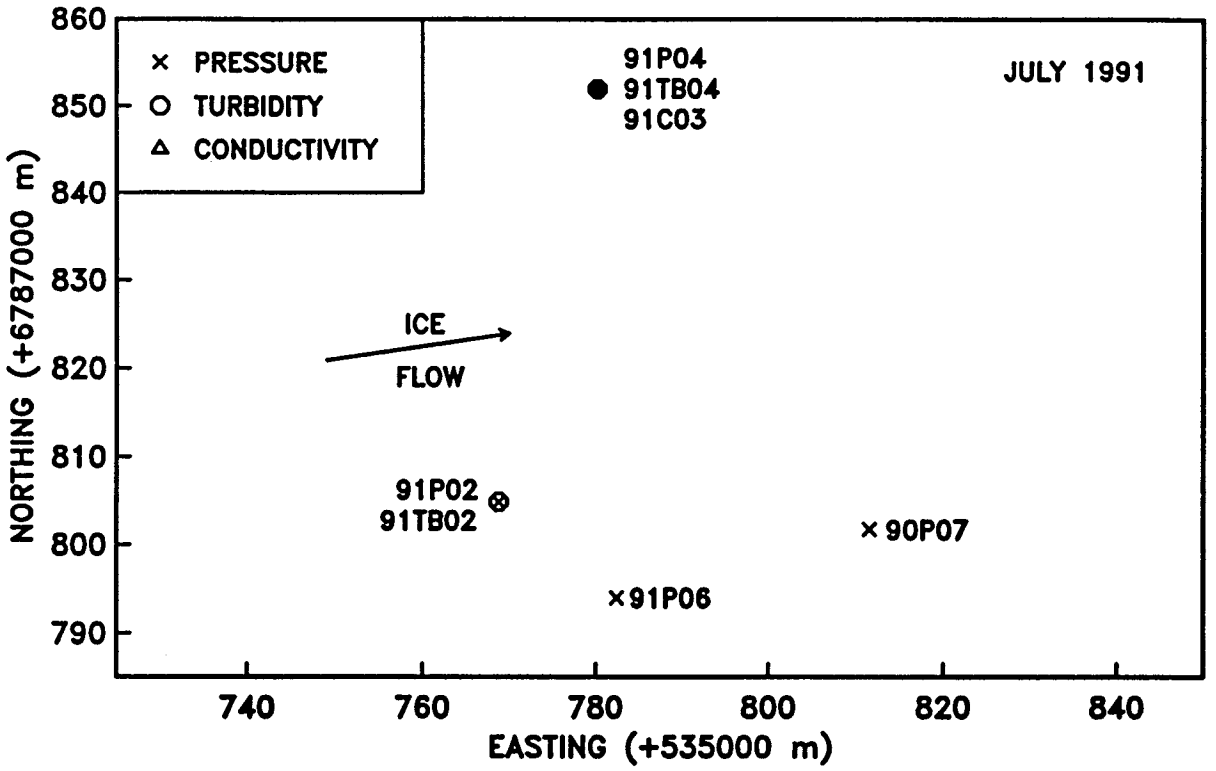

Fig. 5.3: Positions of sensors in July 1991. The solid symbol at the top of the map indicates that a sensor of each type was at this location.

5.3 Summer observations

5.3.1 Water pressure

Summer measurements of subglacial water pressure are shown in Figures 5.4 and 5.5. Between the two figures, a total of 12 summer pressure records are presented. Each record is labeled by a lower-case letter that identifies the particular sensor with which the measurements were made: (a) 89P02; (b) 89P03; (c) 90P01; (d) 90P02; (e) 91P02; (f) 91P04; (g) 89P07; (h) 89P17; (i) 90P04; (j) 90P07; (k) 91P06. Except for 89P03, all sensors were installed in boreholes that were initially connected to the basal drainage system.

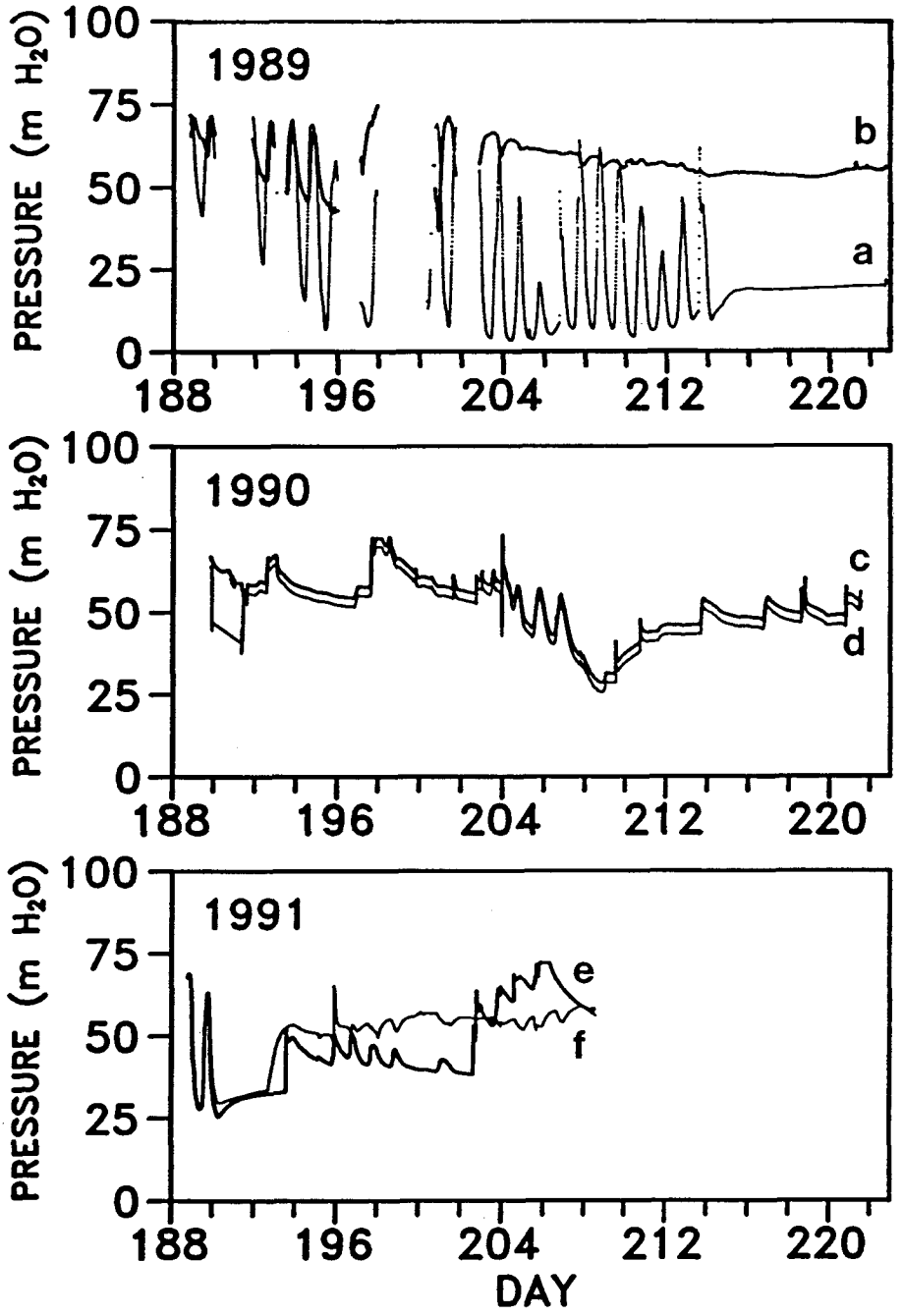

Fig. 5.4: Measurements of subglacial water pressure during three consecutive field seasons. Records are labeled by lower-case letters, each of which identifies a particular sensor: (a) 89P02; (b) 89P03; (c) 90P01; (d) 90P02; (e) 91P02; (f) 91P04. Day 188 corresponds to 7 July.

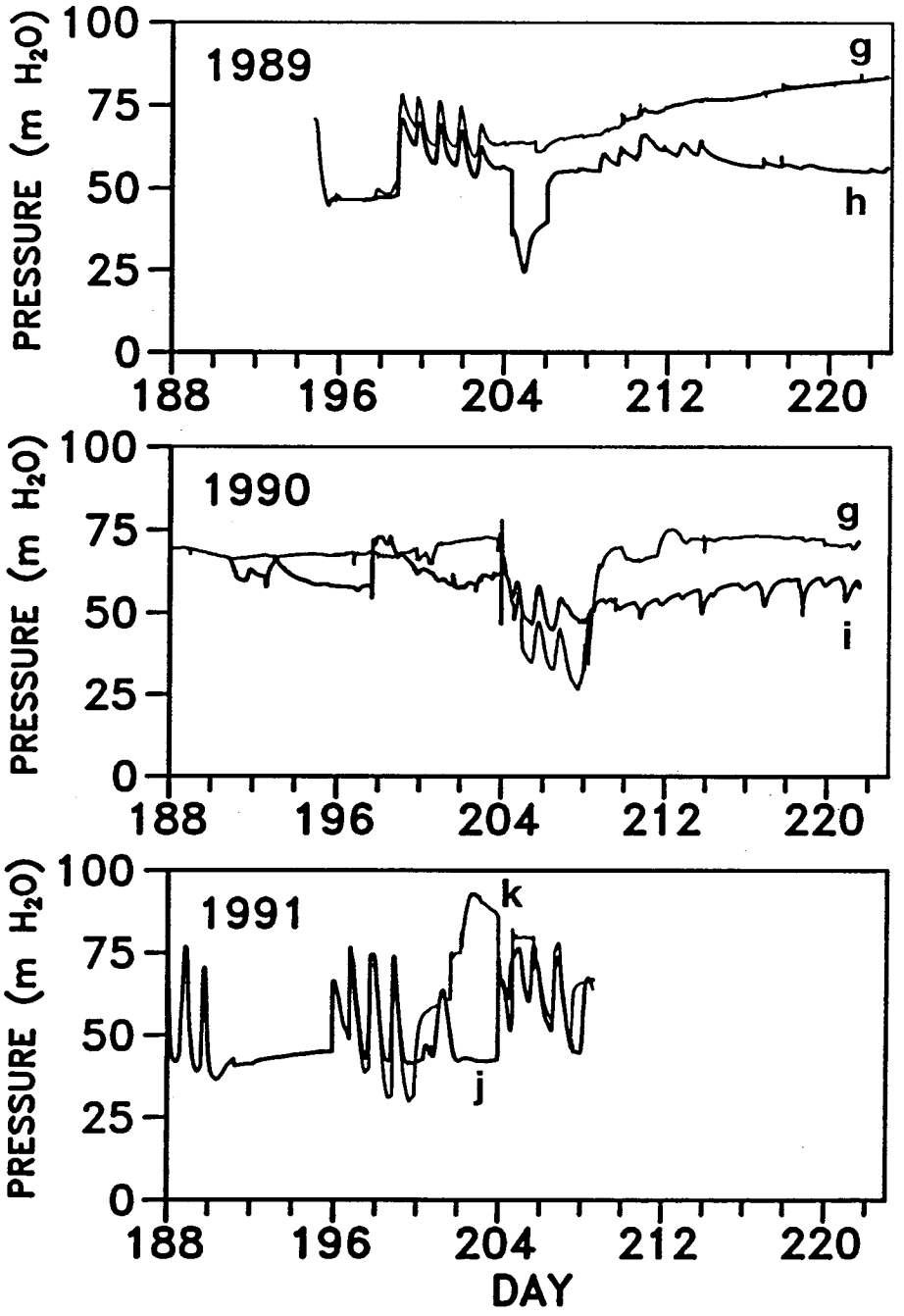

Fig. 5.5: Measurements of subglacial water pressure during three consecutive field seasons. Records are labeled by lower-case letters, each of which identifies a particular sensor: (g) 89P07; (h) 89P17; (i) 90P04; (j) 90P07; (k) 91P06. Day 188 corresponds to 7 July.

Referring to Figures 5.1–5.3, it can be seen that the pressure sensors were all located in a relatively small area (roughly 150 m × 75 m) of the glacier bed. Despite their close proximity, pressure signals from different sensors do not show consistently similar behaviors. (Records (c) and (d) in Figure 5.4 are notable exceptions.) We can list the main features of the pressure records shown in Figures 5.4 and 5.5 as follows:

(1) At any given time, basal water pressure is not uniform over the glacier bed.

(2) Diurnal water pressure fluctuations have been recorded every summer, but there are also periods during each summer when they have been absent.

(3) Diurnal fluctuations appear in two distinct forms, either as quasi-sinusoidal oscillations or as rapid daily increases followed by quasi-exponential decays. Transitional forms between these two signal types can also be discerned.

(4) There may be more than one distinct interval of diurnal pressure oscillations in a summer season.

(5) Diurnal fluctuations have lasted for intervals ranging from approximately three days to more than three weeks.

(6) Diurnal oscillations at a particular location sometimes cease, even though they continue to be recorded by other sensors in the vicinity.

(7) Diurnal pressure excursions can be large, sometimes varying by as much as ~ 65 m water equivalent; daily maxima often—though not always—exceed the hydrostatic ice-overburden pressure.

(8) Pressure fluctuations recorded simultaneously by two or more sensors sometimes show inverse relationships with each other; while one sensor shows a rapid rise followed by a slow decay, the other shows a rapid drop followed a slow rise.

These observations indicate that basal hydraulic conditions are highly variable during the summer, giving rise to a diverse assortment of pressure signals within a small region. In subsequent discussion, we will suggest that the complex, non-uniform behavior

of summer pressure signals is due to a combination of factors: local differences in forcings, unstable drainage structures, heterogeneities in subglacial sediment layers, and mechanical interactions with the overlying ice.

5.3.2 Turbidity

Figure 5.6 shows summer observations of subglacial turbidity. The measurements presented in this figure were obtained from three different sensors: 89TB03 (1989); 90TB06 (1990); 91TB02 (1991). Note the different vertical scales. These records illustrate the different types of turbidity signals that we have observed during summer field seasons—from small amplitude diurnal fluctuations, to large amplitude events.

The small amplitude diurnal fluctuations shown in the 1989 graph of Figure 5.6 are likely associated with diurnal variations in basal water flow. The association is difficult to establish, however, without direct indications of flow variations. (This issue merits special attention and will be examined more closely in a separate section.) The general rising trend apparent in the turbidity signal is due to chemical interaction of the 1989 casting resin with basal water—confirmed by removal and post-mortem examination of another 1989 sensor. This deficiency was corrected in subsequent years.

In the 1990 graph of Figure 5.6, a large amplitude turbidity event is illustrated. Prior to this event, there were no indications of subglacial water flow; evidence from this, and other sensors, suggests that basal water was ponded over a portion of the glacier bed. The rapid rise in turbidity coincided with large changes in basal water pressure and electrical conductivity, as observed by many sensors in different locations. The overall event is described in detail below.

A large turbidity rise, followed by a period of small amplitude diurnal oscillations, is evident in the 1991 graph of Figure 5.6. In this case, a change in subglacial flow conditions—less abrupt and longer lasting than that shown in the 1990 graph—is indicated. Signals of this type might arise if water flow passageways developed in the

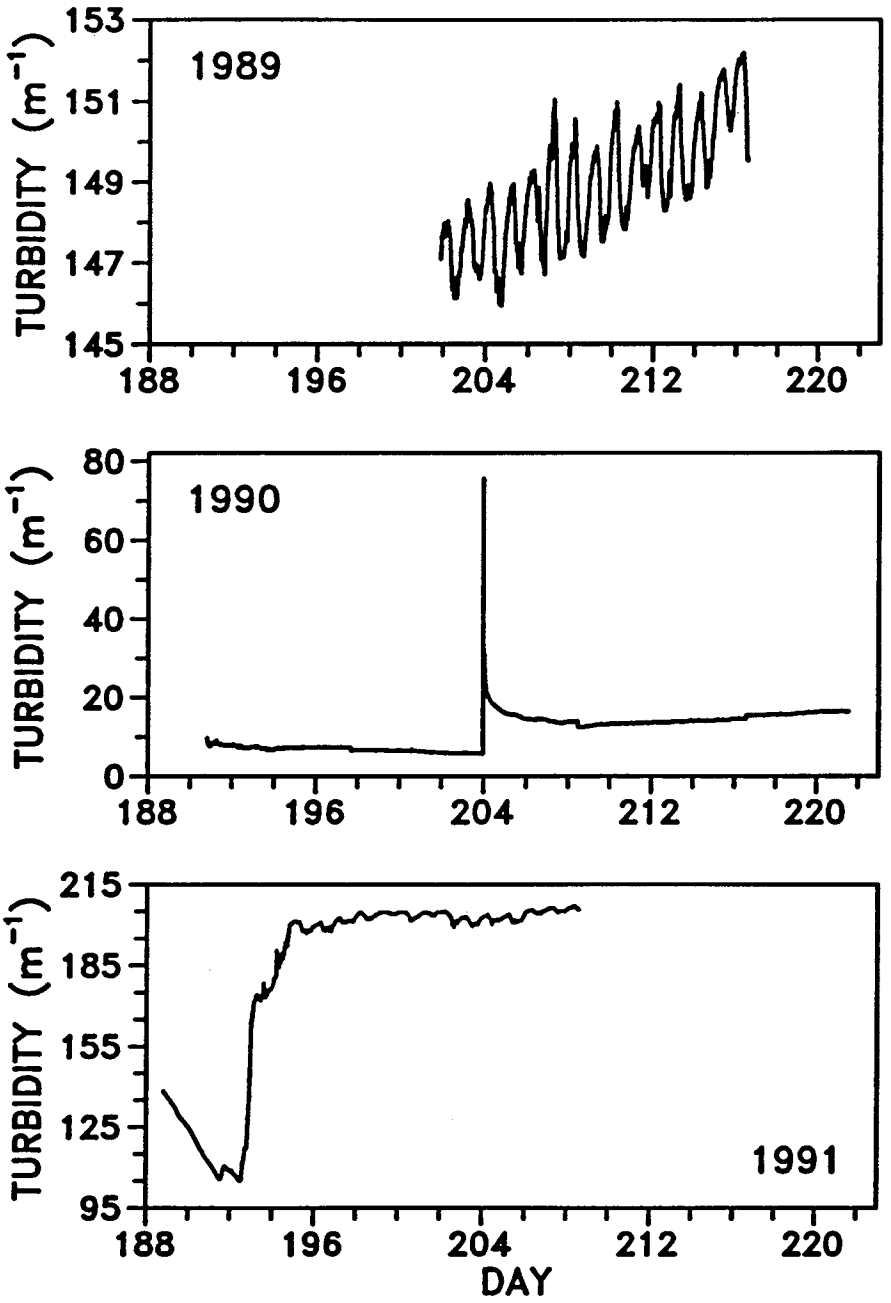

Fig. 5.6: Subglacial turbidity measured with different sensors in 1989 (89TB03), 1990 (90TB06), and 1991 (91TB02). These data illustrate the wide range of turbidity signals that we have recorded during summer field seasons—from small amplitude diurnal fluctuations, to large amplitude events. Day 188 corresponds to 7 July.

vicinity of the sensor, or if the sensor was carried by glacier motion over an area in which drainage was already established.

5.3.3 Electrical conductivity

Summer observations of electrical conductivity are shown in Figure 5.7. The measurements were made with different sensors in 1990 (89C02) and 1991 (91C03). The S.I. unit for electrical conductivity is siemens per meter ($S\,m^{-1}$); we have expressed our results as microsiemens per centimeter ($\mu S\,cm^{-1}$) because this is the more commonly used unit. Note the different vertical scales.

The data shown in the 1990 graph of Figure 5.7 were obtained from a sensor that had been in place at the glacier bed for a full year; this sensor was originally installed and used in 1989. At the beginning of the 1990 field season, the lead wires to this sensor were uncovered at the glacier surface and the sensor was reattached to a datalogger. The large drop in conductivity on Day 204 coincides with the previously discussed turbidity event. Reduction in electrical conductivity suggests that an infusion of fresh surface water—thereby diluting mineralized basal water—accompanied this event.

The 1991 graph of Figure 5.7 shows a long period of gradually increasing conductivity. Similar trends, on various time scales, are also evident in the 1990 graph. Such behavior may indicate increasing ion concentration with increasing contact time between water and basal sediments; in hydrology, it is well known that the conductivity of storm runoff or groundwater depends on the amount of time spent in contact with sediments (e.g., Pilgrim and others, 1979). Note that the increase in conductivity, commencing on Day 192, coincides with rising turbidity, as shown in the 1991 graph of Figure 5.6. Unlike the 1990 "event", in which there was an inverse relation between turbidity and conductivity, the data in 1991 show a direct correspondence. In contrast to the 1990 example, the direct relationship suggests that the two 1991 sensors were

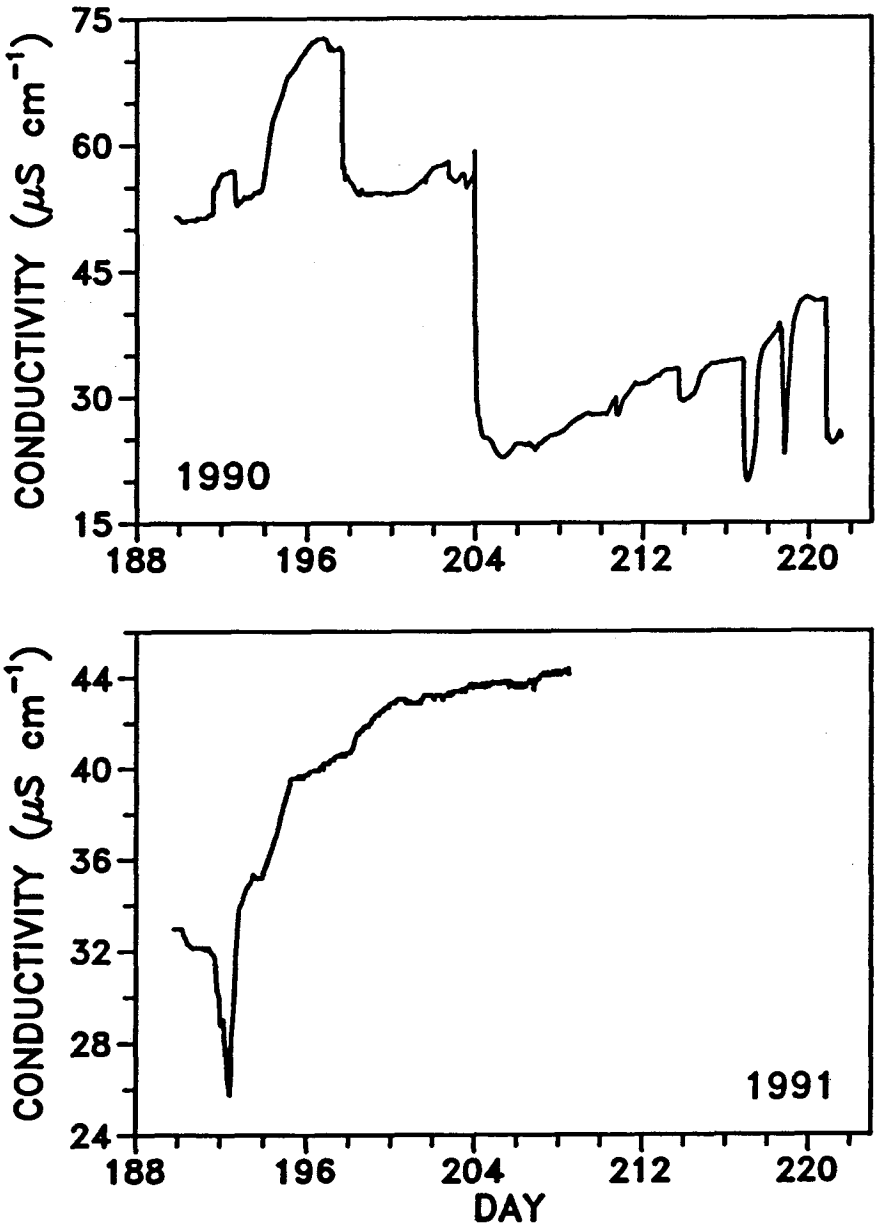

Fig. 5.7: Electrical conductivity of subglacial water measured with different sensors in 1990 (89C02) and 1991 (91C03). Day 188 corresponds to 7 July. The data shown in the upper graph were obtained from a sensor that was installed during the 1989 field season and had overwintered.

hydraulically isolated from each other, but were still subjected to the same glacier forcings.

5.3.4 Special events in the drainage system

In this section we expand our view to include proglacial observations related to the forefield stream. As mentioned in Chapter 1, the forefield stream is thought to be fed principally by surface meltwater pouring off the terminus. Most of the time there are no clear indications that the stream carries basal water. However, infrequent "release events" involving forefield stream transport of previously stored basal water have been recorded. The subglacial origin of the transported water in these events is confirmed by the presence of Rhodamine dye, which had been previously added to the basal drainage system.

Rhodamine dye was released into boreholes connected to the subglacial drainage system in 1983 and in 1985. Each injection involved a substantial quantity (tens of liters) of dye. Following the injections, outlet streams were carefully sampled for many days, but dye was not detected in any of the samples—either the dye had exited the glacier via some route that bypassed the stream sampling sites, or it had been stored beneath the glacier. Evidence gathered since 1985 suggests that both eventualities took place. Analyses of subglacial water samples, obtained from the bottoms of boreholes, confirm that some of the dye from the 1983 and 1985 injections was still present at the glacier bed as late as 1992. It is this dye that labels basal water and clearly indicates a release event.

Episodic release of dyed basal water was first noted in 1986 by Christopher Smart (Smart and Clarke, submitted). Around midnight on 21 July 1986, a debris flow buried the forefield stream site installation. Shortly thereafter, water samples collected at a downstream location contained detectable amounts of Rhodamine dye. The dye continued to be present in the stream for several days following the event. In 1987,

the forefield stream was again monitored by Christopher Smart. Only trace quantities of the dye were found in the stream samples that summer, and there were no further indications of a subglacial release event.

The work reported in the thesis began in 1988 and included a continuation of the forefield stream monitoring program. We collected stream samples at four-hour intervals using an automatic water sampler and, while in the field, we analyzed them for the presence of Rhodamine dye. Appreciable quantities of dye were not detected in any of the 1988 water samples. Near the end of the 1988 season, we released a small quantity (two liters) of Rhodamine dye into a borehole near the glacier terminus. Despite intensive sampling for the following several days, the dye from this injection was also undetected in 1988. Although the borehole appeared to be connected, we now suspect that this dye was inadvertently released in a cold-based region where it became frozen to the bed.

We have continued to monitor the forefield stream in the years subsequent to 1988. Figure 5.8 summarizes our findings of Rhodamine dye in water samples collected during the summers of 1989, 1990, and 1991. In this figure, individual measurements are represented by vertical lines which we have extended to negative values of concentration. The negative segments of these lines have been added only to facilitate the representation of near-zero values; they do not correspond to measured values. Note the different vertical scales in Figure 5.8.

The first water samples that we collected in 1989 contained significant concentrations of Rhodamine dye. The dye continued to be present, in diminishing concentrations, in samples collected over the following week and was only found in trace amounts thereafter. We infer from this that another release event occurred in early July 1989. Dye was also detected in 1990, though in lesser concentrations than the previous year, again indicating a release of stored basal water. Appreciable quantities of dye were not detected during the 1991 field season. (Subsequent to the work reported in this thesis,

Tavi Murray has collected and analyzed water samples from the forefield stream; she found only trace amounts of dye during the 1992 field season.)

5.3.4.1 The 1990 release event

The 1990 release event took place at an advantageous time—we had numerous sensors in operation beneath the glacier throughout the event. The data obtained by these sensors provide a unique opportunity to examine in detail a naturally occurring transition that profoundly altered the basal drainage system. Our observations of this event are summarized in the following paragraphs.

Figure 5.9 shows that subglacial sensors recorded a dramatic and sudden rearrangement of the basal drainage system on Day 203 (22 July) 1990. The event spontaneously occurred just before midnight, causing large disturbances over an area of the bed extending at least 100 m in the direction of ice flow and 50 m in a direction perpendicular to ice flow. The event coincided with a dramatic change in the nature of water pressure signals; diurnal fluctuations were weak or absent prior to the event, but are clearly present in the post-event period. Sudden increases in turbidity, presumably associated with water flow, accompanied the onset of the event. A gradual clarification of subglacial water took place over the following few days. The event also coincided with a substantial decrease in the electrical conductivity of basal water. As previously mentioned in connection with Figure 5.7, the reduction in conductivity is thought to be the result of an infusion of fresh surface water.

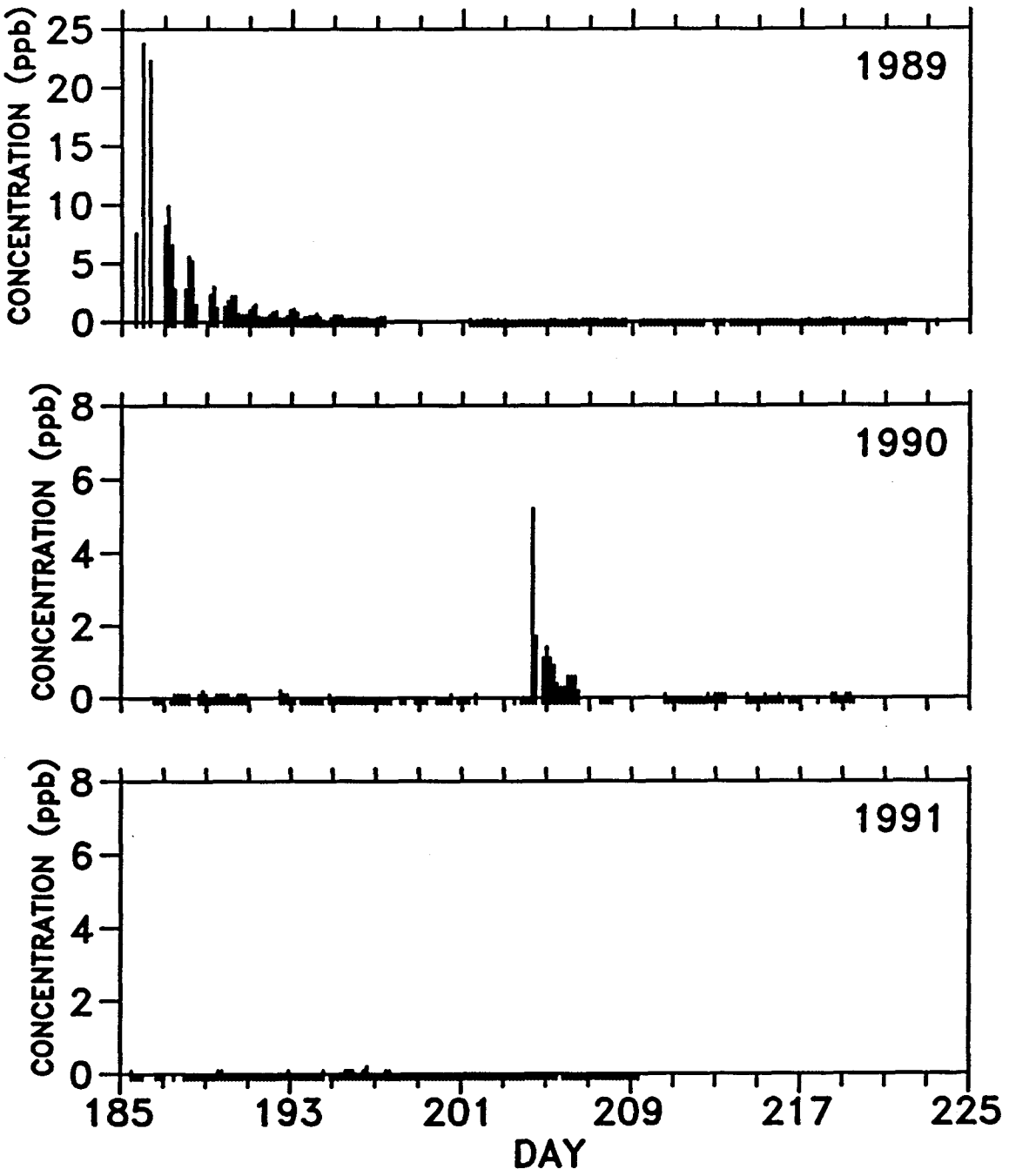

Fig. 5.8: Concentration of Rhodamine dye in water samples collected from the forefield stream during the summers of 1989, 1990, and 1991. Day 185 corresponds to 4 July. The dye was originally released into boreholes connected to the subglacial drainage system in 1983 and 1985; some of the dye has been stored beneath the glacier since then. The presence of dye in the forefield stream clearly identifies periods when basal water is released from the central glacier bed. Significant concentrations of dye were not detected in the summers of 1988 and 1992 (not shown).

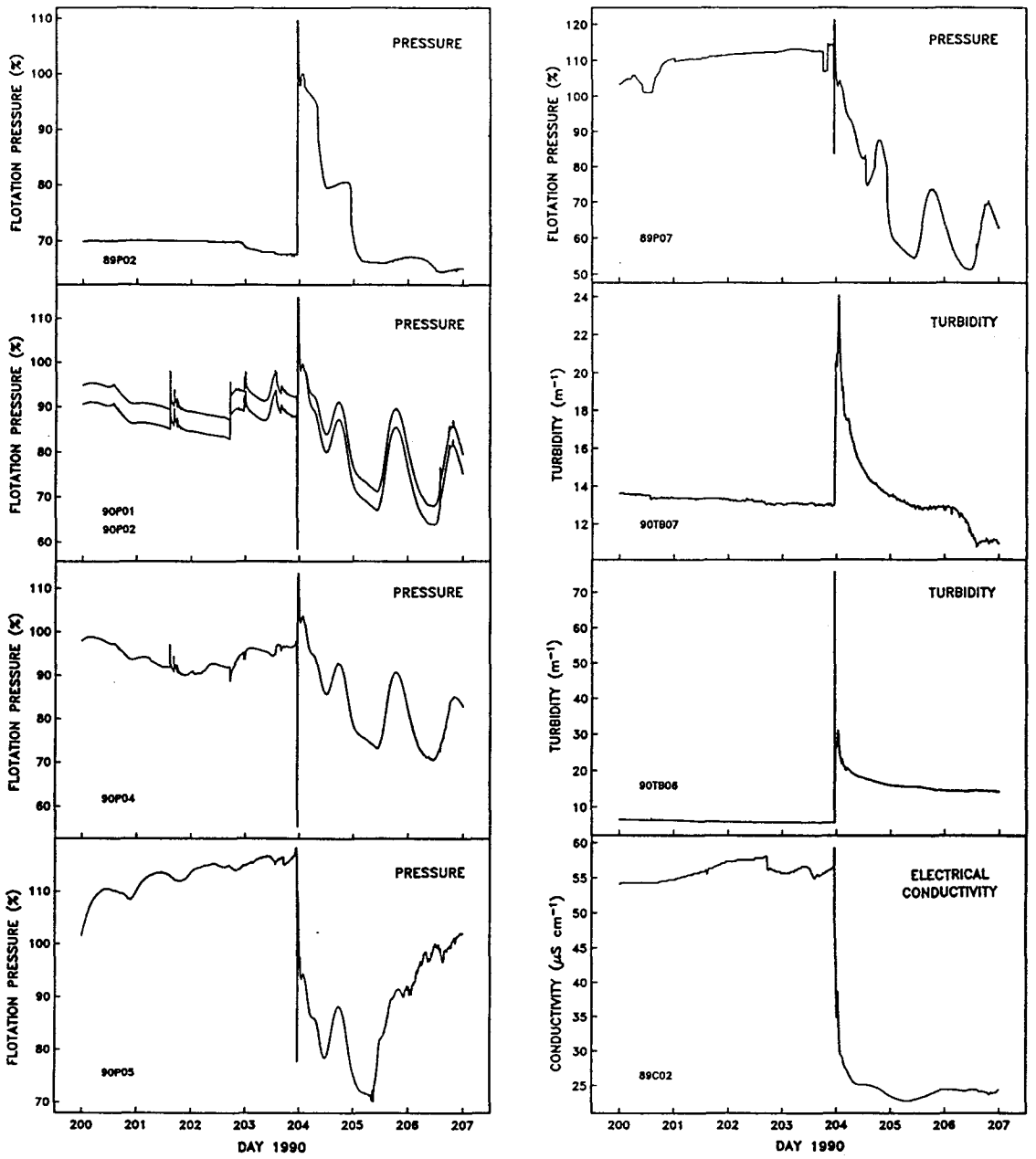

Fig. 5.9: Sudden rearrangement of the basal drainage system as recorded by subglacial water pressure, turbidity, and electrical conductivity sensors. The event spontaneously occurred just before midnight on Day 203 (22 July) 1990 and caused large disturbances over an area of the bed extending at least 100 m in the direction of ice flow and 50 m in a direction perpendicular to ice flow. The event coincided with a dramatic change in the nature of water pressure signals; diurnal fluctuations were weak or absent prior to the event but are clearly present in the post-event period.

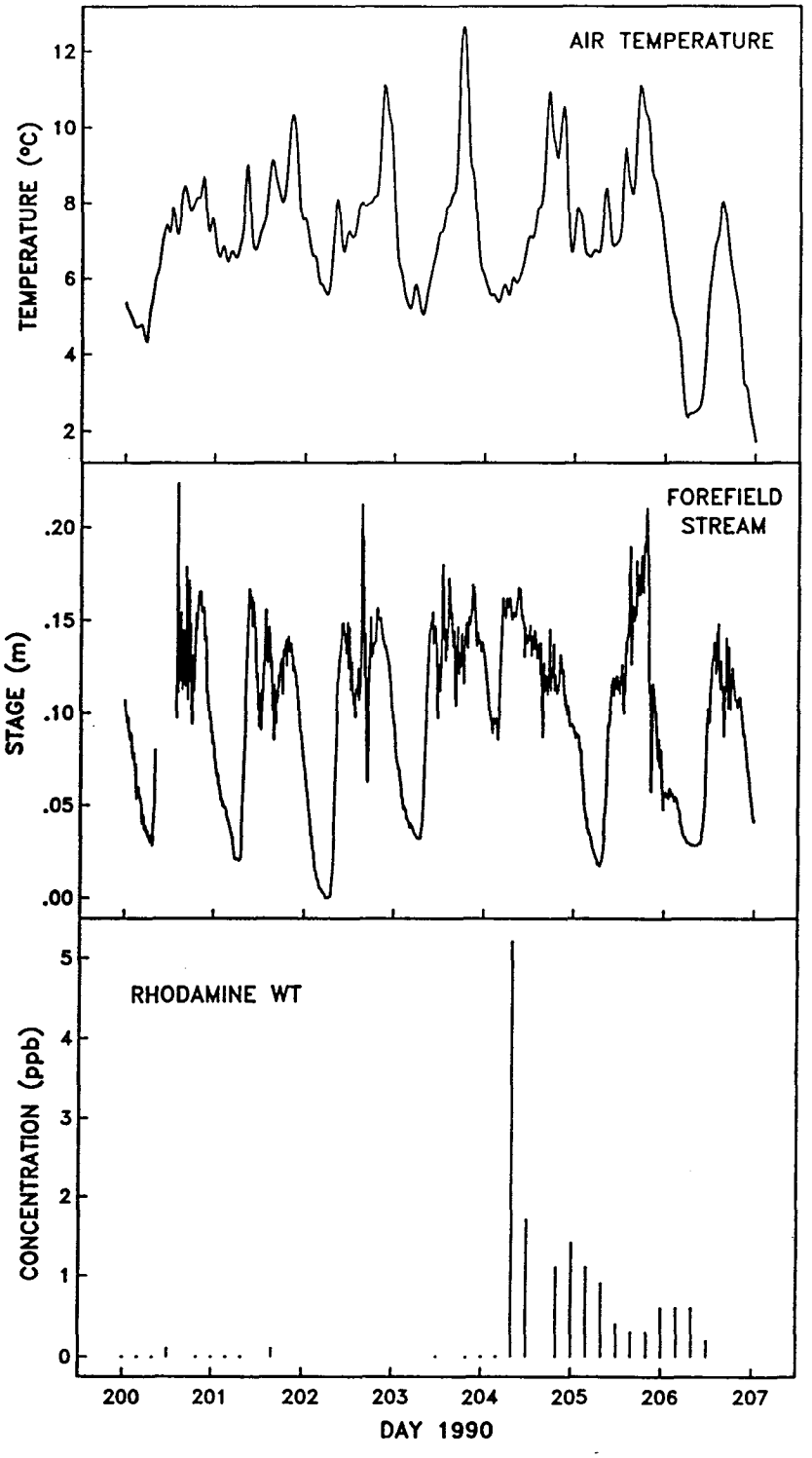

Fig. 5.10: Surface observations surrounding the 1990 release event: air temperature, forefield stream stage, and dye concentration.

Figure 5.10 shows surface observations associated with the 1990 event. Air temperature—which serves as a proxy for surface melt—reached a maximum value (for the entire summer field season) on Day 203 (22 July), suggesting that abundant meltwater might have triggered the event. The forefield stream stage was typically maximum in late afternoon at about 1800 h daily. On the day following the event the maximum was reached at 1000 h. The preceding minimum at 0330 h occurred several hours earlier than the usual time of about 0800 h; it was also approximately four times greater than other daily minima. Water samples collected up to and including 0400 h on Day 204 did not contain appreciable amounts of Rhodamine dye. By 0800 h, however, dye in excess of 5 ppb was present in the stream at the sampling site. The increase in stream stage, beginning at 0330 h on Day 204, likely signaled the first arrival of basal water at the sampling site. The fact that dye was not present in the stream at the sampling site until sometime after 0400 h suggests that the release event also involved water that had been stored in undyed portions of the glacier bed. This observation raises the possibility that release events might occur more often than is indicated simply by those periods in which dye has been detected in the forefield stream. Careful measurements of turbidity and electrical conductivity in the forefield stream would be helpful in further exploring this possibility.

The timing of subglacial events was not uniform throughout the region in which our sensors were located. Figure 5.11 shows that pressure sensors in different locations responded in similar ways, but at different times. In general, effects of the event appear to have propagated in a south-easterly direction. An interesting feature—well-captured by our two-minute sampling intervals—is that the event onset was signaled by an initial reduction in water pressure. (Sensor 89P02, shown in Figure 5.9, is an exception. The different behavior of this sensor suggests that it remained hydraulically isolated throughout the event.) The initial reductions in basal water pressure were

followed by rapid increases to super-flotation values, which then leveled off to near-flotation pressures. Kamb and Engelhardt (1987) reported a very similar pattern of basal pressure variations during the 1978–81 mini-surges of Variegated Glacier, Alaska; they observed "a propagating pressure wave in the basal water system of the glacier, in which, after a preliminary drop, the pressure rises rapidly to a level greater than the ice-overburden pressure at the glacier bed, and then drops gradually over a period of 1–2 d, usually reaching a new low for the summer."

The nature of the pressure signals that we recorded preclude the possibility that the event was initiated by a rupture downstream from the location of our sensors; pressure increases would not be expected following a simple downstream rupture. Instead, we suggest that an enlarging body of basal water at super-flotation pressures was hydraulically lifting the glacier, thereby expanding its boundaries and reducing the ice-overburden stress at surrounding locations. Sudden increases to super-flotation pressures occurred when hydraulic barriers separating the expanding water body from individual sensors were breached. This picture of subglacial events is consistent with the further observation that turbidity began increasing immediately as the pressure rose (Fig. 5.11, note that 90P04 and 90TB06 were in the same borehole). Strong hydraulic gradients, inducing water flow, would have developed as soon as connections were made between the water body and individual water pockets surrounding the sensors. Thus, water flow and turbidity increases would be expected during the rising pressure limbs, not during the initial stages of falling pressure.

Kamb and Engelhardt (1987) attributed the preliminary pressure drops during the mini-surges of Variegated Glacier to the enlargements of cavities ("basal cavitation") containing subglacial water: "A preliminary (ice) velocity increase shortly before the pressure wave arrives is caused by the forward shove that the main accelerated mass exerts on the ice ahead of it, and the resulting preliminary basal cavitation causes the drop in water pressure shortly before the pressure wave arrives." This interpretation is

different from our view of subglacial activity during the 1990 event on Trapridge Glacier. In particular, the apparent hydraulic isolation of sensors at the bed of Trapridge Glacier indicates that a drainage system through which a pressure wave could propagate did not exist prior to the event. It is possible that isolated pockets of water at the bed could have been enlarged in advance of the expanding water body, if the pockets were formed in the lee of stationary obstacles or bedrock steps and if an ice velocity increase preceded the pressure rise. The simple hydraulic jacking mechanism that we have proposed seems more likely, since there are very few indications of stationary obstacles in the deglaciated forefield and no indications of subglacial bedrock steps. Furthermore, hydraulic jacking has been indicated at other times besides the 1990 event, with similar effects on pressure sensors in nearby regions. The inverse relationships that we have sometimes observed between pressure sensors in close proximity to each other suggests that the glacier moves in a "seesaw" fashion; when basal water pressure is increased to super-flotation values in one location the overlying ice is lifted and the pressures in nearby regions are reduced.

Prior to the event, it is likely that only two of the pressure sensors were well-connected with each other: 90P01 and 90P02. The records obtained from these sensors show direct correspondences throughout the 1990 field season (Fig. 5.4). The stable offset between these records is almost entirely due to the different elevations of the two sensors, indicating that basal water was "ponded" in this region for most of the season. Distinct incongruities between other pressure records supports our view that hydraulic barriers separated regions surrounding individual sensors. After the barriers were broken down by the event, pressure signals from previously isolated sensors displayed similar behaviors.

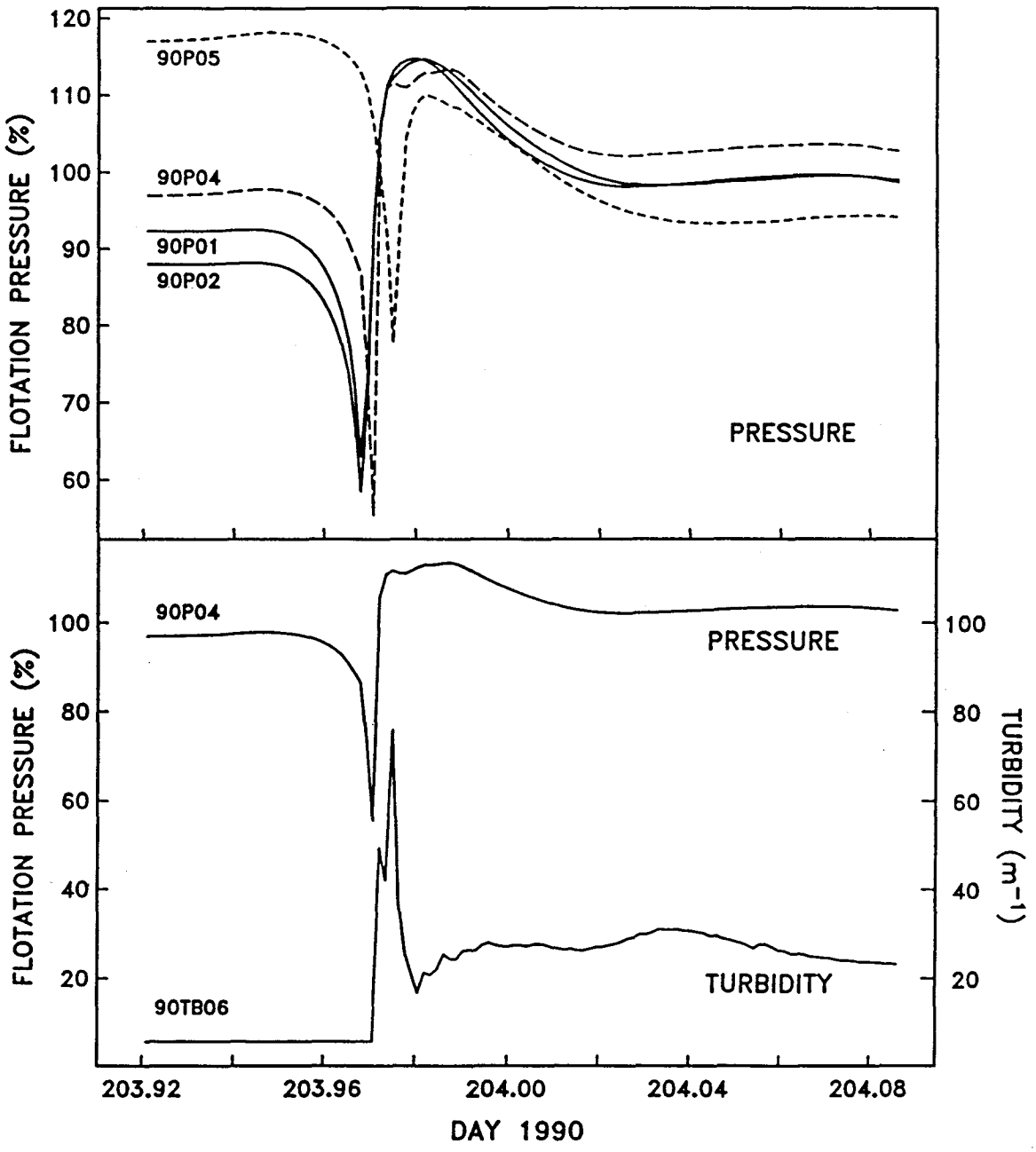

Fig. 5.11: Onset of the 1990 event. Subglacial water pressure records show gradual reductions in pressure, followed by abrupt increases. Turbidity pulses are associated with the rising pressure limbs. These patterns appear at different subglacial locations at different times and, collectively, suggest that the event involved a coupled mechanical-hydrological response.

Figure 5.12 shows calculated hydraulic head gradients between pressure sensors in different subglacial locations during the week of the 1990 event. Dashed lines in this figure represent estimated uncertainty bounds, accounting for the fractional uncertainties in both sensor positions and in the individual pressure measurements. Negative head gradients correspond to flow directed from the first sensor to the second; for example, from 89P07 to 90P01 in the upper graph.

The upper-two graphs in Figure 5.12 show large, negative gradients prior to the event. It is doubtful that these drive real water flow, since the sensors probably were not in hydraulic communication at that time. Unlike the sensors in the upper graphs, those in the lower graph—90P02 and 90P01—were clearly connected with each other prior to the event. The lower graph shows a small, positive, and nearly constant gradient between the sensors prior to the event. A constant gradient of zero would correspond to stationary ponded water. The slightly positive gradient between 90P02 and 90P01 indicates that basal water in the vicinity of these sensors was not stationary, and that a component of the flow-velocity vector was directed upglacier, opposite to the direction of ice flow. This result suggests that, near this location, there might have been a subglacial sink for water or an upstream lateral flow path; these possibilities are discussed further in the following chapter. For approximately one day following the event—at a time when hydraulic communications were well-established between several sensors—calculated head gradients indicate that water flow was directed downglacier, again in a south-easterly direction. On the second day following the event, hydraulic connections between 90P05 and the other pressure sensors were closed, and ponded conditions were again indicated between 90P02 and 90P01. By Day 208 (27 July), nearly all vestiges of the event had been erased.

Based on these observations, we suggest that the 1990 release event was initiated by a sudden influx of surface meltwater, possibly from the draining of a water-filled crevasse. (We point out that an icefall to the northwest of our study area is known

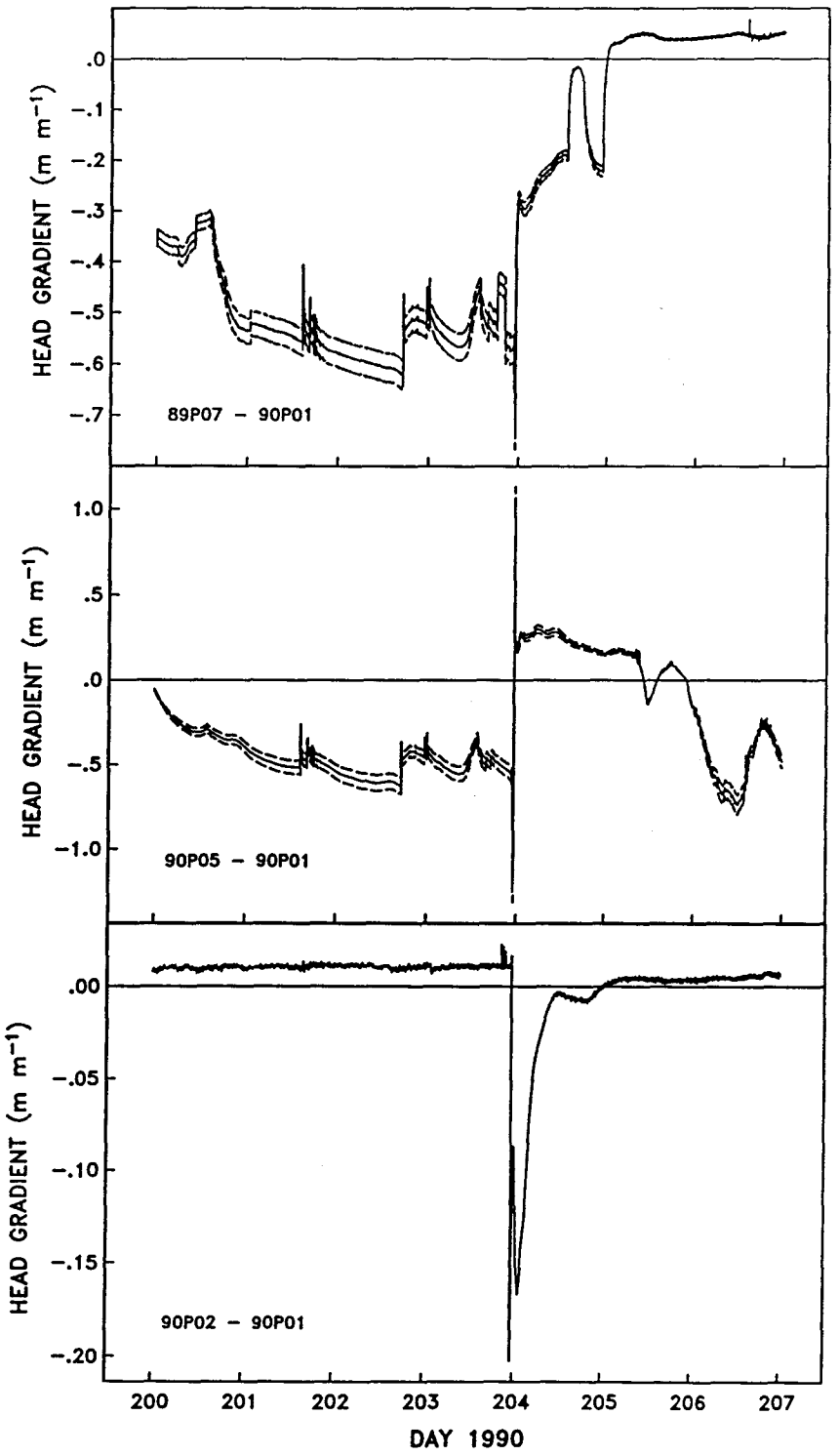

Fig. 5.12: Calculated hydraulic head gradients between pressure sensors in different locations during the 1990 event. Day 200 corresponds to 19 July. Dashed lines are estimated uncertainty bounds.

to contain many water-filled crevasses. The icefall is visible to the right of the central moraine in Fig. 1.2b.) The influx resulted in a coupled mechanical and hydrological response, involving (1) the reorganization of subglacial drainage passageways, (2) sediment mobilization, (3) release of stored basal water, and (4) mechanical jacking of the glacier in advance of a spreading boundary between hydraulically well-connected and poorly-connected regions. Initiation of water flow at a particular location coincided with the opening of downstream connections. Basal water was released into the forefield stream after the advancing hydraulic boundary established an open outlet to the glacier terminus. The opening of a terminal outlet enhanced water flow through the newly-connected regions and likely contributed to the development of an efficient basal drainage system at the ice-sediment interface. The newly-developed drainage system collapsed as the surface and stored water supplies diminished, but hydraulic connections were maintained, to varying degrees, for a period of 1–4 days following the event. After this period sensors again became hydraulically isolated, demonstrating a natural self-healing capacity. Although not disclosed by our observations, the gradual closure of hydraulic connections probably resulted from the combined processes of sedimentation, sediment deformation, and ice infiltration.

5.3.5 Points of discussion

5.3.5.1 Diurnal pressure fluctuations

We have noted that diurnal water pressure fluctuations can occur in two forms, either as quasi-sinusoidal oscillations (QSO) or as rapid increases followed by quasi-exponential decays (QED), and that there is likely a continuous transition between them. Both forms are apparent in record (e) of Figure 5.4 and in record (h) of Figure 5.5. Assuming that both types of signal result from daily meltwater input, transitions between the two behaviors suggest that the drainage system can be reorganized or undergo changes in its hydraulic properties over fairly short time intervals (on the order of a day or two).

In 1990, it was clearly evident that QSO were initiated by a release event during which an efficient subaerial outlet for basal water was established. QSO were also observed following a release event in 1989. However, we are unable to determine from our data whether or not the release event initiated QSO in this case. Although lacking a definite diurnal signature, QED-type pressure fluctuations are evident (records (c) and (d) in Fig. 5.4) prior to the 1990 release event and again following the inferred close-up, when sensors became hydraulically isolated from each other. These observations demonstrate that QSO are associated with an efficient drainage network; they also raise the question of whether QSO are always preceded by release events. We shall further this discussion in the following chapter.

5.3.5.2 Diurnal turbidity fluctuations

The 1989 graph of Figure 5.6 shows diurnal fluctuations in turbidity which are thought to be associated with variations in basal water flow. This association could be demonstrated if the pattern of subglacial water flow was known in the vicinity of the sensor. One approach to estimating patterns of basal water flow would be to calculate head gradients between hydraulically-communicating pressure sensors; fluctuations in hydraulic head gradients would correspond to variations in water flow. We would expect turbidity to be maximum when the gradient is largest and minimum when the gradient is smallest. The crux of this approach is that pressure sensors must be in hydraulic communication with each other, if a meaningful gradient is to be calculated.

During the 1990 release event, strong hydraulic gradients developed between well-communicating pressure sensors (Fig. 5.12) and were associated with large turbidity pulses (Fig. 5.9). In this case, the turbidity signals were clearly due to sediments mobilized by water flow. To explore other types of turbidity fluctuations, we have compared calculated gradients with turbidity records for 12-day periods in 1989 and 1991 (Figs. 5.13 and 5.14). The pressure records shown in the top graphs of Figures

5.13 and 5.14 were used to calculate hydraulic head gradients. We realize that there are few similarities between the pressure records in either 1989 or 1991, and that this casts doubt on the validity of the head gradient calculations. However, there were no better-matching pairs of pressure records that coincided with measurements of turbidity during these years.

In Figure 5.13, the two pressure sensors (89P02 and 89P17) were aligned approximately parallel to the direction of ice flow, and the turbidity sensor (89TB03) was located just off this line (Fig. 5.1). Diurnal turbidity fluctuations show the expected correspondence with head gradient in this case; turbidity rises and falls directly with increasing and decreasing gradient. Small spikes in turbidity are visible near the times of daily minima on Days 209 and 210. These spikes mark the connections of boreholes that were being drilled approximately 25 m away. Interestingly, these connections appear as only minute disturbances in pressure record (h), and they are indiscernible in record (a). These observations suggest that the newly-drilled boreholes were hydraulically well-connected to 89TB03 and only marginally-connected to 89P17, despite the fact that these two sensors were separated by a distance of less than 10 m.

In Figure 5.14, the two pressure sensors (91P02 and 91P04) were aligned approximately perpendicular to the direction of ice flow, and the turbidity sensor (91TB04) was in the same borehole as 91P04 (Fig. 5.1). There is no apparent relationship between the turbidity signal and the calculated head gradient in this case. Pressure record (f), corresponding to 91P04, shows weak diurnal excursions beginning on Day 195, but there are no corresponding turbidity fluctuations. Although the turbidity record shows large variability in the first three days, the signal is relatively featureless thereafter. The gradual rise throughout Day 192 and the sustained, high turbidities recorded in the following days suggest that the sensor might have become packed with sediment. It is interesting that during the period in which turbidity varied the most—Days 191 to 192—there was virtually no change in either of the pressure records, and that nearly

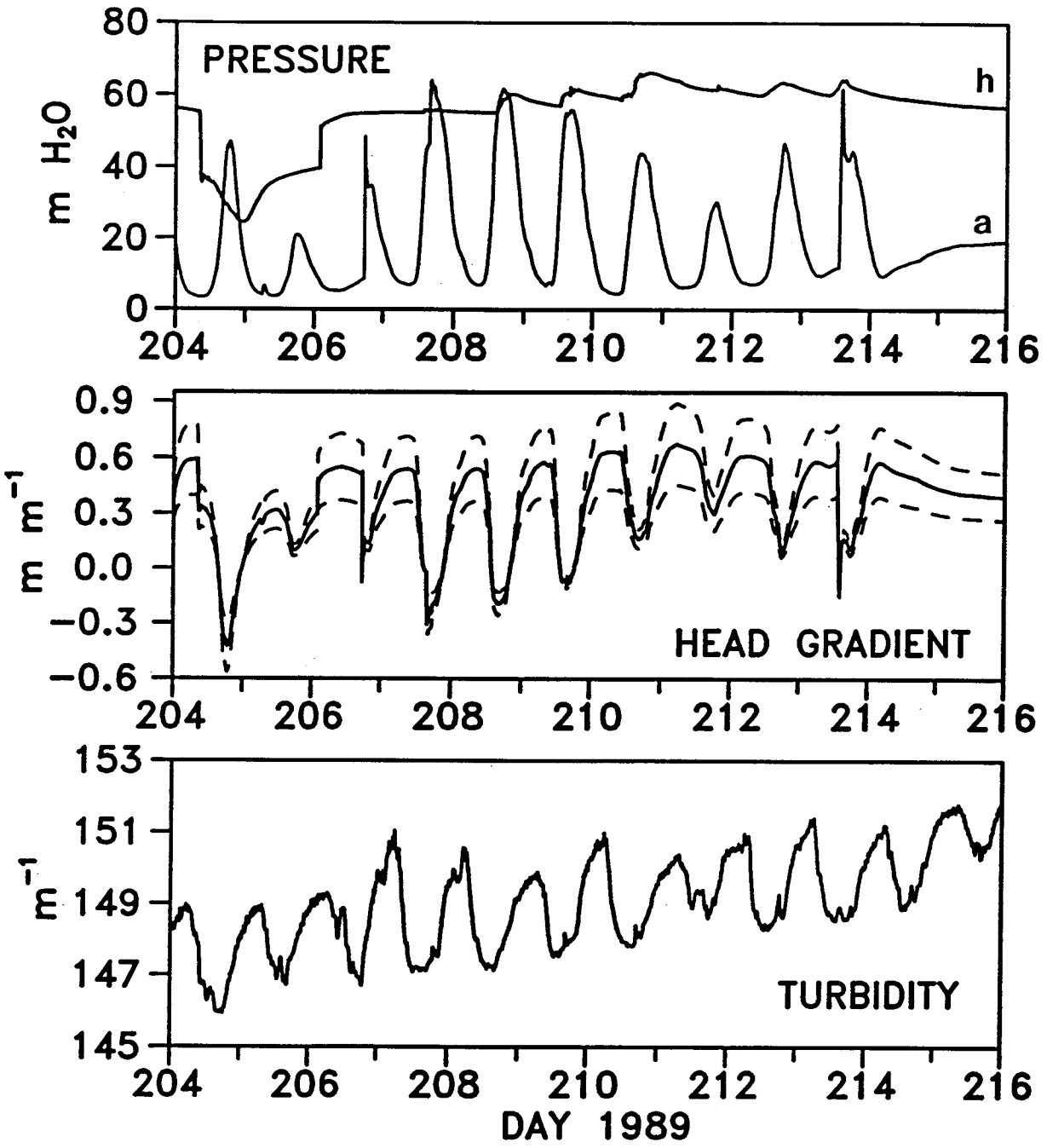

Fig. 5.13: Subglacial water pressure and turbidity measured over a 12 day period in 1989. Day 204 corresponds to 23 July. Individual pressure sensors are identified by lower case letters: (a) 89P02; (h) 89P17. Turbidity was recorded using sensor 89TB03. Hydraulic head gradient between the two pressure sensors is shown in the middle graph. Dashed lines are the estimated uncertainty bounds. Negative gradient values correspond to flow directed from pressure sensor 89P02 to sensor 89P17.

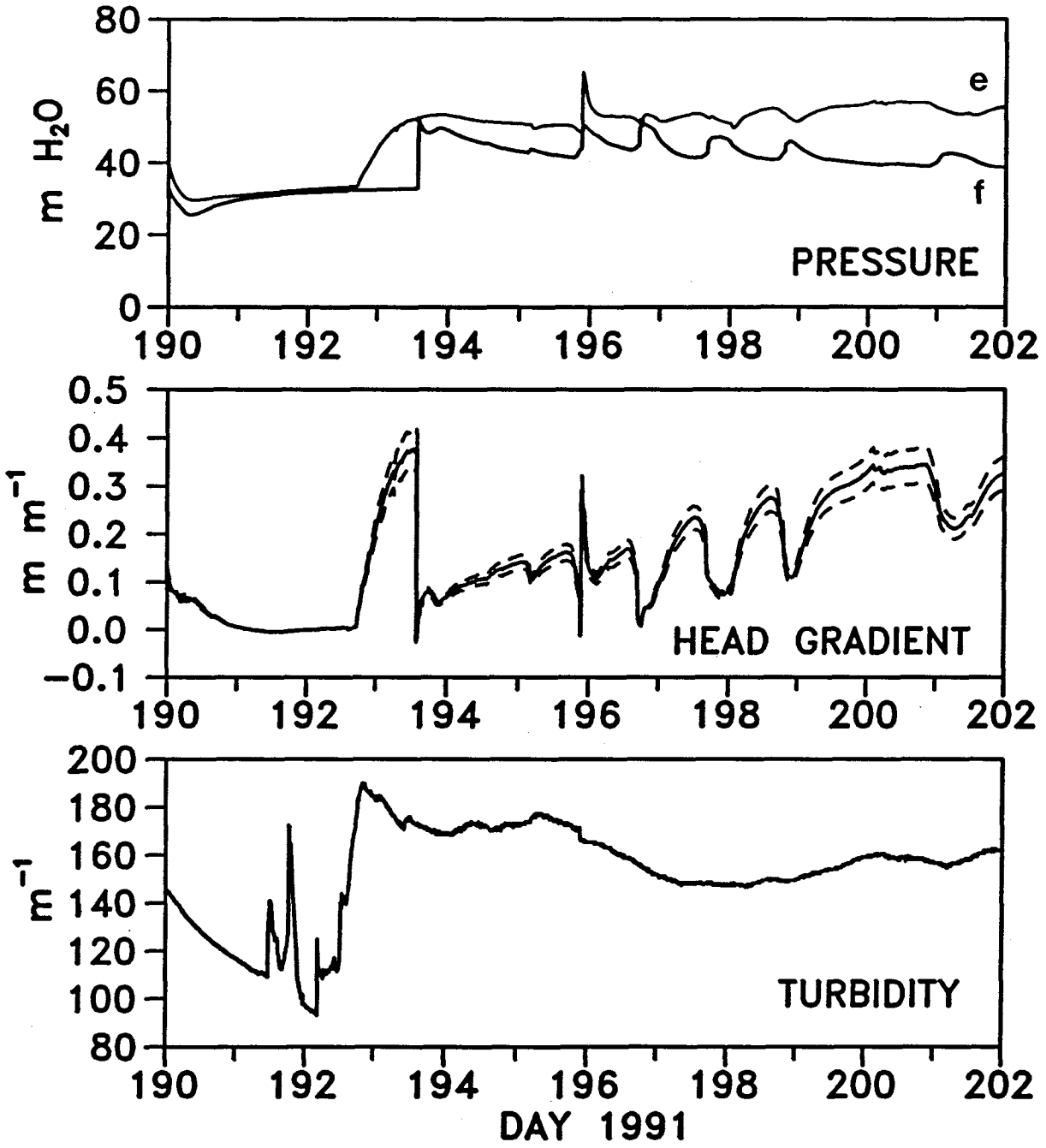

Fig. 5.14: Subglacial water pressure and turbidity measured over a 12 day period in 1991. Day 190 corresponds to 9 July. Individual pressure sensors are identified by lower case letters: (e) 91P02; (f) 91P04. Turbidity was recorded using sensor 91TB04. Hydraulic head gradient between the two pressure sensors is shown in the middle graph. Dashed lines are the estimated uncertainty bounds. Negative gradient values correspond to flow directed from pressure sensor 91P02 to sensor 91P04.

the same pressure was recorded by both sensors. We point out that electrical conductivity was also being recorded in the same borehole as 91P04 and 91TB04 during this time. These measurements, from sensor 91C03, were presented in Figure 5.7 and show a large excursion over Days 191 and 192. Thus, observations of both turbidity and conductivity indicate that basal water quality was changing during this period. How such activity takes place subglacially at constant, non-zero pressure is an enigma.

5.4 Year-round observations

For conceptual ease of presentation, we will refer loosely to "summer" and "winter" conditions. On the basis of signal variabilities, "summer" lasts roughly from early July to mid-September; "winter" constitutes the rest of the year. The summer behavior has already been described in detail and will not be restated here. We have included summer data in the following figures, however, to give a better picture of the year-round behavior of the drainage system.

5.4.1 Water pressure

Year-round measurements of subglacial water pressure are shown in Figures 5.15 and 5.16. Again, we have labeled each record by a lower-case letter that identifies the particular sensor with which the measurements were made: (a) 89P02; (b) 90P07; (c) 90P08; (d) 91P02; (e) 91P08; (f) 89P07; (g) 90P02; (h) 91P05. (Note that the associations between labels and the sensors that they identify are different than those used for summer observations.) Except for 91P05, all of these sensors were installed in boreholes that were initially connected to the basal drainage system. Pressure records (f) and (g) each span two full years. Referring to Figures 5.15 and 5.16, we can list the main features of the winter period as follows:

(1) The transition from summer to winter conditions—signaled by the end of large pressure excursions—begins in late August or early September.

(2) In general, water pressure changes gradually during winter. Diurnal pressure fluctuations are not observed. Changes on the order of 10 m water equivalent usually take place over intervals lasting at least a couple of months. Changes of this magnitude do occur more rapidly, but only infrequently.

(3) Winter pressure trends can be either increasing or decreasing. There is no clear evidence that either behavior is dominant.

(4) In winter, basal pressures typically lie in the range of 40–60 m water equivalent (roughly 75% of the ice-flotation pressure); sensors that were recording pressures lower than this at the end of the summer tend to gradually rise to this pressure range, while those recording higher pressures tend to be lowered.

(5) The transition from winter to summer conditions begins abruptly with large increases in water pressure. The transition sometimes begins as early as mid-May.

5.4.2 Turbidity

Two year-round records of subglacial turbidity are presented in Figure 5.17. These measurements were obtained using sensors 90TB07 (a) and 91TB02 (b). Although we have collected several records of winter turbidity, we only show two of them in this figure because they all exhibit very similar behaviors. Turbidity can vary substantially during the summer months, presumably in association with changing flow conditions; it is virtually constant throughout the winter, when there is likely to be little if any water flow at the bed. In general, turbidity is higher in winter than it is in summer. The transition to higher winter values suggests that sediments might become packed-in around the sensors as excess summer meltwater is evacuated.

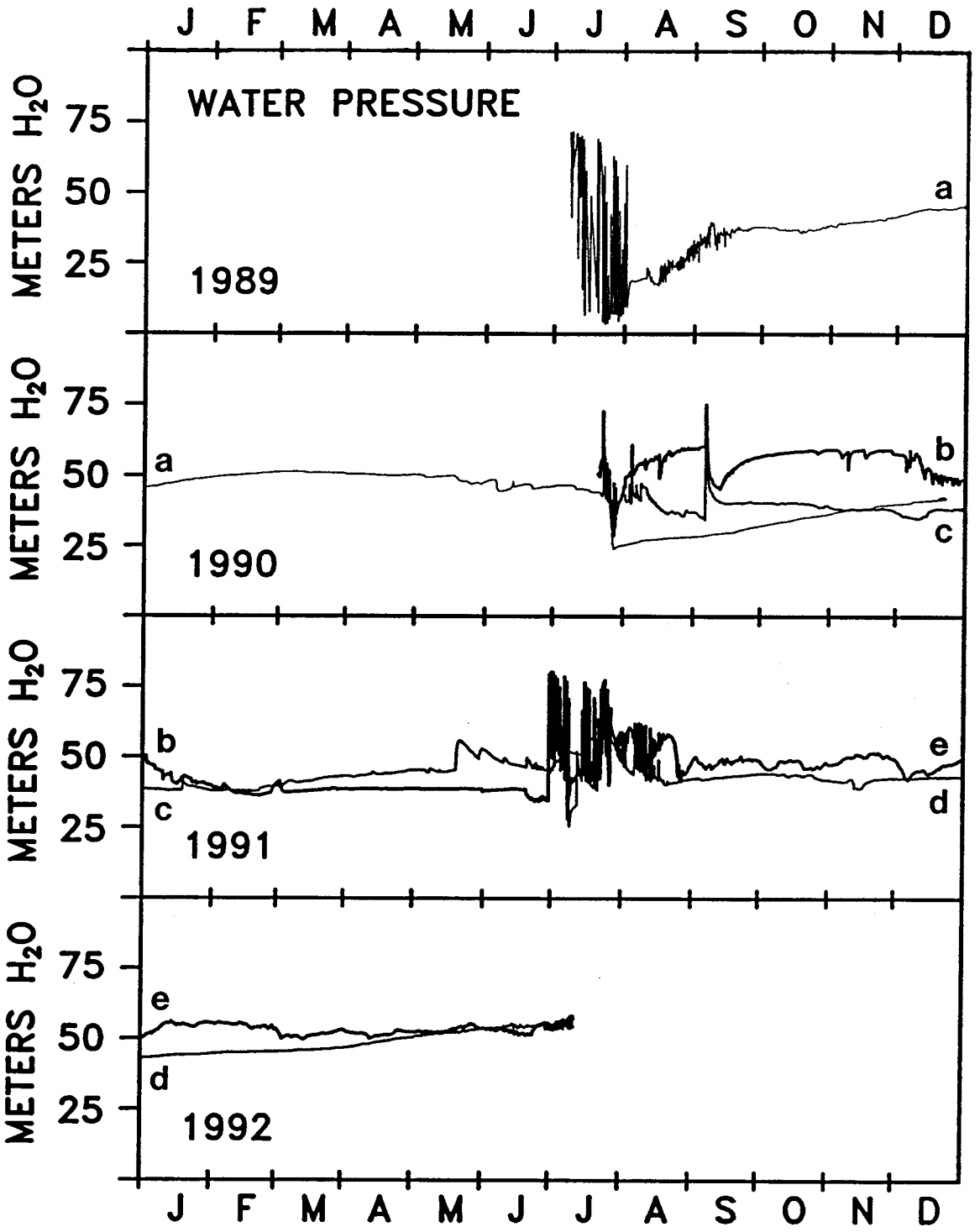

Fig. 5.15: Year-round measurements of basal water pressure. Records are labeled by lower-case letters, each of which identifies a particular sensor: (a) 89P02; (b) 90P07; (c) 90P08; (d) 91P02; (e) 91P08.

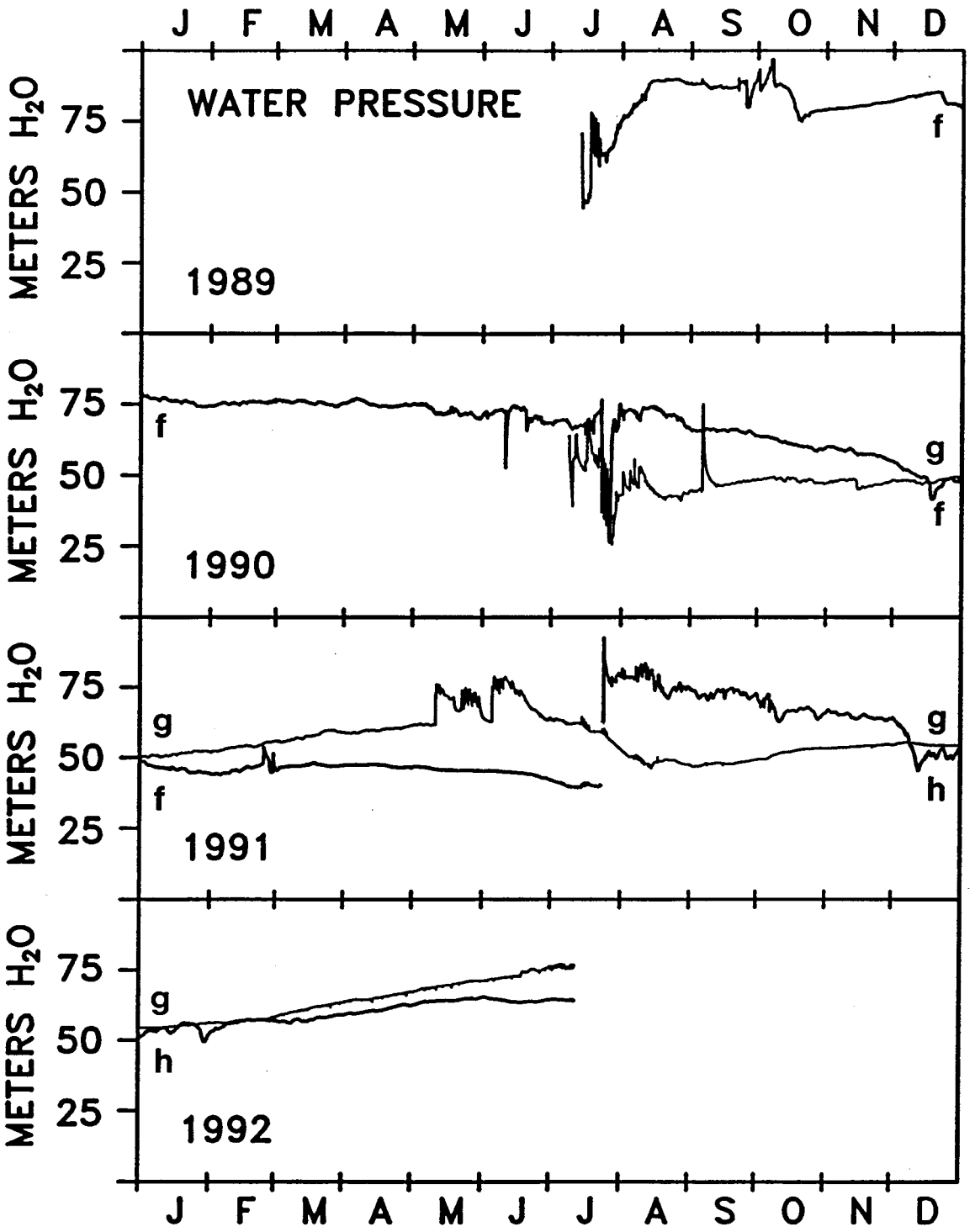

Fig. 5.16: Year-round measurements of basal water pressure. Records are labeled by lower-case letters, each of which identifies a particular sensor: (f) 89P07; (g) 90P02; (h) 91P05. Note that records (f) and (g) each span two full years.

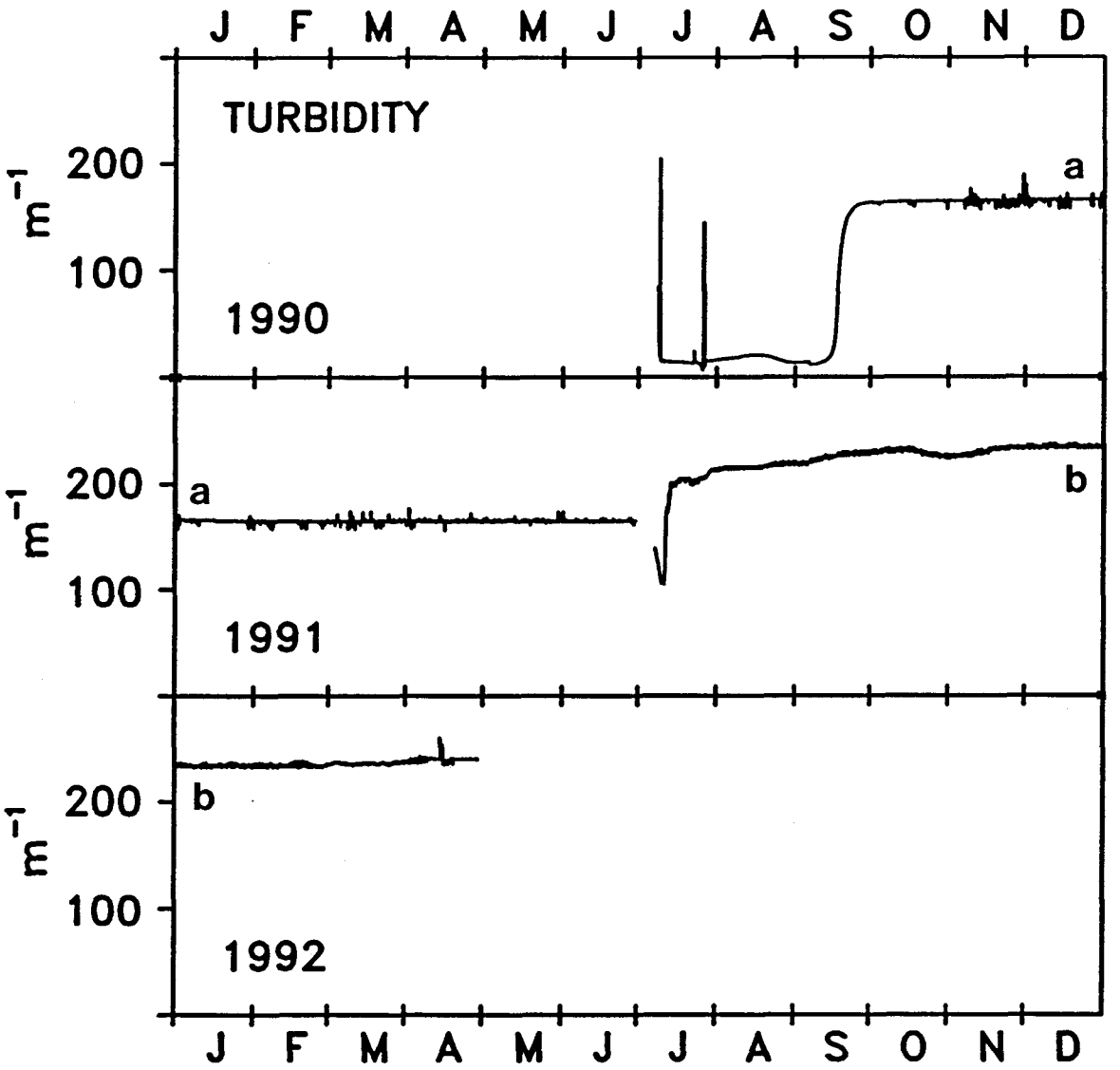

Fig. 5.17: Year-round measurements of subglacial turbidity. Records are labeled by lower-case letters, each of which identifies a particular sensor: (a) 90TB07; (b) 91TB02. During the summer months turbidity varies substantially and over a range of time scales (from < 1 day to ~ 2 weeks), presumably in association with changing water flow conditions. Turbidity is virtually constant throughout the winter months.

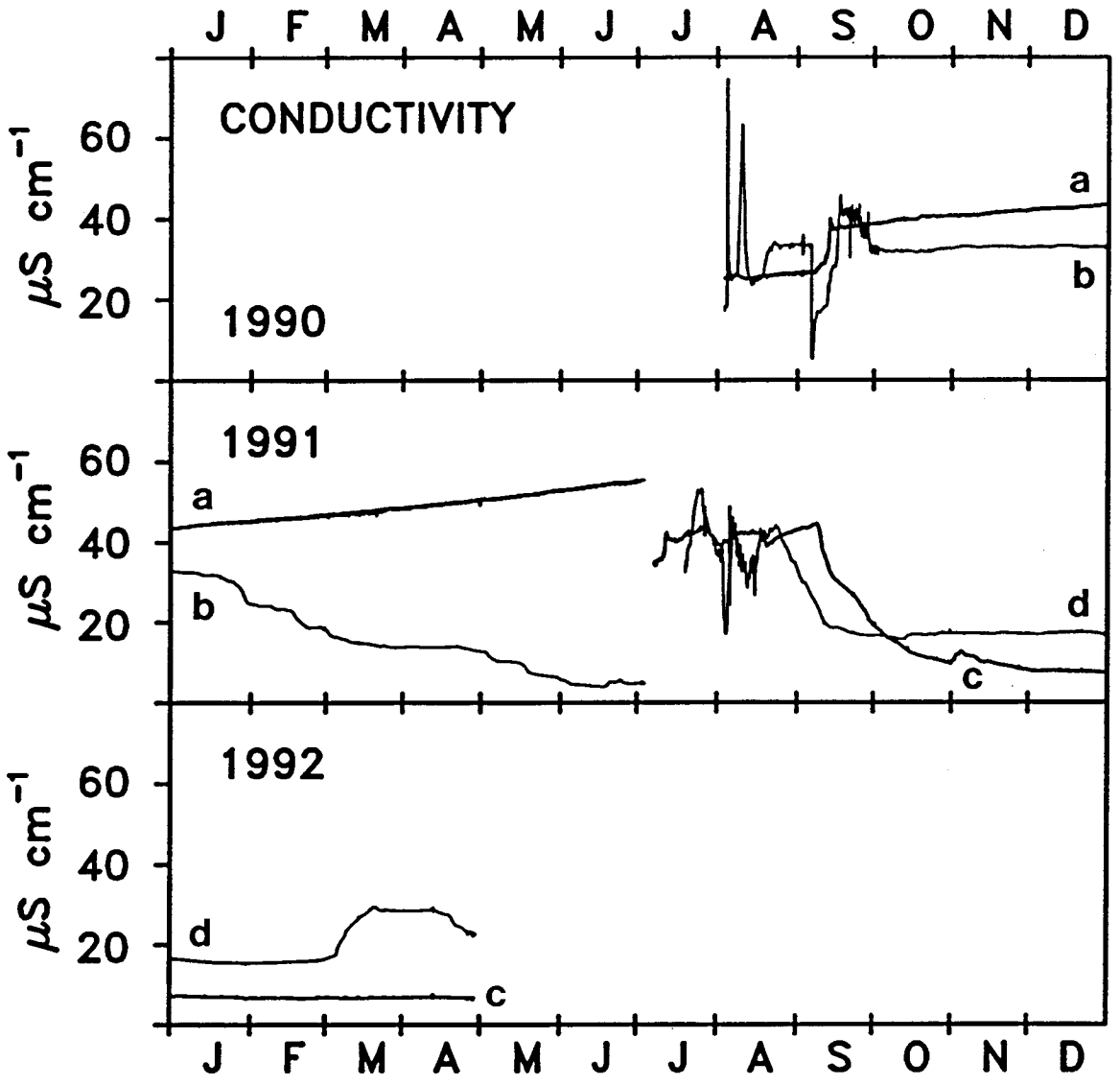

Fig. 5.18: Year-round measurements of subglacial electrical conductivity. Records are labeled by lower-case letters, each of which identifies a particular sensor: (a) 90C06; (b) 90C07; (c) 91C02; (d) 91C06. Conductivity is highly variable during summer and changes only gradually during winter. Note the different winter behaviors illustrated in records (a) and (b).

5.4.3 Electrical conductivity

Year-round measurements of subglacial electrical conductivity are shown in Figure 5.18. Records are associated with individual sensors as follows: (a) 90C06; (b) 90C07; (c) 91C02; (d) 91C06. Like basal pressure and turbidity, the electrical conductivity of subglacial water varies the most in summer and changes only gradually during the winter. Also like basal pressure, winter conductivity trends can be either increasing or decreasing. We have previously mentioned one possible explanation for increasing trends; namely, ion concentration is expected to increase as the contact time between water and basal sediments increases. We have also suggested that conductivity of "old" basal water would decrease if the ion concentration were reduced, say by an infusion of surface meltwater. Since surface meltwater is not added to the system in winter, this mechanism cannot explain the generally decreasing trends that are sometimes observed. Given that Trapridge Glacier has a subpolar thermal regime (ice is coldest near the surface and the melting point is reached only near the bed), one possible explanation for decreasing winter conductivities is that fresh water is continually supplied to the bed as the borehole slowly freezes from the top down.

5.5 Summary of observations

Summer data show rapid, large-amplitude excursions, relative to the year-round signal fluctuations. Subglacial water pressures are highest in summer, often locally exceeding the ice-flotation pressure. Despite frequent periods of high pressure, hydraulic connections between sensors in different basal locations are generally poor or non-existent. Sudden events, probably triggered by an oversupply of surface meltwater, sometimes cause large-scale reorganization of the basal drainage network. These events can lead to the creation of a temporarily well-connected and efficient drainage system. Rapid changes in the "connectedness" of a given basal region are common in summer. Changes

in the nature of signal variations—for instance, QSO and QED, or large turbidity increases followed by periods of diurnal cycling—and the sudden starting and stopping of fluctuations suggest that, at a given location, the routings of both supply and exit passageways are unstable.

Observations made in winter indicate that basal hydraulic conditions change gradually during this time, and that conditions are generally more uniform across the bed than they are in summer. After summer meltwater input has ceased, basal water pressures tend to gradually stabilize at about 75% of the ice-flotation pressure.

Chapter 6

PROPERTIES OF SUBGLACIAL WATER: INTERPRETATION

6.1 Introduction

The fast flow of ice during a glacier surge is enabled by sustained high basal water pressures acting over significant portions of the bed. To understand how sustained high pressures develop and how the subglacial distribution of water influences ice motion, we must first understand the interactions between basal water flow and drainage system configuration in the non-surging state. In this chapter we describe the basal drainage system of Trapridge Glacier at a time when the glacier was not surging.

The observations presented in the previous chapter are interpreted here to infer the configuration of the basal water-flow system. To reach conclusions, it has been necessary to infer general patterns and behaviors from measurements made at a limited number of locations. Decisions regarding the importance of various features and the distinction between typical and unusual behaviors have also been required. Thus, the following interpretations are based, to some extent, on subjective judgements.

In general, a single, stable drainage configuration cannot be identified, since coherent behavior between subglacial sensors is only rarely observed. On the length scales that we have considered ($\lesssim$100 m), basal water appears to moves through and be stored in a highly-variable and disorganized drainage system. The complex behavior of the drainage system points to a dynamic subglacial environment, one in which the basal hydrology is governed by the combined influences of the glacier thermal regime, meltwater input, sediment movement, and mechanical interactions with the overlying ice.

6.2 Transitions between drainage states during the 1990 release event

It is worthwhile to revisit the 1990 release event; the transitions in drainage system morphology that took place during this event set a context for the subsequent discussion of non-event drainage configurations. Figure 6.1 is a conceptual model of the transitions that took place during the 1990 release event.

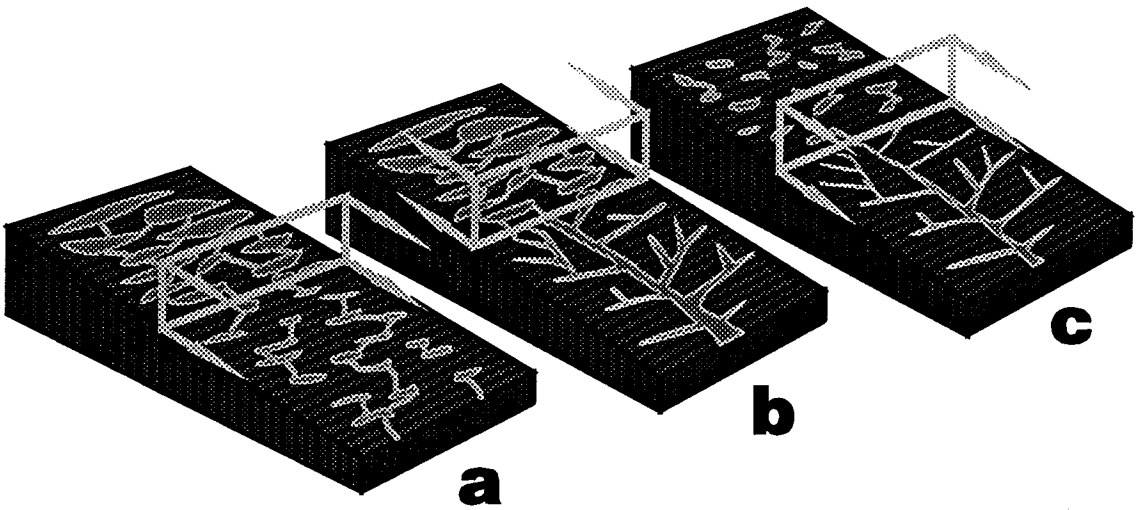

Fig. 6.1: Transitions between drainage states during the 1990 release event

The pre-event drainage system was characterized by disconnected networks of basal water. The event was initiated when a large source of surface meltwater suddenly connected to the glacier bed. The super-flotation pressures that ensued caused extensive bed separation, thereby creating hydraulic connections over large subglacial areas. Water from the surface source filled newly connected areas of the bed. In turn, high pressures in these areas caused further bed separation in surrounding regions. Thus, the transition (depicted in (a) of Fig. 6.1) from a disconnected, low-volume state to a widely-connected, high-volume, high-pressure state propagated downglacier. When the leading edge of the disturbance broke through to the glacier terminus and

a subaerial outlet was established, water flow through the system accelerated due to the resulting decrease in downstream resistance. Increased discharge through the system promoted the growth of preferred flow passageways. As the passageways grew, a branching drainage network was developed, and a second transition—this time propagating upglacier—took place; the high-volume, high-pressure state was replaced by a centralized, lower-pressure state in which water flow was concentrated in main passageways (transition (b) in Fig. 6.1). Water that had been widely-distributed over the glacier bed was captured and evacuated by the centralized drainage network. Water pressures declined as the stored basal water was removed, decreasing bed separation and sealing off hydraulic connections. Thus, the final transition (shown as (c) in Fig. 6.1) involved the erasure of centralized flow passageways as regions containing basal water again became disconnected.

The velocity of the (a) transition is of special interest; it can be compared with the propagation speeds of similar events that have been observed on other glaciers. In the preceding chapter, we inferred from measurements of the forefield stream stage that basal water released during the 1990 event first reached the sampling site at around 0330 h on Day 204 (23 July). From travel time measurements of small Nalgene bottles floated in the forefield stream, we have estimated that, in a reach just upstream from the sampling site, the average stream velocity is approximately $0.9\,\mathrm{m\,s^{-1}}$. The distance between the glacier terminus and the stream sampling site is about 300 m, as determined from 1990 surveys. Thus, the time required for water to travel from the terminus to the sampling site is roughly 5.6 minutes, indicating that basal water was first released into the forefield stream at 0324 h on Day 204. The distance between the glacier terminus and sensor 90P01 was ~ 530 m, and the onset of the pressure rise was first indicated by that sensor at 2314 h on Day 203 (22 July). Together with the estimated time of release at the terminus, these observations suggest that the leading edge of the disturbance propagated downglacier at an average speed of $127\,\mathrm{m\,hr^{-1}}$. This value is very close to

the propagation speed calculated by Smart and Clarke (submitted) during the 1986 release event; they estimated a velocity of $130\,\mathrm{m\,hr^{-1}}$.

As previously mentioned, the 1990 release event has a strong resemblance to the 1978–81 mini-surges observed on Variegated Glacier. It also has many similarities to infrequent motion events that have been observed on Findelengletscher, Switzerland (Iken and Bindschadler, 1986). During the mini-surges of Variegated Glacier, the propagation speed of pressure waves was about $600\text{–}700\,\mathrm{m\,hr^{-1}}$ (Kamb and Engelhardt, 1987, Table III), considerably faster than the speed with which pressure disturbances have traveled during release events on Trapridge Glacier. Waves of high water pressure were also associated with the motion events that were observed on Findelengletscher during the summer of 1982. The velocities of the leading edges of these waves ranged between $94\text{–}178\,\mathrm{m\,hr^{-1}}$ (Iken and Bindschadler, 1986, Table I). The fact that events of this type have taken place on Findelengletscher is noteworthy because this glacier is thought to be non-surge-type.

Our view of the 1990 release event on Trapridge Glacier is that the subglacial drainage system could not adjust quickly enough to accommodate a sudden, large input of water. The response to this sudden input involved the creation of an efficient drainage network through which the oversupply of water was quickly evacuated. Clearly, this event did not trigger a surge of Trapridge Glacier, nor did similar events trigger the last surge of Variegated Glacier. To enable a surge, the development of an efficient drainage network must somehow be prevented. Thus, the drainage network that was created during the 1990 release event (transition (b) in Fig. 6.1) represents something of a "failed" state, in terms of surging. Furthermore, the fact that release events appear to occur only infrequently suggests that the development of a centralized drainage system also represents a breakdown under non-surging conditions—the normal drainage system configuration must somehow be different.

6.3 Drainage system morphology

In this section we will distinguish between two facets of the subglacial drainage system: (1) how water moves along the bed and (2) how water is evacuated from the bed. We consider evacuation first.

It is reasonable to suspect that the primary evacuation mode in winter is by slow seepage through subglacial sediments, since the basal water supply during this time would be insufficient to maintain any kind of conduit-like network. Christopher Smart (unpublished manuscript) and, subsequently, Tavi Murray (personal communication) have detected Rhodamine dye in ice deposits that form every winter on a flood plain in the valley bottom below Trapridge Glacier. Because surface water is presumably frozen during the winter, these findings suggest that a deep groundwater flow system could be involved in evacuating water from the glacier bed.

Smart and Clarke (submitted) have considered the possibility that basal water drains through a low-permeability substrate immediately at the glacier sole, and is evacuated by a more transmissive system below. This view of the subglacial strata is strongly supported by the observed structure and composition of sediments that are exposed in the forefield stream cuts. Figure 6.2 (adapted from John Shaw, unpublished) shows the uppermost layers of sediment in the forefield; a layer of matrix-rich till having variable thickness (0.1–1 m) overlies a thicker layer of cobble-rich till. Discontinuous lenses of sorted gravels are present in the upper till layer. The matrix material of the upper-most layer is a mixture of silt- and clay-sized particles; this layer constitutes the low-permeability substrate considered by Smart and Clarke. The layer of cobble-rich till, which is underlain by alluvial sands and gravels, has a matrix of sandy material, giving it a greater permeability; this is the more transmissive unit. Based on the occurrence of unconnected boreholes, Smart and Clarke have estimated an upper bound on the hydraulic conductivity of the low-permeability layer: $K \leq 3.6 \times 10^{-7}\,\mathrm{m\,s^{-1}}$.

They point out that sources of meltwater in winter—geothermal melting and friction—are unlikely to generate fluxes in excess of $3.2 \times 10^{-10}\,\mathrm{m\,s^{-1}}$, which could easily be accommodated by gravitationally driven flow through the low-permeability upper layer.

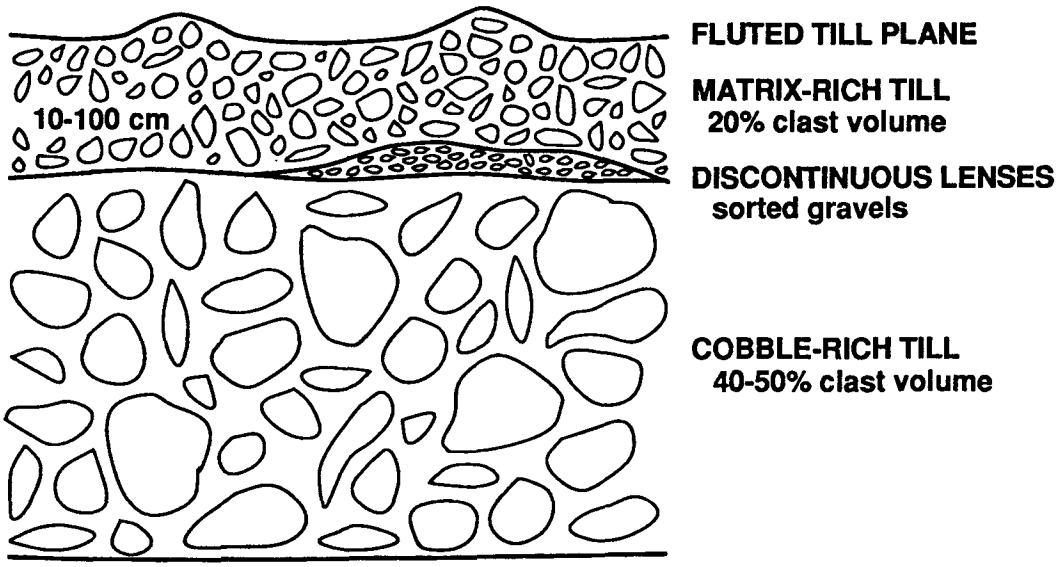

Fig. 6.2: Representative section of near-surface sediments in the forefield. (After John Shaw, unpublished.)

We have seen that there are situations for which the existing subglacial drainage system is insufficient to accommodate the water supplied to it. The 1990 release event, for example, was triggered by such a situation. Water reaching the bed early in the melt season is also likely to encounter an inadequate drainage network, since the system capacity almost certainly will have been reduced during the winter. This situation leads to the high basal water pressures that we observe early in the summer, and is thought to be responsible for the rapid uplift that has been observed on other glaciers at the beginning of the melt season (Iken and others, 1983). To see if groundwater flow can account for normal (i.e., non-release event) drainage throughout the summer, and to place constraints on other possible modes of evacuation, we consider an idealized model of diurnal forcing.

6.3.1 Idealized model of diurnal forcing

Diurnal fluctuations in basal pressure and turbidity, which are only observed in summer, are presumably forced by surface sources of meltwater having englacial connections to the bed. We can model this forcing in a simple way by considering an idealized crevasse (Fig. 6.3a) which collects surface meltwater during the day and discharges an equal amount of water through the basal drainage system at night. To keep the model simple, we will assume that there is no discharge from the crevasse while it is filling and that there is no additional input while it drains. Under this assumption, pressure fluctuations recorded by sensors that are hydraulically connected to the crevasse will be directly related to intervals of filling and discharge (Fig. 6.3b). During periods of quasi-sinusoidal oscillations (QSO), pressure tends to be maximum at $\sim$ 2200 h and minimum at $\sim$ 1100 h daily (e.g., record (a) in Fig. 5.13). Based on this observation, we shall take the time between 1100 h and 2200 h as the interval of crevasse filling; the remaining 13 hours constitute the drainage period.

The geometry of an idealized crevasse is shown in Figure 6.3a. Plausible values for the geometric variables are $w = 2\,\mathrm{m}$, $L = 20\,\mathrm{m}$, and $h = 70\,\mathrm{m}$. With these estimates, $\theta \approx 0.82°$ and the total volume of the crevasse is $1400\,\mathrm{m}^3$. If we consider only 20 m excursions in the crevasse water level—say between 40–60 m, a typical range for QSO—then the daily volume of water input to and evacuated from the basal drainage system is approximately $V_\mathrm{d} = 570\,\mathrm{m}^3$. (As a check, we note that this volume of water corresponds to the melting of 0.02 m of ice over an area of $3.2 \times 10^4\,\mathrm{m}^2$—roughly $180\,\mathrm{m} \times 180\,\mathrm{m}$—which could easily be produced on a daily basis.) Distributing V_d over the assumed drainage interval, $\Delta t = 13\,\mathrm{h}$, gives the average daily discharge through the system: $\bar{Q} = V_\mathrm{d}/\Delta t \approx 1.22 \times 10^{-2}\,\mathrm{m}^3\,\mathrm{s}^{-1}$.

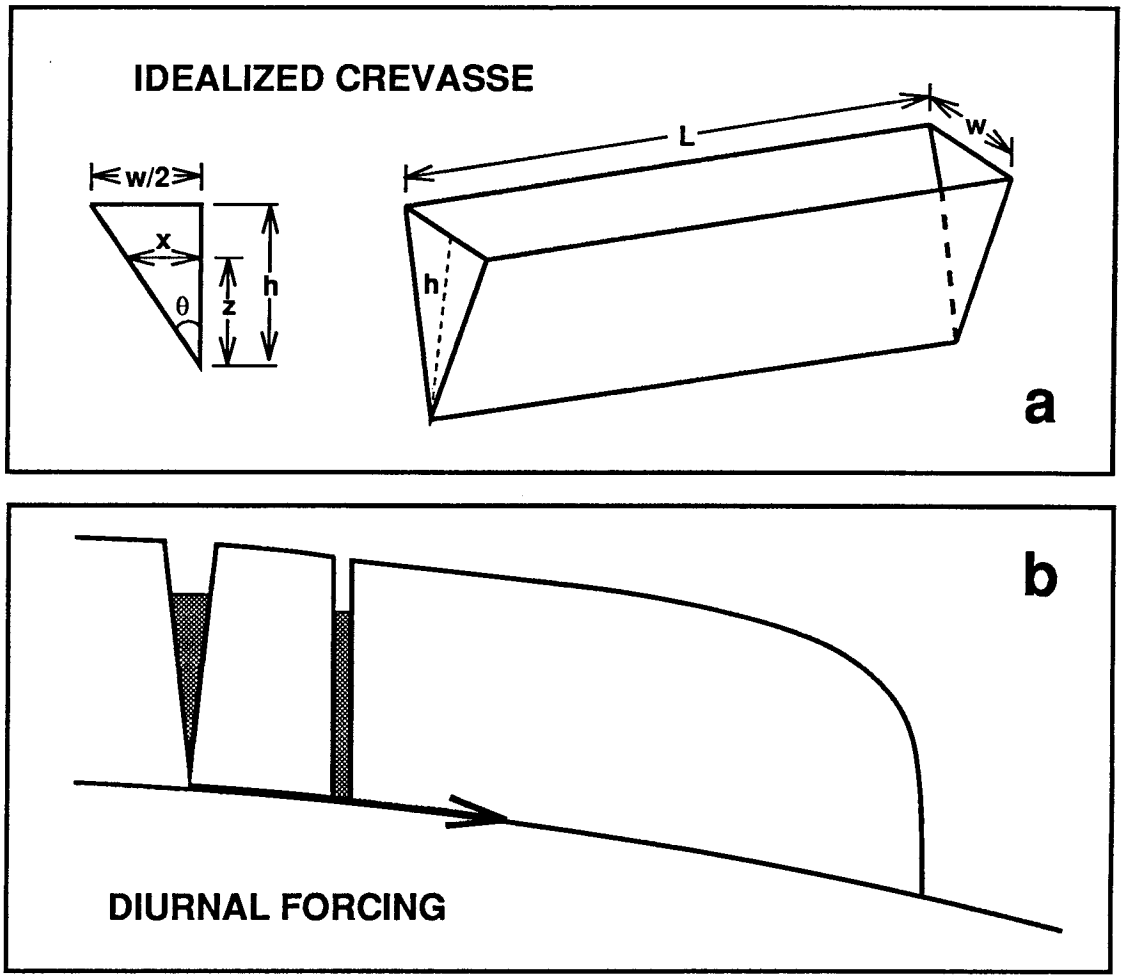

Fig. 6.3: (a) Geometry of idealized crevasse and (b) conceptual model of crevasse water-level forcing basal pressure fluctuations.

6.3.2 Possible configurations for evacuation of basal water

The daily discharge from the crevasse can be used to place physical constraints on possible drainage structures. This, combined with glaciological reasoning, allows us to infer the most likely structures for evacuation of subglacial water. We first consider whether input from the crevasse could be evacuated through one or more discrete conduits. Although obvious outlets for basal water have not been found in the central region of the glacier terminus, we shall consider the possibilities that basal water could be evacuated either through sediment-walled pipes or through unnoticed ice–sediment

tunnels at the terminus. Secondly, we consider whether daily input from the crevasse could be accommodated purely by groundwater flow through the subglacial sediment.

6.3.2.1 Conduit flow

Consider a cylindrical subglacial conduit having radius r and length L. If such a conduit carried the entire daily discharge from the crevasse then the total cross-sectional area of flow would be $A_T = \pi r^2$. Continuity of water flux requires that

$$\bar{Q} = A_T \bar{v} \tag{6.1}$$

where $\bar{v}$ is the mean water velocity in the conduit. Under turbulent conditions, which are typical for water flowing in subglacial conduits, Manning's Equation is commonly used to predict the mean velocity:

$$\bar{v} = \frac{R^{2/3}}{n'} \left(\frac{dh}{dx} \right)^{1/2} \tag{6.2}$$

where R is the hydraulic radius (cross-section divided by wetted perimeter; $R = r/2$ if the conduit is full), n' is the Manning roughness parameter, and dh/dx is the hydraulic head gradient.

Roughness parameter values for straight smooth pipes are not, in general, appropriate for meandering conduits beneath glaciers. Empirical studies (Röthlisberger, 1972; Nye, 1976; Clarke, 1982) have found that, for subglacial ice tunnels, the effects of roughness, sinuosity, and non-circular conduit shape lead to n' values of about 0.1 $m^{1/3}$ s. The head gradient that drives flow is sometimes approximated by using the average slope of the ice surface (e.g., Röthlisberger, 1972; Humphrey and others, 1986). This approximation fails in our case because, over short distances near the glacier terminus, the pressure and elevation components of the hydraulic head gradient are comparable in magnitude. For Trapridge Glacier, the average surface slope over the lower reaches of the glacier is about 7°. Assuming that the glacier is of uniform thickness in this region

and that the horizontal distance between our drilling area and the terminus is 500 m (a plausible estimate), the elevation loss over this distance is only 61 m, which is comparable to the 40–60 m water columns that we are considering. For the present analysis, we will assume that the head gradient has a constant value of 0.22 (61 m elevation head plus 50 m pressure head—the mean of the daily maximum and minimum water levels—divided by a distance of 500 m), considerably larger than the ~ 0.12 gradient obtained using the average surface slope.

The radius of the hypothetical conduit can be found by combining Equations (6.1) and (6.2):

$$r = \left[\frac{4^{1/3} n' \bar{Q}}{\pi} \left(\frac{dh}{dx} \right)^{-1/2} \right]^{3/8} . \tag{6.3}$$

For $\bar{Q} = 1.22 \times 10^{-2}\,\mathrm{m^3\,s}$, $n' = 0.1$, and $dh/dx = 0.22$, Equation (6.3) gives $r \approx 0.08\,\mathrm{m}$, so that the total cross-sectional area of flow is $A_T = 2.16 \times 10^{-2}\,\mathrm{m^2}$. Thus, a single conduit 16 cm in diameter could accommodate the daily crevasse discharge. The total flow cross-section might also be distributed over many smaller conduits. For example, the small seeps that discharge water in the walls of the Forefield Stream have diameters of roughly 0.5 cm. The cross-sectional area of a conduit of this size is $A_c = 1.96 \times 10^{-5}\,\mathrm{m^2}$, indicating that 1100 such conduits could account for the daily discharge.

Thus far, our analysis has shown that conduits of physically plausible size and number could accommodate the estimated daily input. It is conceivable that a single conduit of radius $r = 0.08\mathrm{m}$, carrying basal water and emerging from beneath the glacier, could escape notice—especially if it is hidden beneath fallen ice. It is more likely that smaller conduits, if they exist, would go unnoticed. However, there are a number of reasons for doubting that water is evacuated through a conduit system beneath the glacier: (1) The conduits would have to establish a route through or around the

frozen bed near the terminus. It is obvious how this might have happened during the 1990 release event, when the glacier was temporarily lifted by water at super-flotation pressures. It is not obvious how it could happen under more typical conditions. (2) Conduits would have to maintain hydraulic continuity over long distances—at least an order of magnitude longer than the "connectedness" length scales (tens of meters) that are suggested by our subglacial observations. Furthermore, if the conduits were routed along the ice-sediment interface, portions of the connections would have to be maintained at subfreezing temperatures. (3) Brief intervals of diurnal cycling indicate that surface meltwater reaches the bed irregularly, or at varying locations. Stable conduits require a water supply that is consistently sufficient to overcome inwardly creeping sediment and ice. On the other hand, unstable conduits require that the processes involved in creating passageways and establishing outlet connections are continually repeated.

Although these considerations are in no way conclusive, they support the view that basal water is not evacuated through conduits beneath the glacier. However, basal water might be evacuated through conduits in the glacier—englacial drainage has been inferred from dye studies on other glaciers (Hooke and others, 1988). On occasion, we have observed streams of water emerging from englacial conduits. These conduits were located in the ice cliff that forms the terminus and were approximately 10–20 cm in diameter, similar to the hypothetical conduits that we have been considering. In all likelihood, the englacial conduits that we have observed were probably being fed by meltwater flowing through interconnected crevasses at the surface; meltwater streams on the glacier surface are almost always captured by a crevasse before they reach the terminus. Nevertheless, we cannot dismiss the possibility that englacial conduits might also evacuate basal water. Connections between the basal drainage system and an englacial system could presumably form during incidents involving fracturing of basal ice, and could be sustained by an adequate discharge. Lacking sufficient throughflow,

connections in the cold ice would be expected to close quickly. Although englacial routing of basal water is a distinct possibility, the fact that dye is not routinely observed in the Forefield Stream suggests that it is not the primary mode of evacuation from the bed.

6.3.2.2 Groundwater flow

We have already suggested that winter drainage takes place through a thin ($\leq 1\,\mathrm{m}$), quasi-confining layer of matrix-rich till in direct contact with ice at the glacier sole. The hydraulic conductivity of this layer is thought to be $K \leq 3 \times 10^{-7}\,\mathrm{m\,s^{-1}}$. There is no reason to think that seepage through this upper layer ceases in summer. The question is, can the summer excess of basal water be evacuated through this layer?

Subglacial water flow through the upper till layer will obey Darcy's law:

$$q = \frac{\bar{Q}}{A} = -K\frac{dh}{dz} \tag{6.4}$$

where q is the specific discharge, A is the cross-sectional area perpendicular to the direction of flow, and dh/dz is the hydraulic head gradient across the layer. As previously mentioned, the sediments underlying the upper layer are thought to have a much higher degree of permeability. Thus, if water input to the underlying sediments only occurs across the lower boundary of the matrix-rich till layer, the hydraulic head at that lower boundary will be constant and equal to the elevation head at any given location. If we assume that the upper layer is 1.0 m thick and that water levels fluctuate between 40–60 m, the magnitude of the head gradient across the layer must also fluctuate between 40 and 60. To simplify further analysis, we will take the gradient across the low-permeability upper layer to have a constant value of $dh/dz = 50$.

If basal water is evacuated by vertical drainage through the upper till layer then Equation (6.4) indicates that the daily discharge $\bar{Q}$ from the idealized crevasse will be distributed over an area of the bed given by

$$A = -\frac{\bar{Q}}{K}\left(\frac{dh}{dz}\right)^{-1}. \tag{6.5}$$

Given a discharge $\bar{Q} = -1.22 \times 10^{-2}\,\mathrm{m^3\,s^{-1}}$ with $dh/dz = 50$, and assuming that $K = 3 \times 10^{-7}\,\mathrm{m\,s^{-1}}$, we find that the daily input would be evacuated through a cross-sectional area of $813\,\mathrm{m^2}$, corresponding to a circle of radius $\sim 16\,\mathrm{m}$. At sub-flotation pressures, it is doubtful that the water could be uniformly distributed over a continuous area of this size, since this would require extensive bed separation. Thus, the actual extent of the drainage region most likely would be greater than $813\,\mathrm{m^2}$. This size is plausible; hydraulic connections have been indicated between pressure sensors separated by more than 30 m, especially during periods of QSO. However, for reasons that we will now discuss, uniform drainage through widespread areas of low-permeability till is unlikely in summer.

An underlying assumption in the preceding calculation, which has not been explicitly stated, is that the upper till layer is a homogeneous porous medium. In reality, tills are heterogeneous (Clarke, 1987). For this reason, we have considered the possibility that hydraulic conductivity might be enhanced in localized regions of the matrix-rich till layer. Based on inversions of borehole response test data, we have estimated that, beneath Trapridge Glacier, the hydraulic conductivity of a 1.0 m thick, horizontal flow layer would be about $10^{-3}\,\mathrm{m\,s^{-1}}$ (Fig. 4.9). If we use this as our estimate for vertical flow in a region of enhanced conductivity, we find that an area of only $0.24\,\mathrm{m^2}$ could accommodate the daily input, corresponding to a circle of radius $\sim 0.3\,\mathrm{m}$. The same effect—reduction in areal extent of the drainage region—could also be produced by variations in layer thickness. For example, halving the thickness would double the gradient across the layer and, for a given discharge, would reduce the required evacuation

area by a factor of two. Furthermore, it is reasonable to expect that variations in the thickness of the upper could lead to regions of enhanced conductivity. For a given cross-sectional area, thinner parts of the layer will have larger gradients across them than the thicker parts and could, therefore, drive a greater discharge. An increased discharge, in turn, provides more opportunity for fine matrix material to be removed from the layer, thereby increasing the hydraulic conductivity. Thus, inhomogeneity and variations in the thickness of the upper till layer should lead to regions of preferential drainage beneath the glacier. We think that drainage through such regions is the primary mode of evacuation from the glacier bed in summer. Observations supporting this view are given in the following section.

6.3.3 The concept of "wormhole" drainage

It is inevitable that the upper till layer will have variable thickness and that hydraulic conductivity will not be uniform throughout the layer. These factors will tend to focus the evacuation of basal water through specific regions in the subglacial sediments. Clarke and others (1984) suggested that "preferred flow paths...might pass through the subsole material", in which case the drainage system morphology "would more closely resemble an aquifer". Christopher Smart (unpublished manuscript) has pointed out that permeable, sorted channel fills would provide significant drainage passageways in the subglacial till. For simplicity, we will use the term "wormholes" to refer to regions of preferrential drainage in the subglacial sediments; thus, in the present context, wormholes are simply expressions of variable thickness and inhomogeneity of the matrix-rich till layer.

As previously discussed, variations in layer thickness alone might lead to the creation of wormholes. It might also be possible for wormholes to form in the upper layer by the removal of very fine particles; because of the large gradients across this layer, a strong seepage force would be exerted on grains adjacent to the lower boundary,

making small particles having no downstream constriction prone to piping (Freeze and Cheery, 1979). Wormholes would tend to focus flow toward them, since they would be low-pressure regions. In turn, wormholes would be maintained by water flow through them, since fines could be flushed away, keeping flow passageways open. Wormholes could become plugged with matrix material if the water supply diminishes. They could also be destroyed by the deformation of basal sediments.

There are a number of lines of evidence supporting the idea that drainage through wormholes is the primary mode of evacuation during summer:

(1) Wormholes can explain how water can be evacuated from the central glacier bed during the summer without entering the forefield stream.

(2) The inferred sizes of wormholes (say $< 100\,m^2$) are plausible based on the scales of "connectedness" that we observe. We would expect that different wormholes drain different parts of the bed. Thus, water flow in one region is not necessarily influenced by water flow in another region. Also, wormholes would encourage the preservation of hydraulic barriers between sensors, since water input would be drained away locally instead of building up pressure to the point at which barriers would be breached. These consequences are consistent with the observation that pressure sensors in close proximity with each other often simultaneously show different behaviors.

(3) The forefield sedimentological record contains structures that could be relict wormholes. The discontinuous, sorted gravel lenses (Fig. 6.2) that are found in the lower parts of the matrix-rich till layer are an example of such structures. Three ancillary observations support this possibility: first, sorting within these lenses indicates that water flow took place through them; second, the high values of hydraulic conductivity that we have estimated from borehole response tests are consistent with those expected for gravel deposits; third, if they were to be preserved at all, we

would expect relict wormholes to be visible only in the lower part of the till layer, since deformation would likely have erased their upper portions.

(4) Wormholes could account for both QSO and QED signal types, as well as for the continuous transition between them. Well-formed, highly-transmissive wormholes would give rise to QSO, whereas less-transmissive wormholes would give rise to QED signals; travel paths to wormholes could be similar and the forcings could come from the same source, only the transmissive properties of the wormholes would be different.

(5) Wormholes represent sinks for subglacial water. Thus, they could explain the apparent upglacier components to water flow that are sometimes observed between hydraulically connected sensors.

(6) Wormholes would be stable only for brief periods of time, most likely being destroyed by deformation of the upper till layer; variations in both the rate and direction of basal deformation are known to take place (Blake, unpublished; Blake and others, 1992). This might explain why diurnal fluctuations usually persist only for short intervals.

(7) We would expect wormholes to be created only during the summer when excess meltwater is present at the bed, and that they would tend to be erased in winter. This is consistent with our observations that pressure rises early in the melt season, producing signals that decay slowly and without a diurnal signature. The sudden onset of diurnal fluctuations only occurs after surface meltwater has been at the bed for some time, presumably coinciding with the development of wormholes. We can speculate that the reason basal water pressures tend to become more uniform in winter is because wormholes have been erased; pore-pressures within the upper till layer would tend to slowly even out as inhomogeneity is reduced.

(8) Perhaps the strongest argument in favor of wormhole drainage is the fact that many details of our subglacial observations can be explained by processes that are likely

to occur beneath the glacier. Alternative modes of evacuation fail to explain one or more of the observations that we have just mentioned. For instance, conduit flow cannot easily account for apparent upglacier flow, nor the typical lack of dye in the forefield stream. On the other hand, given the same forcing, it would be difficult to produce the QSO–QED spectrum of diurnal fluctuations by seepage through a homogeneous low-permeability layer, even if such a layer were realistic.

6.3.4 Evacuation of subglacial water

Figure 6.4 summarizes our view of the ways by which water is evacuated from the central bed of Trapridge Glacier. In this figure we have shown the low-permeability layer (LPL), the underlying high-permeability layer (HPL), and the region of frozen bed (FB). A portion of the upper layer constitutes the deforming bed (DB) which must have zero thickness over the frozen region. (The actual shape of the deforming part of the layer is unknown and is simply shown as a triangle for convenience.) The volumes of water transported by each type of system are represented in a relative way by the thicknesses of the arrows (not by their number).

The "winter" mode of evacuation involves slow seepage through a fairly uniform low-permeability till layer and then faster transport through the underlying sediments, eventually entering a deep groundwater flow system. Slow seepage likely takes place on a year-round basis; however, it is probably incapable of evacuating all of the excess meltwater during summer. "Release event" and "englacial" evacuation modes, when they develop, are probably short-lived, since both systems require substantial and consistent throughflow to maintain passageways in cold ice. For the reasons listed above, "wormhole" drainage is thought to be the primary evacuation mode for subglacial water during the summer.

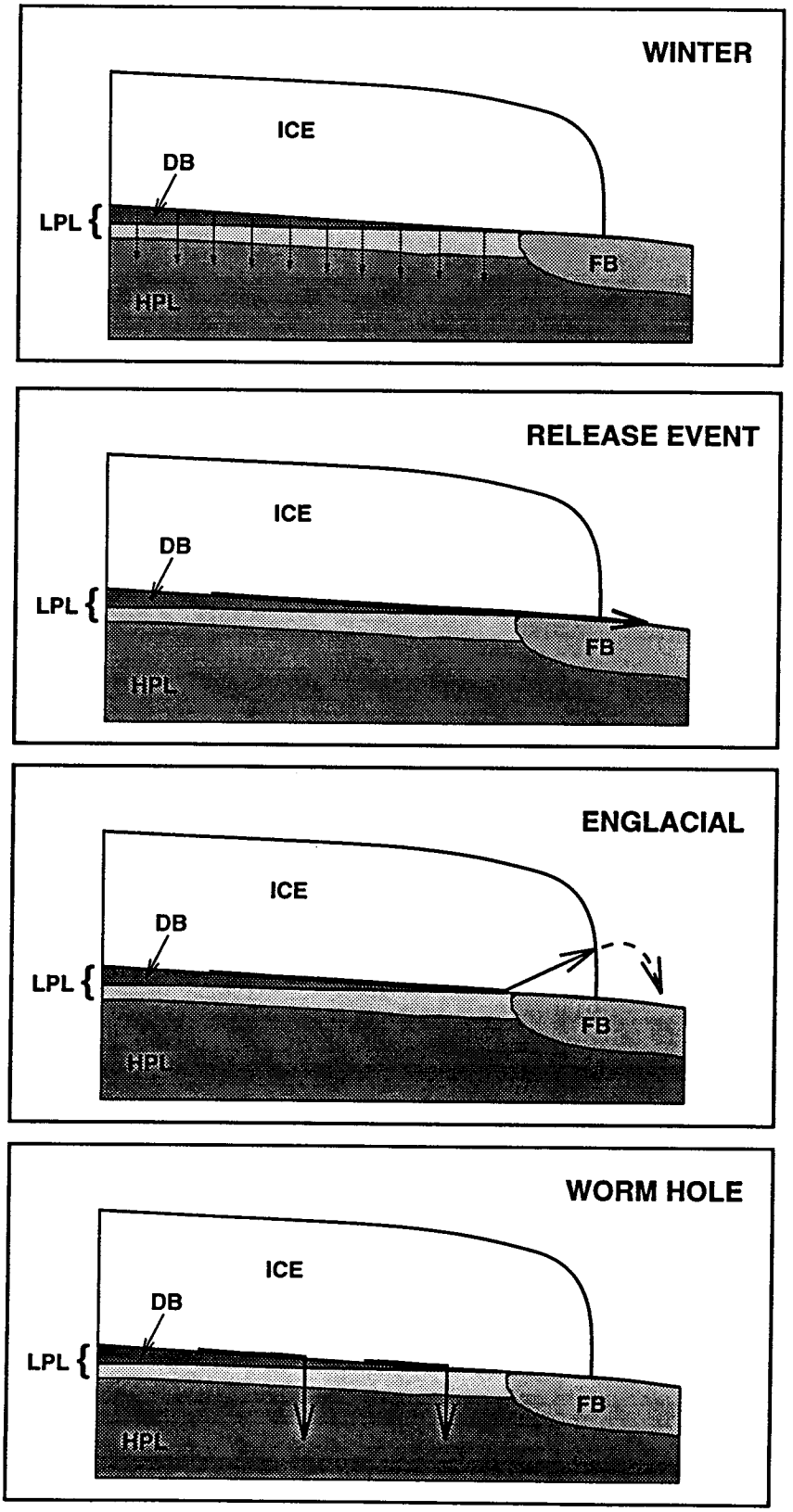

Fig. 6.4: Evacuation modes for basal water

6.3.5 How water moves at the bed

We now turn to the question of how water might be transported along the bed, from regions of meltwater input to wormholes. Several theoretical studies (Shoemaker, 1986; Shoemaker and Leung, 1987; Boulton and Hindmarsh, 1987; Clarke, 1987; Alley, 1989, 1992; Walder and Fowler, 1992) have considered the nature of water flow beneath a glacier or ice sheet that rests on deformable sediments. In general, it is agreed that water from channelized sources will remain in channels beneath the glacier, rather than spread out over the bed. For glaciers having surface meltwater connections to their beds, distributed sources—such as basal melting—represent small volume inputs and are typically neglected.

The study of Walder and Fowler (1992) applies most directly to our situation. Accounting for factors involved in maintaining ice/sediment conduits—inward creep of ice and sediments, ice melt, and sediment erosion—Walder and Fowler found that two distinctly different conduit morphologies could exist subglacially. Adopting their terminology, "channels" have a semi-circular cross-section extending up into the ice and form an arborescent network, much like a traditional R-channel system. "Canals" on the other hand, are wide and shallow and have little upward extension into the ice. Canals will not be organized in a stationary arborescent network; instead they will form a moving distributed system which resembles the constantly shifting geometry of braided alluvial streams. Figure 6.5 illustrates the distinction between an arborescent (dendritic) network and a distributed (braided) network.

According to Walder and Fowler, channel networks are favored when the effective pressure (the difference between ice-overburden and subglacial water pressures) is high and when the hydraulic gradient, approximated by the slope of the glacier surface, is significant (say, ≥ 0.1). Conversely, networks of canals exist under conditions of low effective pressure and small hydraulic gradients. The cohesiveness of the subglacial sediments also plays an important role. Cohesive sediments, such as clays, can maintain

steep banks and are, therefore, conducive to the formation of channels. Non-cohesive sediments, on the other hand, are favorable to the formation of canals. Although subglacial tills typically have a matrix rich in clay and silt-sized grains, the sand and gravel components "will most likely cause the canal to evolve towards a broad, shallow shape" (Walder and Fowler, 1992).

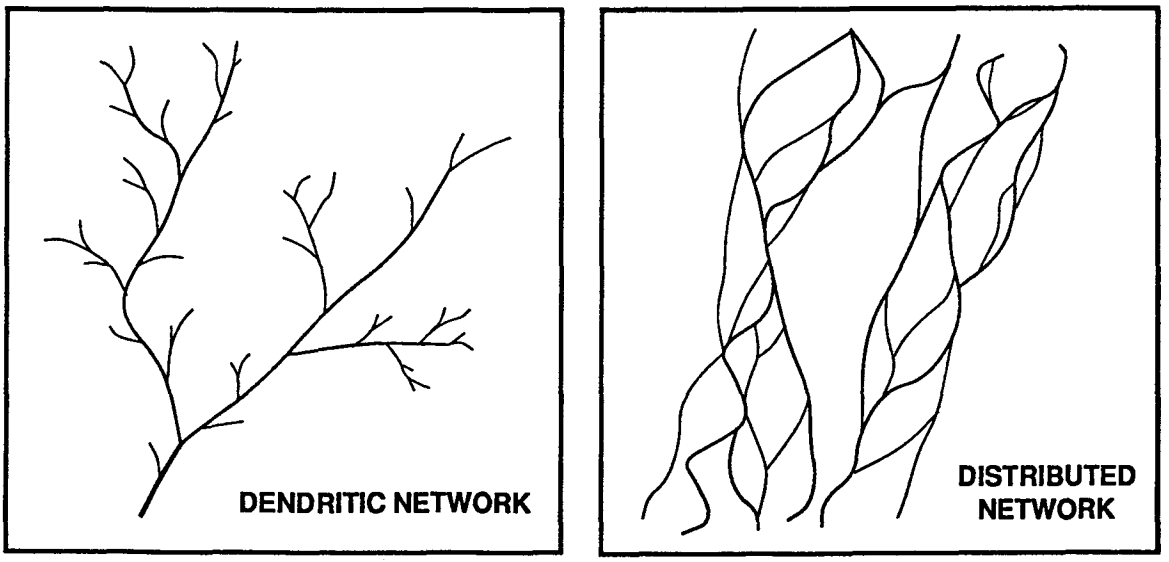

Fig. 6.5: Different drainage networks: dendritic and distributed

For surface slopes characteristic of valley glaciers, a channel network would be expected to form, since, for sufficiently long glaciers, the surface slope is an adequate approximation of the longitudinal hydraulic gradient. However, this expectation is founded on the premise that there is an outlet for basal water at the terminus. For Trapridge Glacier, there is strong evidence that basal water does not exit the glacier at the terminus (ignoring release events), in which case the surface slope does not serve as an adequate approximation of the hydraulic gradient. In the few instances when we can justifiably compute gradients from pressure measurements under normal conditions, we obtain values on the order of 10^{-2} or less. Such small gradients, in combination with

the high basal water pressures (low effective pressures) that we often observe, suggest that basal water should flow through a distributed canal network beneath Trapridge Glacier. (We will discuss the special situation of flow near a wormhole in the next section.)

The shifting geometry of a braided system is in accord with the "on-again/off-again" behavior that we observe with pressure, turbidity, and electrical conductivity sensors. Changing canal positions could leave sensors isolated and then, sometime later, reestablish hydraulic connections. This might explain why diurnal fluctuations sometimes suddenly cease at a particular location, even when surface meltwater continues to be generated daily. A distributed network of meandering canals also complements our picture of wormhole drainage. Input from a single source could be evacuated by wormholes in several different locations, and each wormhole would correspond to the subglacial termination of a particular set of canals. Although canals would be relatively open passageways, clasts that could not be mobilized by flowing water would obstruct the passages, providing additional hydraulic resistance. The sorted gravel lenses in the matrix-rich upper till layer are evidence of clast-obstructed flow passageways.

6.3.5.1 Pattern of water flow near a wormhole

We have reasoned that subglacial water should flow from a source region to a wormhole through a distributed network of broad, shallow canals. However, near a wormhole it is likely that the distributed canals will coalesce into a smaller number of channel-like passageways, forming a more-stable and centralized flow system (Fig. 6.6). There are two reasons for this. First, wormholes form low-pressure regions of the bed. The reduced pressure in these regions will not be felt far from the wormholes, but will be increasingly felt as they are approached. Thus, the hydraulic gradient is increased in the vicinity of a wormhole. Lowering basal water pressure and increasing hydraulic gradient are both conditions that are conducive to channel formation. Second, during

their life-span, wormholes are probably fairly stationary. Thus, channels directing flow into wormholes will have a greater opportunity to be eroded into preferred passageways.

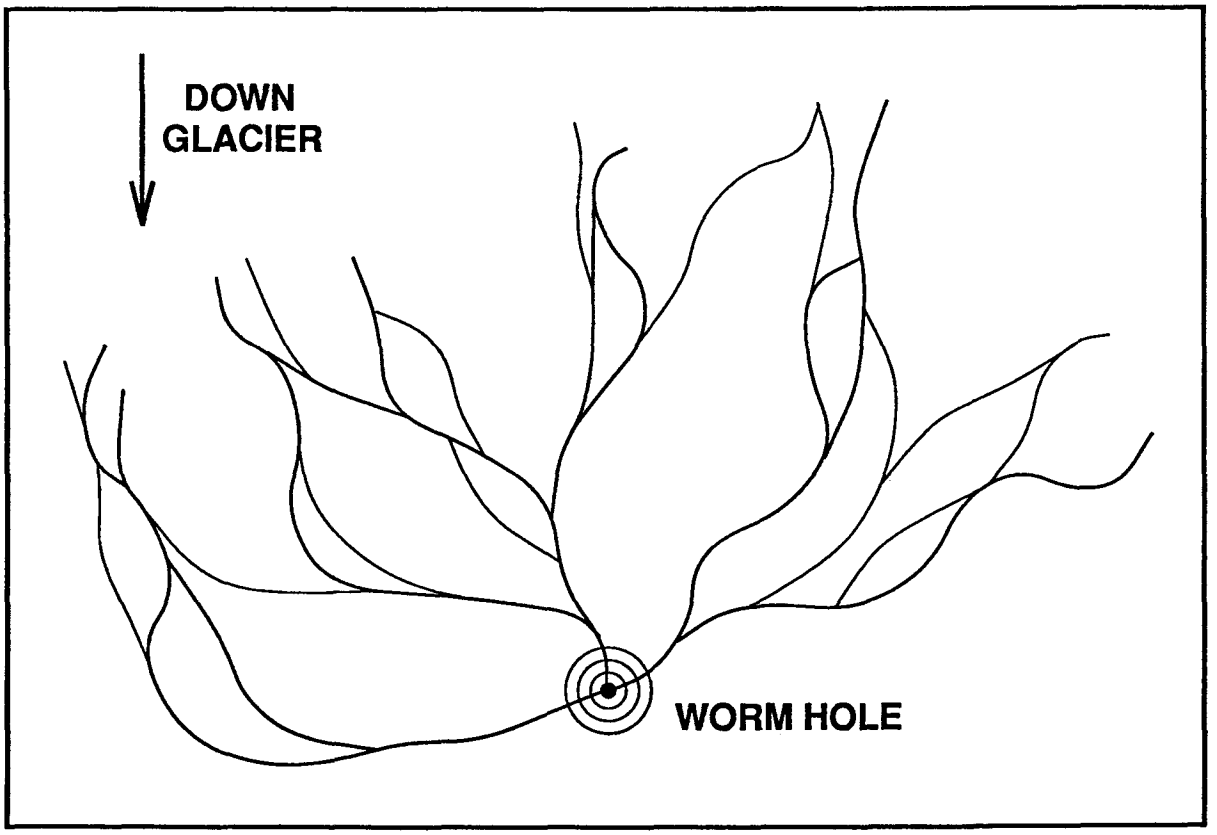

Fig. 6.6: Pattern of water flow near a wormhole

6.4 Summary of drainage system behavior

The following statements summarize major features and annual behavior of the pre-surge drainage system beneath Trapridge Glacier:

(1) In summer, surface meltwater reaches the bed. This water is sometimes temporarily stored at the bed before it is evacuated. Storage occurs because there are no direct connections to subaerial outlets and because the low-permeability till layer immediately below the ice is quasi-confining. Limited and irregular meltwater supply to the bed has a strong influence on the basal hydrology.

(2) Water that reaches the bed during summer is most likely evacuated through outlet regions of enhanced transmissivity in the low-permeability till layer. Eventually this water enters a deep groundwater flow system.

(3) Subglacial water flow passageways migrate over the bed. Water is most likely transported from regions of meltwater input to drainage outlets through broad, shallow canals. The canals branch into distributary networks forming a braided pattern. Canal meandering causes the network of hydraulic connections between different parts of the bed to continually change. Connections between regions of input and evacuation can open and close rapidly (a few hours), and are rarely maintained for more than a few days.

(4) The basal hydraulic system sometimes undergoes profound and rapid reorganizations, leading to the release of stored basal water into outlet streams. Release events occur when the existing subglacial drainage system is insufficient to accommodate a sudden water input.

(5) In winter, there is little, if any, meltwater input. However, there are indications of mid-winter hydraulic activity, presumably in response to mechanical forcings by the glacier. Morphological changes take place throughout the winter and gradually reduce the drainage system's capacity.

(6) High basal water pressures result when surface meltwater first reaches the bed in early summer. The high pressures—often locally exceeding the ice overburden pressure—encourage lateral water migration and the opening of hydraulic connections between larger areas of the bed. The net result is an increase in basal water storage.

(7) At some point during the summer, outlet connections are established and the stored water is evacuated. Diurnal fluctuations in basal water pressure—characteristic of summer conditions—indicate that an effective drainage system develops following the opening of subglacial outlets.

6.5 Concluding remarks

In the preceding discussion we formed a conceptual model of subglacial drainage on a year-round basis for Trapridge glacier. To the extent that they have been identified, general patterns and important features of our data can be explained by the model. Furthermore, the model is based on a realistic picture of the subglacial environment, and on processes that are likely to occur there. On these merits, our interpretations seem reasonable.

Normal summer drainage, as we have described it, is consistent with our borehole response theory. A network of broad, shallow canals, terminating in one or more highly-conductive regions of the upper till layer, constitutes a distributed flow system. In our theory, distributed systems are effectively characterized by estimating the properties that would produce hydraulically equivalent behavior in a uniform porous medium.

In reality, the hydraulic conductivity of the actual system depends on the conductances and path lengths of individual parts of the system—the flow path along the bed and the flow path through the bed. For normal summer drainage, we expect the system to be fairly transmissive, since the path along the bed likely offers little resistance to flow (high conductance) and the path through the upper till layer is probably short. This expectation is supported by transmissivity estimates from borehole response tests.

As a final remark, we point out that borehole response testing has established that a highly transmissive flow system exists beneath Trapridge Glacier. At the same time, measurements of subglacial water properties demonstrate that basal water exists in hydraulically isolated regions of the bed, and dye studies indicate that this water typically does not exit the glacier at the terminus. The paradox created by these apparently conflicting aspects of the subglacial drainage system can easily be understood in terms of our conceptual model.

Chapter 7

SUMMARY OF CONCLUSIONS

In this thesis we have described an investigation of the basal hydraulic system of Trapridge Glacier, a surge-type glacier currently in the late quiescent phase. Because it is a surge-type glacier, the basal drainage system is of special interest; rapid sliding motion that takes place during a surge is thought to be facilitated by disabling the subglacial drainage network. To comprehend why and how such disabling can occur, we must first understand the basic nature of subglacial water flow under non-surging conditions. This study has identified fundamental aspects of the pre-surge drainage system beneath Trapridge Glacier.

The fact that Trapridge Glacier rests on a sediment bed also makes the study of its basal drainage system of interest. Traditional theories of glacier sliding and glacier hydrology build on the premise that basal water flows at the contact between clean ice and impermeable bedrock (Weertman, 1964; Lliboutry, 1968; Kamb, 1970; Röthlisberger, 1972; Nye, 1973; Walder, 1986; Kamb, 1987). For many glaciers this is clearly not the case, and it is now accepted that subglacial debris layers have an important involvement in the sliding of both normal and surging glaciers (Raymond, 1987). The issue of basal water flow in the presence of subglacial sediment has been addressed theoretically by others; however, there are very few data available to guide such discussions. The detailed and long-term observations presented in this thesis provide a framework for current and future discussions of water drainage beneath sediment-based glaciers.

We have taken two different approaches to characterizing the water drainage system beneath Trapridge Glacier: (1) borehole response testing and (2) direct measurements of the properties of subglacial water. In the following paragraphs we summarize the principal conclusions and significant aspects of this research.

7.1 Borehole response testing

Borehole response testing provides estimates of the hydraulic properties of subglacial drainage systems. The basic procedures that we have used are not new—borehole connections have been recorded on other glaciers and ice streams (e.g., Hodge, 1976; Engelhardt, 1978; Engelhardt and others, 1990a), and slug and packer tests are widely used in groundwater studies. However, these techniques have not previously been used to estimate the hydraulic properties of subglacial sediments.

A necessary step for glaciological application of response testing was the development of a borehole–drainage system model that included high-gradient test conditions; standard models, such as those used in groundwater hydrology, do not account for the effects of turbulent flow. These effects can be important for highly-transmissive systems under the high-gradient conditions brought about by hydraulic testing. Our development, given in Chapter 3, includes turbulent effects, and thus leads to new theoretical refinements.

We have shown that our borehole response model can be applied to a variety of distributed drainage systems. As such, it is potentially useful for many wet-based glaciers. We have also pointed out that the distribution of basal hydraulic properties can be quantified by applying our model to many different response tests. This approach is useful for understanding the heterogeneous attributes of subglacial drainage systems.

In Chapter 4 we presented an inversion methodology that is based on our borehole response model. The methodology that we described contributes significantly to the

practice of estimating subglacial hydraulic properties from response test data. Thus, we have shown that inversion should be an integral part of the overall procedure. We have used this method to invert response test data from Trapridge Glacier. Inversions of connection-drainage and slug test data have been extremely successful, and we infer from this that the model comes close to accurately characterizing the basal hydraulic system. Inversions of packer test data were less successful, and we suggest that the additional complexities involved in packer tests renders them less useful than either drainage observations or slug tests.

Inversions of response test data have provided estimates of hydraulic properties in the basal regions in which the tests were performed. Based on these estimates, and the inferred accuracy of the model, we have reached the following conclusions: (1) In response to sudden pressure disturbances, water flow at the glacier sole is concentrated in a hydraulically confined sediment layer (or at least it can be effectively characterized by such a representation); (2) The transmissivity of the flow layer is approximately 3–$30\times10^{-4}\,\mathrm{m^2\,s^{-1}}$; (3) The flow layer must be fairly thin ($\leq 0.1\,\mathrm{m}$), since the hot-water drill does not penetrate deeply into the bed. In this case, transmissivity estimates suggest that the flow layer is comprised of coarse sand or fine gravel. We have also discovered that flow layer compressibility estimates are variable and are largest when estimated from slug test data.

7.2 Measurement of subglacial water properties

As a second approach to characterizing the subglacial drainage system, we have measured water pressure, turbidity, and electrical conductivity directly at the bed of Trapridge Glacier. Turbidity and conductivity were measured with new subglacial sensors that were designed and constructed as part of this research. Measurements were made at intervals ranging from 2–20 minutes for three consecutive years; at present, these observations comprise the only *in situ* multi-year record of the behavior of a subglacial

hydraulic system. Interpretation of the data presented in this thesis has led to a qualitative description of the basal drainage system.

In winter it is reasonable to suspect that basal water is evacuated by slow seepage through subglacial sediments. Sources of meltwater in winter are limited to geothermal melting and friction; these are expected to generate only small fluxes which could easily be accommodated, even by low-permeability sediment. During the summer melt season, we have reasoned that basal water moves along the bed in a distributed network of meandering "canals". The presence of a low-permeability till layer immediately beneath the glacier constrains canals to carry water at the ice–till interface. However, cold ice and frozen bed at the glacier margin inhibits basal water from exiting at the terminus. As a working hypothesis, we have suggested that, during summer, basal water is primarily evacuated from the bed through regions of enhanced transmissivity in the subglacial sediments, eventually entering a deep groundwater system. "Wormholes", as we have called these regions, correspond to areas of reduced thickness and/or increased conductivity in the upper-most till layer.

Our hypothesis suggests lines for future work: (1) prospecting for and careful mapping of wormholes, both subglacially and in the forefield, (2) observation of wormhole creation and evolution—an obvious question is whether wormholes are sometimes artificially created by drilling, (3) analysis of the potential interactions between wormholes and the deformation of subglacial sediments, (4) analysis of the ways in which wormholes could be prevented from forming, thereby promoting surge conditions.

In discussing our data we have pointed out that several factors govern the basal hydrology: glacial thermal regime, basal geology, meltwater supply, discharge capacity, sediment movement, and mechanical interactions with the overlying ice. It is the combined influences of all of these factors that ultimately determines the complex nature of subglacial water flow. In this thesis we have described the basal drainage system in terms of the morphologies of specific drainage states; for example, winter, release

event, and wormhole evacuation modes. By showing how basal processes can interact to bridge between these specific states, we have broadened our description into a realistic, conceptual model of subglacial drainage.

7.3 Final remarks

In summary, this research contributes to the understanding of subglacial drainage in the presence of a sediment bed in the following ways: (1) From a *theoretical* standpoint, we have developed borehole response testing as a tool for assessing subglacial hydraulic properties. Estimates of these properties constrain the types of geologic materials and system configurations that could be responsible for regulating basal water flow. We have shown that our theory can be applied to a wide range of basal flow conditions. (2) In terms of *instrumentation*, we have developed inexpensive and reliable sensors for directly monitoring subglacial water quality. Measurements made with these sensors can provide information about the direction and rate of basal water flow, and can be used to distinguish between inputs of fresh surface meltwater and "old" water that has been stored at the bed. This information also places constraints on the flow system configuration. Thus, the two approaches—borehole response testing and direct measurement of subglacial water properties—provide independent means for assessing possible drainage system morphologies. (3) From an *observational* point of view, we have provided the first year-round records of the behavior of a subglacial hydraulic system based on measurements made directly at the bed. Such data are essential for testing and refining existing theories of basal water flow. (4) From a *conceptual* standpoint, we have developed a realistic model of how water might drain from beneath Trapridge Glacier prior to a surge. This model is potentially applicable for other glaciers having similar thermal regimes and sediment substrates. The model also sets a framework for considering why and how the drainage system could become disabled and bring about the conditions necessary for a surge.

REFERENCES

Alley, R. B. 1989. Water-pressure coupling of sliding and bed deformation: I. water system *J. Glaciol.*, **35**(119), 108–118.

Alley, R. B. 1992. How can low-pressure channels and deforming tills coexist subglacially? *J. Glaciol.*, **38**(128), 200–207.

Alley, R. B., D. D. Blankenship, C. R. Bentley, and S. T. Rooney. 1986. Deformation of till beneath Ice Stream B, West Antarctica. *Nature*, **322**(6074), 57–59.

Bear, J. 1972. *Dynamics of fluids in porous media*, New York, American Elsevier.

Bear, J. and A. Verruijt. 1987. *Modeling groundwater flow and pollution*, Dordrecht, D. Reidel.

Behrens, H., H. Bergmann, H. Moser, W. Ambach, and O. Jochum. 1975. On the water channels of the internal drainage system of the Himtereisferner, Ötzal Alps, Austria. *J. Glaciol.*, **14**(72), 375–382.

Biot, M. A. 1941. General theory of three-dimensional consolidation. *J. Appl. Phys.*, **12**(2), p. 155–164.

Biot, M. A. 1955. Theory of elasticity and consolidation for a porous anisotropic solid. *J. Appl. Phys.*, **26**(2), p. 182–185.

Bird, R. B., W. E. Stewart, and E. N. Lightfoot. 1960. *Transport phenomena*, New York, John Wiley and Sons.

Blake, E. W. Unpublished. The deforming bed beneath a surge-type glacier: measurement of mechanical and electrical properties. (Ph.D. thesis, University of British Columbia, 1992.)

Blake, E. W. and G. K. C. Clarke. 1992. Interpretation of borehole–inclinometer data: a general theory applied to a new instrument. *J. Glaciol.*, **38**(128), 113–124.

Blake, E., G. K. C. Clarke, and M. C. Gérin. 1992. Tools for examining subglacial bed deformation. *J. Glaciol.*, **38**(130), 388–396.

Blankenship, D. D., C. R. Bentley, S. T. Rooney, and R. B. Alley. 1986. Seismic measurements reveal a saturated porous layer beneath an active Antarctic ice stream. *Nature*, **322**(6074), 54–57.

Bliss, J. 1983. *Motorola optoelectronics device data*, Phoenix, AZ, Motorola.

Boulton, G. S. and A. S. Jones. 1979. Stability of temperate ice caps and ice sheets resting on beds of deformable sediment. *J. Glaciol.*, **24**(90), 29–43.

Boulton, G. S. and R. C. A. Hindmarsh. 1987. Sediment deformation beneath glaciers: rheology and geological consequences. *J. Geophys. Res.*, **92**,(B9), 9059–9082.

Bracewell, R. N. 1978. *The Fourier transform and its applications*, New York, McGraw-Hill.

Bredehoeft, J. D., H. H. Cooper, and I. S. Papadopulos. 1966. Inertial and storage effects in well–aquifer systems: an analog investigation. *Water Resour. Res.*, **2**(4), 697–707.

Brugman, M. M. Unpublished. Water flow at the base of a surging glacier. (Ph.D. thesis, California Institute of Technology, 1986.)

Burkimsher, M. 1983. Investigations of glacier hydrological systems using dye-tracer techniques: observations at Pasterzengletscher, Austria. *J. Glaciol.*, **29**(103), 403–416.

Campbell Scientific. 1989. *CR10 measurement and control module operator's manual*, Logan, UT, Campbell Scientific.

Carman, P. C. 1956. *Flow of gases through porous media*, London, Butterworths Scientific.

Clarke, G. K. C. 1982. Glacier outburst floods from "Hazard Lake", Yukon Territory, and the problem of flood magnitude prediction. *J. Glaciol.*, **28**(98), 3–21.

Clarke, G. K. C. 1987. Subglacial till: a physical framework for its properties and processes. *J. Geophys. Res.*, **92**,(B9), 9023–9036.

Clarke, G. K. C. 1991. Length, width, and slope influences on glacier surging. *J. Glaciol.*, **37**(126), 236–246.

Clarke, G. K. C. and E. W. Blake. 1991. Geometric and thermal evolution of a surge-type glacier in its quiescent state: Trapridge Glacier, Yukon Territory, Canada, 1969–89. *J. Glaciol.*, **37**(125), 158–169.

Clarke, G. K. C., S. G. Collins, and D. E. Thompson. 1984. Flow, thermal structure, and subglacial conditions of a surge-type glacier. *Can. J. Earth Sci.*, **21**(2), 232–240.

Clarke, G. K. C., J. P. Schmok, C. S. L. Ommanney, and S. G. Collins. 1986. Characteristics of surge-type glaciers. *J. Geophys. Res.*, **91**(B7), 7165–7180.

Collins, D. N. 1979. Quantitative determination of the subglacial hydrology of two alpine glaciers. *J. Glaciol.*, **23**(89), 347–362.

Cooper, H. H. 1966. The equation of groundwater flow in fixed and deforming coordinates. *J. Geophys. Res.*, **71**(20), 4785–4790.

Cooper, H. H., J. D. Bredehoeft, I. S. Papadopulos, and R. R. Bennett. 1965. The response of well–aquifer systems to seismic waves. *J. Geophys. Res.*, **70**(16), 3915- -3926.

Cooper, H. H., J. D. Bredehoeft, and I. S. Papadopulos. 1967. Response of a finite-diameter well to an instantaneous charge of water. *Water Resour. Res.*, **3**(1), 263–269.

de Marsily, G. 1986. *Quantitative hydrogeology*, San Diego, Academic Press.

De Wiest, R. J. M. 1966. On the storage coefficient and the equations of groundwater flow. *J. Geophys. Res.*, **71**(4), 1117–1122.

Engelhardt, H. 1978. Water in glaciers: observations and theory of the behaviour of water levels in boreholes. *Z. Gletscherkd. Glazialgeol.*, Bd. 14, Ht. 1, 35–60.

Engelhardt, H., N. Humphrey, and B. Kamb. 1990a. Borehole geophysical observations on Ice Stream B, Antarctica. *Antarct. J. U.S.*, **25**(5), 80–82.

Engelhardt, H., N. Humphrey, B. Kamb, and M. Fahnestock. 1990b. Physical conditions at the base of a fast moving Antarctic ice stream. *Science*, **248**(4951), 57–59.

Ergun, S. and A. A. Orning. 1949. Fluid flow through randomly packed columns and fluidized beds. *Ind. Eng. Chem.*, **41**(6), 1179–1184.

Fountain, A. G. 1992. Subglacial water flow inferred from stream measurements at South Cascade Glacier, Washington, U.S.A. *J. Glaciol.*, **38**(128), 51–64.

Francis, J. R. D. 1975. *Fluid mechanics for engineering students*, London, Edward Arnold.

Freeze, R. A. and J. A. Cherry. 1979. *Groundwater*, Englewood Cliffs, Prentice–Hall.

Gambolati, G. and R. A. Freeze. 1973. Mathematical simulation of the subsidence of Venice. *Water Resour. Res.*, **9**(3), 721–733.

Gregory, J. 1985. Turbidity fluctuations in flowing suspensions. *J. Colloid Interface Sci.*, **105**(2), 357–371.

Hach, C. C., R. D. Vanous, and J. M. Heer. 1990. Understanding turbidity measurement. *Technical Information Series - Booklet No. 11*, Loveland, CO, Hach Company.

Hairer, E. and G. Wanner. 1991. *Solving ordinary differential equations II: stiff and differential-algebraic problems*, Berlin, Springer-Verlag.

Hamilton, G. S. Unpublished. Investigations of surge-type glaciers in Svalbard. (Ph.D. thesis, University of Cambridge, 1992.)

Harvey, C. F. 1992. What does a slug test measure in a heterogeneous aquifer? *EOS (Trans. Am. Geophys. Union)*, **73**(43), 215.

Henderson, F. M. 1966. *Open channel flow*, New York, Macmillan.

Hodge, S. M. 1976. Direct measurement of basal water pressures: a pilot study. *J. Glaciol.*, **16**(74), 205–218.

Hodge, S. M. 1979. Direct measurement of basal water pressures: progress and problems. *J. Glaciol.*, **23**(89), 309–319.

Hooke, R. LeB., S. B. Miller, and J. Kohler. 1988. Character of the englacial and subglacial drainage system in the upper part of the ablation area of Storglaciären, Sweden. *J. Glaciol.*, **34**(117), 228–231.

Hooke, R. L., P. Calla, P. Holmlund, M. Nilsson, and A. Stroeven. 1989. A 3 year record of seasonal variations in surface velocity, Storglaciären, Sweden. *J. Glaciol.*, **35**(120), 235–247.

Horowitz, P. and W. Hill. 1989. *The art of electronics*, Cambridge, Cambridge University Press.

Humphrey, N., C. Raymond, and W. Harrison. 1986. Discharges of turbid water during mini-surges of Variegated Glacier, Alaska, U.S.A. *J. Glaciol.*, **32**(111), 195–207.

Hunter, S. C. 1983. *Mechanics of continuous media*, Chichester, Ellis Horwood.

Iken, A. 1972. Measurements of water pressure in moulins as part of a movement study of the White Glacier, Axel Heiberg Island, Northwest Territories, Canada. *J. Glaciol.*, **11**(61), 53–58.

Iken, A. and R. A. Bindschadler. 1986. Combined measurements of subglacial water pressure and surface velocity of Findelengletscher, Switzerland: conclusions about drainage systems and sliding mechanism. *J. Glaciol.*, **32**(110), 101–119.

Iken, A., H. Röthlisberger, A. Flotron, and W. Haeberli. 1983. The uplift of Unteraargletscher at the beginning of the melt season—a consequence of water storage at the bed? *J. Glaciol.*, **29**(101), 28–47.

Jacob, C. E. 1940. On the flow of water in an elastic artesian aquifer. *Trans. Am. Geophys. Union*, **21**, 574- -586.

Jarvis, G. T. and G. K. C. Clarke. 1974. Thermal effects of crevassing on Steele Glacier, Yukon Territory, Canada. *J. Glaciol.*, **13**(68), 243–254.

Jones, G. and B. C. Bradshaw. 1933. The measurement of the conductance of electrolytes. V. A redetermination of the conductance of standard potassium chloride solutions in absolute units. *J. Am. Chem. Soc.*, **55**, 1780–1800.

Kabala, Z. J., G. F. Pinder, and P. C. D. Milly. 1985. Analysis of well–aquifer response to a slug test. *Water Resour. Res.*, **21**(9), 1433–1436.

Kahaner, D., C. Moler, and S. Nash. 1989. *Numerical methods and software*, Englewood Cliffs, Prentice–Hall.

Kamb, B. 1970. Sliding motion of glaciers: theory and observation. *Rev. Geophys. Space Phys.*, **8**(4), 673- -728.

Kamb, B. 1987. Glacier surge mechanism based on linked cavity configuration of the basal water conduit system. *J. Geophys. Res.*, **92**(B9), 9083–9100.

Kamb, B. and H. Engelhardt. 1987. Waves of accelerated motion in a glacier approaching surge: the mini-surges of Variegated Glacier, Alaska, U.S.A. *J. Glaciol.*, **33**(113), 27–46.

Kamb, B., C. F. Raymond, W. D. Harrison, H Engelhardt, K. A. Echelmeyer, N. Humphrey, M. M. Brugman, and T. Pfeffer. 1985. Glacier surge mechanisms: 1982–83 surge of Variegated Glacier, Alaska. *Science*, **227**(4686), 469–479.

Kay, J. M. and R. M. Nedderman. 1985. *Fluid mechanics and transfer processes*, Cambridge, Cambridge University Press.

Kerker, M. 1969. *The scattering of light and other electromagnetic radiation*, New York, Academic Press.

Kipp, K. L. 1985. Type curve analysis of inertial effects in the response of a well to a slug test. *Water Resour. Res.*, **21**(9), 1397–1408.

Krauss, I. 1977. *In* H. J. Morel-Seytoux, ed., *Surface and subsurface hydrology. Proceedings of the Fort Collins 3rd International Hydrology Symposium*, Fort Collins, Colo., Water Resources Publications.

Krimmel, R. M., W. V. Tangborn, and M. F. Meier. 1973. Water flow through a temperate glacier. *Inter. Assoc. Hydrologic Sci.*, Pub. 107, 401–416.

Lliboutry, L. 1958. Contribution à la théorie du frottement des glaciers sur leur lit. *C.R. Hebd. Séances Acad. Sci.*, Ser. D **247**, 318–320.

Lliboutry, L. 1968. General theory of subglacial cavitation and sliding of temperate glaciers. *J. Glaciol.*, **7**(49), 21–58.

MacAyeal, D. R. 1992. The basal stress distribution of Ice Stream E, Antarctica, inferred by control methods. *J. Geophys. Res.*, **97**(B1), 595–603.

MacAyeal, D. R., J. Firestone, and E. Waddington. 1991. Paleothermometry by control methods. *J. Glaciol.*, **37**(127), 326–338.

Mathews, W. H. 1964. Water pressure under a glacier. *J. Glaciol.*, **5**(38), 235–240.

McElwee, C. D., J. J. Butler Jr., and G. C. Bohling. 1992. Nonlinear analysis of slug tests in highly-permeable aquifers using a Hvorslev-type approach. *EOS (Trans. Am. Geophys. Union)*, **73**(43), 164.

Meier, M. F. and A. Post 1969. What are glacier surges? *Can. J. Earth Sci.*, **6**(4), 807–817.

Melik, D. H. and H. S. Fogler. 1983. Turbidimetric determination of particle size distributions of colloidal systems. *J. Colloid Interface Sci.*, **92**(1), 161- -180.

Menke, W. 1989. *Geophysical data analysis: discrete inverse theory*, San Diego, Academic.

Nye, J. F. 1973. Water at the bed of a glacier. *Publication No. 95 de l'Association Internationale d'Hydrologie*, (Symposium on the Hydrology of Glaciers, Cambridge, 7-13 September 1969), 189–194.

Nye, J. F. 1976. Water flow in glaciers: jokulhlaups, tunnels and veins. *J. Glaciol.*, **17**(76), 181–207.

Papadopulos, I. S., J. D. Bredehoeft, and H. H. Cooper. 1973. On the analysis of slug test data. *Water Resour. Res.*, **9**(4), 1087–1089.

Paterson, W. S. B. 1981. *The physics of glaciers.* Oxford, Pergamon Press.

Pilgrim, D. H., D. D. Huff, and T. D. Steele. 1979. Use of specific conductance and contact time relations for separating flow components in storm runoff. *Water Resour. Res.*, **15**(2), 329–339.

Post, A. S. 1969. Distribution of surging glaciers in western North America. *J. Glaciol.*, **8**(53), 229–240.

Prandtl, L. 1952. *Essentials of fluid dynamics*, New York, Hafner.

Press, W. H., B. P. Flannery, S. A. Teukolsky, and W. T. Vetterling. 1986. *Numerical recipes*, Cambridge, Cambridge University Press.

Raymond, C. F. 1987. How do glaciers surge? A review. *J. Geophys. Res.*, **92**(B9), 9121–9134.

Rice, J. R. and M. P. Cleary. 1976. Some basic stress diffusion solutions for fluid-saturated elastic porous media with compressible constituents. *Rev. Geophys. Space Phys.*, **14**(2), 227–241.

Röthlisberger, H. 1972. Water pressure in intra- and subglacial channels. *J. Glaciol.*, **11**(62), 177–203.

Schiesser, W. E. 1991. *The numerical method of lines*, San Diego, Academic.

Schofield, A. and P. Wroth. 1968. *Critical state soil mechanics*, London, McGraw–Hill.

Seaberg, S. Z., J. Z. Seaberg, R. LeB. Hooke, and D. W. Wiberg. 1988. Character of the englacial and subglacial drainage system in the lower part of the ablation area of Storglaciären, Sweden, as revealed by dye-trace studies. *J. Glaciol.*, **34**(117), 217–227.

Sharp, R. P. 1943. Geology of the Wolf Creek area, St. Elias Range. *Bul. Geol. Soc. Amer.*, **54**, 625–650.

Sharp, R. P. 1947. The Wolf Creek glaciers, St. Elias Range, Yukon Territory. *Geog. Rev.*, **37**(1), 26–52.

Sharp, R. P. 1951. Glacial history of Wolf Creek, St. Elias Range, Canada. *J. Geol.*, **59**(2), 97–117.

Shoemaker, E. M. 1986. Subglacial hydrology for an ice sheet resting on a deformable aquifer. *J. Glaciol.*, **32**(110), 20–30.

Shoemaker, E. M. and H. K. N. Leung. 1987. Subglacial drainage for an ice sheet resting on a layered deformable bed. *J. Geophys. Res.*, **92**(B6), 4935–4946.

Shreve, R. L. 1972. Movement of water in glaciers. *J. Glaciol.*, **11**(62), 205–214.

Smart, C. C. and G. K. C. Clarke. Subglacial water release event: Trapridge Glacier, July 1986. *J. Glaciol.*, **submitted.**

Stenborg, T. 1969. Studies of the internal drainage of glaciers. *Geogr. Ann.*, **51A**(1–2), 13–41.

Stone, D. B. and G. K. C. Clarke. 1992. Estimation of subglacial hydraulic properties from induced changes in basal water pressure: a theoretical framework for borehole response tests. *J. Glaciol.*, **in press.**

Stone, D. B., G. K. C. Clarke, and E. W. Blake. 1992. Subglacial measurement of turbidity and electrical conductivity. *J. Glaciol.*, **in press.**

Tikhonov, A. N. and V. Y. Arsenin. 1977. *Solutions of ill-posed problems*, Washington, D.C., V. H. Winston and Sons.

Todd, D. K. 1959. *Groundwater Hydrology*, New York, John Wiley and Sons.

van der Kamp, G. 1976. Determining aquifer transmissivity by means of well response tests: the underdamped case. *Water Resour. Res.*, **12**(1), 71–77.

Verruijt, A. 1969. Elastic storage in aquifers, *in* DeWiest, R. J. M., *ed. Flow through porous media.* New York, Academic Press.

Walder, J. S. 1986. Hydraulics of subglacial cavities. *J. Glaciol.*, **32**(112), 439–445.

Walder, J. and B. Hallet. 1979. Geometry of former subglacial water channels and cavities. *J. Glaciol.*, **23**(89), 335–346.

Walder, J. S. and A. Fowler. 1992. Channelised subglacial drainage over a deformable bed. *J. Glaciol.*, **in press.**

Weertman, J. 1957. On the sliding of glaciers. *J. Glaciol.*, **3** (21), 33–38.

Weertman, J. 1962. Catastrophic glacier advances. *Publication No. 58 de l'Association Internationale d'Hydrologie*, 31–39.

Weertman, J. 1964. The theory of glacier sliding. *J. Glaciol.*, **5**(39), 287–303.

Weertman, J. 1972. General theory of water flow at the base of a glacier or ice sheet. *Rev. Geophys. Space Phys.*, **10**(1), 287–333.

Wilbur, S. Unpublished. Surging versus nonsurging glaciers: a comparison using morphometry and balance. (Ph.D. thesis, University of Alaska, 1988.)

Willis, I. C., M. J. Sharp, and K. S. Richards. 1990. Configuration of the drainage system of Midtdalsbreen, Norway, as indicated by dye-tracing experiments. *J. Glaciol.*, **36**(122), 89–101.

Appendix A

PHYSICAL BASIS OF THE FLUID FLOW EQUATION

A.1 Mass balance equations

Consider a fixed *representative elementary volume* (REV) in fixed coordinates. Fluids and solids may enter or leave the REV only through its surfaces. If ρ_f is the fluid density and n is porosity then the mass of fluid m_f in a fully saturated REV is

$$m_f = \int_V n\rho_f \, d^3r \tag{A1}$$

where the integral is over the total volume V of the REV. If fluid mass is conserved then

$$\frac{dm_f}{dt} = \int_V \left[\frac{\partial}{\partial t}(n\rho_f) + \frac{\partial}{\partial x_j}(n\rho_f v_j)\right] d^3r = 0 \tag{A2}$$

where v_j is the velocity of the fluid relative to the fixed coordinate system. In Equation (A2), and elsewhere, the summation convention is used for repeated indices. Since Equation (A2) must be valid for all REV volumes, the mass balance condition for the fluid component is

$$\frac{\partial}{\partial t}(n\rho_f) = -\frac{\partial}{\partial x_j}(n\rho_f v_j). \tag{A3}$$

Similarly, the solid mass m_s in the REV is

$$m_s = \int_V (1-n)\rho_s \, d^3r \tag{A4}$$

where ρ_s is the density of solids. Conservation of solid mass requires

$$\frac{dm_s}{dt} = \int_V \left[\frac{\partial}{\partial t}((1-n)\rho_s) + \frac{\partial}{\partial x_j}((1-n)\rho_s v_j)\right] d^3r = 0 \tag{A5}$$

where ν_j is the velocity of solids relative to the fixed coordinate system. Thus, the mass balance condition for solids is

$$\frac{\partial}{\partial t}((1-n)\rho_s) = -\frac{\partial}{\partial x_j}((1-n)\rho_s\nu_j). \tag{A6}$$

A.2 Equations of state

We assume that the individual equations of state for the fluid and solid components are as follows: individual solid grains are incompressible, so that

$$\rho_s = \text{constant}; \tag{A7}$$

fluid density is related to pressure p by

$$\rho_f = \rho_0 \exp(\beta(p - p_0)) \tag{A8}$$

where ρ_0 is the fluid density at the reference pressure p_0 and β is the coefficient of fluid compressibility—assumed to be constant under conditions of uniform concentration and temperature. Differentiating Equation (A8) and solving for the compressibility coefficient gives

$$\beta = \frac{1}{\rho_f}\frac{d\rho_f}{dp}. \tag{A9}$$

A.3 The storage equation

The mass balance conditions can be combined with the equations of state to obtain a relation between fluid flowing into or out of the REV and fluid storage within the REV. We will start by expanding Equation (A3):

$$\rho_f\frac{\partial n}{\partial t} + n\frac{\partial \rho_f}{\partial t} = -\rho_f\frac{\partial}{\partial x_j}(nv_j) - nv_j\frac{\partial \rho_f}{\partial x_j}. \tag{A10}$$

Since ρ_s is taken to be constant, Equation (A6) can be simplified and we may write

$$\frac{\partial n}{\partial t} = \frac{\partial}{\partial x_j}((1-n)\nu_j). \tag{A11}$$

Eliminating $\partial n/\partial t$ between Equations (A10) and (A11) yields

$$\rho_f \frac{\partial}{\partial x_j}((1-n)\nu_j) + n\frac{\partial \rho_f}{\partial t} = -\rho_f \frac{\partial}{\partial x_j}(n v_j) - n v_j \frac{\partial \rho_f}{\partial x_j}. \tag{A12}$$

At this point, it is convenient to cast all motions in terms of only one velocity. Following the developments of other authors (De Wiest, 1966; Cooper, 1966; Verruijt, 1969; Gambolati and Freeze, 1973; Clarke, 1987), we shall take the velocity of solids relative to the fixed coordinate system ν_j as our reference. In this case, the volume flux of water q_j relative to the solid matrix is $q_j = n(v_j - \nu_j)$, and Equation (A12) can be written as

$$\rho_f \frac{\partial}{\partial x_j}((1-n)\nu_j) + n\frac{\partial \rho_f}{\partial t} = -\rho_f \frac{\partial}{\partial x_j}(q_j + n\nu_j) - (q_j + n\nu_j)\frac{\partial \rho_f}{\partial x_j}. \tag{A13}$$

After rearrangement and simplification, Equation (A13) becomes

$$-\frac{\partial}{\partial x_j}(\rho_f q_j) = n\frac{d\rho_f}{dt} + \rho_f \frac{\partial \nu_j}{\partial x_j} \tag{A14}$$

where $d/dt = \partial/\partial t + \nu_j\, \partial/\partial x_j$ is the material derivative following motion of the solid grains. Now, from Equation (A9) we obtain

$$\frac{d\rho_f}{dt} = \rho_f \beta \frac{dp}{dt}. \tag{A15}$$

Combining this result with Equation (A14) gives

$$-\frac{\partial}{\partial x_j}(\rho_f q_j) = \rho_f \left(n\beta \frac{dp}{dt} + \frac{\partial \nu_j}{\partial x_j} \right). \tag{A16}$$

From a fixed frame of reference, the velocity of solids ν_j is related to the grain displacement vector $u_j = (u_x, u_y, u_z)$ by

$$\nu_j = \frac{du_j}{dt} \tag{A17}$$

(Cooper, 1966; Gambolati and Freeze, 1973). Furthermore, for small deformations, the incremental strain tensor ϵ_{jk} is defined by

$$\epsilon_{jk} = \frac{1}{2}\left(\frac{\partial u_j}{\partial x_k} + \frac{\partial u_k}{\partial x_j}\right) \tag{A18}$$

(e.g., Hunter, 1983, p. 113). From the last expression, it follows that the incremental volume strain $\epsilon = \epsilon_{jj}$ is given by

$$\epsilon = \frac{\partial u_j}{\partial x_j}. \tag{A19}$$

From Equations (A17) and (A19) we obtain

$$\frac{\partial \nu_j}{\partial x_j} = \frac{d\epsilon}{dt}, \tag{A20}$$

and Equation (A16) can be written as

$$-\frac{\partial}{\partial x_j}(\rho_f q_j) = \rho_f \left(n\beta \frac{dp}{dt} + \frac{d\epsilon}{dt}\right). \tag{A21}$$

The last expression is the storage equation; it shows that the divergence of the mass flux is balanced by the mass of fluid stored in the REV. Thus far our development has been based solely on expressions of mass conservation, equations of state, and the restriction that deformations are small. To make further progress we require expressions for fluid mass flux ($\rho_f q_j$) and incremental volume strain ϵ in terms of the pressure p. These quantities are related by the individual constitutive equations for fluid and solid components.

A.4 Mechanical behavior of the porous medium

In general, the REV will be subjected to an external stress exerted by the surrounding medium, and to an internal stress from the fluid that fills the pores. The external stress will be balanced by intergranular stresses in the matrix and by the hydrostatic pressure in the fluid. Thus, the total stress τ_{jk} acting on the REV can be decomposed into two

components: the effective stresses τ'_{jk}, which represent intergranular forces distributed over the surface area of contact between grains, and the fluid pressure p. For any slice through the REV, a portion of the plane will be occupied by solid-solid contacts. If θ denotes this fraction of the plane area then

$$\tau_{jk} = \tau'_{jk} - (1-\theta)p\,\delta_{jk} \tag{A22}$$

where δ_{jk} is the Kronecker delta (e.g., Bird and others, 1960 p. 719). In Equation (A22) positive fluid pressure means compression and positive stresses mean tension, in accordance with the usual sign convention. For most cases the actual value of θ is small ($\theta \ll 1$) (Bear, 1972, p. 54), so that Equation (A22) reduces to

$$\tau_{jk} = \tau'_{jk} - p\,\delta_{jk} \tag{A23}$$

As a first approximation, our considerations will be restricted to small changes from an initially steady state. If we represent these changes by excursions of incremental total stress σ_{jk}, incremental effective stress σ'_{jk}, and incremental fluid pressure σ then we may write

$$\begin{aligned} \tau_{jk} &= \tau^{(0)}_{jk} + \sigma_{jk} \\ \tau'_{jk} &= \tau'^{(0)}_{jk} + \sigma'_{jk} \\ p &= p^{(0)} + \sigma \end{aligned} \tag{A24}$$

where the superscript (0) denotes the initially steady state. Substitution of Equation (A24) into Equation (A23) yields

$$\sigma_{jk} = \sigma'_{jk} - \sigma\delta_{jk}, \tag{A25}$$

since $\tau^{(0)}_{jk} = \tau'^{(0)}_{jk} - p^{(0)}\delta_{jk}$ in the initial state.

In the field of soil mechanics it is widely known that deformation of a saturated porous medium is a complex process; typically it may be nonlinear, partially irreversible, hysteretic, and dependent on strain history. At present, rigorous and realizable descriptions of the properties that govern this behavior are unavailable. Thus, the usual approach—taken in both soil mechanics and groundwater theories—is to assume that the material behaves as a perfectly linear, elastic solid (e.g., Schofield and Wroth, 1968; Biot, 1941, 1955; Verruijt, 1969; Rice and Cleary, 1976). Obviously, the resulting description will only approximate the true behavior of the porous medium. Under this assumption, deformations of the REV are related to the incremental effective stress by Hooke's law. In terms of the Lamé constants, λ and μ, Hooke's law can be written as

$$\sigma'_{jk} = \lambda\epsilon\delta_{jk} + 2\mu\epsilon_{jk}. \tag{A26}$$

Substituting Equation (A18) into Equation (A26) gives

$$\begin{aligned} \sigma'_{xx} &= \lambda\epsilon + 2\mu(\partial u_x/\partial x), \quad \sigma'_{xy} = \mu(\partial u_x/\partial y + \partial u_y/\partial x) \\ \sigma'_{yy} &= \lambda\epsilon + 2\mu(\partial u_y/\partial y), \quad \sigma'_{yz} = \mu(\partial u_y/\partial z + \partial u_z/\partial y) \\ \sigma'_{zz} &= \lambda\epsilon + 2\mu(\partial u_z/\partial z), \quad \sigma'_{zx} = \mu(\partial u_z/\partial x + \partial u_x/\partial z) \end{aligned} \tag{A27}$$

where it is assumed that the stress tensor is symmetric, so that $\sigma'_{jk} = \sigma'_{kj}$.

A.4.1 Coefficient of compressibility for the porous medium

Although individual grains are assumed to be incompressible and the compressibility of water is very small, the porous medium itself will be compressible if water can escape during compression. A rigorous description of three-dimensional deformation was given by Biot (1941, 1955). However, this description requires an unrealistically large number of parameters to fully characterize the porous medium. To formulate a tractable problem, the true behavior of the porous medium is further approximated by the following assumption: as the volume of pore fluid in the REV changes, displacements occur only

in one direction, and that in this direction the total stresses do not change. Gambolati and Freeze (1973) have pointed out that this assumption is both unsubstantiated and ubiquitous: "The worth of this assumption has never been tested, but it underlies all developments of the classical groundwater flow equation."

If we assume that displacements occur only in the vertical direction then

$$\epsilon = \frac{\partial u_z}{\partial z}. \tag{A28}$$

Also, if the total stresses in the vertical direction do not change then

$$\sigma_{zz} = 0, \tag{A29}$$

since σ_{zz} is the incremental stress component. From Equations (A27) and (A28) we have

$$\sigma'_{zz} = (\lambda + 2\mu)\epsilon. \tag{A30}$$

With Equations (A25) and (A29) we obtain

$$\sigma'_{zz} = \sigma. \tag{A31}$$

Eliminating σ'_{zz} between Equations (A30) and (A31) gives

$$\epsilon = \left(\frac{1}{\lambda + 2\mu}\right)\sigma. \tag{A32}$$

Differentiating Equation (A32) and the fluid pressure relation in Equation (A24), and combining the results with the storage equation (A21), we obtain

$$-\frac{\partial}{\partial x_j}(\rho_f q_j) = \rho_f(\alpha + n\beta)\frac{dp}{dt} \tag{A33}$$

where $\alpha = (\lambda + 2\mu)^{-1}$ is the compressibility coefficient for the porous medium. It should be noted that α is not necessarily a physical constant; we have only considered

small changes from an initially steady state, and the values of λ and μ may vary with the initial state of stress. In the present development, these parameters are assumed to be constants only for a given increment of deformation.

A.5 Simplifying assumptions

Cooper (1966) pointed out that formulations in fixed coordinates, as we have done here, lead to difficulties in the compressibility term for the porous medium. In particular, α has meaning only for a fixed mass of moving solids, whereas p is defined at a fixed elevation z. He demonstrated that this difficulty can be avoided by reformulating the development in terms of a deforming coordinate system that moves with the velocity of solids; for a coordinate system moving with velocity v_j, the material derivative becomes equal to the partial derivative. In fixed coordinate system developments, the material derivative is usually replaced by the partial derivative by assuming that temporal pressure changes are much greater than the rate at which pressure gradients are advected by motion of the solid skeleton:

$$\frac{\partial p}{\partial t} \gg v_j \frac{\partial p}{\partial x_j}. \tag{A34}$$

Further simplification arises if it is assumed that

$$\frac{1}{q_j}\frac{\partial q_j}{\partial x_j} \gg \frac{1}{\rho_f}\frac{\partial \rho_f}{\partial x_j}. \tag{A35}$$

With these assumptions Equation (A33) reduces to

$$-\frac{\partial q_j}{\partial x_j} = \rho_f(\alpha + n\beta)\frac{\partial p}{\partial t}. \tag{A36}$$

A.6 Relationship between fluid pressure and hydraulic head

Fluid pressure is related to hydraulic head h_B as follows: Let ψ be the height of a water column above a point $\mathcal{P}(x, y, z)$ where z is the elevation of $\mathcal{P}$ relative to some datum.

If p_a is the atmospheric pressure acting at the top of the column then the fluid pressure at $\mathcal{P}$ is $p = \rho_f g\psi + p_a$ where g is the acceleration due to gravity. The hydraulic head at $\mathcal{P}$ is given by the relationship

$$h_B = \frac{v_j v_j}{2g} + \psi + z \tag{A37}$$

(de Marsily, 1986, p. 50). In porous media, flow velocities are typically such that kinetic energy losses are dominated by loss of potential energy. If it is assumed that the dynamic head contribution is negligible relative to the piezometric head contribution,

$$\frac{v_j v_j}{2g} \ll \psi + z, \tag{A38}$$

a simplified expression for the hydraulic head at $\mathcal{P}$ is obtained: $h_B = \psi + z$. In this case

$$p = \rho_f g(h_B - z) + p_a. \tag{A39}$$

Differentiating the last expression gives

$$\frac{dp}{dt} = \frac{d}{dt}\left(\rho_f g(h_B - z)\right) + \frac{dp_a}{dt}. \tag{A40}$$

Since the elevation of $\mathcal{P}$ does not change with time, $dz/dt = 0$. Furthermore, $dp_a/dt = 0$ is implicit in condition (A29). Thus, Equation (A40) can be simplified as

$$\frac{dp}{dt} = \rho_f g\beta(h_B - z)\frac{dp}{dt} + \rho_f g\frac{dh_B}{dt} \tag{A41}$$

where we have used Equation (A15) to replace the derivative of fluid density with the derivative of pressure. Because we are considering only small changes, we can make the quantity $h_B - z$ small by a suitable positioning of the datum. Furthermore, if the fluid is only very slightly compressible (water, for instance, has $\beta \approx 10^{-10}\ \mathrm{Pa}^{-1}$) then

the term $\rho_f g\beta(h_B - z) \ll 1$. Thus, the first term on the right-hand-side of Equation (A41) is negligible and we are left with

$$\frac{dp}{dt} = \rho_f g \frac{dh_B}{dt}. \tag{A42}$$

If condition (A34) applies to both fluid pressure and hydraulic head then the last expression reduces to

$$\frac{\partial p}{\partial t} = \rho_f g \frac{\partial h_B}{\partial t}, \tag{A43}$$

and Equation (A36) can be rewritten in terms of hydraulic head as follows:

$$-\frac{\partial q_j}{\partial x_j} = \rho_f g(\alpha + n\beta)\frac{\partial h_B}{\partial t}. \tag{A44}$$

A.7 Concluding remarks

The theory presented here is not new; it is a synthesis of many previous developments. In particular, we have relied on publications by Verruijt (1969) and by Gambolati and Freeze (1973). Our main purpose was to clearly identify the basic assumptions upon which Equation (A44) is founded. In this appendix we have shown that the success of the final equation depends on six fundamental assumptions: the extent to which the saturated, porous medium behaves as a perfectly linear elastic solid, and the satisfaction of conditions (A28), (A29), (A34), (A35), and (A38).

Appendix B

NUMERICAL FORMULATION OF THE BHRT MODEL

Numerical solution of the borehole response-test (BHRT) model is facilitated by using two staggered finite-difference grids upon which nodes are spaced at constant logarithmic intervals. Details of the numerical formulation are given in this appendix.

B.1 Basic equations of the model

The basic equations of the model are

$$h\frac{d^2h}{dt^2} + \left[\left(\frac{8\eta}{\rho_w r_w^2}\right) h\frac{dh}{dt}\right] + gh = g\left(h_B(r_f) - h_T\right), \qquad (B1)$$

$$-\frac{1}{r}\frac{\partial}{\partial r}(r\,q) = S_s\frac{\partial h_B}{\partial t}, \qquad (B2)$$

$$q = -(2K)\frac{\partial h_B}{\partial r}\left[1 + \left(1 + C_2\left|\frac{\partial h_B}{\partial r}\right|\right)^{\frac{1}{2}}\right]^{-1}, \qquad (B3)$$

and

$$q(r_f) = -\left(\frac{{r_w}^2}{2r_f b}\right)\frac{dh}{dt} \qquad (B4)$$

where $C_2 = K^2BS_0(1-n)/2gn^3$ and $S_s = \rho_w g(\alpha + n\beta)$. Expressions (B1)–(B4) correspond to Equations (3.11), (3.20), (3.19), and (3.26) respectively. (The symbols have the same meanings as those used in Chapter 3.) For the subglacial flow layer, the inner boundary condition is given by Equation (B4). At the outer boundary, the prescribed condition may be either constant head

$$h_B(r_{max}) = h_0, \qquad (B5a)$$

or zero head gradient

$$\frac{\partial h_B(r_{max})}{\partial r} = 0. \qquad (B5b)$$

B.2 Finite-differencing

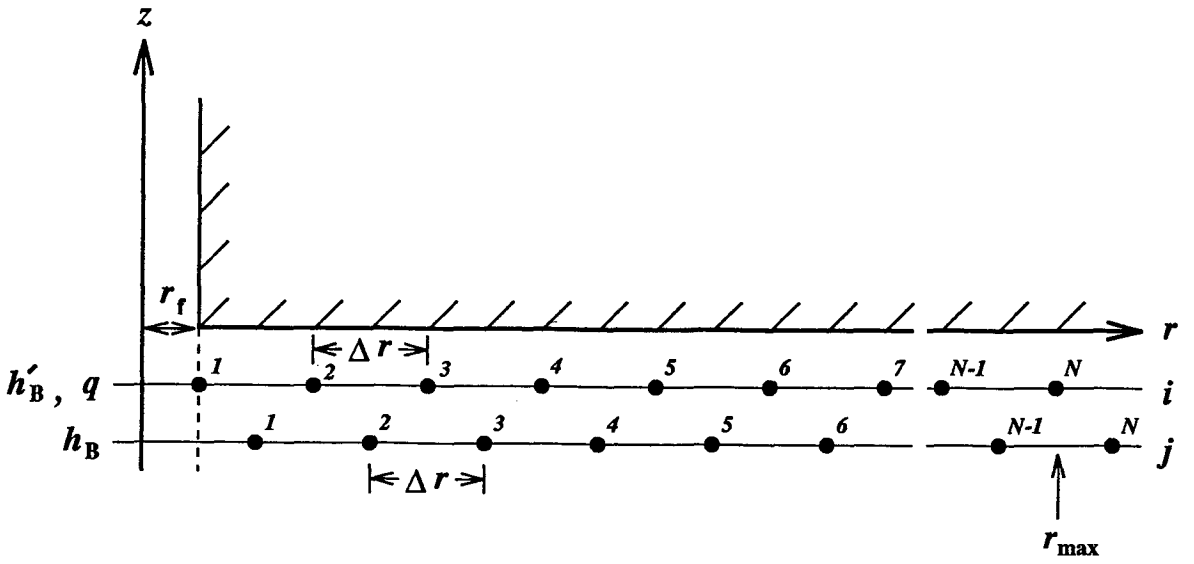

Fig. B.1: Staggered finite-difference grids.

Consider the two staggered grids shown in Figure B1. Each grid has N evenly spaced nodes, and the grids are offset by an amount $\Delta r/2$. The hydraulic head h_B is specified on the j grid, and the head gradient $\partial h_B/\partial r$ and the volume flux q are calculated on the i grid. In terms of these grids, a node-centered, finite-difference expression for the hydraulic head gradient is

$$h'_{Bi} = \frac{1}{\Delta r}\left(h_{Bj}\right)_{i-\frac{1}{2}}^{i+\frac{1}{2}}$$
$$= \frac{1}{\Delta r}\left(h_{Bj=i} - h_{Bj=i-1}\right) \qquad (B6)$$

where the prime indicates a numerical derivative and the subscripts i and j refer to nodes on the appropriate grid.

To obtain a grid having constant logarithmic nodal spacing, we use the transformation

$$R = \ln\left(r/r'\right) \qquad (B7)$$

where $r' = 1.0\,\mathrm{m}$ is a nondimensionalizing constant. Thus, we may write

$$\frac{\partial R}{\partial r} = \frac{1}{r} = \exp(-R), \tag{B8a}$$

$$\frac{\partial}{\partial r} \longrightarrow \frac{\partial}{\partial R}\left(\frac{\partial R}{\partial r}\right) \longrightarrow \exp(-R)\frac{\partial}{\partial R}, \tag{B8b}$$

and

$$\frac{1}{r}\frac{\partial}{\partial r} \longrightarrow \exp(-2R)\frac{\partial}{\partial R}. \tag{B8c}$$

From Equation (B8b) we see that $\partial h_B/\partial r = \exp(-R)(\partial h_B/\partial R)$, so that Equation (B6) becomes

$$h'_{Bi} = \exp(-R_i)\frac{1}{\Delta R}\left(h_{Bj=i} - h_{Bj=i-1}\right). \tag{B9}$$

Note that for N nodes and a maximum radius r_{max}, the constant logarithmic nodal spacing is $\Delta R = (\ln r_{max} - \ln r_f)/(N-1)$.

B.3 Volume flux and fluid flow expressions

With Equation (B9), numerical expressions for the volume flux are as follows:
for $i = 1$,

$$q_1 = -\left(\frac{{r_w}^2}{2r_f b}\right)\frac{dh}{dt}; \tag{B10a}$$

for $i = 2, N-1$,

$$q_i = (-2K)h'_{Bi}\left[1 + (1 + C_2\,|h'_{Bi}|)^{\frac{1}{2}}\right]^{-1}; \tag{B10b}$$

for $i = N$,

$$q_N = (-2K)h'_{BN}\left[1 + (1 + C_2\,|h'_{BN}|)^{\frac{1}{2}}\right]^{-1} \tag{B10c}$$

(constant head boundary) or

$$q_N = 0 \qquad (B10d)$$

(zero flux boundary—since $h'_B = 0$).

Fluid flow in the aquifer is governed by Equation (B2). Computational efficiency is enhanced by **not** eliminating q from this equation. Having obtained numerical expressions for q (Eqns. B10), we can replace the partial derivative $\partial/\partial r$ in Equation (B2) with a finite-difference approximation, eliminating the need for second derivative evaluations. This procedure is based on the numerical method of lines (Schiesser, 1991); it reduces the PDE (Eqn. B2) to an ODE. Using Equation (B8c), the finite-difference approximation of Equation (B2) is

$$\begin{aligned} S_s\left(\frac{dh_B}{dt}\right)_j &= -\frac{1}{r_j}\exp(-R_j)\frac{1}{\Delta R}(r_i\, q_i)_{j-\frac{1}{2}}^{j+\frac{1}{2}} \\ &= -\exp(-2R_j)\frac{1}{\Delta R}\left(\exp(R_{i=j+1})\, q_{i=j+1} - \exp(R_{i=j})\, q_{i=j}\right) \qquad (B11) \end{aligned}$$

where we have included an intermediate step to make clear the connection between the two grids. The right-hand-side of Equation (B11) is a straightforward algebraic expression; if the hydraulic head is specified at all points on the j grid then the right-hand-side quantities can be obtained directly from Equations (B7), (B9), and (B10).

B.4 Borehole water flow expression

To proceed, we define $(N+1)$ integration variables y_j as follows:

$$y_j = \begin{cases} h_{Bj} & (j = 1, N-1) \\ h & (j = N) \\ \dfrac{dh}{dt} & (j = N+1). \end{cases}$$

Using these definitions, we can rewrite the equation governing water flow in the borehole (B1) as

$$y_N \frac{d}{dt}(y_{N+1}) + \left(\frac{8\eta}{\rho_w r_w^2}\right) y_N\, y_{N+1} + g\, y_N = g\,(y_1 - h_T)\,.$$

Dividing the last expression by y_N, and using the fact that $d/dt(y_N) = y_{N+1}$, we obtain

$$\frac{d}{dt}(y_{N+1}) = \frac{1}{y_N}\,[g(y_1 - h_T - y_N)] - \left(\frac{8\eta}{\rho_w r_w^2}\right) y_{N+1}. \qquad (B12)$$

B.5 Basic algorithm

At the beginning of every time step the hydraulic head h_B is known for all nodes on the j grid, either from initial conditions or from the solution at the previous time step. With this information, head gradients are calculated at nodal points on the i grid according to Equation (B9). Once head gradient values have been computed, the flux-vector components are obtained directly from Equations (B10); note that $dh/dt = y_{N+1}$ is an integration variable that is also known, either from initial conditions or from a prior solution. Having computed numerical values for the components of q_j, we use an implicit, fifth-order Runge–Kutta scheme to solve the system of $(N+1)$ equations arising from (B11) and (B12); namely,

$$\frac{d}{dt}(y_j) = \begin{cases} \left[\dfrac{\exp(R_{i=j})\, q_{i=j} - \exp(R_{i=j+1})\, q_{i=j+1}}{\exp(2R_j)\, S_s\, \Delta R}\right] & (j = 1, N-1) \\ y_{N+1} & (j = N) \\ \dfrac{1}{y_N}\,[g(y_1 - h_T - y_N)] - \left(\dfrac{8\eta}{\rho_w r_w^2}\right) y_{N+1} & (j = N+1). \end{cases}$$